AD-758 626

STRENGTH OF PLASTICS

Ya. Nemets, et al

Foreign Technology Division
Wright-Patterson Air Force Base, Ohio

15 January 1973

FTD-HC-23-1044-72

FOREIGN TECHNOLOGY DIVISION

STRENGTH OF PLASTICS

by

Ya. Nemets, S. V. Serensen, V. S. Strelyayev

Approved for public release;
Distribution unlimited.

UNCLASSIFIED

Security Classification

DOCUMENT CONTROL DATA - R & D

(Security classification of title, body of abstract and indexing annotation must be entered when the overall report is classified)

1. ORIGINATING ACTIVITY (Corporate author) Foreign Technology Division Air Force Systems Command U. S. Air Force	2a. REPORT SECURITY CLASSIFICATION UNCLASSIFIED 2b. GROUP

3. REPORT TITLE

STRENGTH OF PLASTICS

4. DESCRIPTIVE NOTES (Type of report and inclusive dates)

Translation

5. AUTHOR(S) (First name, middle initial, last name)

Ya. Nemets, S. V. Serensen, V. S. Strelyayev

6. REPORT DATE 1970	7a. TOTAL NO. OF PAGES 370 376	7b. NO. OF REFS 216
8a. CONTRACT OR GRANT NO. b. PROJECT NO. c. d. T70-01-11	9a. ORIGINATOR'S REPORT NUMBER(S) FTD-HC-23-1044-72 9b. OTHER REPORT NO(S) (Any other numbers that may be assigned this report)	

10. DISTRIBUTION STATEMENT

Approved for public release; distribution unlimited.

11. SUPPLEMENTARY NOTES	12. SPONSORING MILITARY ACTIVITY Foreign Technology Division Wright-Patterson AFB, Ohio

13. ABSTRACT

Results are presented of studies of the resistance of reinforced and unreinforced structural plastics to static and fatigue failure. Attention is devoted to the formation and development of brittle fracture of plexiglas and polystyrene with account for the role of the residual stresses, the deformation and fracture of glass reinforced plastics under static and low-cycle loads, and also fatigue processes in connection with energy dissipation and the fracture condition temporal relationships. The use of the relations governing the resistance of plastics to deformation and fracture for evaluating the strength of structural elements is examined. The book is intended for design engineers, factory laboratory personnel, scientific research workers, and the design institutes.

DD FORM 1 NOV 68 1473

UNCLASSIFIED

Security Classification

14. KEY WORDS	LINK A		LINK B		LINK C	
	ROLE	WT	ROLE	WT	ROLE	WT
Reinforced Plastic Brittle Fracture Fatigue Test Static Test Plastic Strength						

EDITED TRANSLATION

FTD-HC-23-1044-72

STRENGTH OF PLASTICS

By: Ya. Nemets, S. V. Serensen, V. S. Strelyayev

English pages: 370

Source: Prochnost' Plastmass, 1970, pp. 1-336.

Translated Under: F33657-72-D-0853

Requester: FTD/PDTI

PREPARED BY:

TRANSLATION DIVISION
FOREIGN TECHNOLOGY DIVISION
WP-AFB, OHIO.

ic

ABSTRACT

Results are presented of studies of the resistance of reinforced and unreinforced structural plastics to static and fatigue failure. Attention is devoted to the formation and development of brittle fracture of plexiglas and polystyrene with account for the role of the residual stresses, the deformation and fracture of glass reinforced plastics under static and low-cycle loads, and also fatigue processes in connection with energy dissipation and the fracture condition temporal relationships. The use of the relations governing the resistance of plastics to deformation and fracture for evaluating the strength of structural elements is examined. The book is intended for design engineers, factory laboratory personnel, scientific research workers, and the design institutes.

INTRODUCTION

The second half of this century has been marked by a rapid growth in plastic research and production. The broad use of these materials in industry, particularly as structural materials, makes necessary a more profound study of the limiting states of the plastics, which frequently cannot be carried out on the basis of the simple classical tests for determining mechanical properties. The complex shapes and large dimensions of the components of machines and instruments, the nature of the loading, the load variation with time, and the long loading duration in comparison with the standard tests limit the possibility of directly using the results of such tests in evaluating the strength and service life of actual parts. However, it is not advisable to complicate excessively the test methods and give up entirely the old test methods until better and more modern methods have been found for determining the limiting states of the parts under various loading conditions.

We must first of all study the laws governing deformation of the materials and fracture of the parts. It has been established that material defects, particularly in the surface layer, have a decisive influence on strain concentration and onset of damage zones, in which the first cracks later develop. The growth of these cracks takes place differently, depending on whether the loading is static or cyclic. Study of fractures during instantaneous, slow, and cyclic fatigue failure processes makes it possible to find the bases for developing fracture theory.

Stress concentration and local material damage lead to crack formation. A necessary condition for such damage is localization of the strain, whose growth in the material defect zones differs markedly in magnitude and distribution of the strains from the deformation of the specimen as a whole when subjected to standard tensile testing. Even in the case with uniform stress distribution, the material damage is distributed nonuniformly in the material volume and is always concentrated in zones of small dimensions in the vicinity of surface defects. In view of this situation, the possibilities for studying and predicting initial crack formation on the basis of the average values of the material properties as determined in the standard tests are limited.

Crack formation can be successfully studied on the basis of the theory of a quasi-homogeneous medium. Moreover, since we are considering a process which is not associated with bulk damage accumulation, fracture mechanics can be studied on the basis of linear theories. The data available show that the limiting states of the materials of the subject class depend to a considerable degree on the "structural stiffness," defined by such material characteristics as the elastic modulus E and the specific energy K necessary for the development of a new surface in the material. Materials can be divided into three groups depending on the value of K.

If $K < 1$, the material can be considered brittle; for $1 < K < 100$, it is quasi-brittle; and for $K > 100$, it is plastic. Most widely used in engineering are the materials having high values of $\sqrt{EK}$ and of static strength under short-term loading, characterized by the ultimate strength σ_b. In this connection, we can assume that the future belongs to the composite materials, consisting of a plastic or polymer matrix with large values of K and strong fibers which provide high material ultimate strength. With the correct relationship between the volumes of these component parts and a rational form of the fibers, such materials will have low sensitivity to stress concentration and internal defects, and will also have good resistance to creep and fatigue under long-term loading. The development of composite materials is clearly a more realistic approach to providing strength of large structures

than are the attempts to create defect-free homogeneous material. However, criteria have not yet been developed for the resistance to the appearance and growth of cracks in these materials, which have several unusual features in their fracture mechanics.

K kgf·cm/cm^2	E kgf/cm^2	Materials and Conditions
To 0.01	10^4	Perfectly brittle (very low temperature)
From 0.01 to 0.1	From 10^4 to 10^5	Glass, ceramics
From 0.1 to 1	10^4 to 10^5	Polymers in brittle condition
From 1 to 10	10^5 to 10^6	Some viscous polymers and crystalline synthetic materials, cast
From 10 to 100	Over 10^6	Tempered steels, hard steels at temperature below critical
Over 100	Over 10^6	Structural steels

A study of the fracture process and statistical interpretation of this process makes it possible to establish governing laws which will also be useful in the future development of new synthetic materials.

A large number of studies have now been published on investigations of the mechanical properties of the homogeneous and reinforced polymers in the physical, physical-chemical-mechanical, and mechanical aspects. Here the empirical method gives way to a more profound study of the composite material formation techniques. The development of theoretical and experimental studies of composite material strength and stiffness as a function of their structure and structural-fabrication characteristics will provide further progress in this field.

The composite materials based on reinforcing fibers and polymer matrixes are two-phase heterogeneous systems in which the strength and loading of the reinforcing elements have random variations. Transition of such a system to the limiting state will be gradual through the stage of quasi-equilibrium states. This then defines the necessity for a probabilistic approach to examining composite strength

in light of their progressive failure, determining the strength distribution functions and their parameters, and also to structural element strength calculation based on the failure probability criterion, which has not yet been adequately developed for the composite materials.

Systematization of the experimental data on reinforced composite resistance to failure and deformation using governing laws based on the classical assumptions of mechanics of a solid deformable body shows that several characteristics are structure-sensitive, including the size effect, stress gradient influence on the strength, incomplete sensitivity to stress concentration, influence of loading conditions on the strength, dispersion of the strength and elasticity characteristics; and to explain the experimental results it is necessary to use statistical methods and develop the corresponding similarity relationships.

In order to ensure structural element service life while retaining minimal element weight, we must evaluate the allowable stresses for the specified degree of discontinuity of the initial structure, which can be done by considering the process of monotonic and long-term static fracture as a process of progressive damage accumulation in connection with variance of the reinforcing element strength. Therefore, we also need experimental and theoretical justification for the service life distribution function as a function of the stress level, and we need to work out the strength temperature-time relationships as a function of the fracture probability parameter.

In many loading and stress distribution cases, fracture dimorphism may occur as a result of low inter-layer shear strength, and the load-carrying ability of the structural element is determined by the low shear strength of the polymer matrix.

In this book, we examine basically those questions associated with the fracture of both homogeneous and reinforced plastics. In Chapter 1, we show the influence of defects on the brittle static strength of unreinforced plastics and present the corresponding experimental data. In Chapter 2, we analyze the kinetics of fatigue crack

growth in homogeneous plastics under static and cyclic loading within the framework of the temporal concept of strength. The theoretical results are examined in the light of experimental data. Several of the relationships obtained are applicable to calculating the strength and service life of structural parts.

In Chapters 4 through 9, we discuss glass reinforced plastic (GRP) strength. Results are presented of a study of the strength of the reinforcing fibers and the stress-state of the components in the regular GRP structures. Static strength is examined on the basis of statistical representations of the progressive fracture of fibers which are not uniform in strength. The similarity relations applicable to glass reinforced plastic fracture for the uniform stress state and in stress concentration zones are characterized. Experimental data are presented for the GRP failure model and for the statistical evaluation of their parameters. These data are used to justify the allowable stresses and evaluate the failure probability.

The fracture resistance of the glass reinforced plastics under long-term loading is treated as a stochastic process, and the cyclic failure characteristics resulting from the dissipative properties of the glass reinforced plastics are presented. Examples are given of practical strength calculations for the short-term and long-term loading cases.

The publication of the present collection of articles on strength of plastics will be of assistance in acquainting the readers with several new results obtained in the Soviet Union and in the Czechoslovak SSR in this field.

CHAPTER 1

INFLUENCE OF MATERIAL DEFECTS ON FRACTURE MECHANICS*

§1. Theory of Brittle Material Strength

The existing theoretical works and experimental studies in the field of the strength of detail parts made from brittle materials have made it possible to obtain many valuable data on the strength of quasi-homogeneous polymer materials in the glassy hard state. At a sufficiently low temperature, these materials have a tendency toward brittle fracture as a result of rapid fracture crack growth.

In the course of investigations, we examine the static conditions of crack instability in the material as a continuous medium and study the dynamics of crack propagation under certain simplifying assumptions. The phenomenological theories which have been developed are useful for engineering calculations of the strength of quasi-homogeneous materials. In order to evaluate the influence of defects and stress concentrations on the strength of detail parts, we shall examine the known data on this question.

---

*(The specimen tests under brittle fracture conditions whose results are presented in this chapter were performed by I. Zemankov.)

1. Each open defect, which is a free surface of the body and leads to local decrease of the stress state potential energy U_y, may, for certain dimensions, become unstable if the growth of such a defect is not prevented by the surface tension energy barrier U_ν. This basic hypothesis was formulated for a perfectly brittle homogeneous material [1]. For a flat plate of thickness h and width $B \gg h$, with a defect of the subject type oriented perpendicular to the uniaxial tensile stress σ, we obtain from the crack propagation energy condition $\frac{\partial U_c}{\partial l} = 0$, where $U_c = -U_y + U_\nu$ (Figure 1), the expression

$$\sigma_{n\,cr} = \sqrt{\frac{2}{\pi} \cdot \frac{EU_\nu}{l_{cr}}}, \qquad (1)$$

where U_ν — specific surface tension energy in kgf·cm/cm²;

E — material elastic modulus under the assumption that the material is elastic, isotropic, and homogeneous;

l — length of a through crack in the plate. In deriving this formula, we take into account the surface tension energy $2lhU_\nu$ on both sides of the crack.

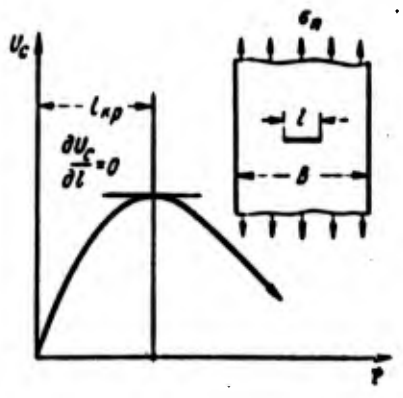

Figure 1. Schematic of energy balance defining defect growth conditions in a plane brittle material specimen.

The energy conditions in this form do not take into consideration the instantaneous stress state at the edge of the crack, and the limiting state is assumed to be independent of specimen size. Thus, we find that the strength of a specimen with a defect depends only on the defect size and the material properties. Formula (1) can be made somewhat more general if we do not examine the stress state in the entire plate, but rather determine the maximum stress at the crack edge in terms of the stress concentration factor and nominal stress $\sigma_{max} = \sigma_n \alpha$ [132, 171]. In this way, we can find the dependence of the limit stress for a brittle material

specimen on the stress concentration factor. In the case of a sharp crack with minimum radius of curvature at the edge, $\rho = a$ (for $\frac{\rho}{l} \ll 1$)

$$\alpha \approx \text{const} \sqrt{\frac{l}{a}}, \tag{2}$$

where a — characteristic dimension of an element of the material structure. Since for a perfectly elastic material with regular atomic or molecular structure $E = \frac{2U_v}{a}$, the above formula can be written in the form

$$\sigma_{прод} = \frac{\sigma_{max}}{\alpha_{кр}} = \text{const} \sqrt{\frac{EU_v}{l_{кр}}}. \tag{3}$$

Consequently, the limit stress $\sigma_b = \sigma_{lim}$ for a perfectly brittle material is inversely proportional to the stress concentration factor corresponding to the initial defect from which the brittle fracture crack develops. In this approach, the stress corresponding to defect propagation is identified with the specimen ultimate strength, which is equivalent to the determining influence of the strength of the weakest part of the specimen on its strength. To obtain a more general model, we can broaden the conditions of application of the relation (3) with account for the influence of specimen size and shape. Formula (2) was derived for a crack of small dimensions in a plate of infinite dimensions. Since, in the general case, α depends on the crack dimensions, its orientation relative to the edges of the specimen, and the nature of the stress state, the specimen strength in the brittle fracture case will also depend on these factors. It should be noted that, in this case, the maximum stress σ_{max} at the crack edge [169] will reach a value at the instant of material fracture, which is determined by the forces of interatomic or intermolecular cohesion. This situation makes it possible to obtain the basic condition for brittle body fracture, expressed by the formula

$$P_{прод} = \text{const}\, \sigma_{max} uh = \sigma_{прод} lh. \tag{4}$$

2. For real materials at temperatures below the solidification point, the properties characteristic for the ideally brittle bodies are not observed, i.e., mutual separation of the atoms while retaining the initial structure does not occur in the vicinity of the crack edges. The complex molecular structure, the form and bonding of the molecular chains, and their orientation with respect to the direction of the stresses acting in the most highly stressed zone at the defect edge, lead to a different nature of the fracture process in different cases for the same defect length and edge rounding radius [146]. In one case, a new v-shaped crack, oriented perpendicular to the maximum tensile stress direction, arises at the defect edge. At the end opposite the point of origin, the edges of this crack converge and transition into the zone where the material integrity is not yet disrupted, however, the material has already undergone large plastic deformations and has acquired — as a result of deformation — a clearly oriented structure, and where part of the internal bonds in the material are already broken [11]. Near cracks of this sort, the described transitional zone is highly localized; in this zone, we observe a very high strain rate and the material capability for plastic deformation is rapidly exhausted [169]. Cracks of the other type do not have such a sharp edge on the unfractured material side. This crack has the nature of a crack with rounded edge near which, once again, there forms a zone of irreversible material deformation which is considerably larger in volume than in the sharp crack case. In the case of this sort of defect, the material retains adequate capability for plastic deformation even with a high deformation rate, which leads to crack edge expansion, considerable transverse narrowing, and formation of a plastic deformation zone. As a result of this, the stress concetration decreases, and the crack becomes less "sharp." Crack growth slows or terminates entirely, and specimen fracture takes place as a result of the occurrence of new cracks of the v-shaped type. The nonhomogeneous structure, the complex residual stress distribution in the microvolumes of the material, and also the nature of the molecular chain orientation with respect to the effective stress direction, complicate the nature of thermoplastic polymer material fracture in the glassy state. The random nature of the distribution of the weak places in the material structure at the edge of the macrodefects leads

to considerable scatter of the data in determining the influence of defects on the strength of these materials under brittle fracture conditions. However, in all cases it is necessary to consider the fact that, prior to fracture of a part made from structural materials, a zone of large irreversible deformations forms at the edge of the defect. Depending on the material structure in the defect zone and the type of defect, the size of the plastically deformed region will be different and crack growth may be determined by different criteria. In one case, the maximum normal stress criterion is controlling; in another, the maximum tangential stress criterion is the controlling factor. In the following, we examine fracture cases which are characterized by minimum resistance to brittle fracture and by minimum duration of loading to fracture. Accordingly, we examine sharp cracks of the v-shaped type and conditions when the maximum tensile stress is the determining factor. Here we assume the existence at the crack edge of a transitional material zone with high local damage level.

In the transition zone ahead of the crack edge, there is accumulation of the material structure defects as a result of large irreversible deformations. In this connection, the energy expended prior to reaching the defect propagation conditions is greater than the expected quantity U_v. We shall assume that, to reach the limiting state, it is necessary to supply the specific energy for the formation of 1 cm^2 of new free surface in the material, determined from the formula $K = U_v + W(T, v_\varepsilon)$. The quantity W depends on the transition zone size and the material capability for local irreversible deformation without loss of integrity [132]. We shall term this quantity the limit local work of deformation. The value of W is determined by the density D of the intermolecular defects which form in the material structure per unit transition zone volume and the specific energy w of these defects: $W = Dws$. Since this specific energy is a function of temperature T and loading rate v_ε, the over-all energy K required for the formation of unit fracture surface also depends on the material temperature and loading conditions. Therefore, specimen strength under brittle fracture conditions is a function of the material loading conditions and temperature. For a specimen deformation rate at the end sections v_ε, the material deformation rate in the transition

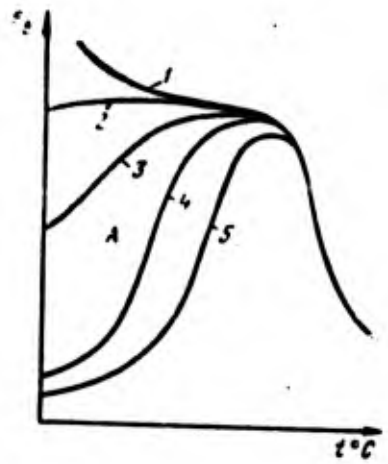

Figure 2. Static material strength as a function of defect size l and stress concentration α:

$1 - \alpha = 1,\ l = 0;\ 2 - \alpha_1,\ l_1;\ 3 - \alpha_2,\ l_2;\ 4 - \alpha_3,\ l_3;\ 5 - \alpha_{max},\ l_{max}\ (\alpha_1 < \alpha_2 < \alpha_3;\ l_1 < l_2 < l_3)$

zone is determined very approximately from the formula $\frac{d\varepsilon}{dt} = v_0 \frac{l_0}{s}$ (where L is the length of the strained volume) and can reach very large values. Under these conditions, the deformation process can be considered adiabatic and therefore, there is local material heating (in certain cases up to the melting point), which also leads tc increase of W. At low temperatures, the transition zone size decreases, the rate of bond failure with increase of the stress decreases, which leads to decrease of W. Usually we can consider the following relation to be acceptable

$$K = l_v + K_0 e^{-\frac{1}{T}}, \qquad (5)$$

where for plastics, with quasi-homogeneous structure in the so-called glassy hard state, the second term on the right side is quite large in the region of normal or somewhat low temperatures. At high temperatures, the value of K is so large that brittle fracture does not take place for a given stress level. Thus, the critical material temperature in the defect zone depends on the stress level, the degree of stress concentration, and the specimen edge loading conditions. In the following, we examine the temperature region in which the crack propagation condition is satisfied, i.e., the temperature region considerably below the critical value. Determination of the quantity K experimentally permits evaluation of the strength of parts made from a material in the glassy hard state in the presence of initial sharp defects and the possibility of brittle fracture. The dependence of the quantity K on various factors is shown in Figure 2.

3. Crack propagation conditions and brittle fracture mechanics are also associated with the level of the elastic deformation energy accumulated in the part or in a system of jointly operating parts. The larger the part, the smaller the size of the defect which is capable of growing for a given stress level and, therefore, the lower the resistance of the part to brittle fracture for a given defect size. This situation follows from an examination of the energy balance with account for the additional term corresponding to the stress reduction in the system resulting from a decrease of the part stiffness with crack growth [40]. If we denote the system stiffness by Δ, for constant deformation measured at the edges of the subject flat plate, we obtain

$$\frac{\partial U_c}{\partial l} = \frac{\partial}{\partial l}\left[-\pi \frac{\sigma_n^2}{2E} l^2 h + K 2lh - \frac{(B-l) h^2 \sigma_n^2 \Delta}{2}\right],$$

hence,

$$\sigma_{np\text{-}p} = \sqrt{\frac{2}{\pi} \cdot \frac{EK}{[l + Eh(B-l)\Delta]_{kp}}}. \qquad (6)$$

It follows from (6) that, the larger the part dimension B, the lower is the limit stress σ_{lim}. With increase of part size, the system of curves shown in Figure 2 shifts into the higher temperature region and the material strength decreases. However, this relation is valid only within certain limits, determined by the boundary conditions, the part shape, and the means of deformation energy supply to the fracture location in the crack growth stage. In studying this question, we cannot restrict ourselves to an examination of the quasi-static problem. We must consider fracture dynamics, whose nature depends on the direction and location of the crack and the technique used to apply the loads to the part. The time factor plays an important role in questions of the strength of the subject plastics. The longer the loading time, the larger is the number of molecular bonds which are broken and the larger is the reduction of the main crack resistance to growth, which shows up in reduction of K. Conversely,

with very fast and short-term loading, even a comparatively large defect may be quite stable, and at the edge of this defect, deformation may occur as a result of which the required molecular bond orientation blocking is realized. In the present chapter, we examine materials for which the relaxation processes do not show up under conventional loading. In all cases we examine fast fracture, in which the crack growth process is measured in thousandths of a second. If we assume that the average value of the energy K expended in forming unit fracture surface is independent of specimen dimensions and loading conditions (which is valid only for certain materials), and if the load magnitude does not change during the fracture process, i.e., the stresses at the specimen edges maintain constant values, the energy balance equation has the form [169]:

$$\frac{\sigma^2_{нач}}{2E} V = 2\bar{K}F,$$

Hence, for $\sigma = \sigma_{lim} = \sigma_b$,

$$\frac{E\bar{K}}{\sigma_b^2 B} = \text{const.} \qquad (7)$$

The quantity $\frac{E\bar{K}}{\sigma_b^2 B}$ is an important material characteristic in the glassy hard state; σ_b is the material ultimate strength; B is the characteristic dimension of the part; V is the volume of the stressed material zone. The characteristic defined by (7) is the ratio of the brittle material constants to the quantity characterizing the specimen volume and stress state. In the case of temperature reduction and considerable material damage in the process of preceding long-term loading, this characteristic decreases. The larger this quantity, the higher is the resistance of the part to brittle fracture.

4. In the case of different relative defect dimensions, the transition zone width s usually does not remain constant. If we assume that the quantity K is independent of crack size, it is necessary to consider that the amount of energy dissipated depends

on the crack length — for example, it is proportional to the quantity l^{λ}. When using this relation under quasi-static conditions, the dependence of the material parameters on crack size is taken into account. This is confirmed by the experimental data presented below. With account for this situation, for the very simple case of a flat plate loaded by uniaxial tensile stress, we obtain

$$\sigma_{разр} = \text{const} \sqrt{\frac{EK}{(1+\lambda) l^{\lambda}}}, \tag{8}$$

where we also have assumed that the crack size is small in comparison with the part dimensions. Under the condition $\sigma_{lim} = \sigma_b$, the following expression characterizing the strength of a brittle material part is valid

$$\sigma_b^3 l^{\frac{3}{2}\lambda} = \text{const}. \tag{9}$$

If geometric similarilty of the local field stress is ensured regardless of the absolute crack size and there is constant energy input to the edge of an expanding crack, we can take $\lambda = 1$. We obtain the expression for determining the ultimate strength

$$\sigma_b^2 l = \text{const}. \tag{10}$$

The relation (10) is confirmed well by test data for brittle quasi-homogeneous materials.

However, if the width of the transient zone remains constant and the stress field at the defect edge is independent of the absolute defect size, the exponent $\lambda = 0$ in (9). This occurs, specifically, for cracks with rounded edge, where large shear deformations arise, and therefore, the ultimate strength of the part is higher than the yield limit. For most plastics at normal temperature $0 < \lambda < 1$. The ultimate strength also varies as a function of λ — for example, for $\lambda = 2/3$

$$\sigma_{\alpha}^{3}l = \text{const.} \qquad (11)$$

For a part of complex shape and loading conditions for which crack growth causes intense reduction of the nominal stress — for example, loading acrylon plastic tubes with internal pressure, when gas leakage through the expanding crack quickly reduces the internal pressure — the quantity λ may exceed one. In this case, $\lambda = 4/3$, and we obtain the formula for the ultimate strength

$$\sigma_{\alpha}^{3/2} = \text{const.} \qquad (12)$$

On the basis of these arguments, we cannot only determine the value of the allowable stress for the parts under brittle fracture conditions for a given temperature and given loading technique, we can also evaluate the permissible defect size [140, 169, 172]. However, for more detailed and concrete calculations in this field, it is necessary to have the values of the basic material constants, which cannot be determined from conventional test data. We must also study the influence of crack and defect orientation in relation to the effective stress direction and the part surface, and also the influence of the stress state at greater distances from the defect edge.

§2. Static Strength of Polymethyl Methacrylate Specimens with Artificial Defects

In order to verify the influence of sharp cracks on the strength of parts under brittle fracture conditions, we made tests at normal temperature of flat specimens made from polymethyl methacrylate (plexiglas) of the "acrylon" type. This material was selected because of the existence of several favorable qualities, including convenience in obtaining artificial cracks by means of impact, good visibility of the defects which are formed, and the possibility of determining the stresses in the vicinity of the defect by the photoelastic method. The glass transition temperature (maintenance of the glassy state) is quite high — on the order of 80° C — and the mechanical characteristics of the material in this state are well known. In tests under

brittle fracture conditions, the material behavior and data correspond to region A (see Figure 2). The nature of the deformation diagram indicates the existence in the material of conditions under which only V-shaped cracks occur. This means that even less sharp artificial defects have an influence similar to that of cracks. The data for methyl methacrylate place it at the borderline of the region of plastics with clearly marked brittleness. The material properties are:

Elastic modulus	$E = 33{,}000$ kgf/cm^2
Specific weight	$\kappa = 1.18$ g/cm^3
Ultimate strength of smooth specimens under static loading	$\sigma_b = 690$ kgf/cm^2

The longitudinal elastic wave propagation velocity in the material, calculated on the basis of the above values, is $c_{max} = \sqrt{\frac{E}{\kappa}} = 1650$ m/sec; the average elastic wave propagation velocity actually measured is 1560 m/sec. Poisson's ratio at 20° C depends on the stress, and, with an increase of the stress from 50 to 100 kgf/cm^2, decreases from 0.32 to 0.305.

For the first series of tensile tests, the notches (artificial defects) on the plane specimens were made by a cutting tool, and their width was 0.2 mm and depth $l = 10 - 20$ mm. The notches were made very carefully and no noticeable residual stresses developed in the material. We tested specimens with single notches differing in location and magnitude of the ratio $\xi = \frac{l}{B}$ of notch depth to specimen width, and also with certain simple notch systems.

For the second series of tests, we used specimens with defects in the form of cracks obtained by means of direct impact. Some of the cracks had uneven edges; therefore, the results of their tests were ignored. However, the exact geometry of the initial crack in the case of small plate thickness does not have any significant influence on the magnitude of the limit stress. The specimen width $B = 100$ mm; thickness was 4 mm. All the specimens were tested at a temperature of 30° C, and the strain rate was about 10 mm/min.

The following was established in these tests. The strength of the acrylon specimens corresponds to (10) with $\lambda = 1$. This means that, in the fast-loading case, the transition zone remains geometrically similar and its size is proportional to the defect size. The stress concentration does not change for large local deformations. During the tests, V-shaped cracks arise whose propagation conditions are apparently determined only by the local normal dissipative stress level. The discrepancies between the test results and calculation using brittle strength theory do not exceed the limits of the experimental data scatter band width.

The average value $\overline{K}$ of the specific fracture energy at the indicated temperature was determined for specimens with average initial crack size and with an artificial defect of simple form occupying the entire plate width. For an initial defect of dimension 10 mm, the scatter of the specific energy values is not excessive, and the difference between the values found for defects obtained by cutting and impact does not exceed 20%. The average value of the specific fracture energy $\overline{K} = 0.3$ kgf·cm/cm^2, i.e., it exceeds by about 50 times the value ($U_v < 10^{-2}$ kgf/cm^2), corresponding to the specific surface tension energy. For a defect smaller than 10 mm, the quantity $\overline{K}$ increases. This question is examined in more detail below.

In all cases, $K \gg U_v$. This means that the specimen material was not perfectly brittle, and the specific fracture energy was determined basically by the strain work in the transition zone ahead of the expanding crack edge.

If we do not consider the energy U_v as a quantity of second order of smallness, we obtain from (5) a relation for $\overline{K}$ of the form $\overline{K} \sim \overline{K}_0 e^{\frac{k}{T}}$. In the following, we present the results of tests at a temperature close to normal. On the basis of the known value of $\overline{K}$ for absolute temperatures in the range $T = 273 - 313°$ K, we obtained the following average values of the constants in the formula presented above: $k = 1.5 \cdot 10^3$ and $\overline{K}_0 \approx 70$.

The following was established in these tests. The strength of the acrylon specimens corresponds to (10) with $\lambda = 1$. This means that, in the fast-loading case, the transition zone remains geometrically similar and its size is proportional to the defect size. The stress concentration does not change for large local deformations. During the tests, V-shaped cracks arise whose propagation conditions are apparently determined only by the local normal dissipative stress level. The discrepancies between the test results and calculation using brittle strength theory do not exceed the limits of the experimental data scatter band width.

The average value $\overline{K}$ of the specific fracture energy at the indicated temperature was determined for specimens with average initial crack size and with an artificial defect of simple form occupying the entire plate width. For an initial defect of dimension 10 mm, the scatter of the specific energy values is not excessive, and the difference between the values found for defects obtained by cutting and impact does not exceed 20%. The average value of the specific fracture energy $\overline{K} = 0.3$ kgf·cm/cm^2, i.e., it exceeds by about 50 times the value ($U_\nu < 10^{-2}$ kgf/cm^2), corresponding to the specific surface tension energy. For a defect smaller than 10 mm, the quantity $\overline{K}$ increases. This question is examined in more detail below.

In all cases, $K \gg U_\nu$. This means that the specimen material was not perfectly brittle, and the specific fracture energy was determined basically by the strain work in the transition zone ahead of the expanding crack edge.

If we do not consider the energy U_ν as a quantity of second order of smallness, we obtain from (5) a relation for $\overline{K}$ of the form $\overline{K} \cdot \overline{K}_0 e^{-\frac{k}{T}}$. In the following, we present the results of tests at a temperature close to normal. On the basis of the known value of $\overline{K}$ for absolute temperatures in the range $T = 273 - 313°$ K, we obtained the following average values of the constants in the formula presented above: $k = 1.5 \cdot 10^3$ and $\overline{K}_0 \approx 70$.

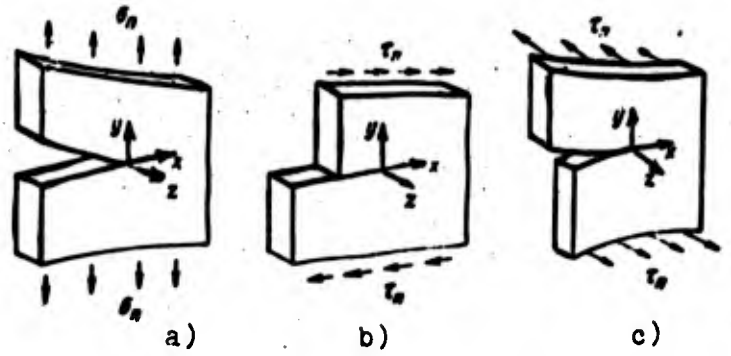

Figure 3. Basic crack types, differing in direction of the relative displacement of the sides.

a — crack opened by normal force; b — crack with displacement of the sides in the direction of crack propagation under the action of tangential stresses; c — crack with displacement of the sides under the action of tangential stresses in the direction perpendicular to the plane of the specimen.

For flat acrylon specimens of different shape with defects, the constant C in the formula $\sigma_b^2 l = C$ depends for a given material temperature on the specimen size and defect orientation. Hereafter, all the data are presented for the basic case for which (1) is valid.

Accordingly, the influence of flat specimen shape, relative defect size, and loading technique in the general case is characterized by the form coefficient ϑ, defined from the relation

$$\sigma_* = \vartheta \sqrt{\frac{ER}{l}}. \tag{13}$$

In the basic case for a central through crack in a specimen of large width $\left(\frac{l}{B} \to 0\right)$ $\vartheta = \sqrt{\frac{2}{\pi}} = 0.8$.

On the basis of theoretical analysis of the stress state at the edge of an elliptic cavity, we can calculate ϑ, using the criterion of maximum stress at the defect edge [211]. Many authors have studied in the recent decades the stress state at the edge of cracks oriented differently in detail parts. Considerable progress in obtaining the

general solution has been achieved as a result of studies by Muskhelishvili and Kolosov [62, 75], and use of functions of a complex variable. The stress state at the crack edge changes as a function of the possibility of mutual displacement of the crack sides (Figure 3) and the edge loading conditions. For a given overall strain, the stress at the specimen surface above the crack decreases as a result of stiffness reduction in this zone of the specimen. Usually we examine the case of statically determinate loading of the specimen edges without account for the influence of the crack on edge deformation. By superposing the particular cases shown in Figure 3, we can determine the stress state for complex forms of loading. The final solutions for certain very simple cases have been presented in studies by Irwin and Westergaard [150, 211]. For the case shown in Figure 3a, the stress state at sufficiently great distance (Figure 4) from the growing crack in the case of plane strain of an infinite flat plate under uniaxial tension is expressed by the following formulas in polar coordinates.

$$\left.\begin{aligned} \sigma_x &= C_1\sigma_n\sqrt{\frac{l}{\rho}}\cos\frac{\varphi}{2}\left(1-\sin\frac{\varphi}{2}\sin\frac{3\varphi}{2}\right);\\ \sigma_y &= C_1\sigma_n\sqrt{\frac{l}{\rho}}\cos\frac{\varphi}{2}\left(1+\sin\frac{\varphi}{2}\sin\frac{3\varphi}{2}\right);\\ \sigma_z &= \nu(\sigma_x+\sigma_y);\ \tau_{xy}=\tau_{yz}=0. \end{aligned}\right\} \quad (14)$$

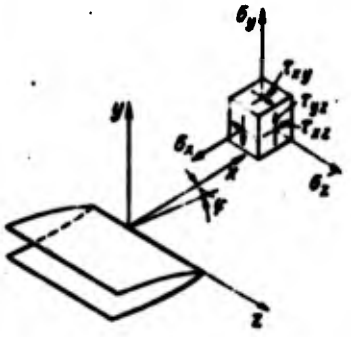

Figure 4. Notations for stress components near crack edge in polar coordinates.

The principal displacements are found from the formulas

$$\left.\begin{aligned} x &= \frac{C_1}{G}\sigma_n l\sqrt{\frac{\rho}{l}}\cos\frac{\varphi}{2}\left(1-2\nu+\sin^2\frac{\varphi}{2}\right);\\ y &= \frac{C_1}{G}\sigma_n l\sqrt{\frac{\rho}{l}}\sin\frac{\varphi}{2}\left(2-2\nu-\cos^2\frac{\varphi}{2}\right);\\ z &= 0. \end{aligned}\right\} \quad (15)$$

For growth of a crack of the second type (see Figure 3b)

$$\left.\begin{aligned} \sigma_x &= -C_2\tau_n\sqrt{\frac{l}{\rho}}\sin\frac{\varphi}{2}\left(2+\cos\frac{\varphi}{2}\cos\frac{3\varphi}{2}\right);\\ \sigma_y &= C_2\tau_n\sqrt{\frac{l}{\rho}}\cos\frac{\varphi}{2}\sin\frac{\varphi}{2}\cos\frac{3\varphi}{2};\\ \tau_{xy} &= C_2\tau_n\sqrt{\frac{l}{\rho}}\cos\frac{\varphi}{2}\left(1-\sin\frac{\varphi}{2}\sin\frac{3\varphi}{2}\right);\\ \tau_{xz} &= \tau_{yz};\ \sigma_z = \nu(\sigma_x+\sigma_y) \end{aligned}\right\} \quad (16)$$

$$\left.\begin{aligned} x &= \frac{C_2}{G}\tau_n l\sqrt{\frac{\rho}{l}}\sin\frac{\varphi}{2}\left(2-2\nu+\cos^2\frac{\varphi}{2}\right);\\ y &= \frac{C_2}{G}\tau_n l\sqrt{\frac{\rho}{l}}\cos\frac{\varphi}{2}\left(1-2\nu+\sin^2\frac{\varphi}{2}\right);\\ z &= 0. \end{aligned}\right\} \quad (17)$$

For growth of a crack of the third type (Figure 3c)

$$\left.\begin{aligned} \tau_{xz} &= -C_3\tau_n\sqrt{\frac{l}{\rho}}\sin\frac{\varphi}{2};\\ \tau_{yz} &= C_3\tau_n\sqrt{\frac{l}{\rho}}\cos\frac{\varphi}{2};\\ \sigma_x &= \sigma_y = \sigma_z = 0;\ \tau_{xy} = 0; \end{aligned}\right\} \quad (18)$$

$$\left.\begin{aligned} x &= y = 0;\\ z &= \frac{C_3}{G}\tau_n l\sqrt{\frac{\rho}{l}}\sin\frac{\varphi}{2}. \end{aligned}\right\} \quad (19)$$

The values of the constants C_1, C_2, and C_3 depend on the specimen type and geometry and the defect shape, but are independent of the variables ρ and φ. For example, in accordance with the Westergaard solution [211] for a flat plate loaded by an axial tensile force and having a regular series of cracks spaced at the distance L from one another (Figure 5), we obtain

$$\left.\begin{aligned} C_1 &= \frac{1}{\sqrt{2}}\sqrt{\frac{l}{\xi}}\operatorname{tg}\left(\frac{\pi}{2}\xi\right)\\ C_2 &= C_3 = 0. \end{aligned}\right\} \quad (20)$$

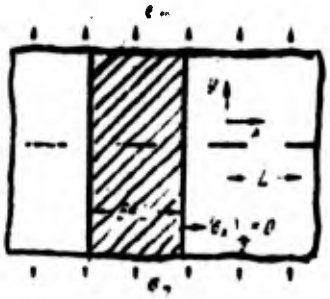

Figure 5. Series of defects in flat specimen loaded by tensile stress.

where $\xi = \frac{l}{L}$. For the limit stress at the crack edges $(\sigma_x)_{\varphi=0} = \sigma_{lim} = A$, where A is a constant of the material, the limiting nominal stress in the plate which causes its failure is

$$\sigma_{appl} = A\sqrt{\frac{\rho}{l}}\,\vartheta,$$

where $\vartheta = \sqrt{\xi \operatorname{ctg}\left(\frac{\pi}{2}\xi\right)}$.

The constant A depends on the material elastic modulus in accordance with the formula $A^2 = Eb$, since the mentioned solution was obtained under the assumption that the material remains elastic until the limit state is reached. However, we must consider the molecular structure of the material and the presence of the transition zone. If the material were perfectly homogeneous down to elementary volumes, then at the crack edge there would be an infinitely large stress for $\rho = 0$.

Actually, we must consider the dimensions of the transition zone and the effective crack edge rounding radius $\rho_{min} = \frac{s}{2}$. Dimensional analysis shows that the product sb has dimensions of kgf·cm/cm², which corresponds to the dimensions of the specific strain work necessary for the development of surface fracture as a result of growth of a crack with transition zone which overtakes the movement of its edge. This specific work is greater than that denoted above by the symbol K. Thus,

$$\sigma_{appl} = \vartheta\sqrt{\frac{EK}{l}},$$

which agrees with the expression obtained from the energy balance conditions. The form factor ϑ depends on the crack shape, part shape, and the nature of the stress state. At points between cracks located with constant spacing in a single series perpendicular to the direction

of the acting stress (Figure 5), the tangential stress is equal to zero by the symmetry conditions, while the stress σ_x is very small for relatively small defects ($l \ll L$). This implies that the expression for ψ can also be used for a flat specimen of finite width B = L with free edges and a defect along the longitudinal axis.

However, in this case, the solution is approximate, and the solution accuracy decreases with decrease of the ratio $\frac{B}{l}$. A more exact solution was obtained by Isida [152]. For $\xi = \frac{B}{l} = 0 - 0.6$, the difference between the Isida solution and that examined here does not exceed 7%. The values of the function $f(\xi)$ in the expression for the form factcr in accordance with the Isida solution and the results obtained using the Westergaard formula (20) for a regular series of defects are compared in the following table:

ξ	0,074	0,207	0,275	0,337	0,41	0,466	0,535	0,592
$f(\xi)$	1,0	1,03	1,05	1,09	1,13	1,18	1,25	1,33
$\sqrt{\frac{2}{\pi}} \times \sqrt{\frac{1}{\xi} \operatorname{tg}\left(\frac{\pi}{2}\xi\right)}$	1,0	1,02	1,03	1,06	1,09	1,11	1,15	1,22

These values were used to plot a graph (Figure 6) which shows that the two theoretical curves agree well with the results of the tests made by the present author. The reason for the discrepancy between the values in the region of defects of very small dimensions is examined below.

Specimen	l in cm	$\xi = \frac{l}{B}$	F_0 in cm^2	F_{min} in cm^2	P in kgf	σ_n in kgf/cm^2
1	0,9	0,091	3,28	2,96	307	94,7
2	0,7	0,0716	2,84	2,64	355,5	125
3	0,7	0,0707	3,07	2,65	318	103,5
4	0,8	0,0816	3,63	3,33	403	113
5	0,85	0,087	3,62	3,3	386	106
6	0,65	0,0675	2,89	2,78	343	119
7	0,6	0,0614	3,01	2,84	412	136
8	0,9	0,0917	3,73	3,39	296	79,2
9	0,9	0,0916	4,22	3,83	311	81,5
10	1,0	0,102	4,0	3,6	350	89,8
11	1,0	0,102	4,13	3,7	373	90,4
13	1,2	0,1246	2,82	2,47	206	73
15	1,3	0,1304	3,07	2,86	280	91
16	1,45	0,1464	3,76	3,21	244	65
18	1,65	0,1716	2,89	2,4	162	61
19	0,45	0,0454	3,17	3,03	467	147
20	0,6	0,061	4,23	3,96	502	119

The table above shows results of tests of specimens of small thickness made from acrylon with sharp notches and artificially obtained initial cracks with central location of the cracks. The table does not include the test data of those specimens in which the plane of the initial crack was not perpendicular to the effective stress. Because of the method used to obtain the initial cracks, the latter were sometimes located in the depth of the specimen and were not perpendicular to the specimen side surfaces. In some specimens, the crack plane was inclined at a 45° angle to the specimen surface and the maximum tensile stress perpendicular to the crack plane was lower — by a factor of two — than for a crack perpendicular to the specimen's longitudinal axis. If the material strength is defined by the value of the maximum tensile stress, the minimum fracture stress for such specimens should be higher by a factor of two.

Figure 7 shows the limit nominal stress for specimens with short cracks as a function of relative crack size.

Since it is not possible, in the impact case, to obtain straight and properly oriented cracks of considerable length, in addition to the specimens listed, we tested 15 specimens with sharp notches at the midpoint of the width. The notch length l for most of the specimens was less than 10 mm; however, some of the specimens had notches with length l = 10 - 30 mm. The magnitude of the form factor ν, based on the test data of these specimens is shown in Figures 6 and 8, which

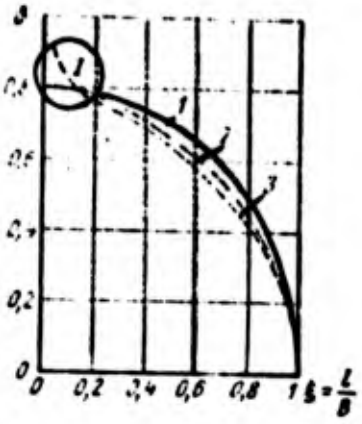

Figure 6. Form factor for brittle fracture of flat specimen of width B with central defect (crack) of length l (I is the region of small defects).

1, 2 — Westergaard and Isida solutions; 3 — present author's experiment.

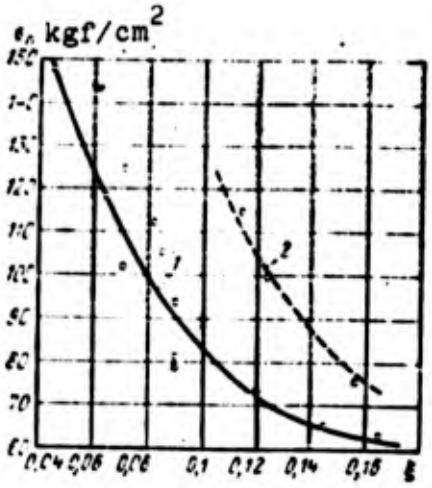

Figure 7. Static strength of plane acrylon specimens with central location of small cracks in region 1 (Figure 6) as function of crack size for defect orientation.

1 — at right angles to the direction of the stresses from the external load; 2 — at 45° angle to the direction of the stress from the external loading.

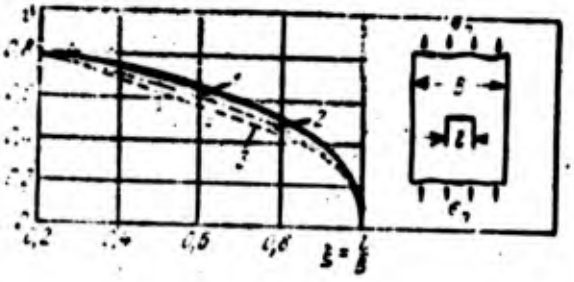

Figure 8. Resistance to brittle fracture of plane acrylon specimens with sharp central defects.

1 — Westergaard theory; 2 — Isida theory; 3 — measurement data.

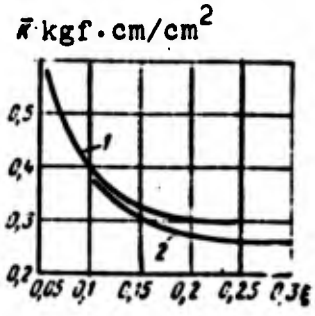

Figure 9. Average values of specific work necessary for occurrence of unit surface fracture in plane acrylon specimen.

1 — specimen with crack; 2 — specimen with sharp notch.

also show for comparison the results of calculation using (20). The theoretical and experimental data diverge somewhat for cracks of long initial length, which indicates the approximate nature of (20).

The calculations using the Isida equations agree better with the experimental results.

On the basis of the cited experimental data we can obtain the material characteristic $\overline{K}$ (Figure 9). In the range of ξ values from 0.05 to 0.1, the quantity $\overline{K}$ does not remain constant and decreases markedly with increase of the initial defect size, which is not in agreement with the theoretical data. The reason for this discrepancy is that, for small crack length, close to the flat specimen thickness, we cannot consider the condition $l \gg h$ satisfied, which was used as an assumption in obtaining the solution. For a short crack length, the stress state at the midpoint of the plate thickness differs from the stress state at its surface. In the thickness of the plate there is a plane strain rather than the plane stress state. In view of this, the elastic modulus $E' = \frac{E}{1 - \nu^2}$ must be used. However, with decrease of the crack size, the resistance to its propagation increases.

For very small cracks ($l_0 \approx 1$ mm), we obtain from the solution for the limit stress with $\overline{K} = 1$ kgf·cm/cm^2 the value of the material ultimate strength $\sigma_b = 700$ kgf/cm^2. Thus, we can assume that the specific fracture work $\overline{K}$ for acrylon varies as a function of the stress state, crack dimensions, and rounding radius at the crack ends in the limits from 0.1 to 1.0 kgf/cm^2. The lower value is obtained in only a few cases when residual tensile stresses were created in the specimen when obtaining the initial defect. The upper value corresponds to very small cracks whose length does not exceed 1 mm. For defects of moderate dimensions, we can take an average value of $\overline{K}$ on the order of 0.3 - 0.4 kgf·cm/cm^2. With oblique positioning of the crack, the resistance of the acrylon specimens to brittle fracture, as we would expect in accordance with the theory of fracture owing to maximum tensile stress in the direction perpendicular to the crack plane, is higher (see Figure 7).

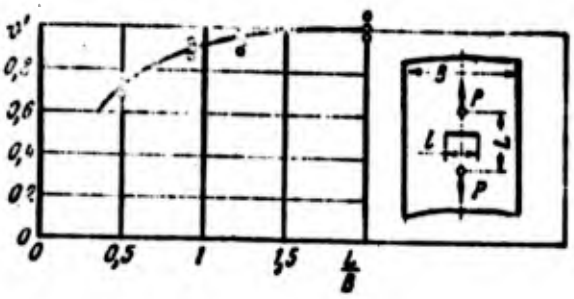

Figure 10. Coefficient ψ' for specimen with defect loaded by central concentrated force.

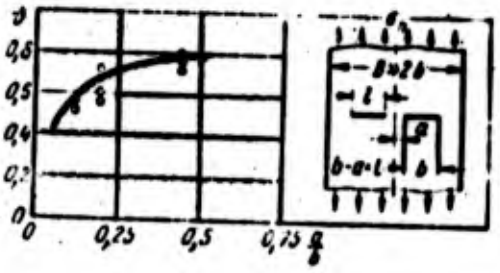

Figure 11. Coefficient ψ for plane specimen of relatively large width with two defects on the same line ($b - a = l$).

In subsequent tests, we determined the brittle fracture resistance of wide plane specimens with central defect, loaded by concentrated forces $P = ph$ applied along the specimen axis at a distance L/2 from the plane of the defect. The theoretical solution for this case was obtained by Barenblatt [9, 10]. If we take $p = B\sigma$ and $L \geq B$, we obtain

$$\theta = \sqrt{\xi \operatorname{ctg}\left(\frac{\pi}{2}\xi\right)}.$$

If the distance from the point of load application to the crack plane is smaller, we can take $\psi_c = \psi\psi'$, where ψ' is the correction factor (Figure 10).

If there are — in a wide plane specimen subjected to a tensile load — two defects of the same length located on the same line (Figure 11), in accordance with the Winnie solution [40] for $\frac{a}{b} < 1$

$$\theta = 4\sqrt{\frac{\left(1+\frac{a}{b}\right)\frac{a}{b}}{\pi\left(1+3\frac{a}{b}\right)^2}}. \qquad (21)$$

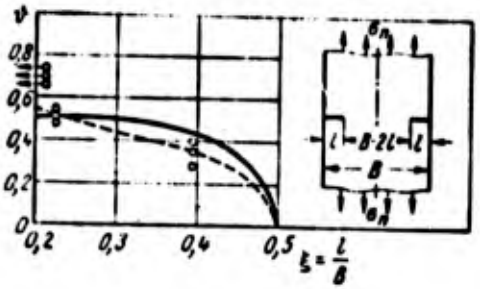

Figure 12. Coefficient ϑ for stretched plane specimen with symmetric location of two defects along the edges.

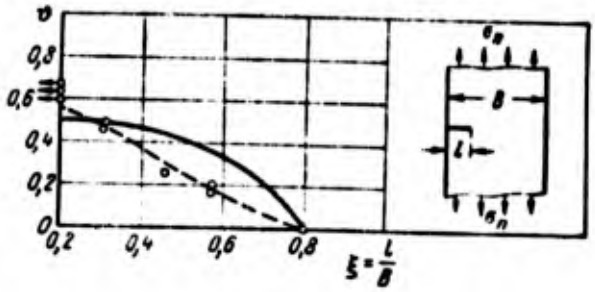

Figure 13. Coefficient ϑ for stretched specimen with one-sided location of defect at the edge.

When $\frac{a}{b} \to 1$, in place of the specimen with two defects, we obtain a specimen with a single crack and $\vartheta \to \sqrt{\frac{2}{\pi}}$. Figure 11 shows that the calculation results agree with the experimental data.

The solution was obtained by Wigglesworth [212] for the case when there are two defects on the sides (Figure 12) of a plane specimen of small thickness and finite width B. The theoretical value of the form factor

$$\vartheta = \frac{1}{\sqrt{\pi}} \sqrt{\frac{\pi\xi}{\lg(\pi\xi) + 0.1\sin(2\pi\xi)}}. \qquad (22)$$

The measurement results for tests of acrylon specimens of this shape are shown in Figure 11. The solutions of several authors for a plane specimen with one-sided notch were presented by Irwin [148]. The theoretical value of ϑ as $\xi \to 0$ is

$$\vartheta = 0{,}9\sqrt{\frac{1}{\pi}}, \qquad (23)$$

where the coefficient 0.9 takes into account the influence of the material surface layer. In this case, the difference between the theoretical calculations and the experimental values is greater than in the preceding case (Figure 13).

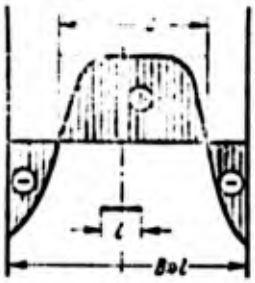

Figure 14. Nonuniform distribution of stresses σ_n in plane specimen with defect (schematic and notations of basic quantities).

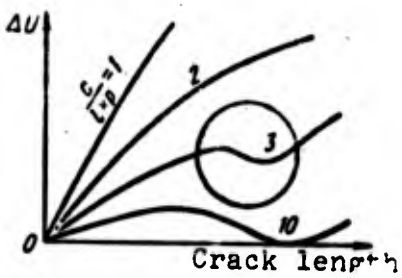

Figure 15. Nature of energy change ΔU during crack propagation in nonuniformly distributed nominal stress field (in accordance with the scheme of Figure 1).

In practice, we often encounter cases of nonuniform nominal tensile stress distribution (Figure 14). In these cases, it is important to know how wide the zone of action of the maximum tensile stress must be in order that we can use the formulas derived under the assumption of uniform stress distribution. In [169], the author, on the basis of an energy balance, showed that, to reach the unstable crack state in accordance with (20) for $\sigma_{max} = \sigma_{lim}$, it is necessary that the width of the maximum tensile stress zone be no less than three times greater than the crack length (Figure 15). Here it is assumed that the magnitude of the nominal stress does not vary along the specimen longitudinal axis.

An important loading mode is bending of plane specimens made from brittle materials with defects. The strength condition has the form

$$\sigma_{max} = \frac{6M_u}{hB^2} = \sigma_{lim} \qquad (24)$$

hence,

$$M_u = \frac{\sigma_{max} hB^2}{6} = \sigma_{lim} \frac{hB^2}{6} \sqrt{\frac{EK}{l}}, \qquad (25)$$

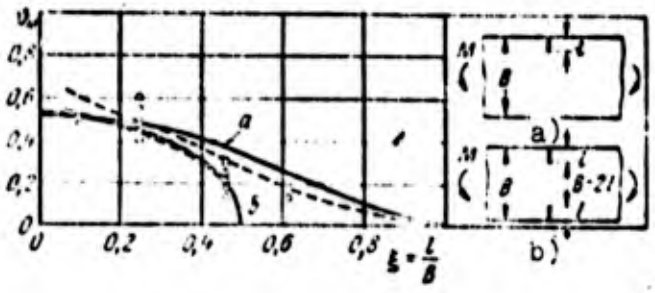

Figure 16. Coefficient ϑ_m for plane specimen in bending with edge defects.

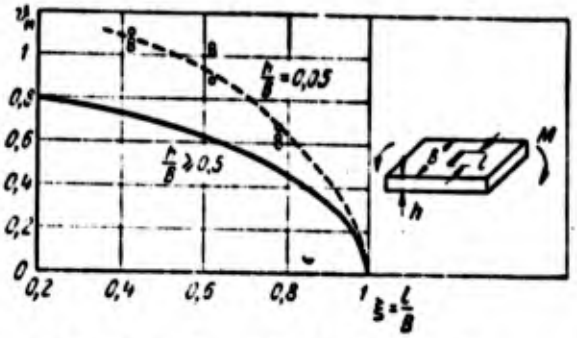

Figure 17. Coefficient ϑ_m for plane specimen of small thickness with centrally located defect in bending in the plane of least stiffness.

where ϑ_m is the form factor, whose magnitude found from the data of acrylon specimen tests is shown in Figure 16. For case a

$$\vartheta = \sqrt{\frac{2}{\pi}} \cdot \frac{1}{f_m(\xi)} \sqrt{(1-\xi)^3 \xi},$$

where $f_m(\xi)$ is a function whose values are shown in the table.

ξ	0,05	0,1	0,2	0,3	0,4	0,5
$f_m(\xi)$	0,55	0,48	0,6	0,66	0,69	0,71

In the case when plane specimens of small thickness with central defect are loaded by a bending moment (Figure 17), the stress $\sigma = \frac{6M_u}{h^2 B}$.

The measurement results are shown in Figure 17. For relatively large specimen width $\xi \to 0$ and $\vartheta_m = \frac{3}{2}\vartheta$, where ϑ is the form factor for the case of uniformly distributed tensile stress. With increase of specimen thickness, the resistance to brittle fracture decreases.

Figure 18. Crack propagation from part-through defect in plane specimen (initial defect shown hatched).

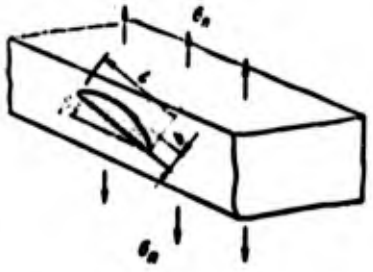

Figure 19. Notations for basic quantities in calculation of the coefficient ψ for semi-elliptic crack in semi-infinite body.

For real parts of more complex forms, which cannot be simulated with the aid of plane specimens, there may be part-through cracks. The surface crack has considerably less influence on the strength than does the through crack. The surface crack initially develops inside the part wall material and only after this does accelerated development of the through crack begin (Figure 18). Irwin [151] studied the stress state at the edge of an elliptic crack in a semi-infinite body whose plane forms the angle β with the uniaxial tensile stress (Figure 19) and obtained the following expression

$$\theta = \frac{1}{1-\nu^2}\sqrt{\frac{2}{\pi}}\cdot\int_0^{\pi}\frac{\sqrt{1-(1-\nu)^2\sin^2\alpha}\,d\alpha}{\sqrt{\sin^2\beta+\nu^2\cos^2\beta}}. \qquad (26)$$

Sneddon [195] studied the case when plane cracks are oriented perpendicular to the tensile stress in an infinite three-dimensional brittle body. The limit stress at a crack of this type of circular form ($\varepsilon = \frac{2b}{l} = 1$) is determined from the formula

$$\sigma_{прод} = \sqrt{\frac{\pi E K}{2(1-\nu^2)l}}. \qquad (27)$$

If we assume that, in the presence of several defects of this type, only a single defect has a definitive influence on the strength and that is the defect which is most unfavorably oriented with respect to the tensile stress direction (defect plane is perpendicular to the stress direction), and if we exclude the mutual influence of the defects, since the distance between them is large in comparison with their dimension ($L \gg 2l$), we can calculate the l_0 corresponding to the static strength of the material. For acrylon with a small initial crack we can take $\overline{K} = 1$ kgf·cm/cm^2. Then the limit stress

$$\sigma_{пред} = \sqrt{\frac{\pi \cdot 33\,000 \cdot 1}{2 \cdot 0{,}9\, l_0}} = 690 \text{ kgf/cm}^2,$$

hence $l_0 \approx 0.1$ cm = 1 mm.

In studying the fracture surface of plane acrylon specimens, residual stresses are detected on both surfaces of the crack in a material layer of thickness about 1 mm. It has been established by the photoelastic method that the stress decreases rapidly in the course of time from the moment of fracture occurrence, and as we move away from the fracture surface, the stress varies following a wave-like law. Residual stresses arise within the limits of half the width of the transition zone as a result of the large irreversible deformations which precede material fracture. Beyond the limits of the transition zone, residual stresses arise as a result of propagation of elastic stress waves from the material fracture location.

§3. Mechanics of Brittle Material Rapid Fracture

Tests of the static strength of small specimens made from a brittle material do not yield the possibility of studying the laws governing brittle fracture crack growth from the defect edge nor of determining the fundamentals of brittle fracture mechanics. Study of crack growth and the brittle fracture onset, even with simplifying assumptions, is a difficult task and is associated with complex theoretical and experimental investigations. Therefore, only a few relationships have been obtained from the field of brittle fracture

Figure 20. Typical stages of brittle fracture crack growth in a plane specimen.

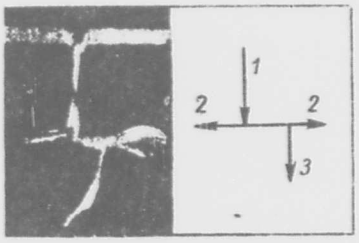

Figure 21. Influence of local stress on crack propagation in acrylon specimen.

1 — initial crack; 2, 3 — direction of primary and secondary cracks.

kinetics. The study of fast fractures is valuable in the aspect that we can study better than in static tests the influence of various factors on the fracture process of a material in the glassy state. Study of brittle fracture mechanics makes it possible to determine more accurately the material resistance to brittle fracture. The basic hypotheses of the subject problem are as follows:

1. The onset and growth of the fast fracture crack in a flat plate made from a brittle material can be subdivided into several stages whose importance for the fracture process depends on the stress level, nature of the initial defect, plate dimensions, and the technique for loading the plate edges. In the macroscopic study case, we can identify five fracture growth stages (Figure 20).

The first stage is characterized by the onset of a crack capable of propagating from the edge of the initial defect. In the second stage, the crack growth accelerates, with the crack propagating along the shortest path, determined by the principal tensile stress. The influence of the initial defect and the crack growth initiation conditions weakens and then disappears completely. The third stage is defined as the stage of crack propagation with practically constant velocity in the uniformly distributed nominal stress field. At the end of the stage, we observe microbranching and then macrobranching of the crack, accompanied by marked changes of the crack propagation

velocity. In the fourth stage, we see the influence of changes in the magnitude and direction of the nominal stress in the section through which the primary crack runs as a result of the considerable reduction of the section load-bearing area. Finally, the fifth and last stage is associated with the slowing or termination of crack growth at the free surface of the part. At each stage, there act the patterns which are characteristic of this stage with regard to crack growth and the criteria for its propagation and development in the body of a new free surface.

2. In the general case, we can assume that the crack velocity and edge displacement direction throughout its growth are determined basically by the direction and magnitude of the maximum tensile stress. This hypothesis is valid when examining the average velocity and direction of the macroscopic displacement of the crack edge in material zones of large extent. In the microvolumes, the nonhomogeneity of the material structure influences the crack propagation conditions.

If there are residual stress centers present inside the part, characterized by high level of the stress values and large extent of their active zones, they combine with the stresses from the external loads. In this case, the direction and velocity of the crack edge macroscopic advance are determined by the overall stress. In compression zones, crack growth decelerates, while in tensile tension zones it accelerates. Figures 21 and 22 show two causes of crack growth in a brittle material. The brittle fracture cracks in plane acrylon specimens 12 mm thick were obtained by impact on a wedge introduced into the edge of a notch. The specimens were annealed for more complete residual stress elimination. The crack propagated along a straight line. The tensile stress from the external load, perpendicular to the section with the notch, was low — on the order of 10 kgf/cm^2. Thus, initial crack propagation took place only under the influence of the dynamic local stress which developed in the notch root zone after the impact. The variation of the crack propagation velocity v is shown in Figure 23. Since the duration of the local stress action at the bottom of the notch and the stressed material volume are limited, the maximum crack propagation velocity v* for the

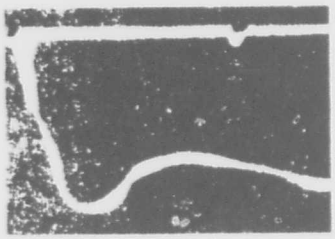

Figure 22. Form of crack in plane acrylon specimen with presence of compressive stress zones.

Figure 23. Variation of crack propagation velocity obtained as result of impact for very low nominal tensile stress level in the specimen ($\sigma_n \leq \sigma_0$).

given material was not reached and crack branching was not observed. During subsequent tests, compression stress centers were formed by crushing the specimen using a screw clamp with circular inserts. The specific pressure on the specimen surface was 50 kgf/cm^2. A tangential tensile stress field (Figure 24) arises near the compression stress center. The influence of the center 1 (see Figure 21), located ahead of the initial crack edge leads to a situation in which, after the subsequent impact on the wedge, introduced into the notch, two new cracks develop and propagate perpendicular to the direction of the initial crack. After this, the clamp was shifted from point I to point II. After a new impact on the specimen, a third crack — which in this case again took a position tangent to the compressive stress region II — propagated from the smooth crack surface (not from its end). At the crack edge we observed a tendency to turn 45° relative to the initial plane. In this region, characterized by very low crack propagation velocity, the shear stress apparently plays an important role and the edge structure has considerable complexity. In Figure 22 we see that, in the case of complex local residual stress zone distribution in the body volume, the crack may propagate along a sinuous path, the tangent to which at each point is perpendicular to the direction of the maximum tensile stress at the given point. Another example is shown in Figure 25; the crack branches and by-passes the compression zone on both sides.

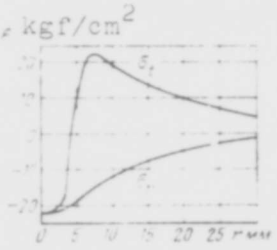

Figure 24. Principal stress variation in specimen material near compressive stress zone.

Figure 25. Form of crack by-passing compressive stress zone in acrylon specimen.

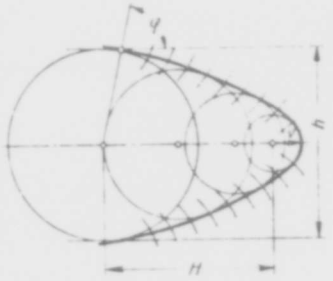

Figure 26. Envelope of instantaneous locations of disturbance front propagating from edge of crack advancing with velocity v in the material of a specimen of finite thickness h and development of relief on the fracture surface.

3. If the distance from the defect edge to the specimen free contour toward which the crack propagates is small, the local specific energy K increases, which slows crack growth. The propagation velocity also varies from point to point through the thickness of the specimen wall, even if the edge of the initial defect is rectilinear through the entire wall thickness. The maximal propagation velocity occurs at the midpoint of the wall thickness which is particularly clearly seen in tests of plane specimens of thickness sufficiently great for the possibility of parabolic crack front formation (Figure 26). The angle of intersection of the parabola and the edge of the fracture surface at the lateral edge of the specimen depends on the crack propagation velocity in accordance with the formula

$$\operatorname{tg} q = \text{const}\, hKv = \text{const}\, \frac{H}{h}. \qquad (28)$$

The thicker the specimen, the more complex is the initial crack growth phase. In testing acrylon specimens whose thickness exceeded considerably the dimension of the initial defect, it was possible to detect several initial fracture points. One of these points was always located at the midpoint of the wall thickness at the bottom

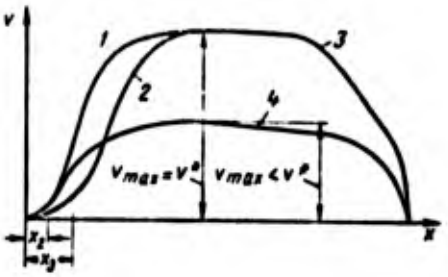

Figure 27. Influence of impact energy and level of nominal stress σ_n on brittle fracture crack propagation velocity in plane acrylon specimens.

1, 2 — large and small energy U; 3, 4 — high and low stress σ_n.

of the notch; another was at the point where the notch reached the lateral surface of the specimen. In the general case, we can consider that the influence of crack geometric symmetry and the maximum value of the third normal stress in the direction of the crack edge will show up at a point midway through the wall thickness. Cracks which develop on the lateral surfaces of specimens made from the brittle materials usually have a characteristic appearance, since the material strength is minimal at the edge formed by the intersection of the specimen surfaces and the notch and defects and microscopic fractures of the intermolecular bonds are most often encountered in this zone. In the case of fracture on the specimen surface at scratches and micronotches, transition zones arise, oriented perpendicular to the defects in accordance with the local material strength reduction and the direction of the principal stresses in the small volumes around the surface defects. However, a crack may develop other than along the line of the surface defect. The interaction of the stress state disturbance accompanying crack growth in the wall thickness and the stress concentration in the microvolumes of the material in the vicinity of surface scratches and irregularities shows up very weakly.

In the surface layer of the material there is always quasi-plastic fracture at a depth of the order of 0.1 mm if the local deformation level is relatively high. As the crack edge approaches the surface, the energy level decreases because of the influence of the free surface.

4. In the first phase of crack growth, the impact energy at the defect location influences its propagation velocity (Figure 27). The greater the impact energy, the faster the crack grows prior to transition to the second stage, and the smaller is the distance x_2.

However, upon reaching a certain value of the impact energy, further increase of this energy does not lead to significant change of the growth process. Experimental data show that when the tensile stress exceeds some limiting value, the average crack propagation velocity depends very little on the impact energy, i.e., in the general case, the propagation velocity depends very little on the crack initiation conditions. The crack initiation conditions play a role only if the nominal stress is relatively low. This situation is very important in practice, since in the case of high stress from an external load, the role of the secondary local stress peaks near the defects becomes less important.

5. The dynamic effect of impact in the specimen defect region shows up, first, in increase of the local stress level in accordance with the relation $\sigma_{max} = \chi\alpha\sigma_n$ (where $\chi = f(U)$ is the coefficient of dynamic stress increase), second, in change of the value of the local specific energy K. In the brittle materials of the acrylon type, the value of K decreases with increase of the loading rate. In certain materials which have — in the glassy state — a clearly defined plastic deformation region, a high loading rate may cause local hardening at the crack edge as a result of corresponding orientation of the molecular chains and increase the resistance to fast fracture crack growth. Such properties are shown, for example, by ductile polystyrene.

The quantity W, which basically determines the value of K, in the general case depends on the crack propagation velocity v. For a brittle material, we can take a very simple relativistic dependence corresponding to a wave nature of the stress state disturbance as the crack edge advances. If we denote by c_d the maximum transverse wave propagation velocity in a body of finite dimensions, we can write

$$K_d = \frac{1}{\left[1 + m\left(\frac{v}{c_d}\right)^2\right]^{\frac{1}{2}}} (K)_{v=0}. \qquad (29)$$

It has not yet been possible to determine the constant m more exactly from test data, since measurement of the defect propagation velocity and the energy necessary for free surface formation on the small crack path segment x_2 traveled during the first stage presents major difficulties.

6. If a plane specimen of length L and width B is weakened by a defect located in the central part of the specimen, its elastic elongation is defined by the formula $p\Delta = \frac{P}{h}\Delta$, where $\Delta = \frac{L}{EB\mu}$ is the specimen compliance and μ is a coefficient whose magnitude depends on the defect shape and location. For example, for a specimen of small thickness with relatively short crack in the central part with $\xi = \frac{l}{B} \ll 1$ and $\frac{h}{l} \gg 1$, we obtain

$$\mu = \frac{2-\xi^2}{2+\left(\frac{\pi B}{L}-1\right)\xi^2}. \tag{30}$$

In the dynamic loading case, the specimen elongation velocity is found from the formula

$$\frac{dL}{dt} = \frac{d(P\Delta)}{dt} = \Delta\frac{dP}{dt} + P\frac{d\Delta}{dt} = v_3,$$

where v_3 is the velocity of the testing machine grips or the average specimen deformation velocity. Upon reaching the load peak corresponding to the specimen ultimate strength, we have $\frac{dP}{dt} = 0$, hence,

$$v_3 = P\frac{d\Delta}{dt} = P\frac{d\Delta}{dl}\cdot\frac{dl}{dt} = P\frac{d\Delta}{dl}v, \tag{31}$$

where v is the propagation velocity of the crack which begins at the defect, and l is the instantaneous crack length. On the basis of the energy balance for a crack initiating at a defect edge, we obtain for a low initial propagation velocity

$$\frac{1}{h}\cdot\frac{dU_0}{dl}=\frac{d\left(\frac{1}{2}P^2\Delta\right)}{h\,dl}=\frac{1}{2h}P^2\frac{d\Delta}{dl}=K. \tag{32}$$

Substituting (31) into this formula, we find

$$v=v_0\frac{P}{2Kh}=v_0\frac{\sigma}{K}B. \tag{33}$$

The initial crack propagation velocity is proportional to the stress magnitude and the loading rate and is inversely proportional to the energy necessary for the development of unit fracture surface. In view of this, dynamic loading with an impact exceeding v_0 and σ, which in the case of acrylon also reduces K, has an unfavorable influence on the specimen strength and leads to increase of the initial crack growth rate. Conversely, in a material for which the value of K increases with increase of the strain rate, the influence of this quantity may be dominant; in this case, dynamic loading does not reduce the material strength.

7. In studying the energy balance, we must consider the kinetic energy of the parts of a brittle material specimen which separate from one another (Figure 28) [141]. Pressure acts at the crack origin on a wedge introduced into the initial notch (in this case, we consider a wedge since, first, in some of the experiments described, the crack was obtained with the aid of a wedge and, second, the wedge simulates the typical v-shaped cracks with wedge-like transitional zone). In the case of fracture of actual detail parts made from brittle materials, the wedge role may be played by other factors which cause local reduction of the potential energy barrier, for example, rapid temperature change with large gradient in the vicinity of a defect. Hereafter, we shall examine only the stationary stress state case and shall not study the dynamic stress field and elastic wave propagation.

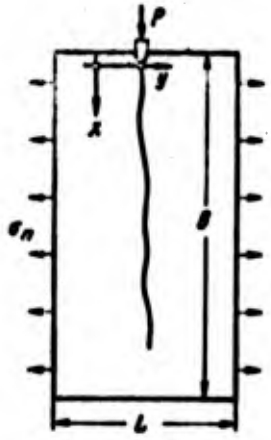

Figure 28. Study of plane specimen brittle fracture mechanics under the action of nominal tensile stress and impact (schematic and notations of basic quantities).

At the edges of a brittle material specimen of width B, length L (L < B), and relatively small thickness h ≪ L, there acts a constant tensile stress perpendicular to the crack propagation line, which is oriented parallel to the specimen width. This basic assumption on the nature of the loading presupposes the absence of change of the nominal stress at the crack edge as it opens. We denote the crack length in the x direction by $l = l_x$, and for reasons of simplification, we shall not consider the influence of tangential stresses. At the distance x from the edge of the initial defect, there acts the bending moment

$$M = \frac{\sigma_n h (l-x)^2}{2} + P(l-x).$$

This expression is obtained from examination of elastic bending of the parts of the specimen on both sides of a notch of depth l. We denote by P the resultant of the wedge pressure on the material for crack length equal to l. We find the elastic deformation energy from the formula

$$U_y = \frac{1}{2EJ}\int_0^l M^2 dx = \frac{\sigma_n^2 h^2 l^5}{40EJ} + \frac{P^2 l^3}{6EJ}. \qquad (34)$$

After substituting into this formula the expression for the specific loading $\frac{P}{h} = p$, we obtain

$$U_y = \frac{1}{E}\left(\frac{l}{L_0}\right)^3 h(2{,}4\sigma_n^2 l^2 + 16p^2). \qquad (35)$$

The maximum crack opening is

$$y_{max} = \frac{4}{E}\left(\frac{l}{L}\right)^2 (3\sigma_n l + 8p) \qquad (36)$$

As the crack expands, the mutually separating parts of the specimen have the kinetic energy

$$U_к = \frac{1}{2} m \left(\frac{dy}{dt}\right)^2 = \frac{1}{2} \varkappa \frac{hL}{2} \int_0^l \left(\frac{dy}{dt}\right)^2 dx,$$

where κ is the density of the material. The crack opening at an arbitrary point with the coordinate x is

$$y = \frac{1}{Ej} \cdot \frac{\sigma_n h}{24} (6l^2x^2 - 4lx^3 + x^4) + \frac{1}{6Ej} ph(3lx^2 - x^3).$$

We obtain the expression for the kinetic energy

$$U_к \approx 120 \left(\frac{v}{c_{max}}\right)^2 \frac{1}{Eh} \left(\frac{l}{L}\right)^5 h^3 (2{,}4\sigma_n^2 l^2 + 16p^2).$$

Hence, we find with account for (35)

$$U_к \cong 20 \left(\frac{v}{c_{max}}\right)^2 \left(\frac{l}{L}\right)^2 U_y, \qquad (37)$$

where $c_{max} = c_d \sqrt{\frac{E}{\sigma}}$.

This means that the kinetic energy is proportional to the elastic strain energy and varies as the square of the product vl. The total energy of the subject specimen is

$$U_c = 2K_0 lh - U_y + U_к, \qquad (38)$$

or

$$U_c = 2K_0lh - \frac{1}{E}\left(\frac{l}{L}\right)^3 h\left[1 - 20\left(\frac{r}{r_{max}}\right)^2\left(\frac{l}{L}\right)^2\right](2{,}4\sigma_n^2 l^2 + 16p^2). \qquad (39)$$

From the condition $\frac{dU_c}{dl} = 0$ for acceleration of the crack advance at the initial instant of time, we calculate for v = 0.

$$\sigma_{n\,lim} = \sqrt{\frac{2K_0EL^3 - 16(pl)^2}{2{,}4l^3}}. \qquad (40)$$

Consequently, the higher the specific pressure owing to the force P acting on the wedge, the lower is the limit stress σ_{lim} required for initial crack growth. In the general case, we can assume that a local load in the defect zone, which causes its expansion, reduces markedly the critical defect dimension and contributes to its instability. This situation shows up to a greater degree for a low level of the nominal stress from the external load. For p = 0, we obtain from the preceding formula

$$l_{cr} = \sqrt[4]{\frac{EK_0L^3}{\sigma_{n\,lim}}}. \qquad (41)$$

If we determine the maximum stress $\sigma_{max} = 12\sigma_n(\frac{l}{L})^2$ at the edge of an expanding crack and take it equal to the local material ultimate strength $(\sigma_b)_l$ in accordance with the brittle material fracture condition, using (41) we obtain

$$\frac{144EK_0}{(\sigma_b)_l^2 L} = 1 \quad \text{or} \quad \frac{EK_0}{(\sigma_b)_l^2 L} = \text{const}. \qquad (42)$$

The left side of (42) is a material characteristic analogous to that defined by (7). We note that the dynamic energy K_d required for the appearance in the body of unit new surface area is understood here to be the average magnitude of the specific energy along the crack growth path. Actually, the instantaneous specific energy varies over a wide range (Figure 29). Its value depends on what crack growth stage is being studied. The amount of energy required per unit fracture area is minimal in the second crack growth stage, when the fracture surface is smooth and its shape is rectilinear. In the third growth stage, macrobranching and microbranching of the crack arise for a sufficiently high stress level. The propagation velocity varies over wide limits and the fracture surface becomes branched. We have previously examined the energy balance to determine the maximal value of the specific energy K_d per unit fracture surface for the dynamic crack growth process and also high stress at the crack edge. Thus, the parameter expressed by (42) has a dynamic rather than static nature. The two quantities calculated using (7) and (42) are approximately the same order of magnitude, although the latter is somewhat lower, since after the initial growth stage, the crack encounters a lower energy barrier than that which develops from the initial defect. This means, for example, that, on the diagram of specimen resistance to brittle fracture versus temperature or loading rate, we can differentiate two limit curves, one of which applies to the crack initiation conditions, while the second applies to the moment when the crack growth rate reaches its maximum. The third limit state corresponds to crack growth termination or its last stage when close to the free surface of the body. In this stage, the energy expenditure is high.

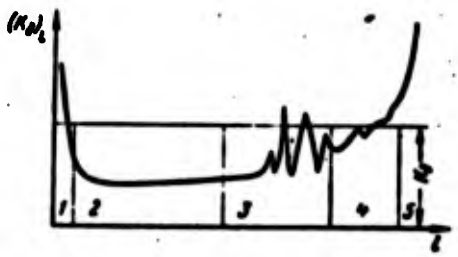

Figure 29. Deviations of the instantaneous value of the specific energy expended in forming unit fracture surface in the case of brittle crack propagation for high stress level.

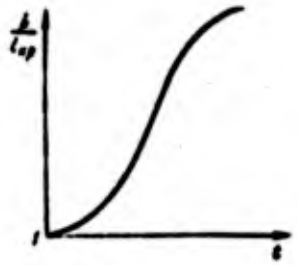

Figure 30. Growing crack length versus time.

In accordance with (37) we have

$$U_y - 2K_d lh = U_y - U_w = U_k \approx 20\left(\frac{v}{c_{max}}\right)^2\left(\frac{l}{L}\right)^2 U_y$$

For $U_w < U_y$, crack growth is possible with velocity determined from the expression

$$\left.\begin{aligned} \frac{v}{c_{max}} &\approx \sqrt{\frac{U_y - U_w}{2U_y}}\cdot\frac{L}{l}, \\ v &\approx 0{,}225 c_{max}\frac{L}{l}\sqrt{1-\frac{U_w}{U_y}}. \end{aligned}\right\} \qquad (43)$$

or

The higher the speed of sound $c_{max} = \sqrt{\frac{E}{\varkappa}}$ and the larger the specimen, the higher is the crack growth velocity. In the general case, the kinetic energy of the separating parts of the plane specimen (Figure 30) can be expressed in the form

$$U_k = \frac{1}{2}\left(\frac{v}{c_{max}}\right)^2 \frac{\sigma_{max}^2}{E} \rho h \zeta,$$

where

$$\zeta = 2\pi \int_0^{2\pi}\int_0^R F(\rho, \varphi)\, d\varphi\, d\rho.$$

Hence, we find the condition for crack growth

$$\frac{d}{dl}\left[-C\frac{\sigma_n^2 \rho h}{E} + 4K_d lh + \frac{1}{2}\left(\frac{v}{c_{max}}\right)^2 \frac{\sigma_n^2}{E} \rho h \zeta\right] = 0. \qquad (44)$$

The coefficient C depends on the stress distribution in the body in the vicinity of the crack edge. For $\sigma_{max} = \alpha_{cr}\sigma_n$ and $l_{cr} = \frac{EK_d}{2C\sigma_n^2}$ we determine the dependence of crack propagation velocity on

crack length

$$\frac{v}{c_{max}} = \text{const}\sqrt{1-\frac{l_{cp}}{l}}. \tag{45}$$

In deriving this formula, we did not consider the dependence of K_d on v, and thus, the expression obtained best characterizes uniform growth of the primary crack. The growth velocity naturally also depends on the specimen geometric form and stress state. In the arguments presented above, this relation is simplified as much as possible. Formula (45) can be rewritten as

$$v = \frac{dl}{dt} = v_0\sqrt{1-\frac{l_{cp}}{l}}. \tag{46}$$

Integrating this expression, we find for $l > l_{cr}$

$$t = \frac{1}{v_0}\left[\sqrt{1-\frac{l_{cp}}{l}} + \frac{l_{cp}}{l}\operatorname{th}\sqrt{1-\frac{l_{cp}}{l}}\right]. \tag{47}$$

A plot of this function is shown in Figure 30.

Upon substitution of the potential energy $U_w - U_y$, we obtain, from the equations of motion in Lagrange form

$$\frac{d}{dt}\left[\frac{\partial(U_w - U_p)}{\partial v} - \frac{\partial(U_w - U_p)}{\partial l}\right] = 0.$$

Hence, we find the crack edge acceleration

$$a_l = \frac{dv}{dt} \approx \frac{3}{40}c_{max}^2\frac{L^2}{l^2}\left[1-\frac{1}{3}\left(\frac{l_{cp}}{l}\right)^2\right] - 2{,}5\frac{v^2}{l}. \tag{48}$$

At the initial moment ($l = l_{cr}$, $v = 0$), the acceleration

$$(a_l)_0 \approx \frac{1}{20} c_{max}^2 \frac{L^2}{l_{cr}^3}. \qquad (49)$$

For $l \gg l_{cr}$ and $v = v_0$, we find

$$(a_l)_{min} \approx \frac{c_{max}^2}{l}\left[\frac{3}{40}\left(\frac{L}{l}\right)^2 - 2{,}5\left(\frac{v_0}{c_{max}}\right)^2\right].$$

In the second crack growth stage, the acceleration of its edge decreases continuously.

In order to determine the order of magnitude of the crack edge acceleration, we take $c_{max} = 1650$ m/sec, $L = 0.1$ m and $l_{cr} = \frac{E\overline{K}}{2\sigma^2} = 3 \cdot 10^{-3}$ m.

Then the maximum acceleration will be $(\alpha_l)_0 = 10^{11}$ m/sec^2. The high acceleration is confirmed by the results of measurements using high-speed movie photography with a rate of 240,000 frames per second. Since the quantity T_{lim} is proportional to $(\sigma_{lim}/\sigma)^2$, the crack propagation velocity in the general case depends on σ^n. In accordance with (45)

$$v = \text{const}\sqrt{1 - \text{const}\,\sigma^2}. \qquad (50)$$

Considering the arguments presented on the dependence on various factors of the specific energy necessary for the formation of unit new surface in the body as the crack grows, we can take

$$K_0 = (K)_{v=0}\frac{e^{-\frac{\delta}{\gamma}}}{\left[1 + m\left(\frac{v}{c_0}\right)^2\right]^2}. \qquad (51)$$

In this case, the quantity K_d, characterizing the fracture resistance of the material, depends on the crack propagation velocity and consequently on crack length, which complicates markedly the solution of the crack propagation differential equation. In all cases, the steady-state crack propagation process rate depends on the stress level. When the temperature is constant, the approximate solution has the form

$$\frac{v}{c_\theta} = \text{const}\sqrt{1-\left(\frac{\sigma_0}{\sigma}\right)^2}\sqrt{1-\frac{\sigma_0}{\sigma}}. \qquad (52)$$

The nature of this relation is shown in Figure 31. If, in this formula, we take the constant having the nature of the lower limit stress equal to $\sigma_0 = 15$ kgf/cm^2, and if we consider the elastic wave propagation velocity in the material to be 600 m/sec, we obtain the dependence of the relative crack propagation velocity on the relative stress shown in Figure 32.

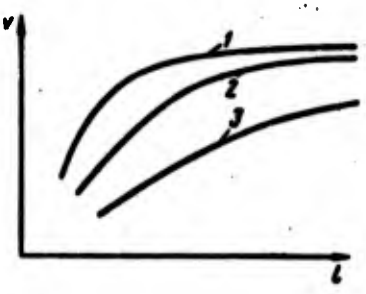

Figure 31. Theoretical dependence of crack propagation velocity on stress in second stage of brittle fracture:

$1 - \sigma_{n1}$; $2 - \sigma_{n2} > \sigma_{n1}$; $3 - \sigma_{n3} > \sigma_{n2}$

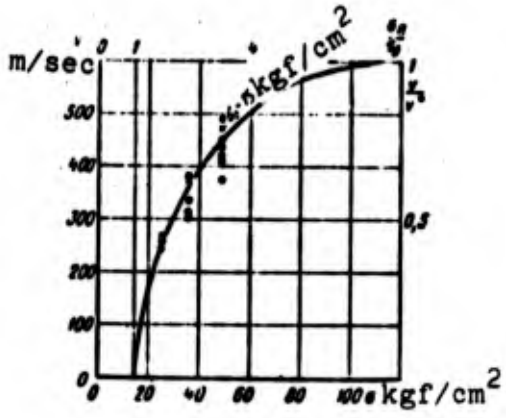

Figure 32. Data from theoretical calculation of crack propagation velocity in second stage of brittle fracture using (52) and data from tests of plane acrylon specimens:

$\times - U = 0.8$ kgf·m; $\bullet - U = 0.25$ kgf·m; $\circ - U = 0.05$ kgf·m

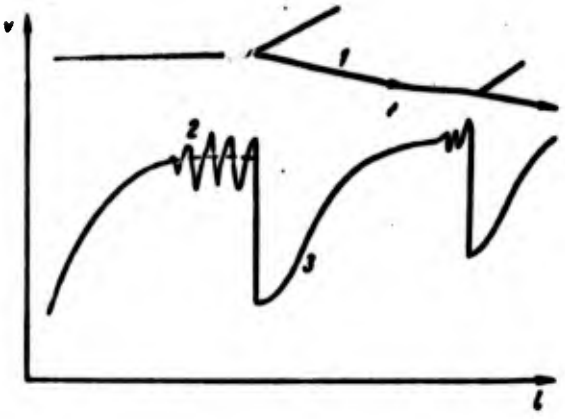

Figure 33. Nature of crack growth with branchings.

1 — primary crack; 2 — microbranchings; 3 — crack propagation velocity after branching.

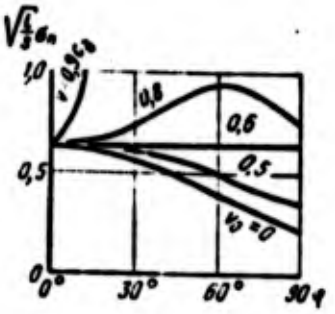

Figure 34. Dependence of maximum stress directions at the edge of crack propagating with velocity v on the nominal stress (after Ioffe).

The value of the specific energy K_d under dynamic conditions amounts to about 1 kgf·cm/cm² at normal temperature. With increase of the nominal stress above a certain value, the crack propagation velocity does not increase, since, at this stress, the maximum possible velocity v — defined by the material properties, i.e., the transverse elastic wave propagation velocity in both parts of the fracturing specimen — is reached.

8. In the third crack growth stage, crack branching begins in the microvolumes, indicated by the nature of the fracture, which is no longer a smooth shiny surface. We see on the fracture surface individual segments and crack divergence traces at the branching points. A schematic of the crack propagation velocity variation in the presence of branching is shown in Figure 33.

After branching, the crack edge again advances at an increasing rate with the acceleration reaching values on the order of 10^{10} m/sec². The crack grows discontinuously. The velocity variation cannot be recorded by the present measurement methods, and in studying fracture mechanics, we usually consider only the average value, which is shown, for example, in Figure 20 by the solid curve. In this case, calculation yields only the apparent value of K_d (Figure 29), and the instantaneous value of K_d may differ significantly from this apparent value.

However, it is important to know the true values of K_d in studying the fracture process using the theory of elastic wave propagation in the material, or when measuring the instantaneous stress values in the vicinity of the crack edge owing to the action of these waves. However, if we deal with the apparent (average) resistance of the material to fracture and the average crack propagation velocity, the maximum crack edge velocity v^* is small in comparison with the speed of sound (for brittle materials, it is about one-third the speed of sound). The maximum crack propagation velocity can be determined by studying the instantaneous stress field near a fast-growing crack [213]. The stress components vary so that upon reaching the maximum velocity v^*, there is a section where the maximum tensile stress acts and forms a definite angle with the crack direction in the first and second stages of its growth (Figure 34). If $v < v^* = 0.6\ c_d$, the maximum tensile stress acts at the section $\varphi = 0$, i.e., the crack propagates perpendicular to the principal stress trajectories for static loading of the part. For a crack propagation velocity $v^* = 0.6\ c_d$, the instantaneous maximum tensile stress acts in oblique sections.

The propagation direction is determined by the direction of the maximum stress, therefore, the crack branches. The branching angle φ_v is the larger, the higher the crack propagation velocity. For example, for $v = 0.8\ c_d$ the branching angle will be 60°. Actually, the propagation velocity does not exceed the value v^*, since there is loss of energy with each branching and crack advance slows.

The maximum velocity varies as a function of the local material properties; therefore, we can obtain different values of the branching angle for very slight deviations from the indicated maximum velocity. Ioffe obtained the mentioned solution under the assumption that the radius of curvature of the crack edge contour increases with increase of the propagation velocity. This assumption, which simplifies the solution, is not justified in practice. Broberg [117] studied an analogous problem under the assumption that the crack edge

curvature radius decreases with increase of the velocity. The solution obtained under the assumption that the crack edge curvature radius remains constant regardless of the crack propagation velocity yields similar results.

In all cases, a tendency toward crack branching appears upon reaching the velocity v^*, however, the angles are different. In the general case, we can consider that the branching angle will be larger the higher the instantaneous value of the velocity. If we consider this relationship established, knowing the branching angle, we can estimate the crack propagation velocity.

Thus, the theoretical solution has been obtained under several simplifying assumptions. Therefore, we must study the branching angle experimentally as a function of crack propagation velocity, material temperature and properties, specimen shape, and loading scheme. A rectangular specimen with side ratio $B/L \to 0$ is more properly considered a beam with transverse deformation waves. In examining a specimen of square form, we should consider the complex wave interaction, then we can expect better agreement with the indicated theoretical solutions. The higher the crack propagation velocity v and the larger the value of K_d, the less will be the influence of the local barriers and material nonhomogeneity (for example, the presence of zones of high strength) on crack propagation. The instantaneous stress field in the vicinity of a propagating crack has been studied experimentally on optically active materials, including polymethyl methacrylate [80, 187]. It has been found that, at the beginning of the third crack growth stage, the stress field changes very little (Figures 35 and 36) and displaces along with the crack edge; therefore, the crack edge radius of curvature may be considered constant. However, upon reaching the zone close to the crack edge, the stress field changes rapidly and the local stresses and crack propagation velocity decrease, which is an indication of the onset of the fifth crack growth stage. In this stage, branching is also observed, even with a lower propagation velocity, because of distortion of the stress field. The stress distribution along the advancing crack edge for different values of the relative velocity v/c_d from

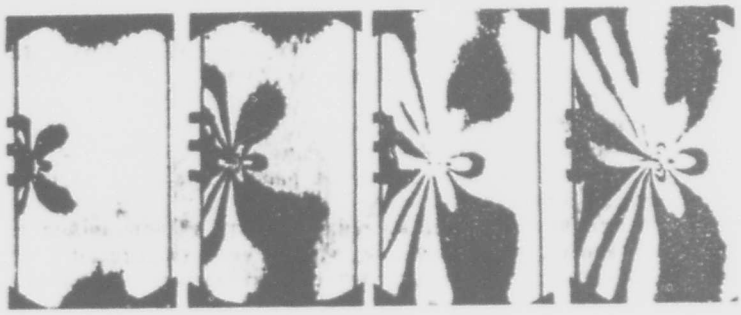

Figure 35. Stress field around uniformly growing brittle fracture crack after Rolf, Lyman, and Hall (σ = 13.4 kgf/mm^2).

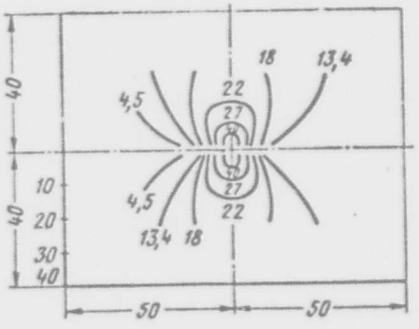

Figure 36. Isochromes of stress field near edge of growing crack in plane ebonite specimen for four crack edge locations (after Wells).

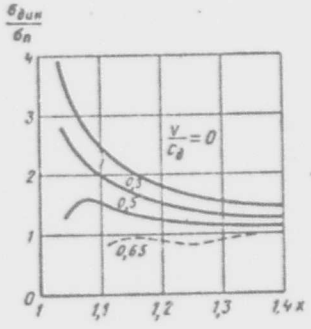

Figure 37. Distribution of principal tensile dynamic stress component for different values of brittle fracture crack propagation velocity.

Smith's data is shown in Figure 37. The crack can branch for a propagation velocity greater than 0.6 c_d. The stress dynamic component decreases with increasing distance from the maximum point and approaches the static value. With increase of the growth rate, the intensity of potential strain energy release at the propagating crack decreases while the kinetic energy changes become larger.

To verify all these hypotheses, tests were made of thin plane specimens of rectangular form made from acrylon and epoxy resin for different stresses, nature of the fracture, and techniques for obtaining initial crack. Measurements were made of the average crack

propagation velocity (without account for sharp short-term deviations) and the elastic deformations in the material (strain propagation law).

§4. Measurement of Brittle Fracture Crack Propagation Velocity

In the beginning of the tests, we verified the possibility of measuring crack propagation velocity and the material dynamic deformations. The experiments were made on thin plane acrylon specimens cut from large sheets, and all the specimens were oriented similarly relative to the sheet edge, and were nearly square in form (300 x 350 x 3 mm). We verified the specimen loading method for stresses σ_n from 5 to 125 kgf/cm^2 and impact on a wedge introduced into a notch in the specimen (Figure 38) to facilitate formation of the initial crack (impact energy was 0.025, 0.05, and 0.5 kgf·m). In some cases, the initial crack was obtained by loading (statically) a special ledge of a notched specimen with high tensile stress so that a sharp crack formed at the bottom of the notch and then propagated through the material web between the ledge and the specimen into the material of the basic specimen. The tests were conducted at 25° C in the glassy hard material state. The crack propagated in the direction of the specimen width B = 300 mm (in later tests, the specimen width was increased to 600 mm) from the initial 5 mm deep V-shaped notch with 60° apex angle. The specimens were clamped in the loading frame (Figure 39) and loaded by a tensile force without any noticeable bending moment. The uniformity of the tensile stress distribution in the crack propagation zone was verified by the photoelastic method. The crack propagation velocity was measured with the aid of indicators working on the principle of current-carrying wire rupture as the crack edge crossed the wires. The current-carrying wires were segments of 30 micron diameter copper wire bonded by a special technique on the prepared specimen surface. The distance between adjacent wires in the direction of main crack propagation was normally 30 mm.

On the basis of detailed study of this measurement method and the calibrations which were made, it can be said that the accuracy of the average crack propagation velocity determination within the

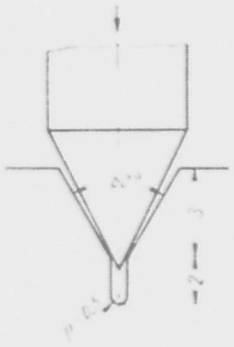

Figure 38. Form of notch and wedge for obtaining initial crack in specimen.

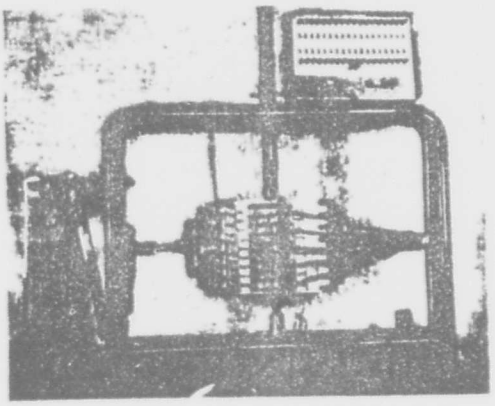

Figure 39. Frame and loading device for studying brittle fracture mechanics of plane specimens.

limits of the wire spacing was no less than 10%. We could also observe crack advance by continuous measurement of the dynamic stress which arises near the edge of the propagating crack. For this purpose, we used resistance strain gages bonded in regular rows to the specimen surface at a distance of 10 mm from the assumed line of main crack propagation. The electrical signals obtained during the measurements were recorded on an oscillograph. The wire indicators were connected to a voltage divider whose output voltage was recorded by a cathode ray oscillograph in the form of a stepped diagram, each step of which corresponded to breaking of the next wire.

Synchronization of oscillograph startup with the moment of crack onset was provided by a special electronic triggering device. This device was controlled from a sensor mounted in the immediate vicinity of the notch edge and triggered several oscillographs, eliminating the possibility of repeated or improperly timed startup. Some of the recording channels were used to record the dynamic strain waves which arise as the crack advances, using strain gages as sensors. Prior to the measurements, the time scaling was established so that the overall diagram length corresponded to 1000 μsec, which for the selected specimen size corresponds to an average crack propagation velocity of no less than 300 m/sec. The ordinate axis scale made it possible to record a dynamic stress of about 100 kgf/cm^2.

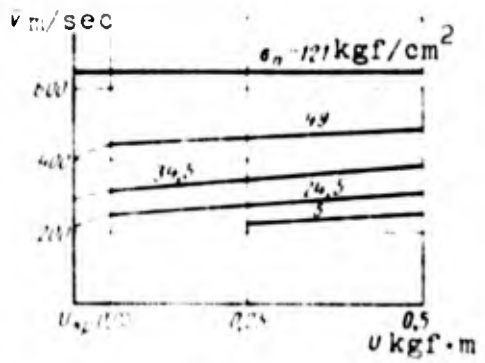

Figure 40. Average crack propagation velocity in plane acrylon specimen as function of energy of impact causing crack onset and stress level in specimen.

The scheme simplifies considerably when measuring only the crack propagation velocity. In this case, only a single oscillograph was used for recording and the voltage divider and the break wires were connected to this oscillograph.

The first segment of the specimen fracture surface was usually mirror smooth; then, as the propagation velocity reaches the order of 0.8 v*, the fracture surface became rough because of crack microbranching and thereafter became stepped, usually in connection with macrobranchings. Finally, the fracture surface structure then became fine in accordance with the large crack propagation velocity reduction. In reducing the measurement results, we determined the velocity v for the individual crack length segments and the average velocity $\bar{v}$ over the entire specimen width. The measurement results show that the impact energy, which facilitates initial crack onset, influences the crack propagation velocity only in the initial crack growth stage. The higher the level of the tensile stress σ_n in the specimen, the shorter is the duration of the first growth stage and the less is the influence of the impact energy on the average crack propagation velocity (Figure 40). If the stress is higher than a certain level, we can obtain the initial crack reliably without impact. This statement is valid for a sufficiently great crack depth and a crack form which provides stress concentration corresponding to the critical concentration factor α_{cr}, i.e., for the critical notch size for the given stress level.

The maximum crack propagation velocity in acrylon, determined as the average velocity in the third growth state, corresponded to the value $0.4\sqrt{\frac{E}{\rho}}$ or $0.63\sqrt{\frac{G}{\rho}} = 0.63\, c_d$. Actually, even with the measurement technique used, we noted local values of the velocity prior to crack

branching exceeding 0.7 c_d, which corresponds to the measured branching angles. The specimen shape was nearly square and permitted the development of a complex system of strain waves and instantaneous stress fields. However, on the whole, the measurement results confirmed the theoretical values of the maximum main crack propagation velocity.

Depending on the level of the stress σ_n, crack branching began for a length (from the initial point) on the order of $l = (0.3 - 0.5)B$, i.e., upon reaching the required crack edge propagation velocity. The cracks which formed as a result of branching usually terminated their growth.

In studying the influence of the energy accumulated in the system, we connected in series with the specimen steel springs in which potential strain energy exceeding by several fold the acrylon specimen strain energy was stored. This stored energy had practically no effect. This shows that the fracture process of the very brittle materials proceeds so rapidly that only part of the potential strain energy near the point of fracture is released. Significant redistribution of the nominal stress because of crack openings does not occur until the crack travels considerable distance from the edge of the specimen.

On the basis of the described preliminary series of tests, we can already draw some conclusions relative to crack propagation velocity. For a high stress level (over 100 kgf/cm^2) the crack propagation velocity variation depends very little on the technique for obtaining the initial crack; the crack grows in the same way when it arises as a result of impact or under the action of high local tensile stress. Crack growth is independent of the amount of potential energy accumulated in the system. The influence of the specimen absolute dimensions on the material fracture process is also diminished to a considerable degree. For a lower stress level (on the order of 50 kgf/cm^2 and lower), the maximum crack propagation velocity in the third crack growth stage is the same as for the higher stress levels;

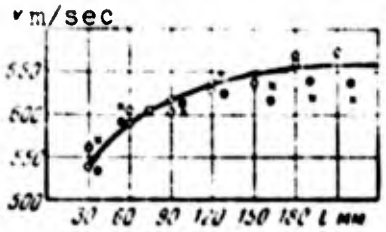

Figure 41. Crack propagation velocity versus crack length for different values of the impact energy (σ_n = 121 kgf/cm²; X - U = 0.25 kgf·m; ● - U = 0.05 kgf·m).

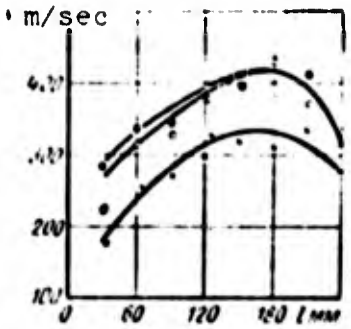

Figure 42. Crack propagation velocity versus crack length for different crack initiation techniques (σ_n = 30 kgf*/cm²): ○ - U = 0.25 kgf·m; ● - U = 0.25 kgf·m; x — twice the static-load tensile stress.

however; the acceleration in the first stage depends strongly on the technique for obtaining the initial crack. The duration of the third growth stage is also different. In the case of crack formation under the influence of high local static tensile stress, the initial propagation velocity is lower; however, the acceleration in the subsequent growth stage is higher than when the crack develops as a result of impact. With a still lower stress level (up to 30 kgf/cm²), the maximum crack propagation velocity in the third stage, if the crack develops as a result of high local stress, generally does not reach the value of the maximum crack velocity obtained as a result of impact, when the crack usually grows under conditions with the required excess energy (Figures 41 and 42).

Figure 43 shows combined traces of the signals from four strain gages located in a row parallel to the fracture plane of one specimen. In this case, the initial crack was obtained under the influence of local static tensile stress in order to avoid superposing the impact effect on the disturbance from crack edge displacement.

On the basis of this recording, we can also obtain the dependence of the crack length on time and therefore, on the propagation velocity (Figure 44).

*Translator's note: Foreign text incorrectly uses kg here.

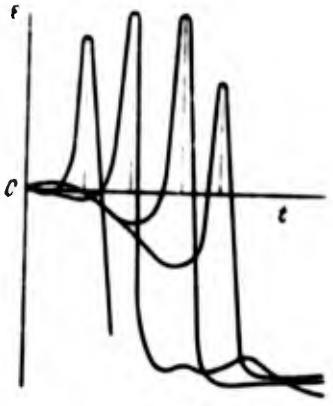

Figure 43. Nature of dynamic strain change during crack propagation in plane specimen.

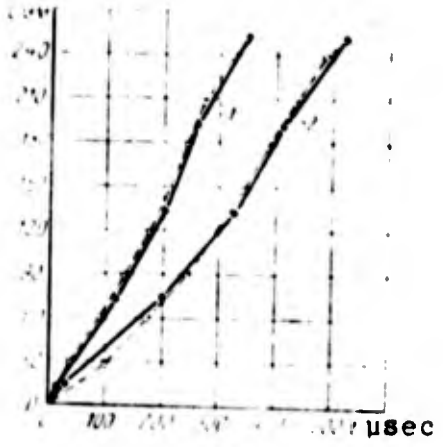

Figure 44. Crack edge advance for dynamic (1) and static (2) techniques for obtaining crack (σ_n = 30 kgf/cm^2).

Comparing the velocities obtained by measuring the dynamic strains during crack propagation (dashed curve) and by breaking of the wires (solid curve), we see that the measurement results agree quite well. The curves also agree well with the nature of the theoretical $l = f(t)$ curve (see §3). In this case, the crack originated as a result of impact. For a temperature of 25°C, the average value of the specific energy required for the formation of unit fracture surface is 30% higher when the crack arises as a result of the influence of static loading than in the impact case.

On the basis of the established possibility for objective study of brittle fracture mechanics, we undertook a second series of tests of plane acrylon and epoxy resin specimens, and studied the influence of nonuniform stress distribution along the specimen edges. The specimens were nearly square (300 x 350 x 3 mm) and rectangular (640 x 350 x 3 mm), respectively. Part of the specimens of both materials were loaded, as in the first series of tests, by uniformly distributed tensile stress. The remainder were loaded so that the tensile stress at the specimen edges was distributed linearly in certain cases, and nonlinearly in others. In certain specimens, individual zones of secondary biaxial stress state were created to simulate the residual stress zones. In the specimens with the secondary local stresses, in addition to the tensile stresses applied to the specimen edges by a

Figure 45. Isochromes showing stress distribution near edge of hole in specimen loaded radially.

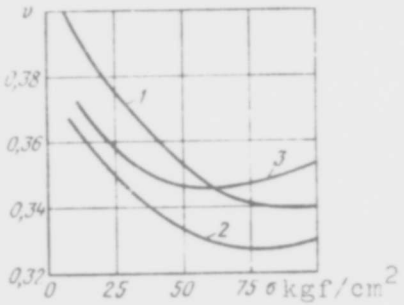

Figure 46. Poisson's ratio for epoxy resin as function of stress and temperature.
1 — 25° C; 2 — 40° C; 3 — 50° C.

lever mechanism, a special loading device was used to create additional biaxial stresses near the assumed fracture surface. This loading device consisted of a 36 mm diameter split steel cylinder which could be expanded by an internal conical core. After creating — with the aid of this device — a uniformly distributed pressure at the surface of a hole in the specimen, the stress distribution was verified by the photoelastic method (Figure 45). It was found to be necessary to introduce a thin rubber ring to equalize the strain distribution between the expandable cylinder and the specimen material in order to ensure a secondary stress distribution which is symmetric relative to the center. In some of the specimens, there was only a single secondary stress center, in others there was a whole series of such centers, located along the assumed crack propagation line. The same secondary stress level at all the centers was achieved by tightening up the conical cores of the split cylinders and verifying the stress magnitude by the photoelastic method.

The tests associated with study of crack propagation in plane specimens were conducted at a temperature of about 25° C. The properties of acrylon under these conditions were described above. The epoxy resins were cast into glass forms and then the specimens were taken out and cooled slowly. In order to eliminate residual stresses, the specimens were annealed several times in a glycerine bath. The

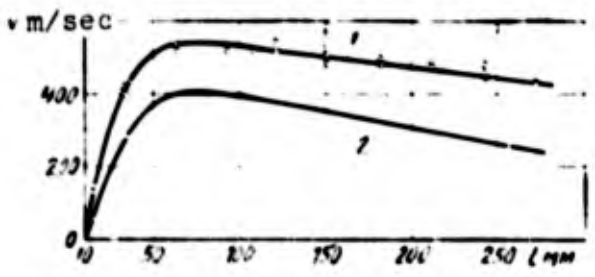

Figure 47. Crack propagation velocity in tests of square acrylon specimens as function of stress level.
1 — σ_n = 62.5 kgf/cm²; 2 — σ_n = 41.5 kgf/cm².

properties of the epoxy specimen material were verified by repeated tests. It was found that the ultimate strength σ_b = 500 kgf/cm², the longitudinal elastic wave propagation velocity in the material c_{max} = 1100 m/sec. The dependence of the Poisson's ratio on the stress is shown in Figure 46. The epoxy resin is just as brittle a material as acrylon.

The crack propagation velocity was measured by breaking current-carrying wires as described in examining the first series of tests. In certain cases, the instantaneous strain values were measured with the aid of strain gages bonded near the supposed crack line in order to check the crack edge displacement velocity. Strain gages were also installed at the specimen edges to determine the distribution of the nominal stress σ_n during the tests. In most cases, the initial crack was obtained with an impact of energy 0.25 kgf·m. The specimens were mounted in the loading device so that the crack propagation direction coincided with the direction of casting. The recording of the dynamic strains, measured by strain gages mounted in the immediate vicinity of the growing crack, and also by lateral strain gages located at considerable distance from the crack, showed that the level of the instantaneous stress values remains practically constant in the third growth stage.

The test results on the square acrylon specimens confirmed the conclusions drawn previously. Figure 47 shows crack propagation velocity as a function of crack length for two values of the uniformly distributed nominal stress σ_n = 41.5 kgf/cm² and σ_n = 62.5 kgf/cm², which corresponds to the relative value $\frac{\sigma_n}{\sigma_b}$. For these stress values, the maximum velocity v^* = 650 m/sec required for crack branching was not reached and the crack propagated along a straight line

Figure 48. Crack shape in square acrylon specimen tested with uniform tensile stress distribution $\sigma_n = 62.5$ kgf/cm^2.

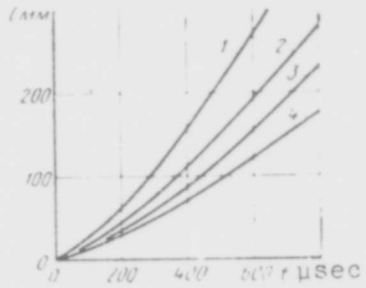

Figure 49. Crack length versus time for brittle fracture.
1 — square acrylon specimen ($l_{cr} = 0.9$ cm; $\sigma_n = 62.5$ kgf/cm^2); 2 — rectangular epoxy resin specimen ($l_{cr} = 1.3$ cm, $\sigma_n = 40$ kgf/cm^2); 3 — square acrylon specimen ($l_{cr} = 2$ cm; $\sigma_n = 41.5$ kgf/cm^2); 4 — square epoxy resin specimen ($l_{cr} = 15$ cm; $\sigma_n = 9.8$ kgf/cm^2).

(Figure 48). The crack length as a function of time is shown in Figure 49. The nature of the curves shown in these figures agrees well with the theoretical conclusions presented in §3. Differentiation of the curves of crack propagation velocity variation with time shows that the initial acceleration of a crack arising under the influence of local tensile stress depends on the magnitude of σ for a low stress level $\frac{\sigma}{\sigma_b} \approx \frac{1}{20} \ldots \frac{1}{10}$.

The square epoxy resin specimen test results permit drawing the same conclusions as in the acrylon specimen tests. The dependence of crack propagation velocity on crack length in the first stages of specimen fracture growth for uniformly distributed tensile stress is shown in Figure 50.

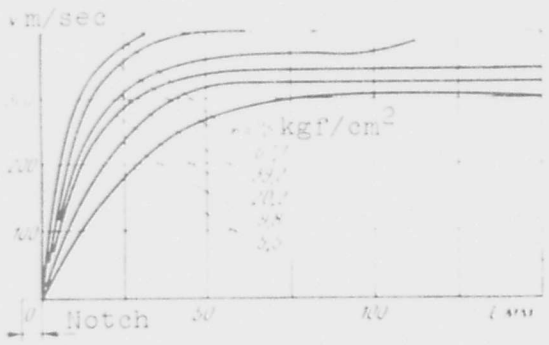

Figure 50. Crack propagation velocity in plane square epoxy resin specimens versus level of uniformly distributed tensile stress along specimen edges (0 indicates crack branching points).

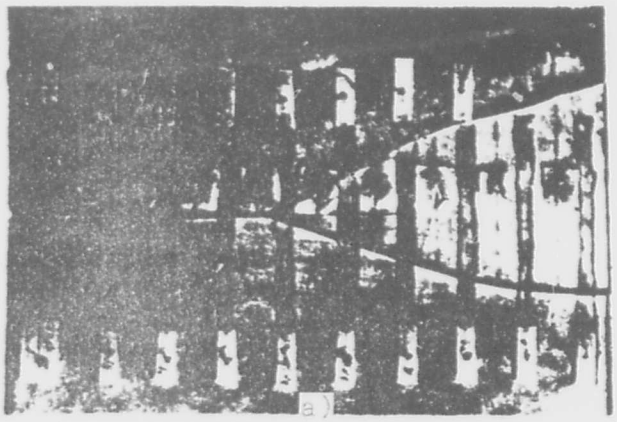

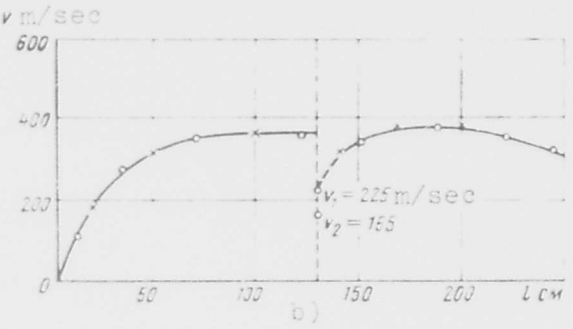

Figure 51. Crack branching during test of square epoxy resin specimen with σ_n = 39 kgf/cm².

a — nature of branching;
b — quantitative data.

With increase of the nominal stress level, there is an increase of the initial crack edge acceleration and of the propagation velocity in the third crack growth stage. A tendency toward crack branching arises when reaching a velocity $v^* = 0.6\sqrt{\frac{G}{E}}c_{max}$ = 400 m/sec. This means that crack branching begins earlier, the higher the level of the nominal stress σ_n. There is also an increase of the number of crack branchings. If $\sigma_n < 38$ kgf/cm², branching does not occur. At higher stresses ($\sigma > \frac{\sigma_b}{10}$), we note on the specimen fracture surface traces of intense crack microbranching and tearing out of material particles. The nature of the branching and diagrams of crack propagation velocity in these cases are shown in Figures 51 through 53. The dependence of the angle φ_v at the first branching (angle between the two crack branches) and the distance x_v (from the initial fracture point to the first branching) on the tensile stress level in the specimen is shown in Figure 54. The higher the nominal stress, the larger is the number of crack branchings and the larger the number of short lateral cracks which branch off from the main crack. Figures 51 through 53 also show the main crack propagation velocity after branching and the

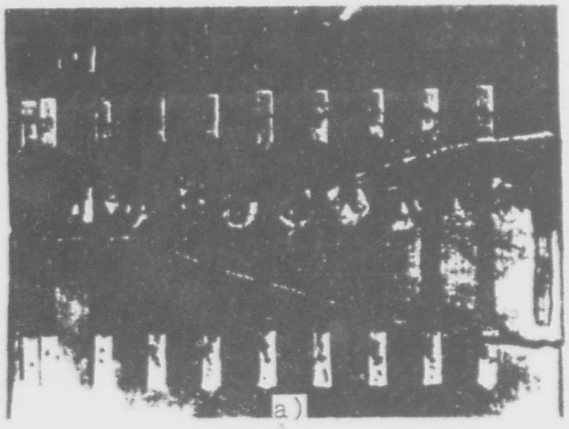

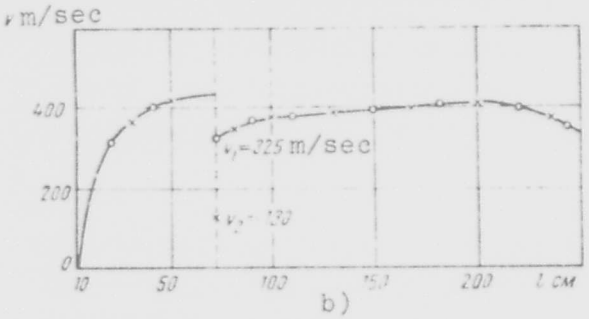

Figure 52. Crack branching during test of square epoxy resin specimen with nominal stress σ_n = 67.7 kgf/cm^2.

a — nature of branching; b — quantitative data.

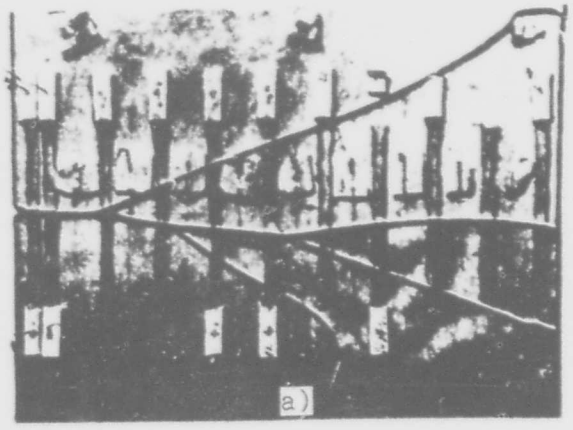

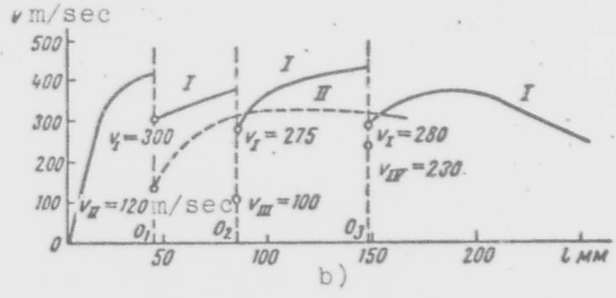

Figure 53. Crack branching during test of square epoxy resin specimen with nominal stress σ_n = 75 kgf/cm^2.

a — nature of branching; b — quantitative data.

velocities v_1 and v_2 of both crack branches. Some of the diagrams show only the velocity of the one branch which propagates with the higher velocity (main crack). We note that the initial crack velocity at the branching point can be measured only on the basis of dynamic strain recording. We can assume that the actual velocity values at the branching point may be somewhat lower than shown in the figures; however, crack growth does not terminate in any of the cases.

For the higher values of the crack propagation velocity, we note prior to the branching point traces of tearing out of material particles and microbranchings, and the surface is reminiscent of a chevron fracture. Beyond the branching point, we again note on the

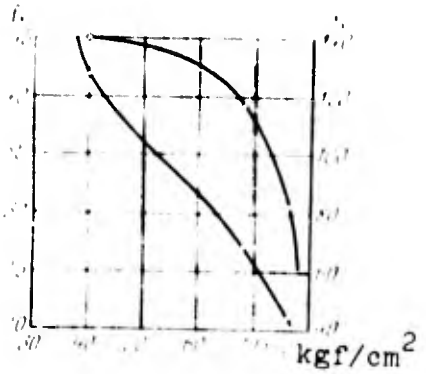

Figure 54. Crack branching angle φ_v and distance from crack origin to branching point versus nominal stress level from data of plane epoxy resin specimen tests.

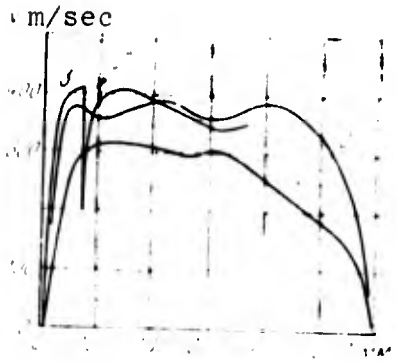

Figure 55. Crack propagation velocity in rectangular epoxy resin specimens: 1 — σ_n = 9.4 kgf/cm²; 2 — σ_n = 40 kgf/cm²; 3 — σ_n = 66 kgf/cm².

fracture surface bright smooth areas corresponding to lower crack propagation velocity. Thus, we can judge the magnitude of the instantaneous crack propagation velocity on the basis of the nature of the fracture.

With increase of the velocity, there is an increase of the overall specific work required for the formation of each running centimeter of fracture surface in a specimen of constant thickness, since the free surface area F_l which actually arises in this case increases because of the numerous crack direction changes and the presence of numerous lateral cracks, which leads to an increase of the product $U_w = K_d F_l$. In this case, the value of K_d diminishes somewhat. After reaching the critical value of this work, crack macrobranching becomes more probable with regard to the energy conditions.

In order to determine the influence of specimen shape, we also made tests of rectangular epoxy resin specimens with the size of the longer side, oriented in the direction of crack propagation, equal to 640 mm. The specimens were loaded along the edges by a uniformly distributed tensile load. Two specimens were tested at a nominal

stress σ_n = 9.4 kgf/cm², two at σ_n = 40 kgf/cm², and the last two at σ_n = 66 kgf/cm². The test results are shown in Figure 55.

Comparison of these results with those of square specimen tests shows that the nature of crack propagation and branching in the rectangular specimens is similar to that observed for square specimens; however, the limit state is reached for a higher stress. Thus, for example, for σ_n = 5 kgf/cm², a crack does not develop in the rectangular specimen, while the square specimen under these conditions fails with a smooth fracture. Crack branching in the rectangular and square specimens begins at practically the same crack propagation velocity v^* = 400 m/sec; however, a stress of no less than 65 kgf/cm² is necessary to obtain this velocity in the rectangular specimen, while a stress of 40 kgf/cm² is sufficient in the square specimen.

The shorter relative distance from the specimen edge to the crack edge in the third fracture growth stage $\left(\frac{l_0}{\frac{L}{2}} \approx \frac{200}{175} = 1.15\right)$ influences both propagation velocity and crack direction. The corresponding relative distance for the square specimen is $\frac{l_0}{\frac{L}{2}} = \frac{100}{175} = 0.57$. Thus, the distance from the crack to the specimen edge and the specimen shape have a very strong influence on the nature of crack growth, since these factors influence the instantaneous stress distribution in the specimen. Specifically, for rectangular specimens with high stresses in the third stage, we see clearly the wavy crack form and periodic change of the propagation velocity, which did not occur in the square specimens. Careful study of the nature of the fracture, specifically x-ray micrography of the material structure at different distances from the fracture surface, showed that the material property changes associated with irreversible energy absorption are distributed in accordance with a periodic law through the thickness of the surface layer. In view of this, the fracture mechanics relations presented above are valid only in the second fracture growth stage, with accelerated crack edge advance. After increase of the velocity to v^*, we must study strain wave propagation in the body and consider the associated dynamic stresses which arise with rapid advance of the

brittle fracture crack in a body of given geometric shape. Nor can we ignore the influence of Rayleigh waves.

The cracks in rectangular epoxy resin specimens at stresses above 10 kgf/cm^2 have a curvilinear form, and they may extend prematurely to the edge of a narrow specimen. The fracture surface has a nonuniform nature and in certain places is reminiscent of a pitted surface, since the crack direction frequently changes by a small angle. The crack propagation velocity measurement data show a large amount of scatter in comparison with the corresponding data for the square specimens. Crack branching occurs at a higher stress than for the square specimens and the acceleration after branching is higher, but is observed in the course of a shorter time interval. Only the single main crack branch which is most favorably oriented in relation to the nominal tensile stress extends to the specimen edge. In the fracture of rectangular specimens, the crack branching point is also preceded by a fracture segment with "chevron" structure. The dependence of crack length on time is shown in Figure 55, where the corresponding data of square specimen tests are also presented for comparison. In the accelerated crack propagation region, the results for the two specimen types coincide and agree with the theoretical data.

An important characteristic of the fracture process is the crack propagation velocity dependence on the nominal stress level. Figure 56 shows the average crack propagation velocity $\bar{v}$ and the velocity v_{max} at the end of the accelerated crack growth state (for example, for $l \approx 80$ mm) as a function of the stress level for square and rectangular epoxy resin specimens. For theoretical study purposes, the v_{max} curves are of greater interest than the $\bar{v}$ curves, since they agree well with the theoretical conclusions presented in §3. If we plot the relation $v^2_{max} = f(l, \sigma^2)$ with account for (45) for the subject fracture growth stage, all the experimental points fall on a single curve (Figure 57). The average velocity $\bar{v}$ naturally depends on the specimen dimension in the crack propagation direction. In the general case, the crack propagation velocity depends on the product of crack length and stress to some power. At the beginning of the second fracture growth stage, the determining parameter for the subject brittle

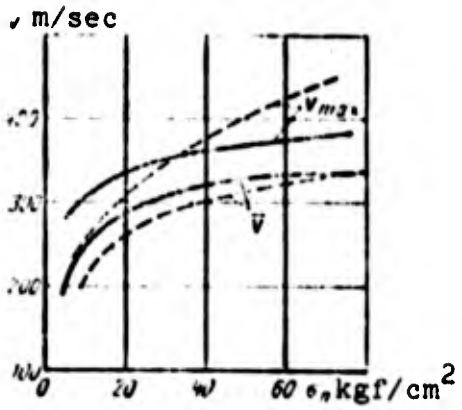

Figure 56. Average and maximum values of crack propagation velocity in square (solid curves) and rectangular (dashed curves) epoxy resin specimens versus stress σ_n.

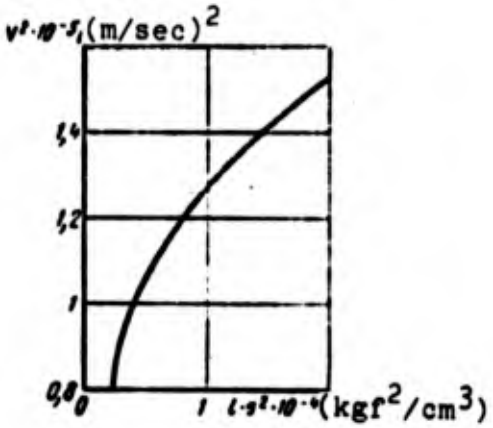

Figure 57. Crack propagation velocity at end of second brittle fracture growth stage for epoxy resin specimens versus theoretical parameter $l\sigma^2$.

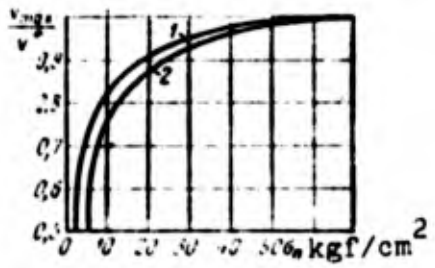

Figure 58. Ratio $\frac{v_{max}}{v^*}$ versus nominal stress level for square (1) and rectangular (2) epoxy resin specimens.

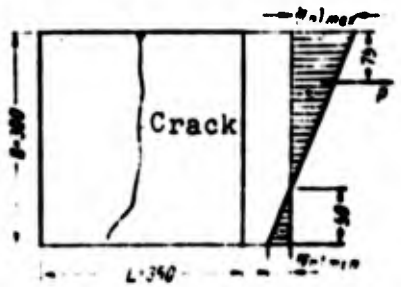

Figure 59. Nominal stress distribution in plane specimens with constant stress gradient.

materials is the parameter $l\sigma^2$, which corresponds to the value $\lambda = 1$ in (9). At the end of this stage and a velocity close to the maximum value, the exponent decreases and the parameter $l\sigma$ becomes determining. The dependence of the maximum relative crack propagation velocity $\frac{v_{max}}{v^*}$ on the stress level for epoxy resin specimens is shown in Figure 58.

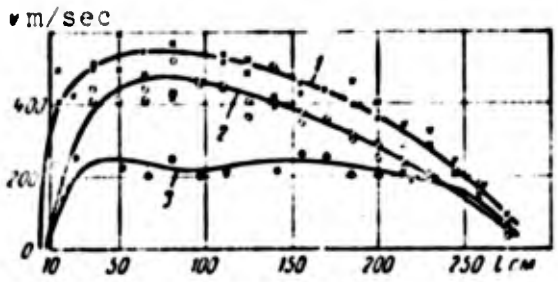

Figure 60. Crack propagation velocity in specimens with linear distribution of nominal stress versus stress level $(\frac{\sigma_{max}}{\sigma_{min}})$.

1 — 104/ — 20.8 kgf/cm²;
2 — 73/ — 14.6 kgf/cm²;
3 — 31/ — 6.25 kgf/cm².

To study the influence of the distribution of the stress σ_n along the specimen edges on fracture growth we tested square specimens loaded by a combined tensile and bending load whose resultant passed 75 mm from the upper edge of the specimen. The stress was distributed linearly along the specimen edges (Figure 59), with the stress reversing direction about 50 mm from the lower edge of the specimen, and the lower part of the specimen was compressed. Prior to obtaining the initial crack, the linearity of the nominal stress distribution was checked on the acrylon specimens by the photoelastic method. Crack propagation in the nonuniform nominal stress distribution field was studied on five square acrylon and four epoxy resin specimens. The values of the maximum nominal tension stress $(\sigma_n)_{max}$ and the maximum compression stress $(\sigma_n)_{min}$ for the individual specimens are shown in the table.

Acrylon	+31/—6.25	+73/—14.6	+73/—14.6	+104/—20.8	+104/—20
Epoxy resin	+13/—2.6	+13/—2.6	+[illegible]/—7.8	+39/—7.8	

The results of the acrylon specimen tests show (Figure 60) that, in the third and fourth fracture growth stages, the nominal stress gradient retards crack advance markedly. The segment of constant crack propagation velocity was very short. The average crack propagation velocity $\bar{v}$ was considerably lower than in the case of uniform tensile stress distribution. If we determine the average value $\frac{\sigma_{n\,max}}{2}$ of the nominal stress in the tension zone, and then interpolate graphically (Figure 40) to find the corresponding value of the average crack propagation velocity for uniform stress distribution, we can

compare the crack propagation conditions for uniform and nonuniform stress distribution. For convenience, the data obtained are summarized in the table.

v in m/sec for Stress Distribution	σ_n in kgf/cm^2	
	[illegible]	[illegible]
Uniform	200	410
Linear	210	300

For the lower stresses, the crack has a wave-like form, as in most cases of crack propagation with small excess energy. Similar results were obtained in studies of square epoxy resin specimens. The values of the average crack propagation velocity are shown in the table.

v in m/sec for Stress Distribution	σ_n in kgf/cm^2		
	6.5	16.4	19.6
Uniform (from interpolation)	250	280	310
Linear	190	230	270

It was not possible in any of the tests to localize the crack, i.e., to stop its growth in the low or compressive nominal stress zone, since the size of this zone was small and in all cases, the crack approached the edge of the specimen under conditions of a quite large kinetic energy margin. However, several centimeters ahead of the fracture peak along the path, the nature of the fracture surface differs from that established in the preceding tests. The fracture appearance indicates oscillations of the crack propagation velocity and abrupt and large crack direction changes (Figure 61).

By analogy with the case of uniform nominal stress distribution, we can determine the crack opening y, the energy components U_y and U_k [see (35) and (37)], and calculate the velocity and acceleration of the crack edge in the second fracture growth state with linear stress distribution $\sigma_n = \sigma_{n\,max} - \frac{\sigma_{n\,max} - \sigma_{n\,min}}{l}x$. In this fracture

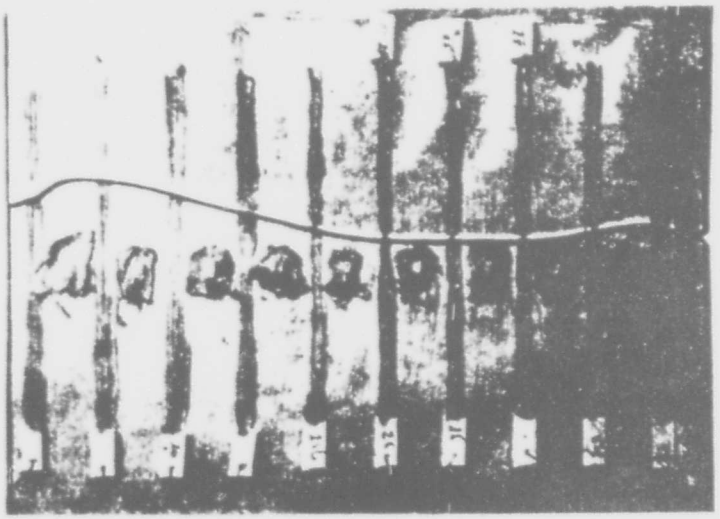

Figure 61. Crack in epoxy resin specimen obtained with linear nominal stress distribution ($\sigma_{n\ max}$ = 13 kgf/cm^2; $\sigma_{n\ min}$ = -2.6 kgf/cm^2).

growth stage, the influence of the constant stress gradient is small for $\sigma_{n\ max} \gg \sigma_{n\ min}$.

All the studies made of brittle material fracture conditions show that the instantaneous value of the crack propagation velocity depends primarily on the local stress and to a lesser degree on the stress gradient, with the magnitude of the stress at a short distance from the crack edge being of primary importance. In view of this, we also made tests with nonlinear stress distribution and local residual stress zones.

In the tests of two square acrylon specimens, the nominal stress was distributed in accordance with the diagrams of Figure 62a, b. The resulting diagrams of crack propagation velocity variation for the two stress levels are shown in Figure 63. Shown for comparison is the curve (dashed) for a square specimen of the same material loaded by a uniformly distributed stress σ_n = 41.5 kgf/cm^2. In the second and third fracture growth stages, the two curves coincide, and the crack propagation velocities differ only in the reduced stress zone. It is interesting to note the wave-like nature of the curves. The edge of the fracture surface has an irregular form.

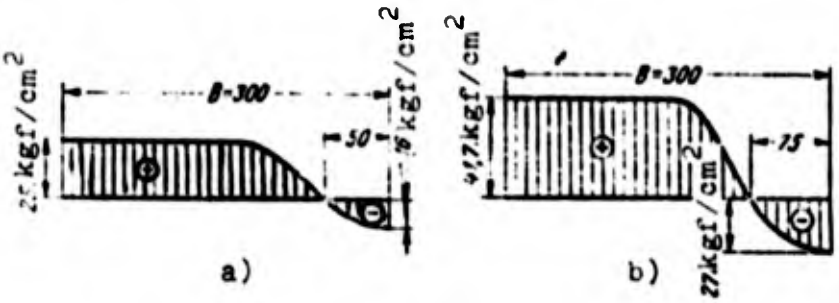

Figure 62. Nonuniform nominal stress distribution along edges of plane acrylon specimens.

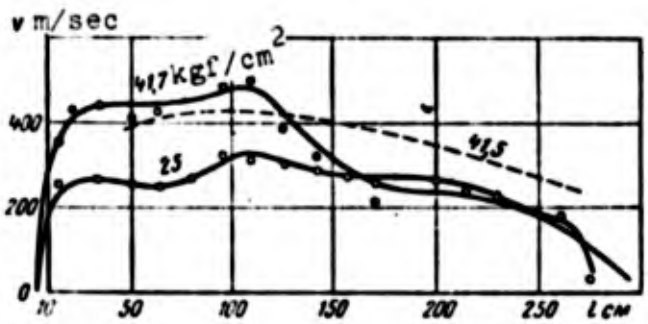

Figure 63. Crack propagation velocity in acrylon specimens with nonuniform nominal stress distribution along specimen edges in accordance with the diagrams of Figure 61 (solid curves).

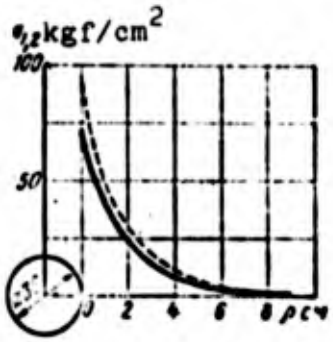

Figure 64. Principal stress distribution in vicinity of hole in two specimens from measurement data.

In addition, we studied brittle material fracture mechanics on six epoxy resin specimens with local secondary biaxial stress zones, located near the crack propagation path. The distribution of the stress $\sigma_1 = -\sigma_2$ in the vicinity of a hole loaded by internal pressure is shown in Figure 64. In four of the specimens, there was only a single local stress zone; in the other two specimens, there were six such zones.

In the first three cases, the crack propagated to the local secondary stress field. In the last case, the crack was only deflected by this field (Figures 64 and 65). In all the specimens, the nominal tensile stress $\sigma_n = 20$ kgf/cm^2 was distributed uniformly. The maximum tensile stress near the edge of the hole at points A was 110 - 120 kgf/cm^2, while at points B it was in the range of 60 - 70 kgf/cm^2.

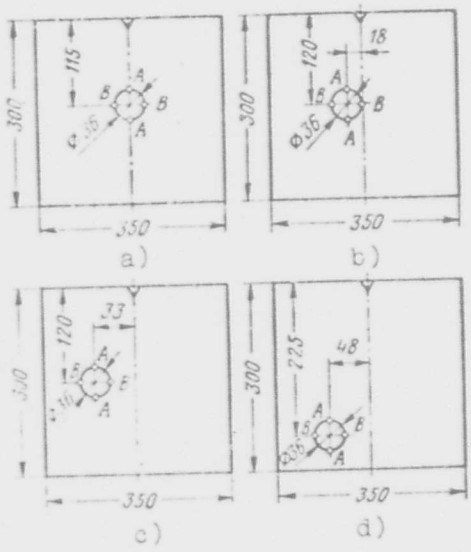

Figure 65. Location in specimens of holes playing role of local stress zones.

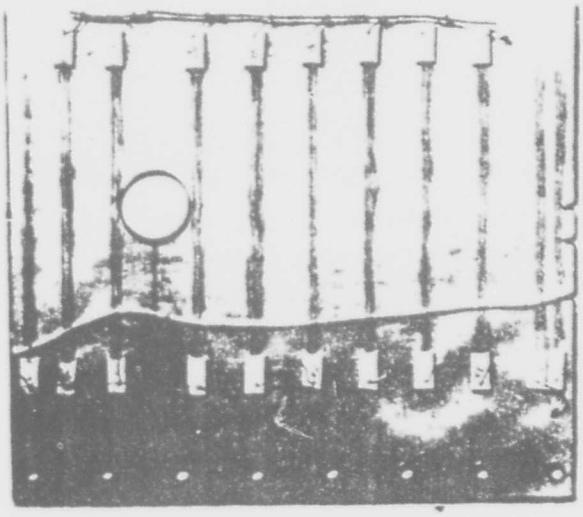

Figure 66. Crack in type g specimen (Figure 65).

With a nominal stress of σ_n = 5 kgf/cm^2, considerable disruption of the initial uniform tensile stress distribution extends to a distance on the order of 50 mm from the edge of the hole. If the crack passes at a distance of more than 20 mm from the edge of the hole, the crack deflection does not bring it to the edge of the hole (Figure 66). Change of the crack direction is observed for the given type of stress state disturbance only to a distance of no more than 50 mm from the edge of the crack.

The crack propagates perpendicularly to the direction of the maximum tensile stress and its velocity of advance depends on the stress level (Figure 67). If there were no secondary stress zone, the crack advance acceleration would be zero and the crack would propagate as shown by the dashed curve. In this case,the crack does not branch, although its propagation velocity reaches a quite high local value. The reason for this lies in the fact that the maximum tensile stress direction is not distorted significantly by the dynamic effects at the propagating crack edge. Under these conditions, several equivalent tensile stress directions are not obtained. Further

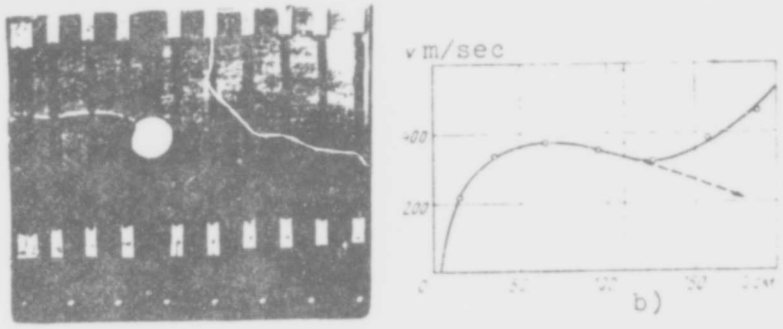

a)

Figure 67. Crack (a) in type α specimen (Figure 65) and crack propagation velocity prior to reaching edge of hole (b).

proof of the single-valued influence of the local stress field on the direction, velocity, and nature of crack propagation in a brittle material is given by the results of tests of specimens with a series of secondary stress zones.

Six secondary stress zones, whose isochromes obtained by the photoelastic method are shown in Figure 68, were created in a square epoxy resin specimen. An example of crack propagation in this complex stress field is shown in Figure 69. The nominal stress σ_n = 20 kgf/cm^2. In the material web between the first two holes, the stress from the external load decreased to less than 5 kgf/cm^2. In addition, a high, nonuniformly distributed tensile stress directed along the tangent to the hole contour was added; this stress was about 30 kgf/cm^2 at the middle of the web, and 90 kgf/cm^2 near the edge of the hole. In exact correspondence with the resultant stress field, the crack suddenly altered its direction by 90°, without branching, however. Conversely, in the material web between the first and second holes of one row, there is a high tensile stress from the external load. The second crack, after beginning from the surface defect of the first hole, accordingly propagated with high velocity on the order of 60 m/sec and branched in the uniformly distributed tensile stress field between the two holes. In this case, the crack branch growth either quickly terminated or the branches quickly altered their direction in accordance with the local stress distribution.

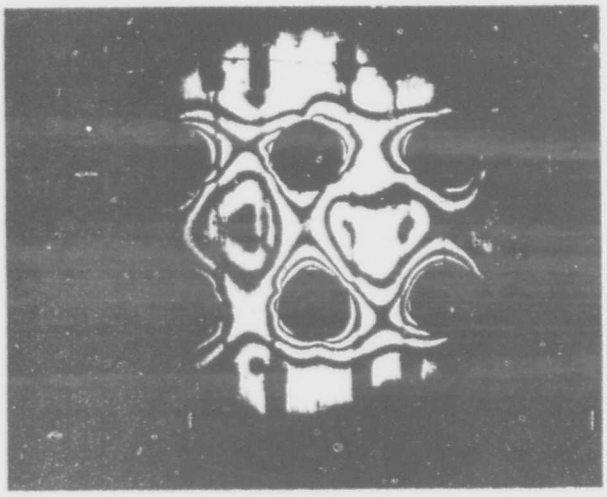

Figure 68. Isochromes of stress distribution in plane specimen with secondary stress zones.

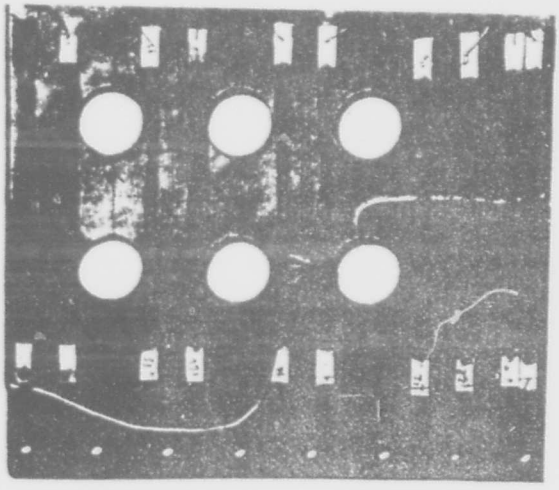

Figure 69. Crack propagation in complex stress field with periodic secondary stress distribution.

These data relate to quasi-uniform thermoplastic materials in the glassy hard solid, which showed marked brittle material properties in the tests conducted. For comparison and to clarify the question of whether fast-fracture mechanics in the static loading case depends on the ductility of the plastic, we made tests of several K475 polystyrene specimens (produced by the BASF firm) and determined the limit stress values. The polystyrene tested is a ductile material whose mechanical properties are covered in more detail in the next chapter, devoted to fracture mechanics under fatigue conditions (see Chapter 2). The material has the following basic properties: ultimate strength σ_b = 200 kgf/cm^2; yield limit σ_T = 178 kgf/cm^2; relative elongation at failure δ = 29%; impact toughness of notched specimens 7 kgf·cm/cm^2; impact toughness of smooth specimens 75 kgf·cm/cm^2. The material tensile diagram is shown in Figure 70. The tensile elastic modulus is 24,000 kgf/cm^2, the Poisson's ratio in the stress variation range studied depends very little on the stress and is ν = 0.34. The speed of sound in the material c_{max} = 1,200 m/sec.

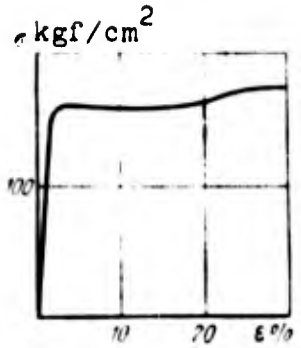

Figure 70. Tensile diagram for K475 ductile polystyrene specimen.

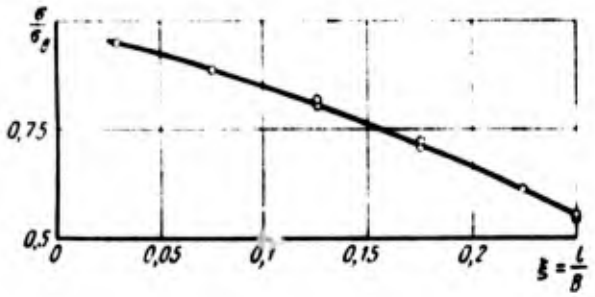

Figure 71. Results of tests of K475 polystyrene specimens with sharp lateral notches subject to static loading.

We first tested nine specimens with lateral notches of the type shown in Figure 38 under static loading. The specimen width B = 40 mm and notch depth l_v were different for the individual specimens and corresponded to the ratios $\xi = \frac{l}{B} = 0.075$; 0.125; 0.175; 0.225; and, 0.25. In all cases, the notch bottom rounding radius was $\rho = 0.5$ mm. The test results are shown in Figure 71. Then we tested two square specimens for which the initial crack started as a result of impact at the location of a 10 mm deep notch. In this case, we measured the crack propagation velocity. To obtain a "brittle" crack, it was necessary to select a tensile stress no lower than $\sigma_n = 85$ kgf/cm² and provide relatively high impact energy 0.5 kgf·m. As a result of the first impact, we obtained cracks 5 and 10 mm long (with account for the notch depth 15 and 20 mm, respectively), which did not grow. For this stress level and K ≈ 2.5 kgf·cm/cm², the critical crack length is

$$l_{kp} = 0{,}5^2 \frac{24\,000 \cdot 2{,}5}{85^2} \approx 2 \text{ cm}.$$

With the second impact on the wedge, the crack began to grow and propagated through the entire thickness of the specimen under the influence of the dynamic load and the 85 kgf/cm² stress from the external load. The nature of the fracture indicated high ductility of the material. There was no crack branching and the average propagation velocity was 180 m/sec, which, for the high stress, corresponds

to an average K = 3 kgf·cm/cm², and exceeds the value for acrylon or the epoxy resin.

§5. Influence of Material Defects in Glassy Hard State on Strength in Presence of Heat Flux

In the preceding sections, we examined the strength of parts with defects for the brittle material state and in the presence of stresses from external forces and moments. However, the theoretical and experimental data show that material defects have a significant effect on the strength in the presence of thermal flux in the wall of the part. A crack oriented perpendicular to the temperature gradient offers considerable resistance along the heat flux path; in the limit, we can consider a crack with surfaces which are completely isolated thermally.

Let us examine the case when the part dimensions are quite large in comparison with the crack dimension. The boundary conditions have no influence on the thermal flux near a crack propagating normal to its plane. The critical temperature gradient ΔT_{cr} deg/cm in an idealized plate with centrally located crack can be found from the energy balance conditions at the crack edge. Then

$$\Delta T_{cr} = \frac{14}{K_T} \sqrt{\frac{K}{\pi (1-\nu^2) E' l}}, \qquad (53)$$

where l is the crack length, K_T is the coefficient of thermal expansion of the material; $E' = \frac{E}{1-\nu^2}$ is the elastic modulus for plane strain; $K = K_0 e^{-\frac{k}{T}}$ is the specific energy required for the formation of unit fracture surface.

In deriving this formula, we assumed that the material temperature does not change with displacement in any direction parallel to the plane of the crack, i.e., the thermal flux is uniaxial. The crack propagation direction at the initial moment does not lie in the crack plane, but forms an angle on the order of 70° with this plane, which is confirmed by both theory and experiment. This is explained by the

nature of the stress state at the crack edge, where high shear stresses develop due to the difference of the material elongations on the two sides of the crack. In contrast with the case when the stress arises under the influence of an external load and the limit value is determined from the formula $\sigma_{lim} = \text{const}\ l^{-1/2}$, with the above simplification $\sigma_{lim} = \text{const}\ l^{-3/2}$.

Thus, the critical crack length for the same material properties is considerably shorter and its growth takes place faster. The difference between the two cases being considered increases with increase of the initial defect size. The crack does not propagate in the plane of the initial defect; therefore, for the exact solution, we must take into account the dependence of the variables on the orientation of the displacing crack edge, since even in the simplified representation of the stress gradient, the crack edge propagates in material having different temperatures at different points. However, the tests of acrylon specimens showed that the final results obtained on the basis of the formula given above are sufficiently exact in all cases.

If we determine the limit stress σ'_{lim} in a plane specimen with crack along the longitudinal axis, loaded by uniaxial tensile stress with uniaxial temperature gradient, then

$$\frac{\sigma'_{lim}}{\sigma_{lim}} = f\left(\frac{K_T E' \Delta T l}{\sigma_{lim}}\right), \tag{54}$$

where σ_{lim} is the stress for the same specimen without the temperature gradient.

It should be noted that $K_T E' \Delta T l \geq \sigma_1$, and the presence of the temperature gradient has an unfavorable influence on the strength of parts with defects. These conclusions are also valid for the steady-state temperature gradient case. In the case of rapid temperature

changes, the influence of the defects becomes still more unfavorable. However, it is difficult to determine sufficiently reliably the maximum temperature gradient and thermal insulating properties of the defect. Plastic parts are very sensitive to temperature gradients and the latter must be considered in selecting the material and designing the parts.

§6. Conclusions from the Study of the Fracture Mechanics of Brittle Materials in the Glassy Hard State under Static Loading

On the basis of our test results, we can note the following facts of interest to designers and engineers:

1. The quasi-homogeneous thermoplastic materials in the glassy hard state when subjected to static loading have marked sensitivity to macrodefects (cracks, voids), and the associated strength reduction depends on the geometric parameters of the defect and its orientation relative to the direction of the effective stress. Determination of the static strength by means of tests of smooth specimens without stress concentration does not yield data suitable for use in calculating the strength of parts of complex form.

2. The direction and velocity of crack propagation from initial defects are determined by the local tensile stress. Compression stress retards crack growth and may lead to termination of its propagation. If the specific energy necessary for the development of unit fracture surface $\overline{K} < 1$ kgf·cm/cm^2 termination of crack growth in the tensile stress zone of action is practically impossible, with the exception of the case when the stresses are less than $1/100\sigma_b$. If the values of the specific energy are higher, crack growth may terminate even with the stresses encountered in practice.

3. Crack instability is determined by the condition $\sigma^2 l = \text{const}$, where the constant quantity depends on the material, loading technique, and geometric factors. With increase of part size, the value of the constant increases. The tests conducted did not disclose any significant influence of the amount of potential strain energy in the

system as a whole on the fracture conditions for the brittle materials, since the fracture velocity of such materials is so high that the energy supplied to the crack from its vicinity plays the dominant role.

4. In determining the static strength of parts made from a brittle material with defects, the magnitude of the specific energy $\overline{K}$ required for the formation of unit fracture surface plays an important role.

The value of $\overline{K}$ must be determined experimentally for each material for different temperatures and presented as a material characteristic along with the other mechanical properties. The most important characteristic of a material is the quantity $\sqrt{EK_d}$. The larger the value of this characteristic, the higher is the real strength of plastic parts in the glassy hard state.

5. Local residual stresses have a significant influence on both crack propagation conditions and fracture process behavior. In view of this, the presence in real parts made from the subject materials of residual tensile stresses of processing origin is dangerous, while the presence of residual compressive stresses is favorable.

6. The maximum crack propagation velocity in a specimen loaded by uniformly distributed tensile stress is $v^* \approx 0.4c_{max}$, where c_{max} is the speed of sound in the material. In the general case, for example, with complex distribution of the residual stresses, higher velocities can be reached without crack branching.

7. The conclusions presented do not extend to the more ductile materials with $K \gg 1$ kgf·cm/cm^2; their strength can be determined by testing smooth specimens using static loading, since they have low sensitivity to defects. In these materials, the initial cracks may not grow. The presence of a filler or reinforcement in the plastic will, as a rule, increase the specific work K considerably. Accordingly, materials with filler have lower sensitivity to notches and

defects and crack growth cannot be determined using the criterion $\sigma^2 l$ = const, obtained for the brittle quasi-homogeneous thermoplastic materials.

CHAPTER 2

FATIGUE CRACK INITIATION AND GROWTH*

§1. Theory of Fatigue Crack Growth

If a plastic specimen is subjected to the action of a sufficiently high stress from a static load, at the locations of specimen surface damage and at small defects material damage zones which are detectable in the transparent materials by reduction of the transparency begin to grow. Initially, the zones are perpendicular to the defect edge; however, as specimen exposure to the loading increases, the zones gradually expand and orient themselves perpendicular to the nominal tensile stress. The initial zones in which cracks later appear are initial damage zones in which the molecular bonds are gradually broken and the capability of the material for plastic deformation decreases. After some time, a crack forms in the material, the sides of the crack separate from one another by a noticeable distance, and form new free surfaces in the specimen. The lower the stress and the longer the duration of the exposure under load prior to failure, the more clearly the local damage shows up in these zones and the more easily the cracks are formed with smaller volume of the damaged material. With further exposure of the material to the load, the resulting crack grows, and according to the experimental studies, the following relation is valid for the subject materials [169]

*Section on damage zones was written by D. Yuraid, and the fatigue crack growth measurements were made by K. Bogatets.

$$l = \text{const}\, f(t). \qquad (1)$$

The constant in the right side of this formula depends on the temperature for a given material and fixed loading.

If we assume that failure of the specimen material takes place because of rupture of the supramolecular formation bonds under the influence of thermal fluctuations during exposure to load, then on the basis of the general theory of processes with thermal activation, we can obtain the following expression for the specimen lifetime [216]

$$t_p = \nu e^{\frac{U-\gamma\sigma}{kT}} = \text{const}\, e^{-\alpha\sigma}. \qquad (2)$$

where ν, the frequency factor, is close in magnitude to the molecular thermal vibration period (10^{-13} - 10^{-12} sec). The stress effect shows up in reduction of the activation energy from U to U - $\gamma\sigma$, where γ depends on the activation volume and therefore on the structure of the material, since the product $\gamma\sigma$ corresponds to the work of the stress on the molecular bonds in the initial supramolecular structure.

The material model on the basis of which the above formula was obtained, is not applicable in the case of quasi-brittle failure of a material in the glassy hard state, since the fracture process is concentrated in the zone near the edge of the initial defects and the specimen lifetime is not determined by the rate and intensity of the fluctuation of the defects distributed randomly in the specimen volume [49]. The material fails in zones of limited dimensions and the specimen lifetime depends, to a considerable degree, on the crack propagation conditions. If these conditions are not connected with interaction of individual cracks which are capable of independent growth, which is valid for low initial defect density, we can use a simplified model to describe the fracture process.

The assumption of small dimensions of the zone in which the material damage develops and absence of interaction of adjacent defects is confirmed by the observations of damage zone growth and distribution in the volume of the material. In this fracture model for the materials in question, the concept of the process with thermal activation, developing under conditions of one-sided influence of the stress, is also justified. This process reduces to rupture of the supramolecular bonds in a limited zone near the defect edge. If we assume that the determining factor is the influence of the excess energy on rupture of these bonds, then we must take into account the stress excess above the minimum limiting stress σ_0 required for initiation of the fracture process, $\Delta\sigma = \sigma - \sigma_0$. The damage zone structure also depends on the stress, and in the present case, the local level, rather than the nominal value, is important. If we define the maximum local stress in terms of the stress concentration factor α, then in the simplest case, the crack propagation velocity can be determined from the formula

$$v = \frac{dl}{dt} = \text{const}\, q\, [\alpha\,(\sigma - \sigma_0)_n]\, e^{q\alpha(\sigma-\sigma_0)_n}. \qquad (3)$$

Here it is assumed that the transition zone — which precedes the crack — displaces along with the crack edge. The movement of the crack edge and transition zone is not necessarily smooth and the two do not necessarily move with the same velocity; however, in deriving the above formla, it was assumed that the crack edge motion is monotonic. If we assume that transition zone movement always leads the crack edge motion, and for the brittle materials α = const, then the preceding formula takes the form

$$v = \text{const}\, q\, [(\sigma - \sigma_0)_n]\, \sqrt{l}\, e^{q(\sigma-\sigma_0)_n\sqrt{l}}. \qquad (4)$$

This implies that the crack growth conditions are determined by the magnitude of the parameter $\sqrt{EK}$, which, as shown in Chapter 1, is equal to $\sigma_n\sqrt{l}$.

In accordance with these simplified concepts, the specimen lifetime is found from the formula $t_p \approx \frac{\text{const}}{v}$, or for $\sigma = \sigma_n$

$$t_p = \text{const} \frac{1}{\eta(\sigma - \sigma_0)} e^{-\epsilon(\sigma - \sigma_0)}. \quad (5)$$

If, as the crack grows, the transition zone dimension s varies as the crack length

$$S = \text{const} \, l,$$

the stress concentration factor $\alpha = 2\sqrt{\frac{l}{s}} + 1$ remains constant during the major part of the specimen loading time to failure [170]. In view of this, the quantity α in (3) can be included in the constant coefficient, and hereafter in the study of lifetime, we work with σ_n in place of σ_{max}. The nature of the strain concentration variation in the transition zone depends on the material properties and defect type. However, in all cases, the fracture process rate varies exponentially as a function of the nominal stress.

The loading time t_p to specimen rupture, determined on the basis of the arguments presented above, agrees well with the known experimental data. This means that, in spite of the complexity of the long-term static fracture process, t_p is determined basically by the process of crack growth prior to reaching the critical dimension. Figure 1 shows the values for two materials (metal and nonmetallic), which imply a linear dependence of the logarithm lg t_p of the loading time to failure on the nominal tensile stress σ_n in accordance with the formula

$$t_p = \text{const} \, e^{-\epsilon\sigma}. \quad (6)$$

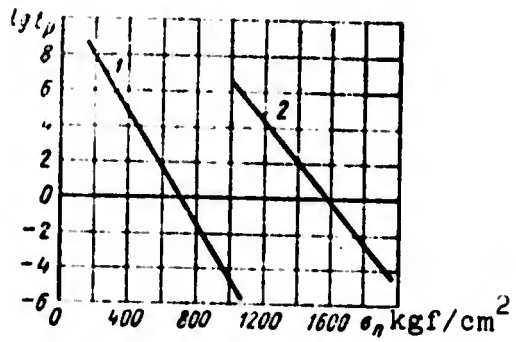

Figure 1. Specimen lifetime as a function of stress for relatively high tensile stress level.

1 — polymethyl methacrylate;
2 — aluminum.

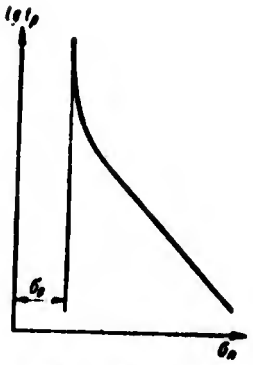

Figure 2. Specimen lifetime versus nominal tensile stress level.

This relation is valid only for stresses which exceed markedly the minimum limit stress σ_0. For lower stresses, the relation (Figure 2) has a more complex nature. In accordance with the arguments presented above, the relation (4) for small initial defect size $l_0 \ll B$ can be represented in simplified form by the formula

$$v = \text{const}\left(1-\frac{\sigma_0}{\sigma}\right)e^{\frac{\sigma-\sigma_0}{\sigma_0}}, \qquad (7)$$

in which we use the dimensionless effective stress coefficient (excess of actual stress above the limit stress level), i.e., the ratio of this stress to the instantaneous value of the ultimate strength, determined for the given loading velocity, and the specimen lifetime is determined by the crack growth law. However, the crack growth time must not exceed the loading duration necessary for appearance in the subject materials of initial cracks which are capable of further growth. The relationship between the loading time to appearance of the initial cracks and the time for their growth up to and including failure of the specimen depends on the stress level, loading conditions, and specimen dimensions and geometric shape.

If the specimen lifetime depends on the duration of both damage stages (crack development and growth), then in determining the lifetime, we cannot utilize the simple formulas derived with account for the ideas on crack growth in the specimen.

The duration of plastic specimen loading in the rubbery state (at a temperature above the point of transition to the glassy state) depends on the material properties in the viscoelastic state, which are determined by its structure (existence of a network, filler, and so on) and by the resistance of the existing defects to growth for the given loading conditions, which are characterized by the local stress state, the effect of the defect edge zone, temperature, and so on.

In the case of low density of the network formed by the molecular chains or unfavorable influence of the external medium, the linear part of the limit curve of the diagram shortens and extremes appear. The monotonic nature of the diagram is always associated with stress concentration at notches and microdefects in the detail.

In this case, the influence of two opposing factors obviously appears as the cracks grow and merge: on the one hand, the retarding influence of the large stress gradients and local changes of the bulk stress state; on the other hand, the large local strains ε near the defect edge, which alter the stress concentration in this zone. We can consider that the influence of the stress state near the defect edge is considerably stronger than the influence of change of the average mechanical characteristics of the material as a result of elastoplastic strain of the molecular network.

If the material strength were determined only by its structure and change of the molecular chain orientation upon loading, the limit stress would be an order of magnitude higher than that actually observed for real specimens with sharp defects. In view of this, the local strains near the defect edge and the change of the stress concentration with defect growth are of decisive importance. In the general case, defect growth is characterized by the equation

$$\lg t = A - B\varepsilon + C\varepsilon^{-2},$$

in which the last term accounts for the stress concentration change in the deformation process.*

There can be extrema of the limiting curve $\lg t_p = f(\varepsilon_p)$ only for some limiting value of the constant C. The larger the actual value of C in comparison with this limiting value, the more clearly the extrema of the limiting curve show up and the larger the distance between these extrema.

In most cases, the initial defects in a specimen are "blunt" notches, which cause stress concentration but are not capable of fast growth. The maximum stress in the peak zone will act for some time before conditions are created for initiation of a sharp crack at the defect edge. In certain cases, relatively large initial defects of the subject type cause such slow damage zone growth that other, smaller defects can appear earlier on the specimen surface.

Macrocrack growth cannot be included among the processes characterizing damage accumulation. However, damage zone initiation and growth is concentrated in a known volume and therefore is a damage accumulation process. Since, in this case, a continuous free surface is not formed in the specimen, rather there is a random process of rupture of the molecular chain bonds as a result of thermal fluctuations under conditions of one-sided action of the stress, if the stress sign is reversed, the process may be to a certain degree reversible. In view of this, damage zone growth to the critical dimension takes place differently, and the preparatory damage accumulation phase occupies a larger part of the overall loading time to fracture than for static

*The concentration factor for a cavity of elliptic shape in an infinite elastic medium is defined for $l = 2a > 2b$ by the formula $\alpha = \text{const}\sqrt{2l/\rho}$. We substitute the value of the radius of curvature $\rho = b^2/a$, then $\alpha = \text{const } 2(a/b)$. In the deformation process, the ratio a/b decreases, and assuming that the material volume is constant, we obtain $\alpha_\varepsilon = \text{const } 2(a/b)(1 + \varepsilon)^{-3/2}$. Actually, the material volume changes and in the general case we can write $\alpha_\varepsilon = (\alpha)_{\varepsilon=0} \times (1 + \varepsilon)^{-m}$ where $m \approx 2$.

loading and a constant value of the tensile stress in the most highly stressed volume of the material. In this portion of the loading time, the linear damage accumulation law is usually not applicable.

In the general case, crack growth with variable stress takes place in stages [170], since the quantity K decreases slowly in the transition zone ahead of the moving crack edge, particularly for small variable stress amplitude. In this connection, fatigue crack growth takes place not following the exponential law $e^{\frac{\sigma-\sigma_0}{\sigma_b}}$, but rather following the power law $\left(\frac{\sigma-\sigma_0}{\sigma_b}\right)^x$, obtained under the assumption of uniform crack growth. The power law corresponds to crack growth by small jumps. However, with a higher stress level, the nature of crack growth is more monotonic and the local value of K required for crack growth is reached faster. Under these conditions, the exponential relation corresponding to the physical bases of the local material damage process may be applicable.

In order to clarify the importance of loading duration prior to the appearance of cracks at notches and defects, we made an experimental study of the crack initiation process. The damage zones in which cracks later develop are defined differently in the works of different investigators [146], for example, "zones of damage under the influence of stress," "crack zones," "silver crack zones," and so on. In the following, we shall use, as before, the term "damage zone."

All investigators consider that the subject zones grow to a definite limiting length, which depends on the nominal stress level, and have very little influence on the resistance of the material to deformation and the ultimate strength σ_b under short-term loading.

Only in certain studies has the connection between the appearance of damage zones and increase of the material brittleness because of corrosion under conditions with stress acting been noted [144]. The views of the investigators on the damage zone structure are different:

some consider the observed material structure defects to be cracks in the stable state or zones of molecular chain bond rupture; others consider that there is a high degree of molecular chain orientation under the stress action without rupture of the bonds. Bartenev [15] considers that the damage zones have a high degree of oriented material structure which has been partly damaged as a result of large strain at normal temperature. This concept is also confirmed by the results of the latest electron microscope studies. One of the reasons for the divergent views of the various investigators on the nature of these zones, which show up clearly because of change of the material optical properties, is the fact that they have examined different defects in different materials. The damage zones in the materials studied in the present work are characterized by a low local value of K but the absence of cracks capable of opening up the newly formed continuous free material surface.

The studies described below were conducted on cast polystyrene and polycarbonate specimens with working section of rectangular cross section of the type used in conventional tensile tests. The specimens were bent in a special loading device which made it possible to observe and photograph a considerable portion of the specimen surface [154]. The loading device was mounted directly on a polarizing microscope and permitted smooth increase of the specimen deformation up to failure. The drive was provided from a motor through a flexible shaft. A schematic of the experimental set up is shown in Figure 3. For the tests with long-term loading, we used an adapter (Figure 4) which permitted simultaneous static loading of 50 specimens by a bending load with five selected values of the deformation. The loaded specimens were taken at definite intervals of time from the loading device and placed in the fixture with the microscope in which they were again bent to the same value of the deformation, and then the specimen surface was examined under the microscope. After this, the specimen deformation was increased to failure or the specimen was tested in tension. The temperature was standard (20 - 22° C).

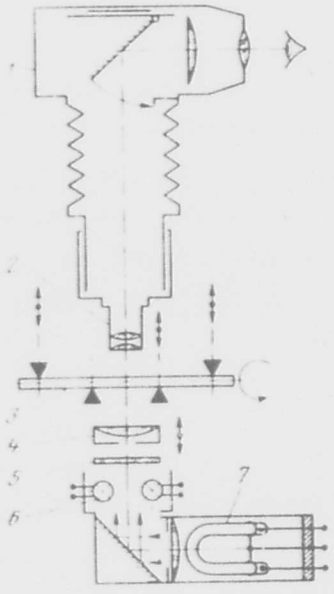

Figure 3. Schematic of experimental set up for studying plastic fatigue.

1 — photocamera; 2 — microscope objective; 3 — test specimen; 4 — condenser; 5 — dark blue light filter with matte surface; 6 — lamps placed circumferentially; 7 — gas discharge tube.

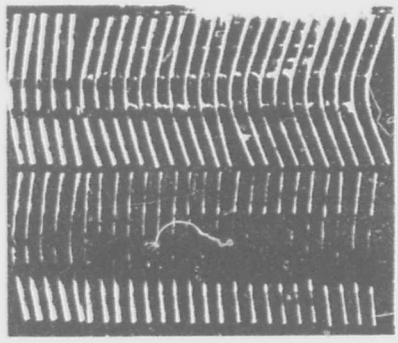

Figure 4. Fixture for simultaneous testing of a large number of specimens with constant deformation.

The basic characteristics of the specimen materials are shown in the following table:

Material Characteristic	Polystyrene Edistor FA	Polycarbonate Macrolon S3000
Molecular weight	200 000	27 000
Elastic modulus E in kgf/cm^2	27 960	18 090
Specimen working section in mm	4 × 6	4 × 10
Melting point in ° C	200	298
Form temperature in ° C	50	90
Injection pressure when casting specimens in kgf/cm^2	30	80

§2. Study of Fatigue Fracture Process for Static Loading of Polystyrene Specimens

The damage zone growth can be observed beginning with a minimum limiting deformation amounting to about 10% of the deformation at specimen fracture under short-term loading conditions. If the deformations are equal to about 60% of the fracture deformation, we observe very fast damage zone growth. The zones show up first of all on the faces of the specimen and then propagate along the direction toward the neutral line, as shown schematically in Figure 5.

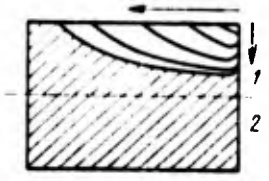

Figure 5. Growth of damage zone and crack in section of polystyrene specimen.
1 — tension region; 2 — compression region.

The transverse dimension of the damage zones cannot be determined with the aid of an optical microscope because of the smallness of the zone, and the zones have the form of hairline shadows. These damage zones differ from the cracks and wedge-like zones observed in the polycarbonate specimens.

Figure 6 shows damage zone growth for the constant deformation case. For this experiment, we selected a specimen with defects in the form of longitudinal cracks beneath the surface of the material. The damage zones show up not only on the faces of the specimen but also on the crack surfaces, oriented approximately parallel to the tensile stress direction.

The dependence of damage zone length on the exposure time for constant deformation is shown in Figure 7. The fresh damage zones which form as a result of fast deformation may disappear after several hours exposure to a compressive stress approximately equal in absolute magnitude to the tensile stress which led to the appearance of these zones. The fresh zones expand upon subsequent increase of deformation of the same sign, and in the specimen of small thickness, approach the specimen neutral line before cracks appear in the material. The damage zones can be differentiated from the cracks, which appear later,

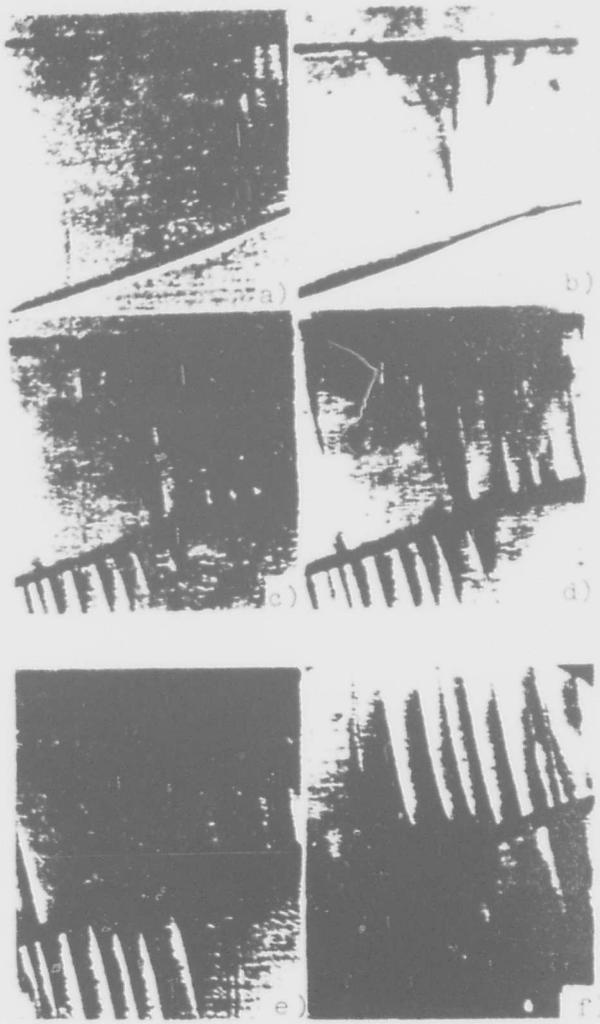

Figure 6. Damage zone propagation in polystyrene specimen with constante bending deformation x202.

a — t = 0; b — t = 4 min; c — t = 20 min; d — t = 42 min; e — t = 2 hrs; f — t = 24 hrs.

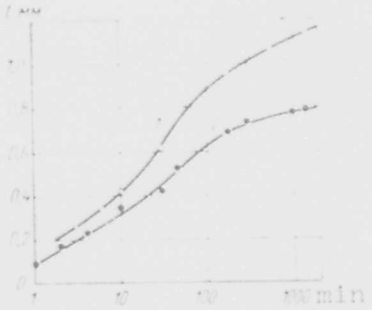

Figure 7. Crack length in polystyrene specimen as function of exposure time under load.

1 — O — specimen deflection y = 0.5 mm; 2 — • — y = 0.32 mm.

only by means of careful observation. In the case of small specimen thickness, when the damage zone propagates to the specimen neutral axis prior to crack initiation, the part of the fracture surface corresponding to damage growth will be mirror smooth, since as a result of aging, the capability of the material for deformation is exhausted.

Under favorable conditions, the described experimental set up makes it possible to observe the damage zone growth right up till the moment which is followed in a small fraction of a second by fracture. The time interval from crack initiation in the damage zone until complete fracture of the specimen is very short in all cases, and varies in the range from 0.1 to 0.01 sec. To study brittle fracture crack

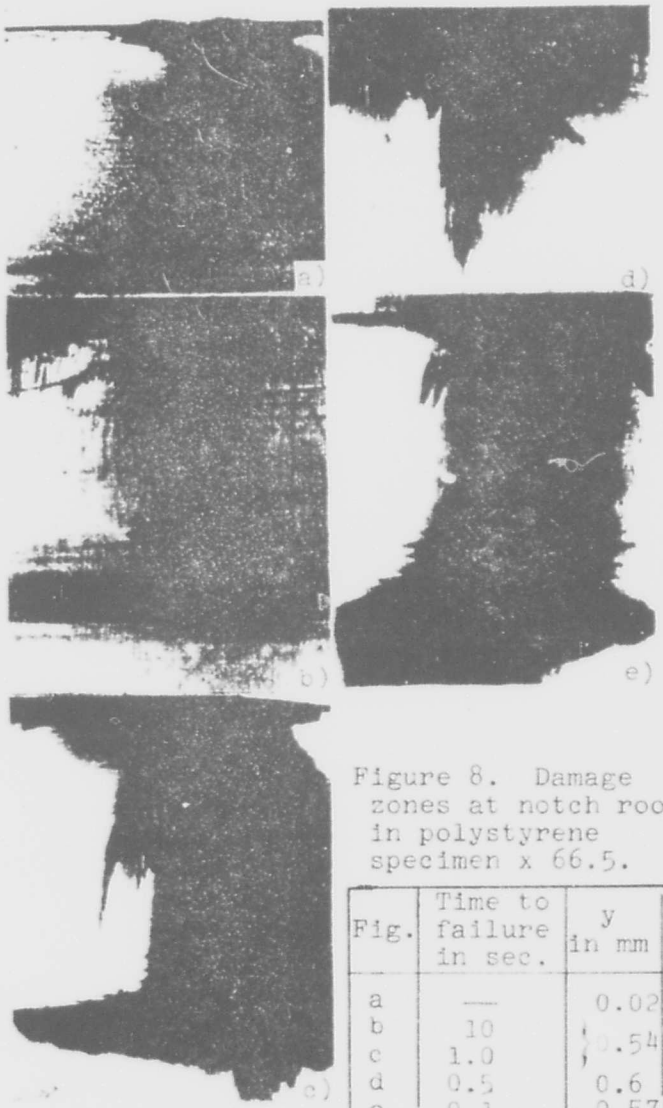

Figure 8. Damage zones at notch root in polystyrene specimen x 66.5.

Fig.	Time to failure in sec.	y in mm	t in min	T °C
a	—	0.02	5	
b	10	0.54	8	
c	1.0		9	20
d	0.5	0.6	7	
e	0.1	0.57	26	

initiation we used specimens with a sharp notch, which made it possible to focus the microscope field of view on the crack propagation zone. Figure 8a shows a view of the zone around the notch at the beginning of specimen loading. A characteristic feature of this stage is growth of the first damage zones in the direction of lower stress gradient. Obviously, more favorable conditions are created for gradual rupture of the molecular chain bonds with a lower stress gradient. It is possible that the shear stresses play a significant role. Figures 8b - d show the condition of the different specimens prior to failure. The damage zones at the notch develop in the course of a short time interval. Adjacent zones merge and the material transparency decreases, which is a sure indication of onset of the phase of fast appearance of a small open crack at the notch root (see Figure 8c). During the fraction of a second prior to complete failure of the specimen, we can note under the microscope fast expansion of the fracture zone grouping region, which has the nature of very intense local deformation, accompanied by heating and softening of the material (Figure 8e).

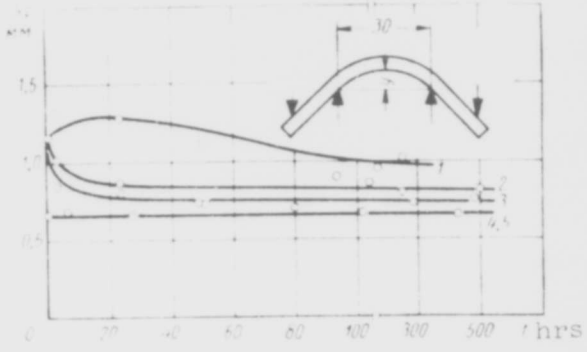

Figure 9. Reduction of fracture deformation y_p of polystyrene specimens subjected for time t to constant deflection y.

1 — y = 0.57 mm; 2 — y = 0.31 mm; 3 — y = 0.21 mm; 4, 5 — notched specimen.

Figure 10. Comparison of fracture surfaces of polystyrene specimens tested with strain rate dy/df = 0.135 mm/min (x 66.5).

a — initial specimen (only mirror smooth part of fracture surface is shown); b — specimen subjected for 300 hours to strained state with deflection y = 0.2 mm.

In the case of long-term specimen loading in the course of tens and hundreds of hours, the damage zones do not expand significantly; however, their nature changes markedly. In this case, there is material brittleness increase and reduction of the local value of K, primarily in those cases when the specimen is subjected to small permanent deformation. The hardening effect does not show up because of molecular chain orientation as a result of plastic deformation. The resistance of the specimens to brittle fracture decreases to about 60% of the initial ultimate strength for fast loading. Thus, in the damage zone opposing processes take place: orientation of the molecular chains (some hardening) and local breaking of the chains (local reduction of the material strength and ductility).

We see from the diagram (Figure 9) that, in the first time period of exposure to load, the strength of specimens deformed by preloading by a high load increases somewhat. Only with further long-term exposure at a low deformation level does the effect of material damage begin to dominate, showing up in reduction of K and increase of the material brittleness. However, specimens with a notch do not show such clear-cut reduction of resistance to brittle fracture. In the loading duration range studied, the material hardening effect shows up near the bottom of the notch. This is explained by the fact that blunt notches do not cause as rapid damage growth as do sharp surface defects.

In those cases when the test specimen is subjected to long-term deformation, the dimension of the mirror smooth part of the fracture corresponds to the dimension of the damage zones observed. However, the dimension of the smooth part of the fracture on both sides of the specimens is about 10 times smaller than on specimens fractured with fast loading (initial specimens), while the remaining fracture surface is smoother and regular wavy lines are noticeable on the surface (Figure 10). Microscopic observation of prestrained specimens with developed damage zones did not detect any indication of fast fracture crack initiation, its growth takes place very rapidly.

§3. Study of the Fracture Process for Long-Term Static Loading of Polycarbonate

When loading specimens to deformations close to the elastic limit, we can observe the formation of a smaller number of minute damage zones on the faces of the specimens. In contrast with polystyrene, the number of zones is considerably less and their further growth takes place differently. In the first growth phase, they have the form of hairline shadows, and it may be difficult to differentiate the damage zone from a crack (Figure 11). The first damage zones appear not at the bottom of the notch, but rather on the specimen surface which has not been mechanically damaged, in regions remote from the notch (Figure 12). In the case when a damage zone does develop near the bottom of the notch for relatively small deformation,

Figure 11. Damage zones in polycarbonate specimen tested with constant deformation y = 2.21 mm, with an exposure in the deformed state for 24 hours (X 202).

Figure 12. Cracks near notch in specimen shown in Figure 11 (x 101).

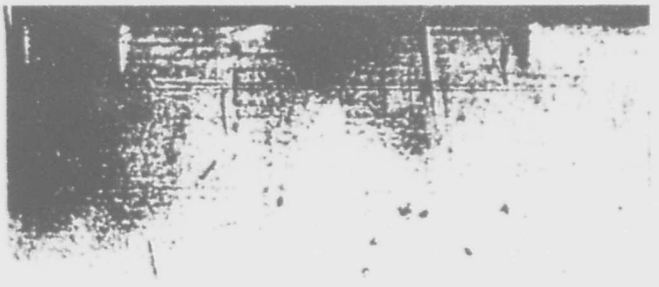

Figure 13. Simultaneous growth of damage zones on surface and at bottom of notch in polycarbonate specimen (x 66.5) (y = 1.32 mm; t = 288 hours; T = 21° C).

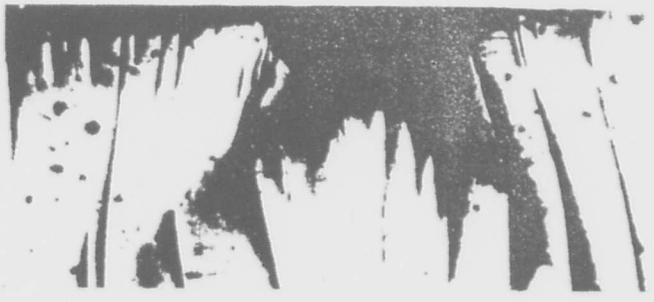

Figure 14. Growing cracks in polycarbonate specimen (x 66.5).

the zone will not be any more marked in comparison with the zones on the undamaged specimen surface, which is most hazardous with respect to subsequent failure (Figure 13). The orientation of the developed damage zones in the vicinity of the notch after long-term specimen deformation is shown in Figure 14. The growing cracks have the form of sharp wedges and are definitely open, at least at some depth below the material surface (Figure 15).

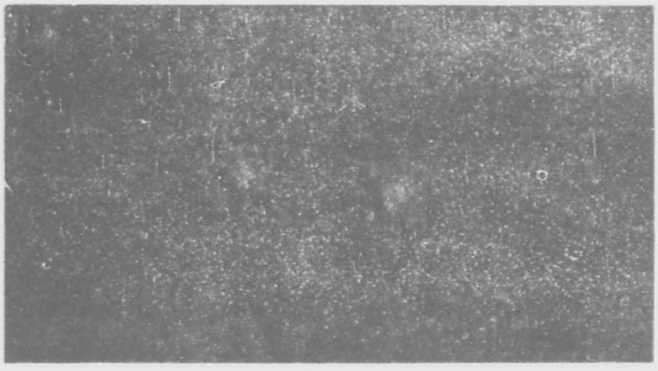

Figure 15. Wedge-like cracks outside notch zone in specimen shown in Figure 14 (x 133).

Figure 16. Open cracks with blunt edge in polycarbonate specimen (x 66.5) (y = 0.96 mm; t = 22 hours; T = 22° C).

Figure 17. Open crack with rounded edge in polycarbonate specimen (x 66.5) (y = 1.32 mm; t = 189 hours; T = 22° C).

In addition to the filamentary and wedge-like cracks, in certain cases, we encounter open cracks of small length with rounded edges as a result of large plastic deformations (Figure 16), which upon further loading, behave like an artificial notch with rounded bottom. Typical for the specimens examined are easily visible lines in the lateral directions around the notch, whose nature depends on the directions of the neighboring zones, and growth of new zones from the rounded edge of the old zone (Figures 17 and 18). These data show that if the damage reaches in its growth a stronger material zone before the critical magnitude is reached, its nature may change. Hence, we also see how important is the statistical interpretation of the characteristics of resistance to brittle and fatigue fracture for the subject materials [28, 101]. Similar to the situation observed in testing specimens with

Figure 18. Appearance of crack shown in Figure 21 after increasing deflection to the value y = 2.4 mm with velocity dy/dt = 0.135 mm/min.

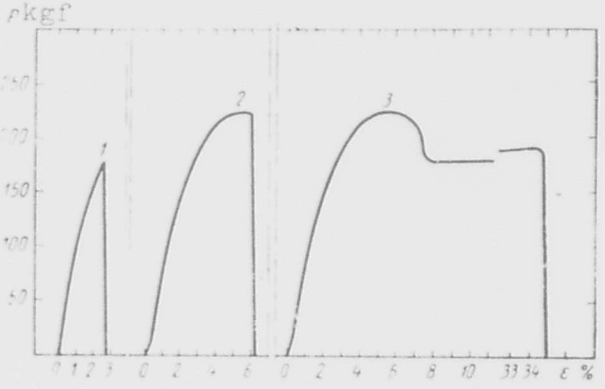

Figure 19. Tension diagram of polycarbonate specimens recorded on an Instron TT-DM machine.

1 — specimen without notch, cross section area F = 0.394 cm^2; 2 — specimen with notch 0.1 mm deep and bottom rounding radius ρ = 0.001 mm; F = 0.392 cm^2; 3 — specimen subjected to prestrain for 24 hours (y = 1.32 mm; T = 22° C; F = 0.389 cm^2).

artificial notches, with the development of defects of the type being considered and further loading of the specimen, the specimen does not fail in any case as a result of crack propagation from this defect.

The V-shaped cracks grow fastest and therefore, they determine the specimen fracture conditions. The transition of the open crack which arises in the damage zone to the wedge-like transition zone is a gradual process. In view of this, the breaking of the molecular bonds takes place gradually, and the sharp nature of the defect is retained if an obstacle in the form of a region of high strength material is not encountered along the defect propagation path.

There is a connection between the appearance of damage zones which are visible under the microscope and increase of the material's brittleness. In all cases of damage zone appearance in a specimen subjected to long-term constant deformation, filamentary or wedge-like cracks which are visible under the microscope develop and further deformation leads to fracture of the specimen at a stress lower than the value

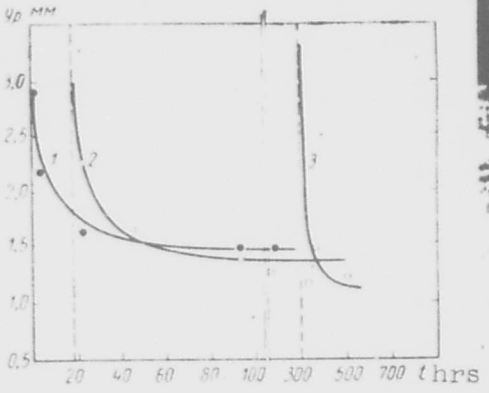

Figure 20. Decrease of fracture strain y_p of polycarbonate specimens after preliminary exposure in bent condition.

1 ● — y = 1.32 mm;
2 ○ — y = 0.95 mm;
3 ○ — y = 0.57 mm

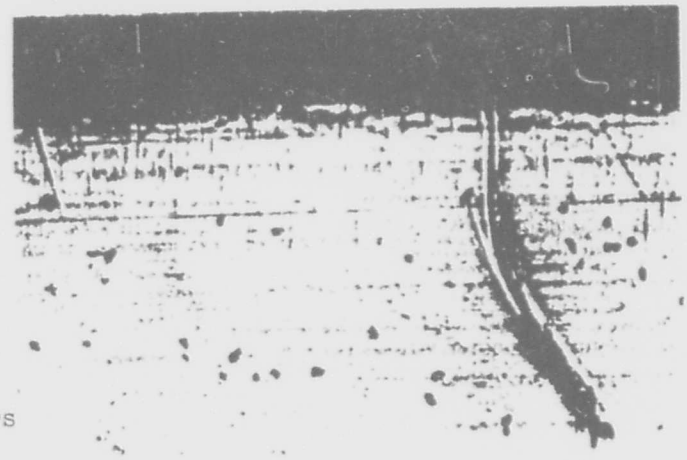

Figure 21. Surface defects in polycarbonate specimen detected with maximum reduction of plasticity under the influence of long-term exposure in the strained state. (x 66.5) (y = 0.57 mm; t = 337 hours).

corresponding to the limit σ_b, which agrees well with brittle fracture resistance theory. Figure 19 shows the characteristic curves corresponding to the tension diagrams of an undamaged specimen, an initial specimen with artificial notch, and a specimen subjected to static damage during long-term constant deformation. The notched specimens which were subjected to long-term constant deformation did not fail along the notch in any of the 60 cases. During the bending tests, fracture occurred at a distance of 5 - 10 mm from the notch, frequently at the location of a processing defect.

The influence of loading duration and prestrain magnitude on reduction of the material ductility shows up very clearly. The brittleness increase and decrease of the local value of K in the case of long-term loading to relatively small deformation are most important. Under these conditions, we obtain the lowest value of the brittle fracture resistance and material deformation in the fracture process (Figure 20). The cracks may not be visible to the naked eye and are seen only under the microscope (Figure 21). Local orientation of the molecular chains is not observed; however, rupture of the

molecular chain bonds during long-term loading may be very significant.

The damage zone growth process is very sensitive to changes in specimen fabrication technology. For example, even slight variations of the procedure used in pressure casting the specimens, which do not lead to any change in the tensile diagram of the basic material, have a marked influence on the material structure defect growth duration, and consequently, on the local brittleness increase.

We can draw the following conclusion on the basis of study of the conditions for the onset of local material strength disruptions. For both materials studied, it was found that small long-term deformations lead to the appearance of damage zones which play an important role in the brittle fracture process. The local ductility reduction shows up to a greater degree in the polycarbonates than in polystyrene. The external appearance and damage zone behavior of polystyrene indicate that, in this case, zones of small extent with large deformation develop in the material at low temperature, and in these zones, there is orientation and gradual breaking of the overloaded molecular chains. The fact that long-term loading at low strain level leads to the appearance of damage zones which facilitate the growth of fracture macrocracks indicates that the usual laboratory atmosphere should be considered an active medium. In the case of long-term specimen deformation, there is marked material damage under the influence of the thermal activation process taking place primarily on the specimen faces.

In contrast with polystyrene, the damage zones develop more slowly in the polycarbonate; however, the stage of their transition into cracks takes less time. The wedge-like cracks observed in the tests are apparently the result of further damage zone growth. In the polycarbonates the influence of local material damage dominates over the hardening resulting from local deformation at low temperature. The short cracks with rounded edges, which are observed in certain cases in the polycarbonate specimens, appear in those cases when the crack runs along the entire damage zone length and its edge enters

the region of less damaged material. As a result of the large deformation, there is redistribution of the stress, its peak decreases, and crack growth may stop. In view of this, the material resistance to brittle fracture depends on the local material properties, namely, the local value of K, which characterizes the material ductility.

The results of the experimental studies conducted show that material structure defect growth, which leads to failure of the material, is associated with the characteristics of the supramolecular structure of the surface material layer of specimens fabricated by pressure casting. The influence of structural notches is secondary. It is interesting to note that even small deformations in the case of long-term material exposure under a stress exceeding the lower limiting value cause a supramolecular structure change which influences the growth of cracks which develop later.

Comparing Figures 12 and 13, we see that the specimens held for a longer time at a small strain show greater tendency for the appearance of cracks. This latent polymer structure damage is not observed in the standard material strength tests under fast loading conditions. The damage does not show up in change of the tensile elastic modulus or ultimate strength or the limiting strain in the macrovolumes in the fracture process. Irreversible changes of the crystalline structure have also been detected in the crystalline polymers under conditions of small long-term deformations, corresponding to an initial stress level on the order of 50 kgf/cm^2. The data available are not yet sufficient to construct a physical model of the material damage process.

A series of comparative tests in a vacuum is necessary to verify the influence of the small amounts of active substance vapors present in the air, and also the influence of air itself. The experimental studies in this field are complicated because of the fact that the quality of the specimens obtained by pressure casting is not known, and also, because of the residual stresses in the specimen material surface layer. When storing specimens, the residual stresses can have the same effect as a small long-term deformation. The relaxation

processes in the material have also received very little study, and this prevents considering that the damage zone growth dependence on the stress level, which actually occurred in the described experiments, is uniquely established. Further experimental studies are required; however, we can already state that the damage of the materials tested is a highly localized process and the low strength of materials in the glassy condition is associated with the presence of damage zones.

In those cases when the crack, as it grows, extends beyond the limit of the initial zone of maximum material damage in the long-term loading process, crack growth may stop. Loading duration plays an important role; therefore, in all calculations of the strength of detail parts made from the subject materials, we must take into account the proposed duration of part exposure to loading. The long-term action of low stresses which exceed some limiting value also has a significant unfavorable influence. Upon reversal of the stress sign, the incompletely developed damage zones may terminate their growth and cracks may not appear; or their growth may stop. Therefore, the crack growth pattern may be disrupted in the case of low alternating stress values. In this case, the difference between the properties of the surrounding material and that in the damage zone is particularly large. However, the lower the stress, the lower is the crack edge acceleration and the higher its resistance to propagation.

It is important to establish how the crack porpagation process depends on the external load variation with time and the geometric shape of the detail. Let us examine the case when the material is moderately brittle ($l_{cr} \ll B$), and the stress level is quite high $\sigma \gg \sigma_0$. In studying crack propagation, we can use the simplified formula (6). We consider a specimen of simple geometric shape loaded by a variable tensile stress which does not transition into a compressive stress. We assume that, at the high stress level, the material damage process takes place uniformly and reverse damage zone development does not have a significant influence on the process in question. In accordance with the principle of partial damage irreversibility under the action of the stress σ_1 in the course of the time Δt_1, the

corresponding relative shortening of the specimen lifetime is defined by the quantity $(\Delta t/t_p)_1$. Similarly, the action of the stress σ_2 in the course of the subsequent time interval Δt_2 causes the relative lifetime shortening $(\Delta t/t_p)_2$.

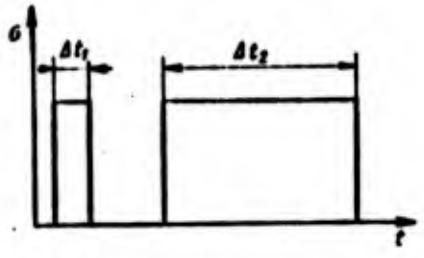

Figure 22. Two stages of specimen loading to failure with constant maximum stress level.

In the first approximation, the individual local material damages are summed using a linear law, and relative damage equal to unity corresponds to reaching the limiting state and fracture of the specimen. If we consider that the stress remains constant during the individual time intervals and changes abruptly upon transition from one interval to another, the condition for specimen fracture for this simplified crack growth model may be expressed by the formula

$$\sum_{i=1}^{n} \left(\frac{\Delta t}{t_p}\right)_i = 1. \tag{8}$$

In the general case of continuous stress change in time $\sigma = \sigma(t)$ without change of the stress sign, the limiting state with account for (6) is defined by the condition

$$\int_0^{t_p} \frac{dt}{t_p(\sigma)} = \int_0^{t_p} \frac{dt}{Ce^{-c\sigma}} = 1. \tag{9}$$

Tests of cellulose acetate film specimens were made for experimental verification of this condition. The specimens were tested with two different loading duration values in accordance with the scheme of Figure 22 [50]. The test results confirmed the validity of simple individual damage summation using the formula $\Delta t_1 + \Delta t_2 = t_p$,

where t_p is the duration of specimen loading by constant stress to failure.

In practice, when fatigue loading specimens, there is not a discontinuous loading change with very rapid increase to a constant maximum value and subsequent sudden decrease to zero. Usually, the loading changes more or less smoothly but following a more complex law. In order to simplify the problem, we shall first examine the case of stress variation in time following a linear law with constant stress change rate v_σ. In this case, the stress at the moment of time t is equal to $\sigma = v_\sigma t$. Upon substitution of this expression into (9) we obtain

$$\int_0^{t_p} \frac{dt}{Ce^{-cv_\sigma t}} = 1.$$

After determining the limiting stress from the condition

$$Ce^{c\sigma_e} = t_p, \tag{10}$$

as a result of integrating the preceding expression, we find

$$\frac{1}{t_p} - \frac{1}{C} = cv_\sigma.$$

Since usually $t_p \ll C$, we can take

$$t_p \cong \frac{1}{cv_\sigma}. \tag{11}$$

Taking the logarithm of (10), we obtain with account for (11)

$$\ln C - c\sigma_e = \ln t_p = \ln \frac{1}{cv_\sigma},$$

or

$$\sigma_e = \frac{1}{c}[\ln(Cc) + \ln v_\sigma]. \tag{12}$$

We see from this formula that the limiting stress varies approximately as the logarithm of the loading rate. We note that the resistance to fracture is also expressed in terms of the strain rate [86]. This situation is confirmed by the well-known fact of increase of resistance to crack initiation at high strain rates. The specimen or detail lifetime $t_p = 1/cv_\sigma$ is inversely proportional to the loading rate

$$t_p = \frac{\text{const}}{\frac{d\sigma}{dt}}. \tag{13}$$

Actually, the fracture process does not develop monotonically, since the material strain is not distributed uniformly but is concentrated in zones in which the crack subsequently develops. In these zones, the strain rate is significantly higher than the average strain rate determined by the rate of displacement of the testing machine grips. The ratio of the local strain rate to the average value is determined approximately by the ratio of the specimen size to the damage zone size.

We can examine similarly the case of specimen unloading with a linear law of stress variation in time. We assume that, at the initial time ($t = 0$), the specimen is loaded by the maximum stress $\sigma_{max} = \sigma_1$, and is then gradually unloaded to σ_2, at which the specimen lifetime is exhausted. Under these conditions, specimen failure takes place not at the maximum stress but at a lower stress $\sigma_2 = \sigma_1 - v_\sigma t_p$; in accordance with (6), the condition $Ce^{-c\sigma_2} = t_{p2}$ must be satisfied in the unloading process. This example emphasizes once again the practical importance of analysis of material damage accumulation under static loading. As a result of integrating (9) in application to the case of linear stress reduction from the initial value σ_1 at the time $t = 0$, we obtain

$$\sigma_e = \sigma_1 - \frac{1}{C}\ln(1 - cv_\sigma t_{p1}).$$

where t_{p1} denotes the specimen lifetime when loaded by a constant stress equal to the maximum value of the variable stress $\sigma_{max} = \sigma_1$. We see from this formula that, for specimen fracture in the unloading process, a definite limiting stress change rate required

$$(v_\sigma)_{пред} = \frac{1}{ct_{p1}} = \frac{1}{Cc} e^{c\sigma_1}. \qquad (14)$$

In the case of a higher rate, the specimen will not fail. The simplified relation obtained on the basis of (6) is applicable only under the condition that the minimum stress in the unloading process, reached at the instant of specimen failure, exceeds by a sufficient magnitude the lower limiting stress value σ_0. Otherwise, we must use the more complete formula (7) in the integration. The results obtained show that the higher the initial stress, the higher the stress change rate during unloading $(v_\sigma)_{lim}$ may be for which specimen failure is still possible. The stress differential $\sigma_1 - \sigma_2$ during specimen unloading, which characterizes the stress reduction at failure, increases with reduction of the unloading rate v_σ. We can examine similarly the more general case of load reduction with time in the specimen unloading process. Such a study may be of interest, for example, in application to the part of the tension diagram beyond the maximum load limits. In the case of rapid load change, for example in the case of impact or high strain rate within the limits of a small volume of the material, fracture is more difficult. If the crack growth in the detail takes more time than increase of the load to the maximal value σ_{max} and the load is rapidly reduced after reaching the maximum value, fracture may not occur. However, since there is a definite amount of potential strain energy in the detail, the local stress change does not follow precisely the external load change and the instantaneous dynamic equilibrium conditions differ from the equilibrium conditions for static loading. The faster the detail fracture process takes place, the more important is the role played by the amount of potential strain energy accumulated in the material of the detail.

Figure 23. Material damage intensity versus frequency f of repeated tensile loading of specimen.

In the very high loading rate case (impact conditions), it is obvious that the material resistance to fracture increases, since the crack growth duration exceeds the duration of the period of load increase to the maximum value. If the stress is quickly reduced to the minimum limiting value, we again cannot expect realization of the process leading to specimen fracture. In contrast, repeated loading accomplished at high rate leads as a result of local hysteresis in the most highly stressed zones to local heating of the material, which accelerates the damage process since in the materials in question, this temperature increase is always associated with thermal activation. Accordingly, the dependence of the damage intensity on the frequency of repeated loading by a tensile load has the nature shown in Figure 23; this relationship has an extremum in the region of moderate frequencies. A low loading frequency and extended exposure under load are not favorable because of the manifestation of material fatigue at the stress corresponding to the upper limit of the cycle. In view of this, the loading frequency must always be specified in material tests. Test results at one loading frequency cannot be carried over without experimental verification to other frequencies. The use of the linear damage summation law in those cases when we must consider periods of action of loading of different amplitude and frequency is permissible only in a narrow frequency range near the extremum of the curve (Figure 23).

In calculating the strength of details, it is important to know the laws governing the material fracture process under cyclic loading. If the effective stress is considerably below the ultimate strength for short-term loading, the detail will fail as a result of fatigue after a large number of loading cycles. For a variable stress amplitude lower than the fatigue limit, the material damage process takes place so slowly that in practice we consider that it is absent entirely [170]. In view of this, for a high loading frequency, the

strength under conditions of cyclic fatigue damage is determined by the magnitude of the parameter $\sigma_{ef}/\sigma_b = \sigma - \sigma_0/\sigma_b$. Analysis of experimental results shows that crack length increases exponentially with increase of the number of loading cycles. In this case, we need consider only the number of loading cycles during the time of crack growth $N_{ef} = N - N_0$, without taking into account the number of loading cycles N_0 required for the appearance of the initial crack which is capable of further growth. In the simplest case, the fatigue crack length can be determined from the formula

$$l = \text{const}\left(\frac{\sigma - \sigma_0}{\sigma_0}\right)^{\varkappa} e^{\varkappa(N-N_0)}, \tag{15}$$

derived under the assumption of quasi-uniform fatigue crack growth. The crack growth by stages actually observed is taken into account in this case only by the fact that we use the curve of lg l versus lg $\frac{\sigma - \sigma_0}{\sigma_b}$ rather than the curve of lg l versus $\frac{\sigma - \sigma_0}{\sigma_b}$. If the variable stress amplitude is larger, crack growth is accelerated and becomes practically uniform. These conditions correspond to an exponential dependence of crack length on relative stress. This situation is valid for $\frac{\sigma - \sigma_0}{\sigma_b} > \frac{1}{3}$. Actually, plastic details usually work at a lower stress at which we would expect discontinuous crack growth.

Summing up the partial damages when study fatigue crack growth in the region of small stress amplitudes which do not differ significantly in frequency, we can use a linear summation law in accordance with (8), which can be rewritten in the form

$$\left(\frac{N_{3\phi}\Delta t^*}{t_p}\right)_1 + \left(\frac{N_{3\phi}\Delta t^*}{t_p}\right)_2 + \cdots = 1, \tag{16}$$

where $(\Delta t^*)_x$ is the effective duration of detail operation at the constant stress σ_x. If we define the effective duration using the

formula $\psi\Delta t_x$, where ψ is a coefficient which depends on the shape of the loading cycle, the limiting lifetime expressed as the limiting number of loading cycles is equal to

$$\sum_1^n \left(\frac{N_{x\psi}(\psi\Delta t)}{[N_{x\psi}(\psi\Delta t)]_{max}}\right)_x = 1,$$

or

$$\sum_1^n \left(\frac{N_{x\psi}}{(N_{x\psi})_{max}}\right)_x = 1. \tag{17}$$

Here, we consider only the number of cycles during the crack growth time, including the growth stoppage periods between the fracture stages.

We usually use, as the material fatigue characteristic, the limiting stress amplitude as a function of the number of loading cycles to fracture, i.e., the classical fatigue curve; we can also use the curve for the stage of formation of a crack of critical length. An important role is also played by the number of loading cycles N_0 to crack appearance, which essentially determines the number of loading changes required for the appearance, which essentially determines the number of loading changes required for the appearance of the first noticeable crack in the damage zone. Hereafter, we take a crack of length l_0 = 1 mm as this crack (Figure 24).

The experimental data available at the present time show that the dependence of the number of loading cycles to the appearance of the first crack capable of further growth on the stress amplitude has the form of the diagram shown in Figure 25. If rapid material damage in the most highly stressed zones is not observed at the loading frequencies, the curve of σ versus lg N_0 has a linear nature. On the basis of (15), we can find the number of cycles required to obtain a crack of definite length. The corresponding relation in the coordinates lg σ - N_{ef} is also linear. Summing the numbers of cycles in both stages, we obtain the total number of cycles to failure. In

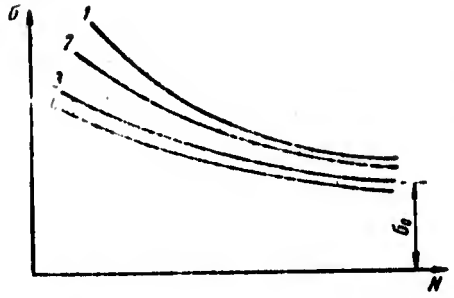

Figure 24. Fatigue curves based on constant crack length parameter.

1 — specimen fracture ($l = l_{cr}$); 2 — l = const; 3 — $l = l_0$; 4 — appearance of damage zones.

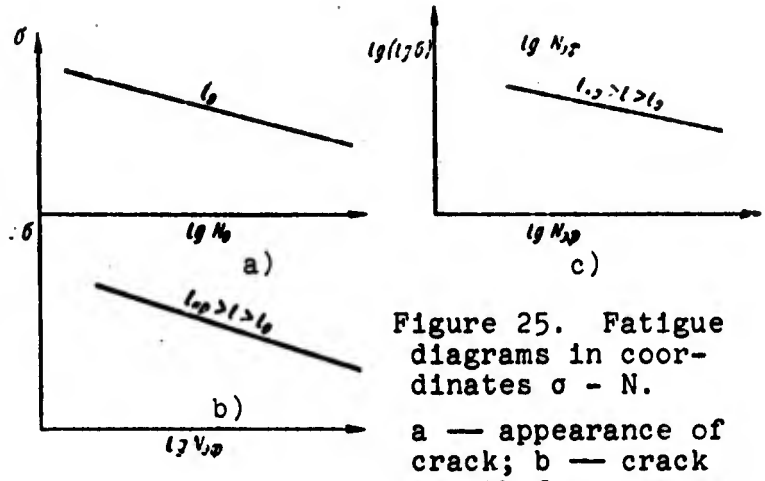

Figure 25. Fatigue diagrams in coordinates σ - N.

a — appearance of crack; b — crack growth for $\sigma \gg \sigma_0$; c — crack growth for $\sigma \geq \sigma_0$.

this case, we take the limiting crack length equal to the critical length for the given part shape and dimensions.

Fatigue crack growth in the depth of the detail depends on the nominal stress level and on the average mechanical properties of the material. In the case of crack growth by stages, it is necessary to differentiate the number of loading cycles in the individual crack growth stages and the number of cycles in the periods of crack growth stoppage, during which local mechanical aging of the material near the crack edge takes place. In the beginning of its growth, the crack is always relatively stable, as long as its length is considerably less than the critical length $l \ll l_{cr}$, and only local overloading of the molecular chain bonds leads to damage near the crack edge and creation of conditions for further crack growth. The crack growth duration in the case of repeat loading propr to reaching the critical length depends on the material type, level of the residual stresses of the first kind, and the temperature of the part.

A schematic of fatigue crack growth with low variable stress amplitude is shown in Figure 26. The number of loading cycles from crack appearance to failure is expressed by the difference $N_{ef} = N_{cr} - N_0$, where N_{cr} is the total number of cycles to failure and N_0

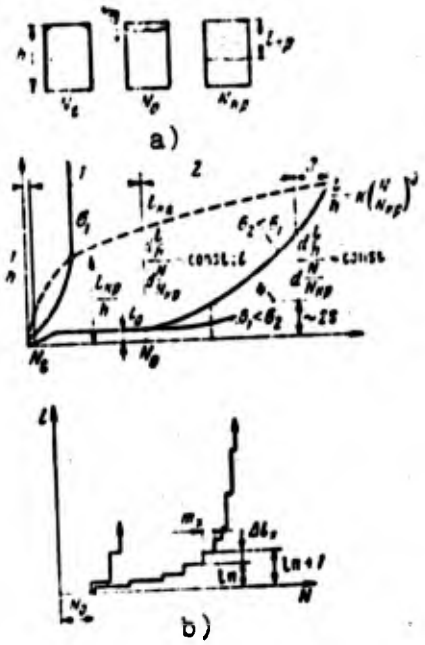

Figure 26. Schematic of fatigue crack growth.

a — crack propagation diagrams in relative coordinates; b — crack growth by stages for low stress level; 1, 2, 3 — crack growth stages; 4 — crack growth stoppage.

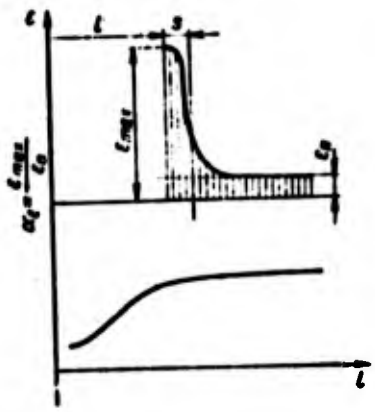

Figure 27. Strain concentration in transition zone near crack edge.

is the number of cycles to crack appearance. This number of cycles N_{ef} is subdivided into n stages, each of which corresponds to m loading cycles in the stoppage period between two stages. During stoppage the material is gradually damaged near the crack edge as a result of repeated loadings and the local value of K decreases until the possibility of a new crack "jump" is reached after $(m)_n$ cycles. Thus, between the individual crack advance stages, a process of volume damage accumulation takes place. Near the crack edge, we observe strain concentration in accordance with the scheme of Figure 27. The nature of the strain changes as a function of crack length and distance from the crack edge to the specimen edge. When the material is no longer capable of deforming in the vicinity of the crack edge, a new crack growth stage starts and the crack length changes abruptly from the value l_n to the value l_{n+1}. On the basis of this, we obtain the following expression for the total number of cycles.

$$N = N_0 + n + \sum_{n=1}^{n} (m)_n = N_0 + n + M = N_0 + N_{ef}. \qquad (18)$$

As the crack develops, there is a gradual decrease of the number of loading cycles in the crack growth stoppage periods in the remaining portion of the section in the increasing stress field and the crack length increment increases in each jump. As the crack propagates from the bottom of the initial notch, it moves into a region of the section with different loading cycle and different value of the stress gradient [163]. If the crack length is small, i.e., the distance from the bottom of the initial notch to the crack leading edge is small, the stress field at the crack edge is determined by the notch geometric shape and depth. In the variable loading case, there is a symmetric stress cycle near the crack edge. When the crack reaches a length of the same order as the notch depth, the influence of the initial notch decreases and the strain cycle near the crack edge becomes pulsating in the case of sign-alternating external load. This is explained by the fact that, under the influence of the tensile stress, the crack opens up and the load is transmitted through the material near the crack edge. In the course of half the cycle, a compressive stress acts, the crack closes up, and the load is transmitted through the crack side contact surface. With increase of the crack length in a brittle material, on the one hand, the strain concentration near the crack edge increases; but at the same time, the stress cycle becomes less damaging because of reduction of the effective stress amplitude. Moreover, in the case of loading of real details, the stress in the remaining part of the cross section increases with increase of the crack length. Because of this, the strain level near the edge of a growing crack is difficult to express by a simple formula. The number of crack "jumps" plays an important role in the detail fracture process because of crack propagation into the depth of the material. The crack dimension increment in a brittle material in each jump depends on the stress pulse and crack length. For the materials studied in the glassy condition, the limiting stress for which further crack growth is possible is determined from the brittle fracture conditions (see Chapter 1) in the form

$$\frac{\sigma_{прод}}{\sigma_в} = \text{const}\sqrt{\frac{(se_{max})_n}{l_n}}, \qquad (19)$$

where s_n is the dimension of the transition zone near the crack edge at the n^{th} growth stage; $(\varepsilon_{max})_n$ is the average value of the limiting deformation in this zone.

As a result of repeated local deformations, including the irreversible component, the dimension s_n increases up to certain limits; however, the capability of the material for local deformation decreases rapidly at the same time, which leads to progressive decrease of the product $(s\varepsilon_{max})_n$ near the crack edge as the number of loading cycles increases. Upon reaching the limiting stress value determined by (19), equal to the stress level in the remaining portion of the section, the next crack "jump" takes place. The higher the stress amplitude, the smaller is the number of loading cycles required for further crack growth after stopping. In the high stress case ($\sigma \gg \sigma_0$), crack growth takes place practically uniformly. The stages are clearly manifested only in the case of low stresses, which exceed only slightly the lower limiting value σ_0. In practice, the stress amplitude from the basic loading of the detail may be small; however, overloads are encountered. Under these conditions, crack growth depends specifically on the short-term overloads and the magnitude of the corresponding stress impulses. In this case, the number of loading cycles to failure is usually very large, since the basic load with low stress level causes practically no material damage.

The stress pulse duration must be sufficiently long for realization of the material damage process [169]. When the conditions which define the possibility of jump-like crack propagation are satisfied, the crack length is found from the formula

$$l_n = \text{const} \cdot (\sigma\sqrt{\sigma})_n l_{n-1}. \qquad (20)$$

In view of this, for the stress level usually encountered, for which crack growth by stages is characteristic, (15) is valid and thus, the crack length is a power-law function of the stress. The constant in (20) depends on the part dimensions and the elastic

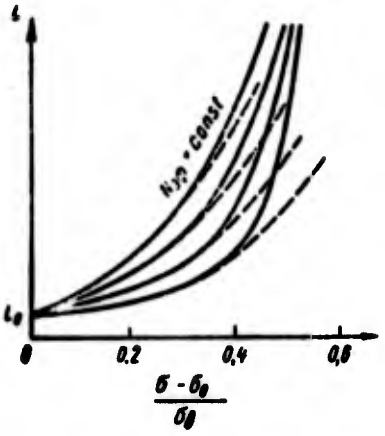

Figure 28. Fatigue crack propagation conditions as function of stress.

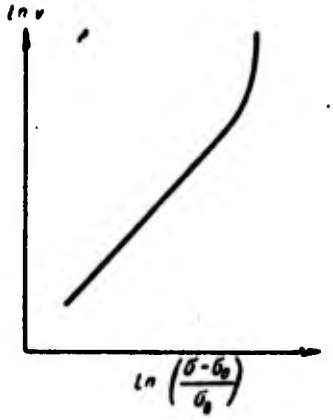

Figure 29. Fatigue crack propagation velocity as function of relative stress.

strain wave propagation velocity. If we examine the relation for the crack length after n growth stages as a function of the initial length l_0, the corresponding formula will have the form

$$l_n = (\text{const})^{\frac{2n-1}{2(n-1)}} l_0^{\frac{n}{2}} \prod_{s=1}^{s=n} \left[(l\,\Delta\sigma)_s^{\frac{1}{s+1}} \right]. \qquad (21)$$

In the case of a large number of stress pulses, we obtain from (21) the relation for crack length as a function of stress in the form $l = l_0 \sigma_{ef}^{\kappa}$, where the exponent $\kappa > 1$ depends on the rate of increase of the nominal stress level because of progressive weakening of the part section by the growing crack. The results of the tests conducted show that, for $\sigma_0 < \sigma < 3\sigma_0$, the exponent may be on the order of $\kappa = 2 - 3$. For example, for $\sigma_0 \approx \sigma_b/\sigma$, the power-law relation presented above can be used up to a relative stress value $\frac{\sigma - \sigma_0}{\sigma_b} \approx 0.35$. For a larger stress amplitude, we must take an exponential relation of the form $c^{\frac{\sigma-\sigma_0}{\sigma_b}} \approx$ (Figure 28).

The crack propagation velocity variation is shown in Figure 29. These theoretical studies show that, if the remaining part cross section area did not decrease as the crack length increases, and if overload periods were not encountered, we would observe a tendency toward termination of crack growth. This tendency is particularly clearly seen in the bending or torsion of a part, since the nominal stress decreases in the direction toward the center of the section. Compressive stress stops crack growth.

The number of loading cycles prior to the appearance of the initial fatigue crack is of great importance. The quantity N_0 depends on the stress amplitude and the material temperature. The higher the stress amplitude, the smaller is the ratio $\frac{N_0}{N_{ef}}$ and the larger the portion of the total number of cycles to failure constituted by the number of cycles necessary for crack propagation through the entire section of the specimen or detail. In actual detail parts, cracks develop at defects, particularly in the surface layer — i.e., in zones of relatively large value of the local variable stress amplitude. Under these conditions, initial cracks may appear early; however, further crack growth may take place slowly. As the crack edge moves away from the initial defect, the local stress concentration increases, however, the shape of the stress cycle becomes more favorable.

The phenomenological theories of the fatigue process can be used only with certain known limitations. The most serious drawback of these theories is the fact that the fatigue process is regarded as continuous and monotonic, while in reality the individual process stages differ significantly. A more complete picture of the subject process can be formulated only on the basis of results of experimental studies.

§4. Measurement of Crack Growth Velocity

When constructional materials are used, the resistance of the material to fracture under variable stresses is very important. In order to predict the service life of details operating with variable

stresses, it is necessary to know the laws governing fatigue crack initiation at spots where defects are located and in the stress concentration zones on the surface of the details and the conditions for growth of these cracks into the depth of the material up to the point of part failure. It is particularly important to know the material behavior under variable stresses in the case when it is highly sensitive to notches and has low resistance to fatigue crack growth. Numerous examples are known of failure of plastic parts associated with the fact that the designer did not know and did not take into consideration in the design the fatigue characteristics of the material, did not properly evaluate the allowability of defects, and did not have data on the influence of notches on the part service life. On the basis of the analysis presented above, we can conclude that we cannot restrict ourselves in strength calculations to only the fatigue curve obtained by testing conventional smooth specimens.

We must differentiate at least four stages in the development of fatigue fracture:

1) damage growth at material defect locations or in stress concentration zones;

2) appearance in the damage zone of an initial fatigue crack;

3) gradual crack growth in the cross section of the detail;

4) final brittle fracture of the detail.

Each stage has its own governing laws and occupies a certain part of the overall part service life. N_t loading cycles are required for the realization of certain irreversible local material damage and the appearance of a crack; N^* additional cycles are required for the formation in the damage zone of a fatigue crack of length l_0. Thus, $N_0 = N_t + N^*$ loading cycles must be realized prior to the beginning of fatigue crack growth into the depth of the material. After this, the crack gradually grows to the depth $l = l_{cr}$ during the next $N_{ef} = N = N_0$ loading cycles (Figure 26a). The final phase is brittle fracture of the remaining part of the section during the last loading cycle.

If there are in the detail sharp cracks of dimension on the order of l_0 which arise in the surface layer of the material during fabrication, then the number of loading cycles required for crack growth may be considerably smaller, since in this case, the lifetime is determined essentially only by the period of crack growth to final fracture. The required number of loading cycles is the minimum number of cycles which determines the shortest detail lifetime which must be taken into account by the designer. The crack which arises as a result of nonuniform loading or local overloading during fabrication does not have near its edge the material fatigue damage zone. Therefore, N_0' loading cycles, where $N_0' < N_0$, must first be accomplished in order for such a crack to grow.

We later studied the possibility of quantitative calculation of detail part service life when subjected to variable stresses by using (15) to determine fatigue crack growth. Since, in practice cases, in which the stress does not have a constant amplitude are encountered more frequently (load is not steady-state), we undertook an experimental study of fatigue crack growth with variable stress amplitude. The objective of this study was to investigate the possibility of using the superposition principle to analyze crack growth conditions with variable stress amplitude and develop a method for calculating the lifetime of details under these conditions, when the material temperature is constant.

The studies were made with low loading frequency in order to maintain reliably the normal specimen temperature and exclude the relaxation process influence. The specimens were made from three different materials. We took as a relatively ductile material the grade K475 polystyrene of the BASF firm, the brittle material was "acrylon" PMMA, and the material with intermediate properties was "suspension" PVC.

Using the technique described in Chapter 1, for these materials, we determined the critical crack length l_{cr}, which was equal to about 4 cm for the K475 polystyrene, less than 0.5 cm for acrylon at the same temperature, and about 1 cm for the PVC.

Fatigue Crac s in K475 Polystyrene with Constant Amplitude of Variable Stress

The basic mechanical properties of this material were determined by tensile tests of specimens of section 10 x 8 mm (working section length 50 mm); the nature of the resulting tension diagram is shown in Figure 30. The material has a clearly defined yield limit and good plasticicity properties (average elongation at failure is 30%). The average value of the yield limit of the specimens tested practically coincides with the ultimate strength 178 kgf/cm², since there is practically no hardening of the material during plastic deformation. The tensile tests were conducted at a strain rate of 10 mm/min and temperature 20° C. For complete elimination of residual stresses the specimens were annealed for 16 hours at 81° C (3° C below the softening temperature of the material). The remaining properties of the material are presented in the following table:

Figure 30. Tension diagram of annealed K475 polystyrene specimen.

E in kgf/cm²	G in kgf/cm²	Density	Thermal Conductivity in kcal/m·hr °C	Coefficient of Thermal Expansion in Interval from 0 to 80° C in 1/°C
24,000	8,000	1.2	0.145	10^{-5}

In the following, we present data from tests of specimens with a symmetric variable-stress cycle, conducted on a special testing machine with eccentric drive (Figure 31). The testing machine capacity was sufficient to apply a load of ±1000 kgf with frequency from 300 to 3000 cpm. The specimens were mounted in the machine grips with zero eccentricity. The preload which developed as the specimens were mounted in the machine was eliminated by changing the dynamometer position. An optical microscope was used to read the dynamometer indications. During machine operation, the light beam passing through the instrument slit forms in the field of view of the optical device

a light band whose width is proportional to the load amplitude. The load was measured after starting up the machine. During the tests, the dynamometer was used to check the load and monitor the symmetry of the loading cycle at equal time intervals. In accordance with the test objective, it was important to maintain a constant amplitude of the load. This condition was satisfied exactly until obtaining a crack 45 mm long. For a longer crack we observed considerable distortion of the loading cycle shape as a result of reduction of the load amplitude because of reduced stiffness of the specimen. Symmetry of the loading cycle was maintained by corresponding adjustment.

The fatigue crack growth on the smooth specimen surface was observed with the aid of a microscope and magnifying glass. A scale with 0.1 mm divisions was provided on the specimen surfaces. The first readout of the number of loading cycles was made for a crack length of 10 mm, and thereafter at 15, 20, 25, 30, 35, and 40 mm. In several cases, the interval was still smaller. The tests were made at a constant temperature of 21° C and loading frequency 1000 cpm. In order to exclude heating of the specimen, the temperature at the critical section was monitored by means of a thermocouple.

A notch whose shape corresponded to a stress concentration factor of 1.85 was made in the surface of the specimen (Figure 32). The notch was made very accurately by machining prior to annealing. Thin strips of silver coating with a depth of 1 mm were applied on both sides of the specimen below the notch. The conductive layer was connected through a transistor relay with the testing machine shutoff switch. The electrical circuit was broken when the crack width reached 1 mm, and the test was stopped. Although we were not able to obtain a conductive layer through the entire thickness of the specimen at the bottom of the notch, the described method provided reliable signalling of the appearance of an initial crack of length $l_0 = 1$ mm and verified the presence of a crack on both sides of the specimen.

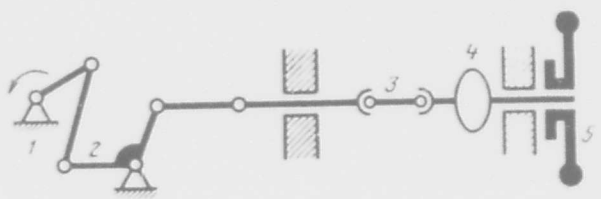

Figure 31. Schematic of Pulsator-500 fatigue testing machine.

1 — eccentric; 2 — crank arm; 3 — test specimen; 4 — dynamometer; 5 — screw tensioner.

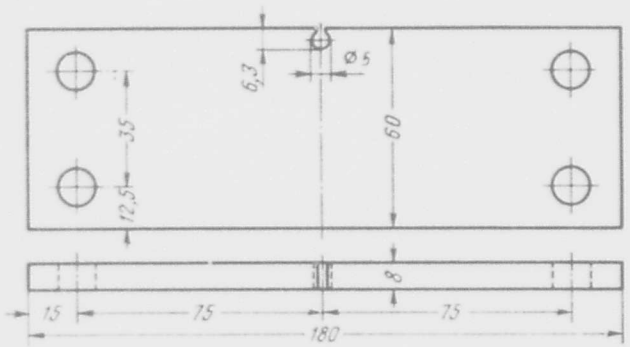

Figure 32. Specimen with notch for experimental study of fatigue crack propagation.

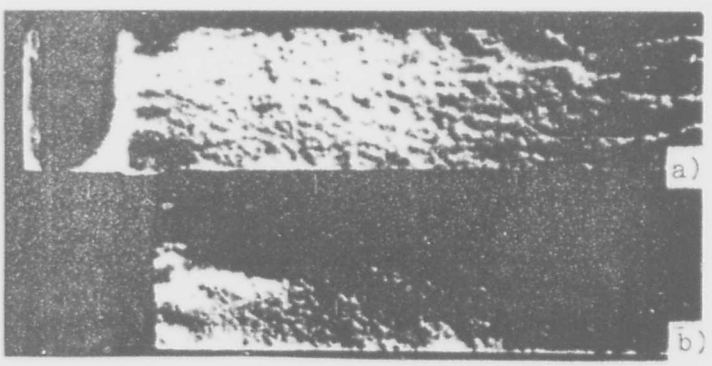

Figure 33. Initiation of several cracks across width of specimen.

a — σ = 88 kgf/cm^2; N_0 = 42,200; N_{ef} = 68,500; b — σ_a = 78.5 kgf/cm^2; N_0 = 57,400; N_{ef} = 84,500.

Fatigue crack growth was easily noted. Appearance of the crack was preceded by the appearance of a narrow whiteish strip below the root of the notch.

After growth of this strip to a depth of 1 - 1.5 mm, the initial crack of length 0.5 - 1 mm suddenly appeared. In view of this, we take hereafter $l_0 \approx 1$ mm. In spite of the fact that the stress at the root of the notch was high, the crack length found indicates that the local ductility K in the zone in question decreased as a result of the local fatigue process by an order of magnitude in comparison with the value obtained in strength tests of the basic material subjected to fast single-cycle loading. In all cases, the initial crack propagated from the root of the notch along the white strip perpendicular to the direction of the maximum tensile stress. Microscopic study showed that a dense system of parallel narrow zones arose first at the root

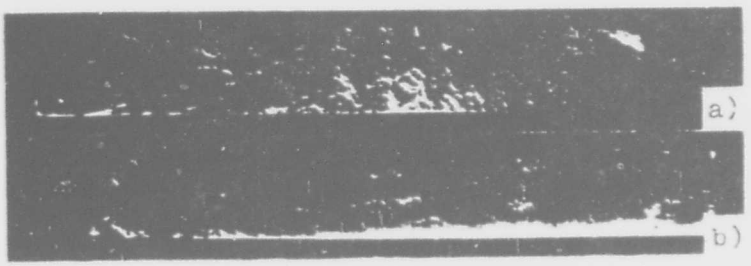

Figure 34. Fracture surface in the case of fatigue failure of ductile polystyrene specimens.
a — σ_a = 78.5 kgf/cm^2; b — σ_a = 85 kgf/cm^2.

of the notch, and these zones expanded as the number of loading cycles was increased. At that instant when they merged and the length of the whiteish strip reached about 1 mm, a fatigue crack, observed on both sides of the specimen, suddenly appeared. Study of the fracture type (Figure 33) showed that several parallel cracks developed through the thickness of the specimen below the bottom of the notch, and these cracks expanded with the formation of a wedge-like zone. At a depth on the order of 1 mm, the disruption of material integrity extended to the entire specimen thickness, and a single fatigue crack front formed. Of all the initial cracks, those on the specimen faces began to grow first of all.

In plotting the diagrams presented of crack growth variation in the limits l_0 - l_{cr} with number of loading cycles we used the arithmetic average value of the crack lengths on both faces of the specimen. When studying specimen fracture (Figure 34), the traces of crack growth by stages were clearly visible. The results of crack edge displacement measurement for a low loading frequency also confirm the existence of stages. The higher the stress level, the more monotonic and uniform is the crack growth and the less marked are the stoppage traces. The final failure of the remaining part of the section is characterized by high crack propagation velocity in accordance with brittle fracture theory.

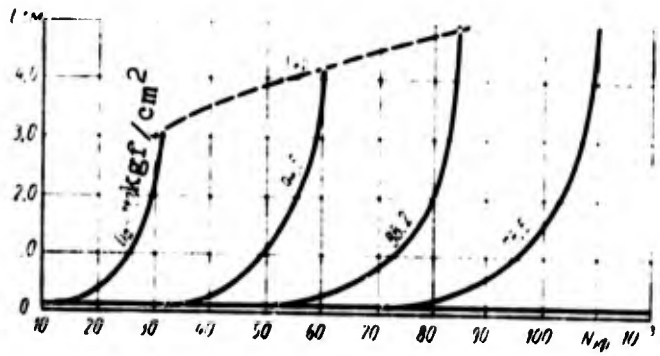

Figure 35. Fatigue crack growth in plane ductile polystyrene specimens for different values of the variable stress amplitude.

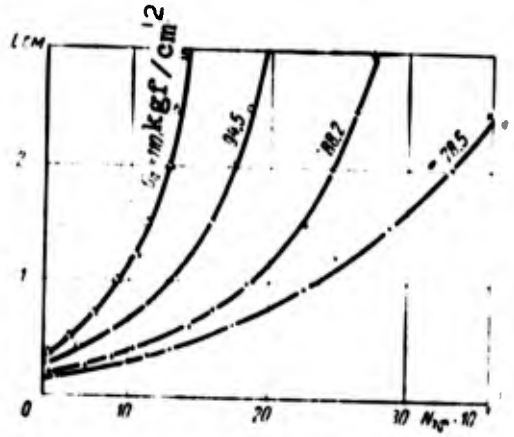

Figure 36. Crack length versus number N_{ef} of loading cycles from fatigue test data.

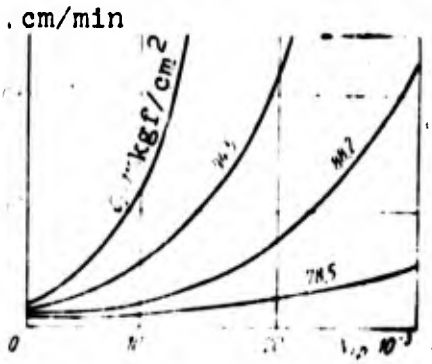

Figure 37. Fatigue crack propagation velocity in polystyrene from data of tests with different variable stress amplitudes.

Fatigue damage development can be traced right up to final failure of the specimen from the fracture appearance. The traces of the four crack growth stages can be identified clearly on the fracture surface. The nature of the fracture agrees well with the scheme of Figure 26. In the studies described, each test was repeated two or three times. The measurement results (Figure 35) were averaged; the crack growth curves were analyzed by the least squares method. For the first stage of the tests, the stresses were selected in the range from $\sigma_b/1.7$ to $\sigma_b/4$, which is most frequently encountered in practice: $\sigma_a = \pm 110; \pm 94.5; \pm 88.2; 78.5$ kgf/cm². The crack length as a function of the number of loading cycles $l = f(N_{ef})$ for the indicated stress levels is shown in Figure 36, and the crack growth velocity is shown in Figure 37. In the case shown, the intermittent crack growth nature is not reflected and the experimental points are connected by a smooth curve. For the indicated stress levels, the fracture growth states have short duration and it is difficult to measure them reliably.

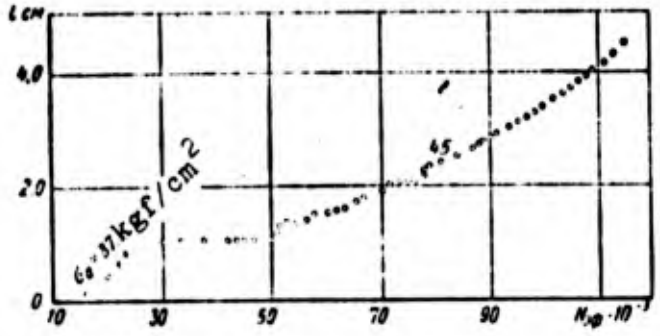

Figure 38. Crack growth for small variable stress amplitudes, close to the minimum limiting stress.

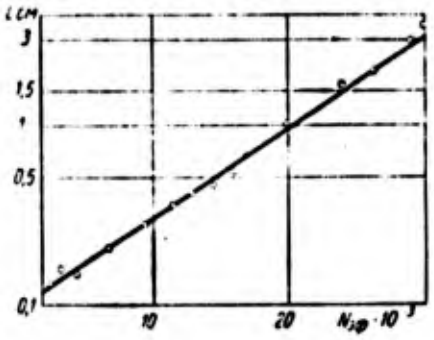

Figure 39. Linear dependence of logarithm of fatigue crack length on number of cycles N_{ef} from data of specimen tests with stress amplitude σ_a = 78.5 kgf/cm².

For completeness of the picture, we also studied secondary tensile stress loading; i.e., the influence of loading cycle asymmetry with domination of tension. It was found that tension reduces specimen life because of reduction of the critical crack size.

The tests showed that, for a variable stress in the range from ±40 to ±45 kgf/cm², the initial crack below the notch did not appear even after 10^6 loading cycles. In this case, we noted limited local material damage in the notch zone; however, this was not sufficient for crack formation. In those cases in which, after obtaining the initial crack under the action of high variable stress, the stress level decreased to the value σ_0, crack growth either stopped or slowed down markedly and the growth stages became longer. As an example, Figure 38 shows the results of specimen testing with the initial stress amplitude ±87 kgf/cm², which is maintained until obtaining a crack of length l = 10 mm, with subsequent reduction of the stress amplitude to ±45 kgf/cm². When testing other specimens under these same conditions, we observed complete termination of crack growth upon reduction of the stress. Crack growth with a variable stress amplitude close to the value σ_0 is characterized by large scatter of the test results as a function of the local changes of the material properties from specimen to specimen and from point to point.

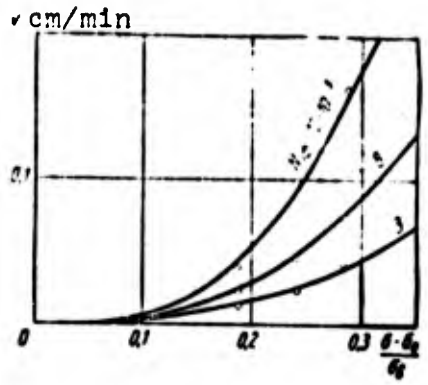

Figure 40. Fatigue crack propagation velocity in polystyrene versus relative stress for low stress level.

In analyzing the results of the first series of tests we plotted curves of lg l versus $N_{ef} = N - N_0$ (Figure 39). In all cases, the relation is linear with approximately the same slope. On this basis, we can consider the following relation to be valid

$$l = \text{const}\, e^{\kappa (N - N_0)}.$$

For a given material temperature and not too high relative stress, the constant in the formula is a power function of the stress of the form $(\frac{\sigma - \sigma_0}{\sigma_b})^{\kappa}$ (Figure 40). For higher stresses, in the $\frac{\sigma - \sigma_0}{\sigma_b} = \frac{1}{3}$ range, we observe rapid increase of crack growth velocity with increase of the stress and the power-law relation presented above cannot be used. As a result of analysis of the test results for K475 polystyrene specimens with low and moderate variable stress level, we obtained the relation

$$l \cong 1{,}2\left(\frac{\sigma - \sigma_0}{\sigma_0}\right)^3 e^{\frac{1}{6}(N - N_0)}. \qquad (22)$$

We determine the crack propagation velocity $v = \frac{dl}{dN}$ by differentiating

$$v \cong \text{const}\left(\frac{\sigma - \sigma_0}{\sigma_0}\right)^{\kappa} e^{\kappa (N - N_0)}.$$

This relation can be used to study fatigue crack growth. If we know the crack growth rate and the critical crack size, we can calculate specimen life with stress concentrators and initial defects. The critical length of a fatigue crack propagating from one side of a plane specimen, in accordance with the test data, is determined by the approximate formula

$$l_{cr} \simeq 1{,}2\left(\frac{\sigma_b}{\sigma}\right)^2. \qquad (23)$$

The resulting quadratic relation agrees with the energy criterion for crack growth in a quasi-brittle material. We note that the constant in this formula does not coincide with the corresponding value for the case in which the crack is obtained as a result of impact or static overload, since for fatigue loading, the specific work K at the crack edge is always less than for the initial material.

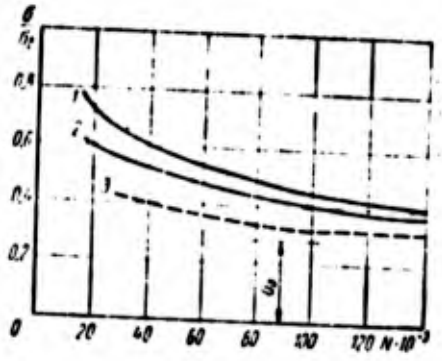

Figure 41. Limiting fatigue curves for K475 polystyrene. 1 — fatigue failure; 2 — appearance of initial crack of length l = 1 mm capable of further growth; 3 — initial material damage which shows up in the formation of a white zone.

Equating the critical crack length to the corresponding value as the crack develops by stages in the process of fatigue failure, we obtain the condition for specimen failure with constant-amplitude variable stress

$$1{,}2\left(\frac{\sigma_b}{\sigma}\right)^2 \simeq 1{,}2\left(\frac{\sigma-\sigma_0}{\sigma_b}\right)^2 e^{\frac{1}{6}(N-N_0)}. \qquad (24)$$

Hence, we obtain the number of loading cycles from the moment of crack appearance at the notch location until specimen failure

$$N_{ef} = N - N_0 \simeq 6 \ln\left[\left(\frac{\sigma_b}{\sigma}\right)^5 \frac{1}{\left(1-\frac{\sigma_0}{\sigma}\right)^3}\right]. \qquad (25)$$

Substituting into this formula σ_b = 178 kgf/cm² and σ_0 = 45 kgf/cm², we obtain the values N_{ef} shown in the following table:

σ in kgf/cm^2		±110	±91.5	±88.2	±78.5
$N_{ef} \cdot 10^{-6}$ cycles	Calculation	23	29	33	39
	Experiment	20	28	33	39

The number N_0 of loading cycles prior to the appearance of the damage zone at the notch established in the tests, the number N_{ef} of cycles prior to the appearance of a crack of length l_0 = 1 mm, and the number N of cycles to specimen failure are shown as functions of σ/σ_b in Figure 41. The values of N_0, N_{ef}, N for the variable stress amplitudes selected for these tests are presented in the following table:

Stress in kgf/cm^2	$N_0 \cdot 10^{-6}$	$N_{ef} \cdot 10^{-6}$	$N \cdot 10^{-6}$
±110	12	20	32
±91.5	33	28	61
±88.2	51	33	84
±78.5	71	39	110

For a large variable stress amplitude, the number of loading cycles necessary for crack extension exceeds the number of cycles required for unstable crack appearance. For a small variable stress amplitude, the number of loading cycles to crack appearance is nearly twice the number of loading cycles during the time of crack growth to failure of the specimen. Hence, we see how important it is to avoid the presence of sharp surface notches of dimension $l \geq l_0$ in plastic details working under variable stresses.

Since the critical crack length is independent of the dimensions and geometric shape of the detail or specimen, for evaluation of the material strength, it is insufficient to know the fatigue curve (Wöhler curve). We need to have the curve of σ versus N_0, and in certain cases, we also need the analogous curve for a definite fatigue crack length (see Figure 41). The curve $\sigma = f(N_0)$ depends very weakly on the dimensions and shape of the specimen and characterizes the local resistance of the material to fatigue failure at the point of

stress concentration on the surface of the specimen. The scatter of the experimental data used in plotting this curve depends to a considerable degree on the local residual stresses of processing origin and on the influence of stress concentration. In view of this, the curve may vary as a function of specimen fabrication technology and the properties of the material surface layer of thickness on the order of 1 mm. A high level of residual stresses of the first kind throughout the entire specimen volume or detail part volume does not have any significant effect on the number of loading cycles prior to the appearance of the surface crack; however, for a brittle material, it has a strong influence on fatigue crack growth and in the tensile stress case, reduces the detail part fatigue life. This explains the large reduction in the number of loading cycles to failure of certain of the specimens tested, which had not been annealed and had residual tensile stresses. In plane specimens of small thickness, the biaxial residual stresses act analogously to the secondary static tensile stress and make the loading asymmetric, which causes reduction of the critical crack length. The results of the described tests show the importance of eliminating residual stresses in plastic details.

Fatigue Cracks in K475 Polystyrene with Variation of Variable Stress Amplitude

A second series of tests was devoted to studying the damage accumulation law for fatigue crack growth in polystyrene. If the crack growth rate after change of the variable stress amplitude from σ_1 to σ_2 is not dependent on the preceding stress level and is a function only of σ_2 and crack length, we can take a linear crack length increment summation law and use (17) in studying the failure process of a detail with an initial defect.

The test results confirmed this assumption completely. Figure 42 shows the fatigue crack growth diagram in the coordinates $l - N_{ef}$ for a specimen initially loaded by a variable stress with amplitude ± 94.5 kgf/cm^2; after reaching a crack length $l = 1$ cm, the stress was reduced to ± 56.7 kgf/cm^2. After this, the crack growth rate decreases markedly and corresponds to the new stress level. This

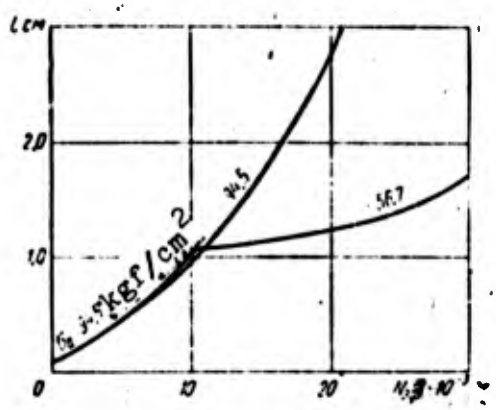

Figure 42. Fatigue crack growth for constant and variable stress amplitude.

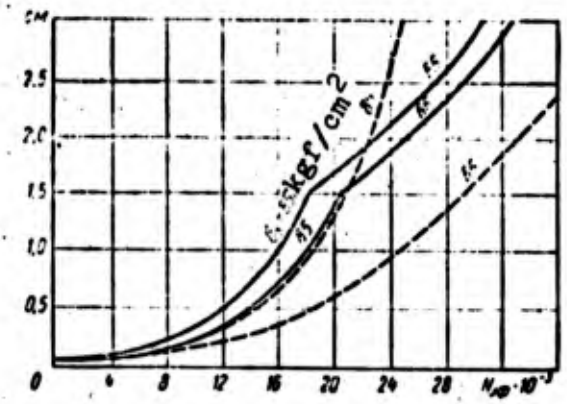

Figure 43. Fatigue crack growth rate in two polystyrene specimens as function of variable stress amplitude.

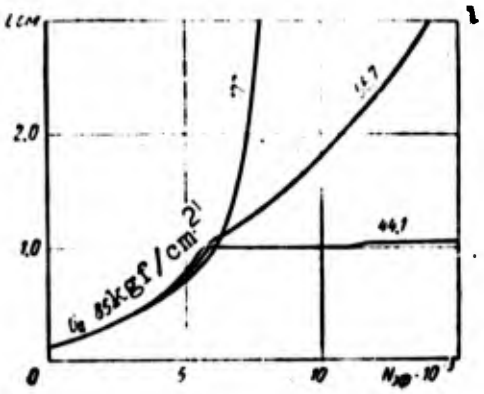

Figure 44. Fatigue crack growth rate variation for three different stress levels established after initiation of crack with l = 1 cm.

nature of the relationship in question is explained by the fact that the crack actually propagates in material which was not damaged by the preliminary loading at the higher variable stress level, since the damage takes place only in the immediate vicinity of the crack edge. Since the crack edge constantly extends into new volumes of the material, the heredity effect is not observed, which makes it possible to use the linear crack length increment summation law.

Figure 43 shows the curves $l = f(N_{ef})$ of crack length as a function of the number of loading cycles for the cases when the specimen was loaded by a variable stress with constant amplitudes $\sigma = \pm 85$ kgf/cm^2 and $\sigma = \pm 66$ kgf/cm^2, and when the specimen was first loaded by a stress with the amplitude ± 85 kgf/cm^2 and then after the crack reaches the length $l = 1.5$ cm, the amplitude was reduced to the value ± 66 kgf/cm^2. From the moment of stress reduction, the crack growth takes place with the velocity corresponding to the new, reduced stress level

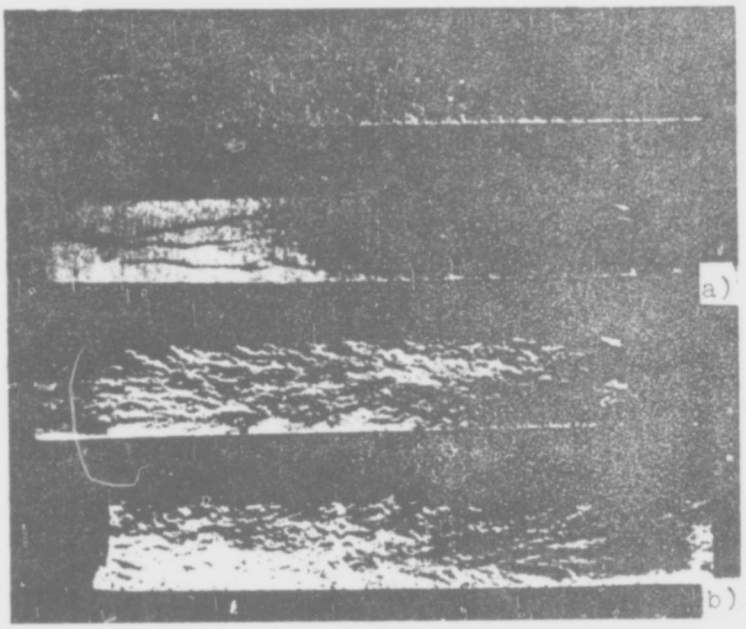

Figure 45. Specimen fracture surfaces after fatigue testing with constant and variable stress amplitude.

and crack length 1.5 cm. Figure 44 shows the results of tests of three specimens which were first loaded by a stress with amplitude ±85 kgf/cm^2. After the crack reached the length l = 1 cm, the stress amplitude in one specimen was reduced to the lower limiting value σ_0 = ±44.1 kgf/cm^2; in the second specimen, the stress was established at σ = ±56.7 kgf/cm^2; and in the third, it was increased to ±107 kgf/cm^2. In the first case, after a very long interruption in crack growth, unsteady and very slow crack growth analogous to that shown in Figure 38 again started.

Photographs of the fracture surface obtained in the described tests are shown in Figure 45. The fatigue crack growth in the cases associated with the curves described above actually takes place non-uniformly, and in the photographs we see clearly the traces of the individual stages. For the high stress level (90 - 110 kgf/cm^2), the traces can be noted only in the beginning of the growth. For the low stress level, the crack growth stages last longer and their traces on the surface are spaced at larger distances, but the stages shorten

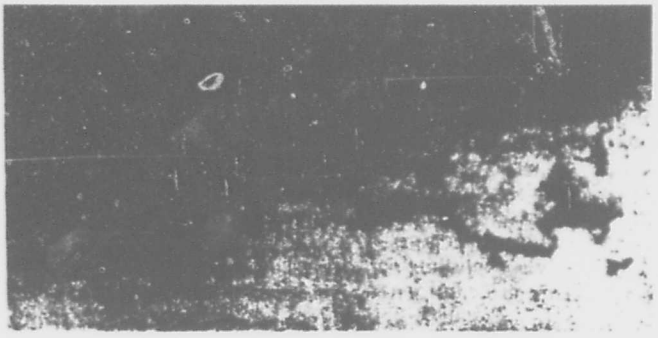

Figure 46. Propagation of secondary cracks from fracture surface in the case of fast growth of main fatigue crack (x 300).

with increase of the stress. At an average amplitude level on the order of 60 kgf/cm^2, the distance between adjacent crack stoppage traces is 1 - 2 mm. As the crack grows into the depth of the specimen material, this distance increases; however, this does not denote a corresponding increase of the crack "jumps," since with increase of the stress the growth stages become less well defined because of area reduction of the remaining portion of the section.

After reaching a length of about 30 mm, i.e., as the crack edge approaches the midpoint of the specimen width, it grows nearly continuously and the stoppage traces on the fracture surface disappear. The existence of secondary cracks (Figure 46) was established in studying the fracture surface of specimens with fast fatigue crack growth.

Fatigue Cracks in Acrylon and Suspension PVC Specimens

In addition to the tests of specimens made from ductile polystyrene, we made similar studies of more brittle materials. In these tests we noted first of all considerable scatter of the experimental data for the variation of crack length with number of loading cycles. Figure 47 shows the results of PVC specimen tests for a constant variable stress amplitude ±72.8 kgf/cm^2 and loading frequency 750 cpm. The final brittle fracture of acrylon specimens, for which the critical crack length at a stress of 100 kgf/cm^2 is only a few millimeters, occurred so fast that it was not possible to record the fatigue growth stage. The specimen life was essentially defined by the number of cycles required for the formation of the material damage zone at the edge of the initial notch and the appearance of a crack

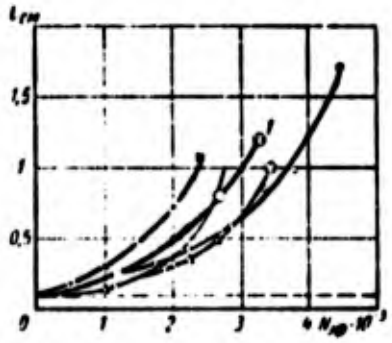

Figure 47. Curves of fatigue crack growth in PVC σ_a = 72.8 kgf/cm^2.

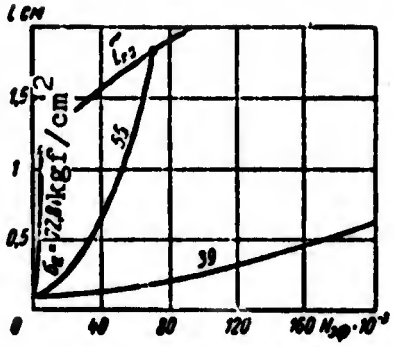

Figure 48. Fatigue crack growth in PVC for different variable stress amplitudes.

capable of growth. In view of this, the further study was made on PVC specimens. Figure 48 shows the averaged curve of crack length versus number of loading cycles from data of analysis by statistical methods of specimen test results for three values of the stress amplitude σ = ±72.8; ±55; ±39 kgf/cm^2. Comparison of the fracture surfaces of the specimens tested at high and intermediate values of the variable stress amplitude showed that, in the first case, it is difficult to identify the segments of fatigue and final failure, and the entire fracture surface is completely smooth. In the second case, the surface corresponding to fatigue failure is more noticeable. The dependence of crack length on number of loading cycles is the same as in the preceding case, and the corresponding diagram in the coordinates N - lg σ is a straight line (see Figure 47). Accelerated crack growth in accordance with the exponential relation begins at a comparatively low value of the relative stress; therefore, the dependence of crack length on stress is somewhat different. In the tests, we determined the minimum limiting stress, whose value for the brittle material was very low (on the order of 30 kgf/cm^2).

§5. Conclusions from Results of Fatigue Tests of Plastics at Normal Temperature

The tests conducted showed that the materials studied are subject to static and fatigue damage at normal temperature. Since real parts always work under conditions of long-term static or variable loading,

the material strength characteristics associated with long-term loading or the number of loading cycles are of decisive importance in the question of industrial use of plastics. The tests conducted made it possible to establish the following:

1. In the static loading case, the material strength is defined by a diagram of the type shown in Figure 2, and a lower limiting stress exists. If the stress is lower than this value, the material damage will be negligibly small.

2. The process of damage accumulation under static loading and variable stresses subdivides into individual stages, during the course of which different material damage laws act. In both cases, we can identify four fracture growth stages:

a) appearance of damage zones on the surface of the part at the locations of defects;

b) appearance in the damage zone of a crack after exceeding the local capability of the material for deformation;

c) crack growth into the depth of the specimen material until reaching the critical crack length, which decreases under fatigue conditions;

d) final brittle fracture of the part.

3. For fatigue fracture of the part, the stress level must be higher than the minimum limiting value which, however, is quite low, particularly for the brittle materials.

4. The linear summation law for the elementary growing-crack length increments is maintained quite accurately during fatigue crack growth.

5. The allowable crack length in parts working under variable stresses can be determined from the formula

$$l(\sigma - \sigma_0)^n \simeq \text{const.}$$

The exponent κ depends on the brittleness of the material. For ductile materials we can take $\kappa = 3$ [140].

6. A more complete physical model of damage accumulation for the quasi-brittle materials is necessary for studying damage zone nature and the conditions for damage zone initiation [116].

CHAPTER 3

EXAMPLES OF STATIC STRENGTH CALCULATION OF EPOXY RESIN PARTS

§1. Thin-Wall Tube Loaded by Internal Pressure

Let us assume that in the tube wall at a considerable distance from the closed ends there is a crack of semicircular form whose plane is perpendicular to the maximum tangential stress. The stress concentration factor at the crack is higher than at the point of transition from the cylindrical wall to the flat closure, and therefore, the tube strength is determined by the strength of the cracked cylindrical wall. The material temperature is +10° C.

The ultimate strength of the epoxy resin under static loading is σ_b = 500 kgf/cm², the elastic modulus E = 25,000 kgf/cm².

In the calculation we shall consider the material to be quasi-homogeneous. For the given temperature the epoxy resin behaves like a brittle material. In accordance with the data of Chapter 3, the average value of the specific work for formation of unit fracture surface can be taken equal to $\overline{K}$ = 0.4 kgf·cm/cm².

a) In the absence of any significant defect in the wall ($l < l_0$ = 1 mm), the static strength would be determined by the maximum stress condition $\sigma_{max} = \sigma_{lim}$, since the material is in the glassy state.

The maximum stress acts in the circumferential direction, and for the elastic material condition is found from the formula

$$\sigma_{прод} \cong p\frac{\beta+1}{\beta-1},$$

where $\beta = \frac{b}{a} = \frac{7}{5} = 1.4$. Hence, we find the value of the excess internal pressure required for tube failure with $\sigma_{lim} = \sigma_b$

$$\sigma_{прод} \geqslant \sigma_b\frac{\beta-1}{\beta+1} = 500\,\frac{1{,}4^2-1}{1{,}4^2+1} = 170 \text{ atm}.$$

Actually, the limit pressure will be somewhat higher because of the influence of the large nonlinear deformations prior to wall failure and the three-dimensional stress state, since the stress distribution in the tube section changes somewhat prior to failure.

b) In accordance with (27) (Chapter 1), the limit stress for a plane specimen with initial crack is determined for a circular crack shape by the expression

$$\sigma_{прод} = \sqrt{\frac{\pi EK}{2(1-\nu^2)l}}.$$

Actually, the crack has a semicircular form, but one side of the crack extends to the inner surface and therefore, corresponds to a circular crack in a solid specimen, which is also confirmed by (26). The difference between the stress distribution in the curved tube wall and in a flat specimen can be considered with the aid of a correction factor in accordance with the formula

$$\sigma_{прод} = \frac{1}{1+0{,}16\frac{l^2}{ab}}\sqrt{\frac{\pi EK}{2(1-\nu^2)l}} =$$

$$= \frac{1}{1+0{,}16\frac{0{,}5^2}{5\cdot 2}}\sqrt{\frac{\pi 2500\cdot 0{,}4}{2(1-0{,}3^2)0{,}5}} \simeq 180 \text{ kgf/cm}^2.$$

The crack length is quite large and exceeds the dimension of the transition zone at its edge ($l_0 \approx 1$ mm), which permits use of the expression characterizing material strength in the brittle state. Then we find the rupture pressure for a tube with defect, examining

the average tensile stress in the wall, perpendicular to the defect plane

$$p_{np\partial} \cong \frac{h\sigma_{np\partial}}{\frac{a+b}{2}} = \frac{2 \cdot 180}{6} = 60 \text{ atm.}$$

In the present case, it is nearly three times smaller than for a tube without defect. Upon decrease of the temperature, the static strength of a tube without a defect increases with increase of σ_b, while for a tube with crack, it decreases in accordance with reduction of the quantity $\overline{K}$.

§2. Static Strength of Epoxy Resin Rotating Disk

Let us examine a rotating disk of constant thickness h = 2 cm, outer radious b = 20 cm, radius of central shaft hole in the disk a = 20 cm. On the surface of the central hole, there are radial cracks of depth l = 0.5 cm through the entire disk thickness. The limiting rpm n_{lim}, corresponding to fracture of a disk without cracks, can be found on the basis of the epoxy resin ultimate strength σ_b = 500 kgf/cm^2 using the formula

$$\sigma_{np\partial} = \text{const}\, b^2 n^2_{np\partial}\left[1 + \frac{a}{b} + \left(\frac{a}{b}\right)^2\right] \leq \sigma_b$$

In accordance with (13) (Chapter 1), for a disk with defect, we obtain

$$(\sigma_{np.\partial})_l = \sqrt{\frac{2}{\pi} \cdot \frac{E\overline{K}}{l}} = \text{const}\, b^2 (n_{np\partial})^2_l \frac{1 - \left(\frac{a}{b}\right)^3}{1 - \frac{a}{b} - \frac{l}{b}}.$$

The decrease of the limiting disk rpm for a/b = 0.1 and l/b = 0.025, is determined by the ratio

$$\frac{(n_{прим})_t}{n_{прим}} \approx \sqrt{\frac{1}{\sigma_0}\sqrt{\frac{2}{\pi}\cdot\frac{E\overline{K}}{l}}} = \sqrt{\frac{0,8}{500}\sqrt{\frac{25000\cdot 0,4}{0,5}}} = 0,47.$$

§3. Determining Number of Loading Cycles to Failure

Assume that we are required to determine for the tube examined in §1 the number of loading cycles prior to fatigue failure with alternating pressure amplitude p = 40 atm.

The critical crack length is found from the expression

$$\sigma_{прим} = \frac{a}{2h} + \frac{b}{2h}p = 120 \text{ kgf/cm}^2 \approx \frac{1}{1+0,016\frac{l_{кр}^2}{Rh}}\sqrt{\frac{\pi E\overline{K}}{2(1-\nu^2)l_{кр}}}.$$

For E = 25,000 kgf/cm², $\overline{K}$ = 0.4 kgf·cm/cm², and ν = 0.35, we obtain l_{cr} = 1.2 - 0.5 = 0.7 cm - 7 mm.

If we assume that the fatigue crack growth law in the subject material corresponds to the relation derived in Chapter 2, the number of cycles to tube failure can be determined from the condition

$$\Delta l \cong 1,2\left(\frac{\sigma-\sigma_0}{\sigma_b}\right)^3 e^{\frac{1}{3}\Delta N}.$$

For σ_b = 500 kgf/cm² and the value of the lower limiting stress for the epoxy resin σ_0 = 25 kgf/cm², we obtain

$$\Delta l \cong 1,2\left(\frac{40-25}{500}\right)^3 e^{\frac{1}{3}\Delta N} = 0,7.$$

Hence, we find the number of cycles to failure

$$\Delta N = 60\,000.$$

STRENGTH OF REINFORCED PLASTICS

CHAPTER 4

STRENGTH OF REINFORCING GLASS FIBERS

§1. Mechanical Properties of Glass Fibers

The theoretical strength of solid bodies and polymers in the glassy state has been studied in [61, 143, 174, 194]. Kobeko indicates that, if the theoretical strength of glass is calculated on the basis of the chemical and electrical interaction forces of the particles of an amorphous body, the strength amounts to about 0.1% of the tension elastic modulus determined experimentally. The relation $\sigma_m = 0.1E$ is applicable for bonds of various types. The strength of quartz glass is 1200 kgf/mm^2, that of soda glass of nonalkali composition is 700 - 800 kgf/mm^2, that of glass of alkali composition is 400 - 600 kgf/mm^2.

In [174], relations based on the assumption that the work of the external forces transitions during fracture into potential energy of the newly forming free surfaces were presented for calculating the theoretical strength of glass

$$\sigma_m = \left(\frac{\alpha_{max} E}{r_0}\right)^{1/2}, \qquad (1)$$

where r_0 is the equilibrium interparticle distance, α_{sur} is the free surface energy of the solid body.

In examining the molecular attraction layer thickness $h = 2r_0$, a similar relation has been obtained. If $E = 10^4$ kgf/mm^2, the σ_m values lie in the range 1000 - 2000 kgf/mm^2. The specific surface energy necessary for formation of unit surface in crystalline and amorphous bodies [194] is equal to $10^2 - 10^3$ erg/cm^2 and the layer thickness — $h = 5 \cdot 10^{-8}$ cm.

To evaluate the theoretical strength of glass, Griffith used the dependence of glass fiber strength on diameter which he obtained on the basis of energy balance conditions, extrapolated into the region of very small transverse fiber dimensions, comparable with the "molecular" dimensions. According to Griffith, the theoretical strength of glass is ~1100 kgf/mm^2. However, experimental data show that the strength of real fibers is considerably lower than the theoretical value.

The comparatively low strength of glass fibers of different diameter has been noted in studies by Griffith, Reinkober, Aslanova, Zhurkov, Bartenyev, and Andreyevskiy [3, 5, 17, 51, 186]. The basic reason for the decrease of their strength lies in the presence of numerous defects distributed over the highly developed surface of the fibers.

A high stress concentration arises at the crack tips in the case of tensile stresses, and failure occurs when these stresses reach some critical value which is sufficient for crack propagation.

According to Griffith, a crack oriented perpendicular to the tension direction grows if the elastic energy reduction in the specimen is equal to or greater than the potential energy increase which takes place during the formation of new fracture surfaces. The energy of a specimen with a crack is

$$W = W_0 - \frac{\pi c^2 \sigma^2}{4E} \delta + 2c\alpha_{sur}. \qquad (2)$$

where W is the energy of the specimen with crack; W_0 is the energy of the specimen without crack, ν is Poisson's ratio; δ is the specimen thickness; c is the length of an interior crack of elliptic form.

From the condition $dW/dc = 0$, the nominal critical stress

$$\sigma_n = \frac{2}{\sqrt{\pi}} \sqrt{\frac{\gamma_{эф} E}{c}}. \tag{3}$$

A refinement of this relation is given in [11].

As a rule, glass fiber strength increases with decrease of the diameter. Generalized data of various studies are shown in Figure 1.

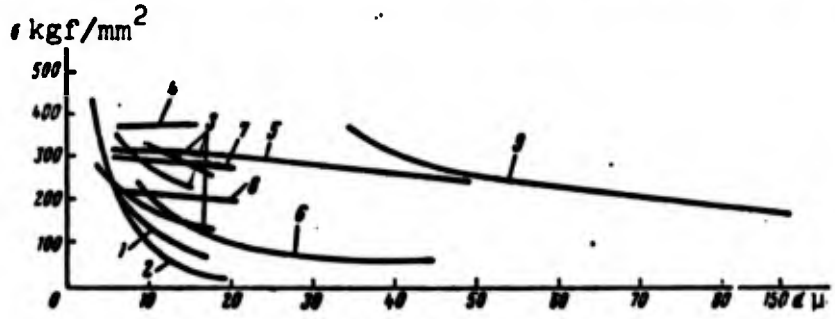

Figure 1. Dependence of fiber strength on diameter.
1, 3, 4, 5, 6 — [3]; 2 — [143]; 7, 8 — [17]; 9 — [161].

According to Griffith, the strength increase with reduction of the elementary fiber dimensions is explained by the fact that orientation of the molecules takes place in the surface layer during fabrication of these elementary fibers. The empirical dependence of the strength on the fiber diameter is approximated [143] by a function of the form

$$\sigma = A + \frac{B}{d}, \tag{4}$$

where A and B are constants which are determined from the experimental data. Similar arguments were given by Murgotroyd [168], who assumed

that, as the fibers are drawn from the melt, the chain structure of the glass forms, in which the molecules are arranged parallel to the drawing direction.

In Reinkober's experiments [186], the fiber surface was treated with a 40% hydrofluoric acid solution in order to identify the role of the surface layer. The breaking strength increase in elementary fibers of 20 micron diameter was ~200% in comparison with a fiber not subjected to etching. This marked effect of surface layer removal was not manifested when etching and testing the fibers immediately after fabrication.

An experimental evaluation of the fiber surface layer influence on resistance to fracture was made by Zhurkov [1, 51], who used long-term annealing of elementary fibers at a temperature of 580° C with subsequent slow cooling. In this case, mechanical orientation of the molecules should be eliminated, since it leads to difference between the strength of the annealed and nonannealed fibers. The experiment showed that the monofilament strength is practically the same before and after annealing.

Reinkober's data on fibers tested immediately after production, and Zhurkov's results, make it possible to consider that the marked increase of fiber strength when the surface layer is etched is apparently explained by the removal of the most nonhomogeneous and most highly damaged layer, i.e., removal of defects on the surface of the fibers.

Later Aleksandrov and Zhurkov [1] showed that the nonhomogeneities which create local overstresses are distributed through the volume of the specimen; however, the surface defects are the most dangerous. It was assumed that the probability of nonhomogeneity existence on the surface is proportional to the magnitude of the surface area. With decrease of the fiber diameter, the probability of the appearance of a dangerous nonhomogeneity on the surface diminishes, which leads to increase of the strength in the statistical sense.

Kontorova [64] developed the statistical concepts of fiber strength and attempted to evaluate the strength of glass monofilaments as a function of defect (crack) size and orientation. Cracks oriented perpendicular to the load are most hazardous. Kontorova suggested a relation for calculating the strength in the presence of a crack of arbitrary orientation, based on the Griffith criterion

$$\sigma_\theta = \frac{1}{\sin^2\theta}\sqrt{\frac{E\sigma_{0\min}}{\pi c}}, \tag{5}$$

where θ is the angle between the direction of the force and the long axis of the crack.

When drawing fibers, the cracks are oriented along the drawing direction. The larger the degree of drawing, characterized by the die and fiber diameter ratio, the greater the number of longitudinally oriented cracks and the higher the fiber strength. The function representing the probability that in a fiber of diameter d obtained by drawing from an initial rod of diameter d_0 there will be a crack of length c oriented perpendicular to the drawing direction, is written in the form of the exponential relation

$$pdV = \kappa \exp\left[-\beta\left(\frac{d_0}{d}c - \hat{c}\right)^2\right] dV, \tag{6}$$

where $\hat{c}$ is the most frequently encountered crack dimension; dV is the elementary volume; k and β are constants. With decrease of d, this function decreases rapidly and the probability of dangerous crack occurrence diminishes.

Bartenyev [17] analyzed the strength of glass fibers and studied the strength of real and "defect free" fibers, obtained by etching their surface to a depth of 1 - 2 microns. The results showed that, with reduction of the fiber diameter, the surface layer becomes less defective, since the difference in the strength level before and after etching decreases with reduction of the fiber diameter. However, in all cases, the strength increases after removal of the surface

layer. The experimental results showed that the dependence of the strength on the diameter weakens marked for fibers which have been subjected to etching. This must be considered a consequence of elimination of a considerable portion of the defects.*

The magnitude of the ductile deformation during drawing of glass fibers, characterized by the drawing ratio α, has been proposed as the physical factor determining fiber strength. According to the experimental data, the fiber strength is connected with the drawing ratio by the empirical relation

$$\sigma = A + B\sqrt{\alpha}, \tag{7}$$

where $\alpha = 1 + \varepsilon$; ε is the ductile deformation during drawing. If we assume that the viscous glass melt is incompressible, then $\sqrt{\alpha} = d_0/d$, where d_0 is the die diameter. Similar results were obtained in experiments by other investigators [13, 175, 201]. The ratio d_0/d is one of the parameters of the relation (6), considered by Kontorova.

In the expression for the probability of dangerous defect occurrence, it is suggested that we consider, in place of the fiber volume V, its surface area S, since the influence of surface defects on strength is stronger. For a comparatively narrow range of fiber diameter variation, the surface area S is replaced by the fiber length L, which is considered the basic factor (dimension) defining the glass fiber strength scale effect. In this case, the fracture probability is connected with L and the strength is determined by the following Weibull type equation [206]

$$\sigma = CL^{-1/n}, \tag{8}$$

*J. Fischer and J. Hollowman showed [135] that the presence of 10^3 defects per square centimeter is sufficient for the manifestation of strength dependence on the dimensions in the statistical sense.

where C is a constant which depends on the drawing ratio, glass composition, and temperature at the instant of drawing; n is a constant accounting for the nature of the defect distribution on the surface (homogeneity exponent according to Weibull). According to the experimental data for alumoborosilicate fibers n = 4 and C = a + b $\sqrt{a}$, where a = $AL^{-0.25}$ and b = $BL^{-0.25}$ [see (7)], and a depends on the chemical composition and temperature of the glass melt, b depends only on the chemical composition of the glass. The following relations have been obtained for alumoborosilicate glass monofilaments

$$a = 1.117^{\circ}C_{\text{г}} - 1220;\ b = 1.15.$$

We note that these parameters are associated with crack formation on the surface of the fiber, since they determine the fiber production conditions.

In evaluating the functioning of fibers in composites fabricated from fibers of a single diameter, the dominant influence of L on the strength apparently must be considered well-founded, since crack opening from a defect located within the fiber is more difficult than from a fiber surface defect which arises during fabrication of the fibers and composite. However, the magnitude of the fiber diameter influences the strength of the basic fiber bundle and this influence depends to a considerable degree on the type of glass (Figure 2).

For industrial fibers, the strength dependence on diameter shows up clearly, although the strength level of fibers of different types varies over a wide range [56, 161].

The dependence of fiber strenth on length is characterized by the data of Table 1 and Figures 3a, b [3, 5, 53], which confirm the validity of (8).

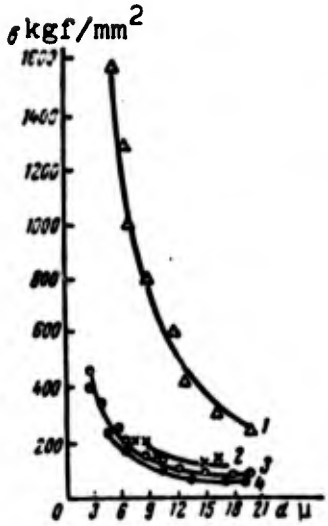

Figure 2. Fiber strength versus diameter.

1 — quartz; 2 — fused basalt; 3 — alumoborosilicate; 4 — Na-Ca-Si fibers.

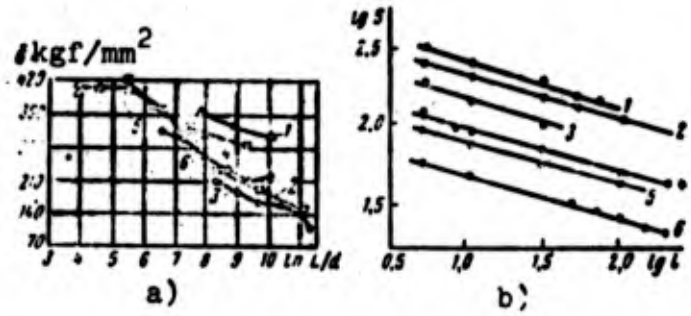

Figure 3. Average monofilament strength versus length.

a) 1, 2, 3 — E-glass; 4, 5, 6 — S-994; 1 — minimally damaged fibers; 2, 3 — fibers taken from yarn; 4 — monofilament wound on cardboard drum during drawing; 5, 6 — fibers taken from yarn; b) 1 — 5.2 μ diameter; 2 — 6.3 μ diameter; 3 — 12.6 μ diameter; 4 — 23.5 μ diameter; 5 — 38 μ diameter; 6 — 120 μ diameter.

Most of the data obtained indicate a linear dependence of strength on length on a logarithmic scale. In this case, the strength level is determined by the degree of fiber damage (Figure 3a) [65]. The series of data for short S-994 glass fibers (L < 2.5 mm) does not confirm the length dependence of the strength. As will be shown later, this is due to the difference between the surface defects of the long and short fibers.

TABLE 1

STRENGTH OF 9 - 10 MICRON DIAMETER FIBER AS FUNCTION OF LENGTH

Fiber Length in mm	Fiber Diameter in μ	$\sigma_{b\,a}$ in kgf/mm²	Fiber Length in mm	Fiber Diameter in μ	$\sigma_{b\,a}$ in kgf/mm²
5	9,0	150	90	9,7	76
10	9,5	122	185	9,7	87
20	10,0	121	1560	10,0	72
45	9,0	115			

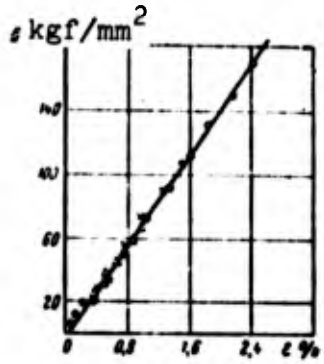

Figure 4. Diagram of elementary fiber deformation.

• — ∅ 100 μ; Δ — ∅ 54 μ; x — 19 μ; 0 — ∅ 6 μ.

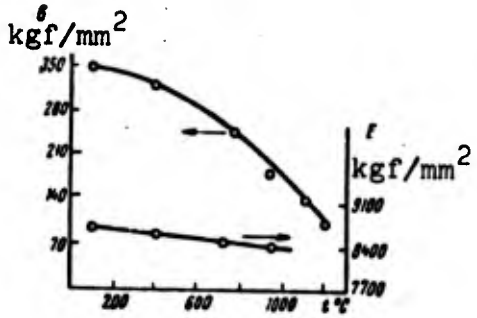

Figure 5. Influence of temperature on strength and elastic modulus of E-glass fiber [203].

The elastic properties of the glass fibers depend on the chemical composition. The values of the elastic moduli for the most widely used glasses are: quartz fiber E = 10,000 - 12,000 kgf/mm², alumoborosilicate (low alkali) 7000 - 8000 kgf/mm², Na-Ca-Si (alkali) 4000 - 6500 kgf/mm².

In very carefully conducted experiments [1, 3, 51, 52, 161], it was found that the elastic modulus is independent of the fiber dimensions. Thus, for diameters of 10 - 80 microns [1], the influence of fiber dimensions on the elastic characteristics does not show up, for diameters of 12 - 250 microns [161] E = 7600 - 8100 kgf/mm², for fibers of diameter 6 - 100 microns [52], the modulus remains practically constant.

The strain diagram for glass fibers is linear up to failure, the deformations at failure decrease with increase of the fiber diameter. The elongation of the 5 - 20 micron diameter fibers which are used in practice amounts to 3 - 1.5%. The strain diagram for fibers of various diameters is shown in Figure 4. A marked reduction of breaking strain with increase of the fiber diameter was also obtained by Reinhardt [185]. Poisson's ratio for glass fibers is 0.04 - 0.22 [168].

The strength and elastic modulus of the glass fibers decrease monotonically with temperature increase (Figure 5) [202].

§2. Influence of Glass Fiber Defects on Their Strength

Defects randomly distributed along the length may appear with length increase of a constant-diameter fiber. In [19, 189] attempts were made to identify the influence of these defects on the monofilament strength and classify the defects with regard to degree of hazard.

According to Schmitz [189], the defects encountered in glass fibers can be divided into three forms: A are interior submicrocracks of dimensions of order 10^{-4} cm, B and C are surface cracks of different size (B are smaller defects, which are frequently encountered; C are larger defects, which are rarely encountered). Defects of essentially different types show up in strength testing of fibers of different length.

Figure 6a shows the approximate zones of defect occurrence. For example, for fibers 10^{-2} cm long, interior defects A dominate; for fibers 10^{-2} and 10 cm long, defects B are encountered most frequently, ahd the presence of defects of types A and C is possible. For fibers of length greater than 10 cm, the strength is determined by type C defects. Each defect type yields a definite strength distribution and corresponding integral curve. *

Figure 6b shows the influence of defects [189] on the limit strength probability density curves of glass fibers from 0.05 to 1.5 cm long. In the shorter fibers, there are defects of type B, the density curve has a single maximum, and the integral curve 1 (Figure 6c) is a straight line without a break. With increase of fiber length type B and C defects are encountered on the surface of the fiber. In this case, the probability density curve has two maxima and on the integral curve, we note a break which depends on the ratio of the number of fractures caused by type B and C defects. Thus, with increase of the length, part of the glass fibers fail from defects B and part from defects C (see Figure 6c, curves 2,3,4). The strength of the long fibers is determined only by C defects, which are most hazardous and characteristic for these fibers. The probability density curve

*Defects of type A were not found experimentally since it was not possible to test very short fibers.

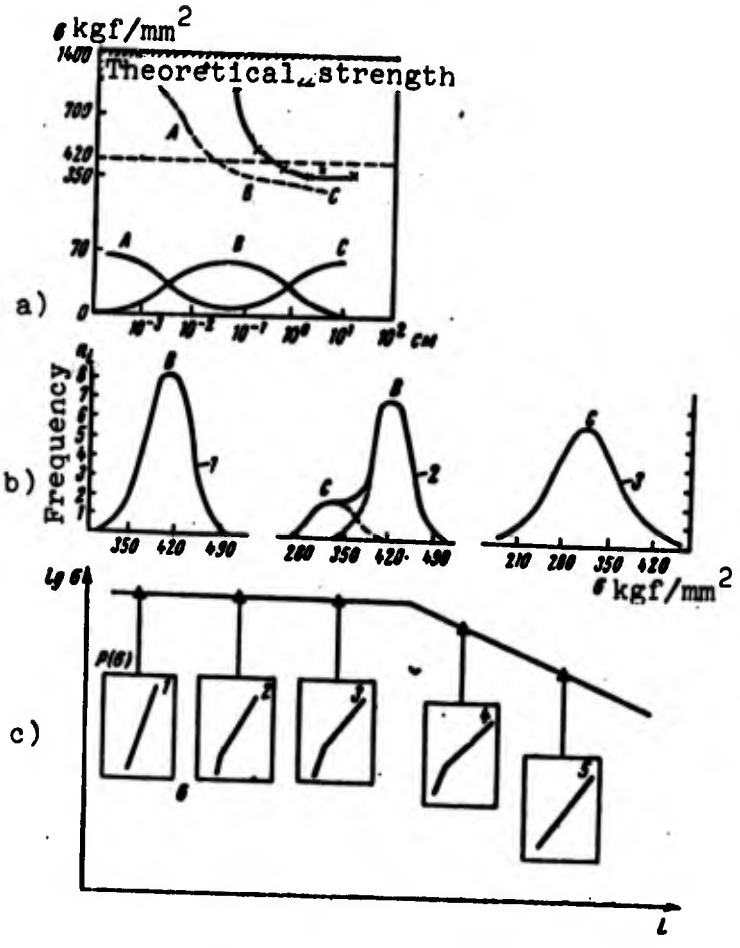

Figure 6. Regions of defect occurrence.

a — theoretical and experimental dependence of strength on length; b — influence of defects on probability density curves for the strength limits of glass fibers of length 0.05 cm (1), 0.25 cm (2), and 1.5 cm (3); c — integral curves of glass fiber strength limit distribution in the presence of defects of two types.

has a single maximum, the corresponding integral curve 5 (Figure 6c) has no break, and its slope differs from that of curve 1. With increase of the length, the curves shift in the direction of lower breaking stresses, and the minimum strength values can be found by testing long fibers in accordance with the hypothesis of weak-link strength [182, 206].

The mixed distributions 2, 3, 4 (Figure 6c) are easily identified graphically. Figure 7a shows the integral curve for S-glass fibers 7 cm long, which has a break. The strength of ~30% of the fibers is

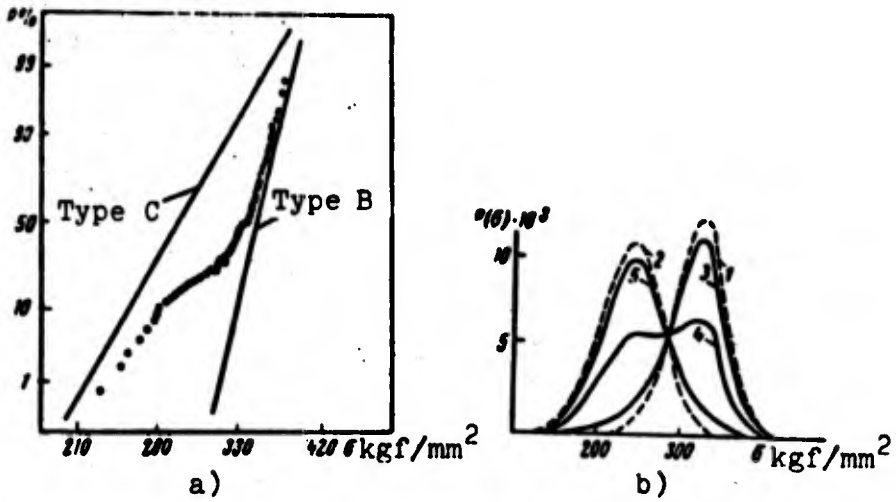

Figure 7. Experimental curves of tensile strength limit distribution of glass fibers.

a — integral strength distribution curves of S-glass monofilaments (l = 7 cm, ε = 0.006 min^{-1}); b — curves of strength probability density of 10 μ diameter monofilaments: 1 — 3 mm; 2 — 10 mm; 3 — 50 mm; 4 — 150 mm; 5 — 400 mm.

determined by C defects while that of ~70% is determined by type B defects. A similar result was obtained in analyzing the data for E-glass [189]. The probability scale along the ordinate axis was taken in accordance with the normal distribution law.

Bartenyev [19] proposed an analytic description for the fiber strength distribution functions in the presence of defects of the three types. In Figure 7b we see the transition from the distribution with a single maximum for short fibers to the analogous distribution for long fibers through the mixed distributions. In the presence of all three defects, the experimental curve has a single maximum rather than three. This is explained by the fact that the strength level of the larger portion of the defects is equal to σ_b, which is reflected on the distribution curve in the form of a single maximum corresponding to this level. The scatter of the breaking stress magnitudes does not permit identifying the other two maxima.

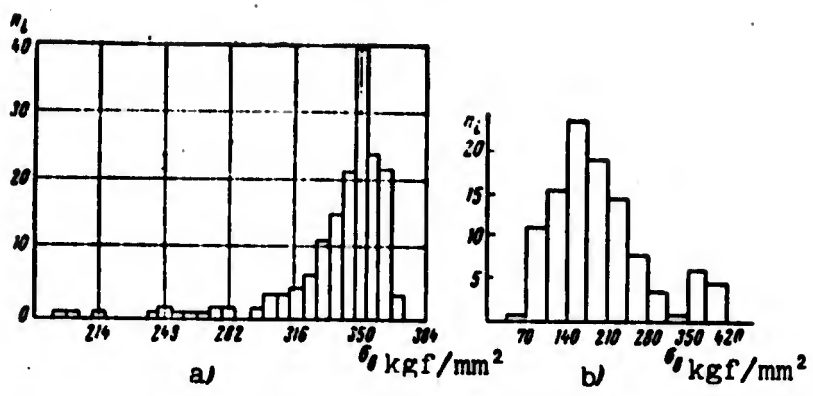

Figure 8. Histograms of glass fiber strength limit distribution.

More reliable statistical data [153, 181] show that the monofilament strength distribution curves are, as a rule, asymmetric. Testing of fibers of other types (1000 specimens) also yielded an asymmetric distribution curve [158]. Figure 8 shows strength distribution histograms of E-glass fibers of diameter 12 microns ($\bar{\sigma}_b$ = 340 kgf/mm², v = 9%) (178 tests) [181] (a); and 25 microns ($\bar{\sigma}_b$ = 192 kgf/mm²) (206 tests) [153] (b).

In analyzing large-scale fiber strength tests, Wollhaus [65] found that the experimental data are approximated well by straight lines in the coordinates

$$\ln \ln \frac{1}{1-P(\sigma)} - \ln(\sigma_0 - \sigma_u),$$

corresponding to the Weibull distribution, where $P(\sigma)$ is the cumulative probability; σ_u is the minimal strength observed experimentally for $P(\sigma) \approx 0$. The distribution function slope characterizes the fiber strength limit scatter and depends on the fiber surface damage. Figure 9 shows monofilament strength distribution curves for $\sigma_u = 0$.

For a sufficient number of tests, the breaks in the curves resulting from the presence of defects show up clearly in the Weibull coordinates. Figure 10 shows the data from 206 tests of fibers in the coordinate grid

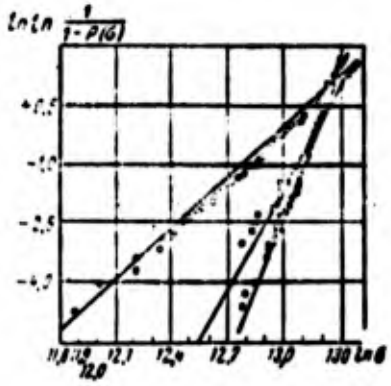

Figure 9. Statistical distributions of glass fiber strength corresponding to different fabrication regimes [65].

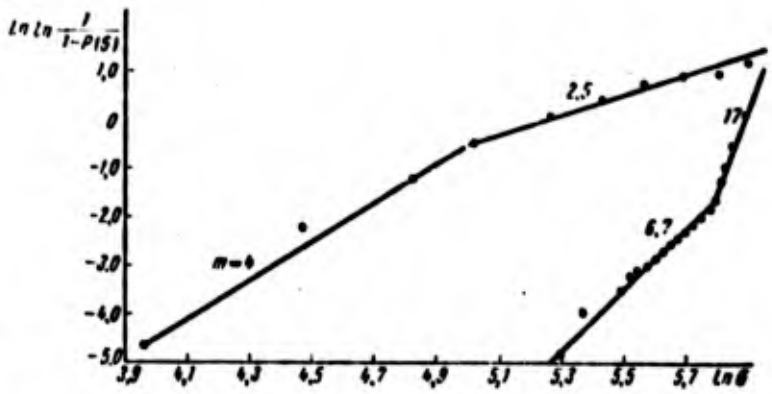

Figure 10. Strength distribution curves for fibers with various defects whose histograms are shown in Figure 8.

$$\ln\ln\frac{1}{1-P(\sigma)}-\ln\sigma$$

where defects of two types are seen (exponent m = 4 and 2.5). Also shown are the analogous data of [181] for which the exponents m are equal to 6.7 and 17. According to the experimental data, the coefficients of variation of the static strength of industrial glass fibers are equal to 10 - 50%, depending on the fiber production and treatment conditions.

§3. Influence of Time on Glass Fiber Strength

The data on time dependence of glass fiber strength and deformability are limited. At normal temperatures and normal humidity (~50%), glass and glass fibers are brittle materials; the influence of time on the strength is slight and is explained primarily by the chemical action of the adsorbed moisture. As a rule, in a vacuum, no strain rate effect is observed.

Let us examine the results of studies [190] of the fracture of E-glass of diameter 10μ and length 25 mm. The equation for the curve of long-term glass fiber strength is a power function of the stress [16, 190]:

$$\sigma^n \tau = \text{const.} \tag{9}$$

The cracking (loss of specimen load-carrying area) velocity is

$$v = \kappa_1 \sigma^n + v_0, \tag{10}$$

where k_1 is a constant; σ is the nominal stress; n is an exponent; v_0 is the cracking velocity for zero stress.

The velocity v is a function of temperature in accordance with fracture process activation theory [121]; the fracture process activation energy at normal temperature for glass is about 20 kcal/mole.

Long-term static fracture takes place in two stages. Initially, cracks develop from existing defects — this is the incubation period, which lasts for 90 - 95% of the overall life, then fast fracture of the glass fibers starts at an increasing rate (Figure 11). The second segment is not described by a power function with constant exponent n with change of the stress level [190]. However, correlation analysis of the experimental data in constructing the relation lg σ - lg τ shows that it can be taken to be linear. For fibers of different types, n - 16 - 26. For such values of n, the difference between the power relation and the exponential relation which follows from fracture activation theory [190] is not significant.

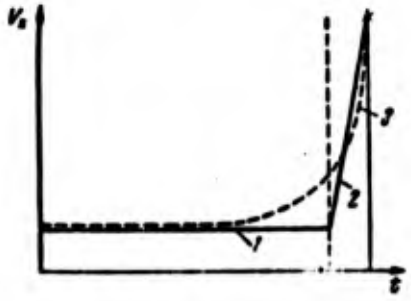

Figure 11. Glass fiber fracture process for long-term static loading.
1 — incubation period; 2 — fast fracture; 3 — theoretical relation based on (10).

The stress level has a marked influence on the glass fracture process [13]. In the case of higher stresses, the crack opening is greater; therefore, moisture penetration into the depth of the microscopic cracks is facilitated and the relative influence of the ambient medium increases. Under the action of small loads in atmospheric conditions, the glass fiber breaking energy corresponds approximately to

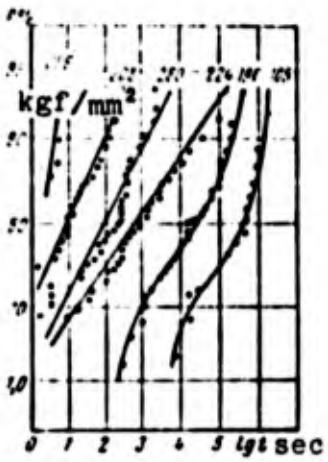

Figure 12. Monofilament life distributions for long-term static loading.

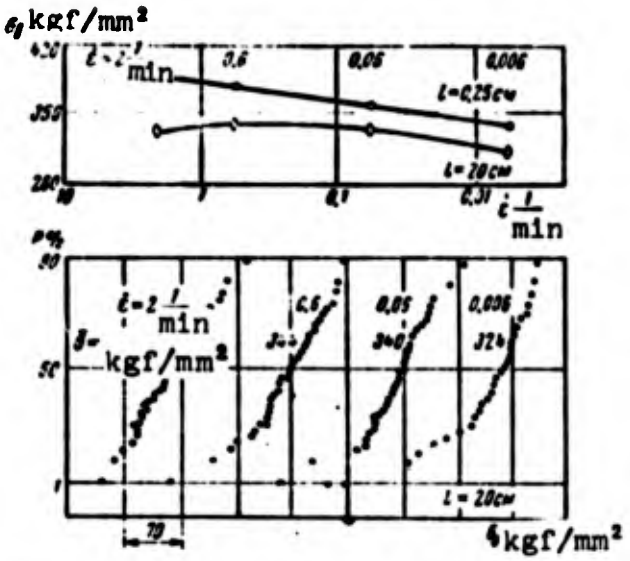

Figure 13. Monofilament strength as function of strain rate and strength limit distributions as function of strain rate parameter.

the magnitude of the free surface formation energy. This confirms the possibility of variation of the exponent n of the long-term strength curve. For high stresses, the distribution of the logarithms of the life follows the normal law (Figure 12). In the region of low and high probabilities for the low stress levels, we observe deviations of the points from the straight lines, indicating the existence of upper and lower life thresholds.

The scatter of the lifetime depends very weakly on the stress level, which justifies the use of linear correlation analysis for analyzing the results of long-term fiber strength tests.

The influence of strain rate on the strength of glass fibers 0.25 to 20 cm long, is shown in Figure 13, which also shows the corresponding strength limit distribution curves for constant strain rates; the average value of the stress is noted and the scales are shown along the abscissa axis. Characteristic of these data is increase of the scatter with decrease of the strain rate and approach to the minimum strength values (appearance of sensitivity threshold with respect to stresses). With increase of the length, the strain rate effect diminishes, which is apparently due to defects on the

surface of the longer fibers. The available experimental data for fibers show (Figure 13) that there is a linear relationship between the strength and the logarithm of the strain rate.

From the test results for regimes $\dot{\varepsilon}$ = const and $\dot{\sigma}$ = const, an evaluation was made of the lifetime summation condition. Table 2 shows the calculation sequence for the rate $\dot{\varepsilon}$ = 0.06 1/min. Determination of the sum of the relative lifetimes showed that for glass fibers, we can take $\sum \frac{\tau_{\sigma_i}}{(\tau_{\sigma_i})_p} = 1$, where τ_{σ_i} is the time of action of the stress σ_i; $(\tau_{\sigma_i})_p$ is the lifetime from the long-term strength curve for the given stress level σ_i. The lifetimes were summed from the experimental long-term strength curve and a linear $\sigma - \varepsilon$ relation for the fibers, where ε increases in proportion to the time.

TABLE 2

COMPARISON OF GLASS FIBER LIFETIMES IN LONG-TERM STRENGTH REGIME AND FOR LOADING WITH CONSTANT STRAIN RATE

Range of σ in kgf/mm²	Average Fracture Time for σ = const $(\tau_{\sigma_i})_p$ in sec	Time τ_{σ_i} in Tension Experiment for $\dot{\varepsilon}$ = 0.06 min⁻¹, in sec	$\frac{\tau_{\sigma_i}}{(\tau_{\sigma_i})_p}$	Total Time in sec
0–70	10^6	10	0,0000[illegible]	—
70–140	$3 \cdot 10^5$	10	0,0[illegible]	0,0000[illegible]
140–210	$5 \cdot 10^4$	10	0,[illegible]	0,0[illegible]
210–280	$1{,}2 \cdot 10^3$	10	0,[illegible]	0,00[illegible]
280–294	$5 \cdot 10$	2	0,0[illegible]	0,00[illegible]
294–308	15	2	0,1[illegible]	0,01[illegible]
308–322	5	2	0,[illegible]	0,18[illegible]
322–336	2,2	1	0,[illegible]	0,58[illegible]
		In all		1,0[illegible]

Elastic effects are essentially absent for glass fibers at normal temperature and relative humidity (~50%), and the glass fibers behave in tension like brittle elastic bodies. The magnitude of the inelastic deformations reaches hundredths of a percent. Even in the

presence of nonpolar ambient media [3], the after-effect deformations for stresses up to 140 kgf/mm^2 are completely reversible. The elastic aftereffect in glass fibers is explained by the combined action of stress and the ambient medium on surface defects in the fibers [3].

§4. Strength of Glass Fiber Bundles

A composite consisting of parallel fibers and a matrix can be considered a bundle of connected fibers. In the first approximation, the strength of such a material is determined by the maximum load which the aggregate of reinforcing fibers (disconnected bundle) can withstand. Failure of a fiber bundle was apparently first analyzed in [130, 182].

Equilibrium of the bundle is possible if, for a small load, none of the fibers break, or in the process of sequential breaking of the weak fibers, a point is reached where the remaining fibers support the existing load; otherwise, the redistribution of the load between the remaining N - 1 and so on fibers leads to their sequential failure.

The material of the glass reinforced plastic type is a statically indeterminate system of N fibers, whose strengths and loadings are characterized by random deviations. Then, the load on the bundle is, in general form

$$Q = N\int_{\varepsilon}^{\bar{\varepsilon}} d\varepsilon_0 \int_{0}^{\bar{E}} f(\varepsilon, E)\,\psi(\varepsilon_0, E)\,dE. \qquad (11)$$

where N is the initial number of fibers in the bundle; f(E, ε) is a function of the load on the fiber; $\int_{\varepsilon}^{\bar{\varepsilon}} d\varepsilon_0 \int_{0}^{\bar{E}} \psi(\varepsilon_0, E)\,dE$ determines the number of fibers remaining at the moment of reaching the quasi-equilibrium state.

If the load-deformation curves for all the fibers are identical in form and differ in scale, the ratios between the stress in the fiber and its strain correspond to Hooke's law, the probabilities of the quantities E and ε_b are independent, then in the simplest case we can take the stress distribution in the bundle to be uniform, considering the variance of the elastic modulus small and the law of plane sections valid.

The connection between the overall load Q_i on the bundle and the load q_i on the i^{th} individual fiber, will be

$$Q_i = N q_i \int_{q_i}^{\infty} p(q)\,dq. \tag{12}$$

where p(q) is the breaking load probability density for the fibers.

The breaking load Q_{max} for the fiber bundle with $q_i = q_{cr}$ is equal to

$$\frac{d}{dq}\left[q_{cr}\int_{q_{cr}}^{\infty} p(q)\,dq\right] = 0. \tag{13}$$

Equations (12) and (13) can be solved graphically as follows. If the probability of the fiber not exceeding the breaking load q is denoted by

$$P(q) = \int_0^q p(q)\,dq = a\left(\frac{1}{q}\right) = a(w), \tag{14}$$

where a(w) varies from 1 to 0 upon breaking of the fibers forming the bundle and characterizes the degree of bundle failure, then the load on the bundle is

$$Q = N\frac{1}{w}[1 - a(w)]. \tag{15}$$

hence, a(w) = 1 - (Qw/N), and for a constant force, there will be a linear relationship between a(w) and w in the coordinates a(w) - w (Figure 14). The line AB intercepts segments on the axes equal to 1.0 and 0, N/Q or 0, 1/q. The ordinates of the straight line yield

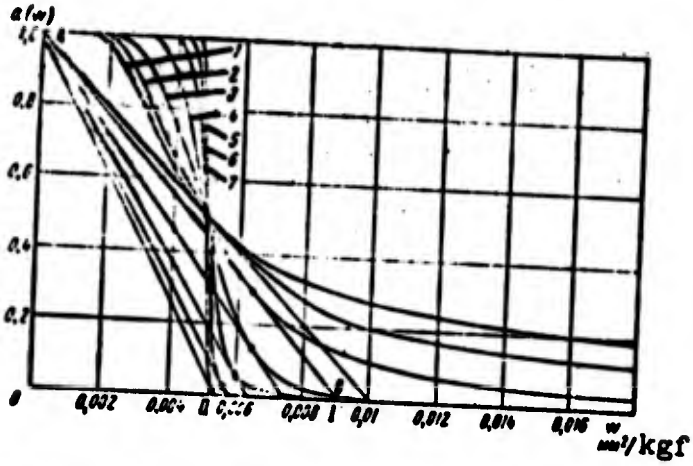

Figure 14. Maximum load on fiber bundle versus monofilament strength variance for constant average strength 200 kgf/mm² for normal distribution law.

the maximum permissible number of failed fibers in the bundle for a given stress level if we assume that condition (14) holds.

The conditions for determining the maximum load can be written in the form

$$Q = \frac{N[1 - a(w)]}{w}; \qquad (16)$$

$$\frac{d}{dw}\frac{[1 - a(w_{max})]}{w_{max}} = 0. \qquad (17)$$

From the curve of statistical fiber strength distribution (Figure 14), we can find the number of fibers actually broken for the load levels q_1. Up to the point I for a load Q on the bundle, the fraction $Na(w_I)$ of the fibers breaks and equilibrium occurs, since the strength of the remaining filaments is sufficient to withstand the load Q. Therefore, the additional number $N[a(w_{II}) - a(w_I)]$ of the fibers can break; and, at the moment II, on each fiber there will act the load $q_{II} = 1/w_{II}$. In the interval $a(w_{II}) - a(w_I)$, a series of quasi-equilibrium states occurs.

Curve	σ_{cr} in kgf/cm²	•	a (w)
		in %	
1	200	80	50
2	177	68	42.5
3	156	48	30
4	136	28	14
5	118	16	5.5
6	110	8	2.5
7	108	2.5	1.0

Upon additional failure of even a single fiber, complete failure of the fiber bundle occurs. The maximum load on the bundle corresponds to the point of tangency of the straight line AB (with increase of the load the line rotates) to the fiber strength distribution curve for $w = w_{max}$. The points w_I, w_{II} correspond to (16) and the point w_{max} corresponds to (17).

In [130] it was shown that, for large N and any fiber strength distribution function, if the fiber failure probability P(q) is such that I - P(q) approaches zero faster than 1/q, the average bundle breaking stress distribution approaches asymptotically the normal distribution with the mathematical expectation

$$\bar{q}_0 = q_{max}[1 - P(q_{max})] \tag{18}$$

and the mean-square deviation

$$s_{q_0} = q_{max}\sqrt{\left\{\frac{1}{N}P(q_{max})[1 - P(q_{max})]\right\}}. \tag{19}$$

The maximum stress in the fiber is obtained by maximizing the quantity represented in the form of the product of the force in the fiber by the number of unfailed fibers

$$\frac{d}{dq}[q[1 - P(q)]]_{q=q_{max}} = 0. \tag{20}$$

In determining the breaking load on a small bundle, knowing the fiber strength limits, we can — after expanding the breaking loads into a variational series in decreasing order:

$$q_1 > q_2 > q_3 > \cdots > q_n \tag{21}$$

— write the equilibrium condition in the form $Q \leq q_r r$, where r is the sequential number of the filament in the series. Then the maximum load will be

$$Q_{max} = \max [rq_r]. \tag{22}$$

An illustration of this simple rule is the test results presented in [130] (Table 3).

TABLE 3

DETERMINING BREAKING LOAD FOR BUNDLE WITH SMALL NUMBER OF FIBERS

Tensile force q in g	8.2	6.1	5.7	5.2	4.4	3.3
Number of unfailed fibers r	1	2	3	4	5	6
Load on bundle $q_r r$	8.2	12.2	17.1	20.8	22.0	19.2

The maximum load for the bundle is equal to 22. This rule is also valid for quite large numbers of fibers. Data on tests of E-glass fibers are presented in [181] (Table 4 and Figure 15). The values in Table 4 and Figure 15 agree quite well.

TABLE 4

EXAMPLE OF DETERMINING BREAKING LOAD FOR E-GLASS FIBER BUNDLE

Number of unbroken fibers in bundle	178	17,7	176	175	174	172	171	170
Strength levels in kgf/mm^2	186	193	200	214	220	249	256	263
Load in kgf/mm^2·f	33 100	34 200	35 200	37 400	38 200	42 800	43 700	44 700
Number of unbroken fibers in bundle	169	167	165	164	162	158	149	140
Strength levels in kgf/mm^2	270	276	284	291	298	305	312	319
Load in kgf/mm^2·f	45 600	46 100	46 900	47 700	48 300	48 200	46 500	45 300
Number of unbroken fibers in bundle	130	114	92	52	27	4		
Strength levels in kgf/mm^2	326	333	340	347	354	361		
Load in kgf/mm^2·f	42 400	37 900	31 300	18 100	9550	1470		

Here f is the area of a single fiber.

Figure 14 shows curves of the strength distribution of fibers with different variance, on the basis of which we can find the maximum load which a bundle can support. Curves 1, 2, 3 characterize fibers

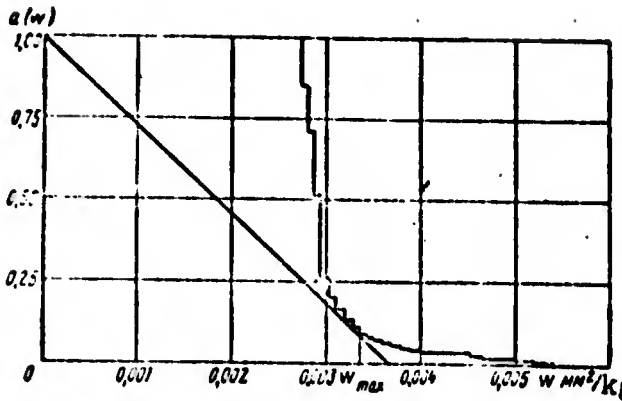

Figure 15. Graphical determination of maximum load on bundle consisting of 178 E-glass fibers.

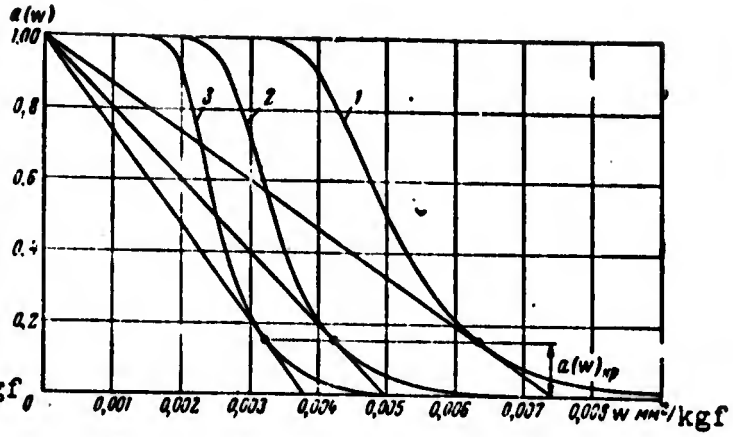

Figure 16. Maximum load on fiber bundle versus average monofilament strength for constant variance ($v = 20\%$, $a(w)_{cr} = 15\%$).

with the same average strength and coefficients of variation 10, 20, and 40%, with normal distribution law; with increase of the fiber strength variance, the maximum load on the bundle decreases by 14 and 25%. Figure 16 shows fiber bundle strength distribution curves for average strengths of 200, 300, and 400 kgf/mm² and 20% coefficient of variation. Analysis of Figures 14 and 15 shows that with increase of the variance, the number of damaged fibers increases; for constant variance, the degree of failure at the moment of reaching the maximum load is practically constant.

Curve	$\bar{\sigma}$	σ_{cr}
	in kgf/mm²	
1	200	156
2	300	226
3	400	312

The failure of a bundle of parallel fibers was analyzed by Bartenyev [20] for the normal fiber strength distribution. The maximum force

$$Q_{max} = N q_{kp} \int_{q_{kp}}^{\infty} p(q)\,dq \qquad (23)$$

and the nominal load on a fiber in the bundle at the moment of fast fracture initiation

$$q_n = \frac{Q_{max}}{N} = q_{kp} \int_{q_{kp}}^{\infty} p(q)\,dq \qquad (24)$$

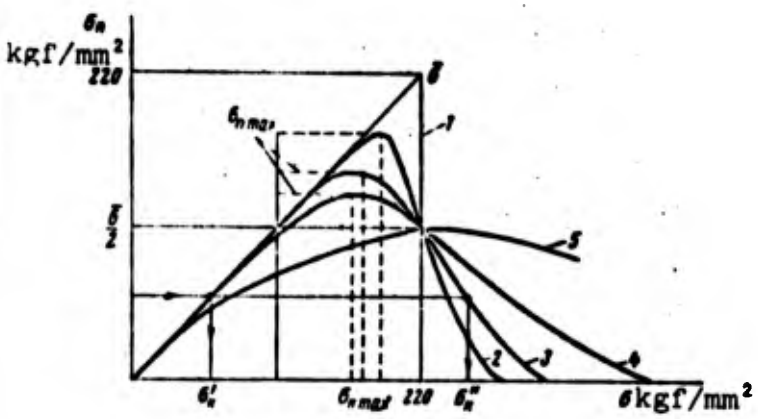

Figure 17. Equilibrium stress σ_k in glass fibers versus applied load Q for different values of the variation coefficient v:
1 — 0%; 2 — 8.8%; 3 — 17.6%; 4 — 31%; 5 — 80%.

were determined from the maximization condition

$$\frac{dQ}{dq_{cr}} = \int_{q_{cr}}^{\infty} p(q)\,dq - q_{cr}p(q_{cr}) = 0. \quad (25)$$

This equation is an implicit function of q_{cr} and can be solved graphically or by trial and error. The relation obtained in [20] between the nominal stresses in the fibers and the effective stresses

$$\sigma_n = \sigma \int_{\sigma}^{\infty} p(\sigma)\,d\sigma. \quad (26)$$

is shown in Figure 17 and makes it possible to find the stresses corresponding to the moment of maximization of the effective load on the bundle as a function of monofilament strength variance. The curves 1 - 5 correspond to the respective coefficients of variation 0, 10, 18, 30, and 80%. The indices σ'_k and σ''_k show the interval of possible equilibrium states and the stress $\sigma_{k\ max}$ is the breaking point. Regardless of the magnitude of the variance, the curves 1 - 5 cross at the point $(\bar{\sigma}, \bar{\sigma}/2)$. Hence, it follows that any bundle will withstand the load yielding the nominal stresses $\bar{\sigma}/2$. Thus, the minimum load

$$Q_{min} = \frac{\bar{\sigma}}{2} Nf,$$

where f is the area of a single fiber; $\bar{\sigma}$ is the average strength of the fibers in the bundle.

Chapter 5

STRENGTH OF GLASS REINFORCED PLASTIC AS A REINFORCED COMPOSITE

§1. Stress State of Components in Regular Glass Reinforced Plastic [GRP] Structures

The basic phenomena which determined the stresses in a reinforced polymer matrix will be examined on models with a certain periodic arrangement of the fibers. Then we shall analyze the stress state of composite material structural elements in connection with external loading and thermal and shrinkage phenomena.

Theoretical and experimental studies [74, 119] have shown that stresses arise at the fiber-matrix interface both during composite solidification as a result of difference in glass fiber and matrix thermal expansion coefficients, and under the influence of external loading because of the different Poisson's ratios of the matrix and the fibers.

Polarization-optical studies of models of glass-fiber composite cells made from one, two, and several fibers have made it possible to establish that, for an epoxy matrix at the solidification temperature 130° C, the chemical shrinkage stresses are not large (1.5 - 2.0 kgf/cm^2). The magnitude of the residual shrinkage stresses depends on the thermal regimes: heating and cooling rates, polymerization temperature, and duration of polymer exposure at this temperature.

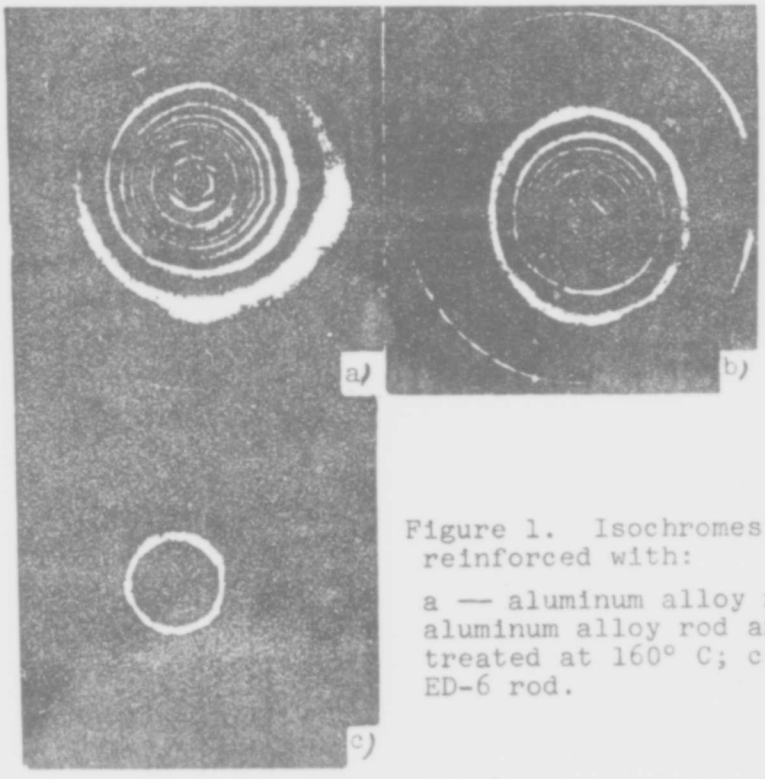

Figure 1. Isochromes for polymer reinforced with:

a — aluminum alloy rod; b — aluminum alloy rod and re-heat-treated at 160° C; c — hardened ED-6 rod.

Slight relaxation (by about 10%) of these stresses can be achieved by re-heat-treatment. It has been shown experimentally that the basic factor in residual stress formation is thermal shrinkage in the solidification process, and also the mutual influence of nearby fibers.

The stress state of the matrix is characterized by compressive radial stresses and tensile tangential and axial stresses σ_r, σ_θ, σ_z. The residual stresses σ_r depend linearly on the difference between the thermal expansion coefficients of the glass fibers and the polymer matrix. Figure 1 shows the isochromes after solidification of a model reinforced by a single rod. For the epoxy matrix, the radial stresses are equal to 110 kgf/cm^2; the tangential and axial stresses are, respectively, 125 and 185 kgf/cm^2. The residual stresses reach their maximum values at the fiber-matrix interface and are close to zero at a distance of 3 - 4 radii from the fiber.

Figure 2. Isochromes for two closely positioned reinforcing rods.

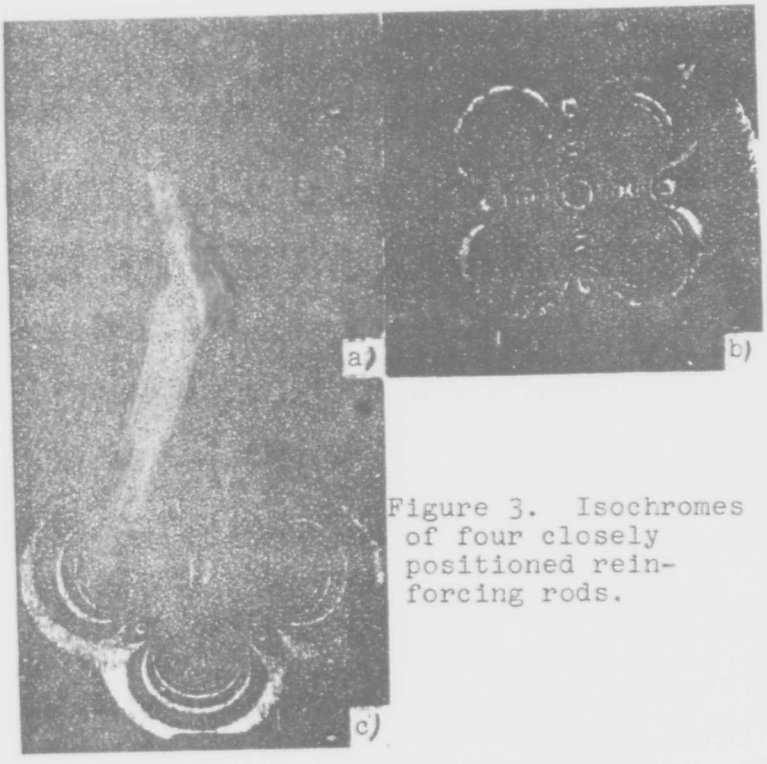

Figure 3. Isochromes of four closely positioned reinforcing rods.

In the case of reinforcing by means of two rods, the mutual influence effect arises, and the stress state of the matrix between the fibers is determined by superposing the diagrams for the case of reinforcing by single fibers (Figure 2). With reduction of the distance between the fibers, the mutual influence effect increases, which is confirmed by the isochromes for a model with four reinforcing elements (Figure 3).

The model parameters were selected to simulate glass-reinforced-plastics with 55(a), 40(b), and 35%(c) fiber content by volume. For the model (Figure 3a, b, c) the matrix stress-strain state is characterized by large stress gradients. Most highly stressed is the segment between the two neighboring fibers because of stress fields interaction at the neighboring fibers. For a distance between the fibers corresponding to a reinforcement ratio 80 - 85%, the equivalent (based on max elongation theory) residual stresses amount [74] to 78 - 86% of the binder breaking strength. The distribution of the principal stresses across the section of the cell is shown in Figure 4. In section CD, the stress σ_θ changes sign as we approach the center of

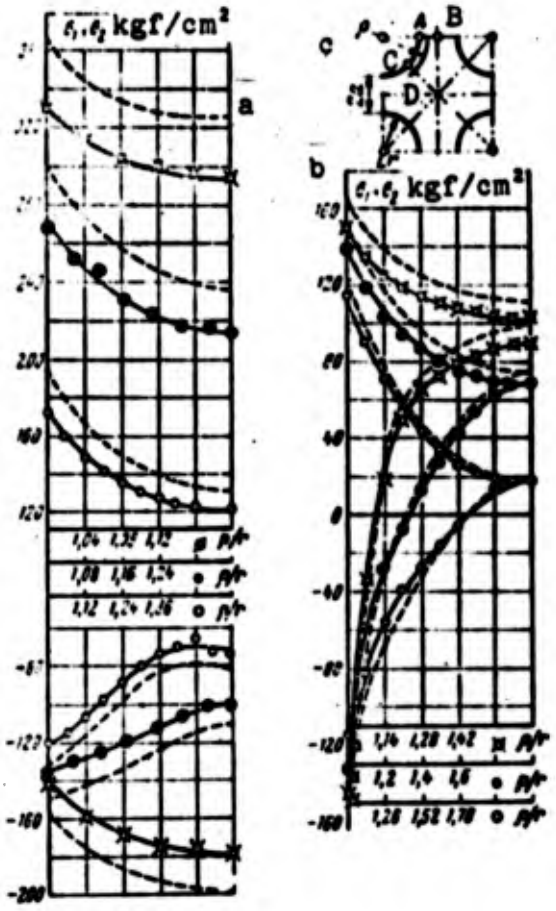

Figure 4. Principal stress distribution.

a — through section AB; b — through section CD of elementary cell; c — Oi - 2a = 6 mm; ●2 - 2a = 4 mm; ■3 - 2a = 2 mm for unidirectional glass-reinforced-plastic.

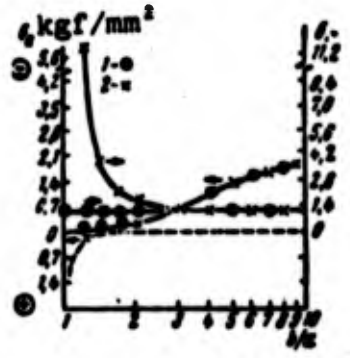

Figure 5. Variation of axial and radial stresses in GRP as a function of the distance between fibers.

the polymer cell, where the stresses $\sigma_\theta = \sigma_r$. Because of the mutual influence, the stresses in the section CD also depend significantly on the fiber packing density.

Figure 5 [118] shows the axial and radial residual stresses versus fiber packing density, defined by the ratio b/a, where a is the fiber radius, b is the radius of the inscribed circle of the matrix for hexagonal positioning of the fibers. For b/a = 1, the fibers touch (limiting case of dense packing). For typical composites, the glass content amounts to 25 - 65% of the volume, and the ratio b/a varies in the range 1.9 - 1.2. Figure 5 shows curves for two cases: $1 - p = \text{const}\ \frac{a^2}{b^2}$; $2 - p = \text{const}\left[\frac{a^2}{\rho^2} + \frac{a^2}{(2b-\rho)^2}\right]$.

Case 1 is characteristic for a fiber surrounded by an infinite matrix; case 2 accounts for the influence of adjacent fibers. The curves are plotted for a composite using a polyester matrix and

polymerization temperature 75° C. Radial residual and axial tensile residual stresses in the resin of 210 and 140 kgf/cm² were obtained for the polyester glass-reinforced-plastic with volumetric fiber content ~50%. The initial stress state leads to the appearance of tangential stresses at the locations of random fiber failure; however, as Sutton [198] has shown, at the fiber ends these stresses do not exceed 10% of the axial stresses in the matrix, therefore the tangential stresses in the matrix are small in this case.

The approximate values of the radial stresses arising upon temperature change [119] are found from the formula

$$\sigma_r = \Delta T \frac{(\alpha_m - \alpha_a) E_m}{(1 + \nu_m) + (1 - \nu_a) \frac{E_m}{E_a}},$$

where α_m and α_a are the linear expansion coefficients of the resin and fibers; ν_m and ν_a are the corresponding Poisson's ratios.

These stresses can be estimated by examining the numerical values of the parameters for a polyester binder and glass fiber ($\alpha_m = 10 \cdot 10^{-6}$; $\alpha_a = 0.5 \cdot 10^{-6}$ 1 °C; $\frac{E_m}{E_a} = 0.059$; $\nu_a = 0.22$; $\nu_m = 0.34$), hence $\sigma_r = 2.94\Delta T$ kgf/cm². It has been shown experimentally [176] that, upon heating a reinforced polymer to some temperature, the residual stresses σ_r can be reduced to zero; upon cooling they arise again. For the epoxy composite, this temperature is 120 - 130° C, and is close to the polymerization temperature. The influence of solidification temperature on the residual stress magnitude for the polyester composite was characterized in [33]. With an increase of the polymerization temperature, the stress state in the binder was evaluated from the isochromes; the stress state increased markedly. In this case, the condition of the fiber surface also is of definite importance. For coated fibers, the stresses in the binder are large [33]; the smallest residual stresses arise in models with fibers whose surface is coated with a lubricant.

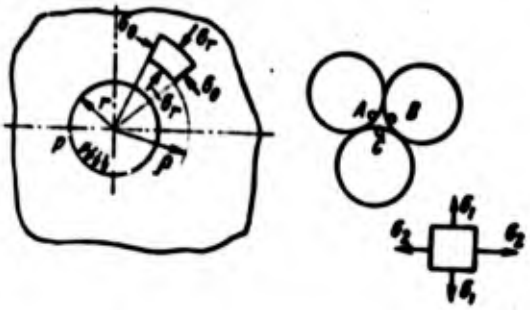

Figure 6. Stresses in matrix under axial tension of composite for nondense and dense fiber packing.

Figure 7. Radial stresses in matrix as a function of Poisson's ratio of the material.

1 — extremely dense packing; 2 — hexagonal dense packing; 3 — nondense packing.

Under the action of the external load, secondary radial stresses which depend on the relationship between the coefficients of transverse strain of the reinforcement and matrix, which can be calculated approximately [29] for a given axial deformation, arise at the interface between the fiber and the matrix. Borzova [29], studying the tension problem for a viscoelastic medium filled with glass-fiber rods, showed that in the transverse section plane the stress distribution depends only on the reinforcement and matrix Poisson's ratios and the viscosity characteristics.

Two fiber packing cases were analyzed in [118, 119]: nondense and dense packing, when the binder forms between the contacting fibers a closed volume in the form of a triangular curvilinear prism. Positive radial stresses, which decay with increase of ρ (Figure 6), and also tangential stresses of reversed sign arise at the interface under the action of compressive loading [119]

$$\sigma_r = -\varepsilon \frac{(\nu_m - \nu_a) E_a E_m}{(1+\nu_m) E_a + (1-\nu_a-2\nu_a^2) E_m} \cdot \frac{r^2}{\rho^2}; \qquad (1)$$

$\sigma_\theta = -\sigma_r$, where ε is the axial strain; r is the fiber radius.

The maximum values of these stresses can be related with the axial stresses σ_{mz} in the matrix from the external force

$$\sigma_r = -\sigma_{zz}\frac{(\nu_m - \nu_a)E_a}{(1+\nu_m)E_a + (1-\nu_a-2\nu_a^2)E_m};$$
$$\sigma_\theta = -\sigma_r. \qquad (2)$$

which yields for the subject polyester composite the quantitative relation

$$\sigma_r = -0{,}0707\sigma_{zz}.$$

In many cases, the occurrence of tensile radial stresses at the fiber-matrix interface during compression (negative axial strain) apparently leads to lower values of the strength in comparison with tension. Under the action of tensile stresses, a compressive stress σ_r arises, which combines with the residual stress to increase the pressure of the matrix on the fiber and contributes to better adhesion of the fibers. The residual axial tensile stresses combine with the stresses from the external force, and in certain cases may cause failure of the polymer matrix.

For dense packing of the fibers in the case of axial elongation, we observe triaxial tension at all points of the polymer binder. The isochromes are arranged symmetrically relative to the center of the prism. The tensile stresses at points A, B, C (see Figure 6) reach ~350 kgf/cm^2 in the case of adhesive treatment of the fibers. An approximate estimate of the stresses in the matrix [118] can be made for a given axial strain ε from the relation

$$\sigma_r = \varepsilon\frac{(\nu_m - \nu_a)E_mE_a}{(1+\nu_a)E_m + (1-\nu_m-2\nu_m^2)E_a}. \qquad (3)$$

The following relation is proposed for intermediate fiber packing density cases

$$\sigma_r = -\varepsilon\frac{(\nu_m - \nu_a)E_mE_a(q-1)}{(1-\nu_m)E_aq + (1-\nu_m-2\nu_m^2)E_a + (q-1)(1-\nu-2\nu_a^2)E_m}, \qquad (4)$$

where q = 1.55 for conventional hexagonal packing.

The radial stresses at the fiber-matrix interface for dense and nondense packing are shown as a function of the matrix Poisson's ratio in Figure 7, where the ordinate axis is the ratio of the radial stresses to the axial stress in the matrix. The curve for nondense packing (b/a > 3) shows that for the typical resin Poisson's ratio (~0.34) the radial stresses are equal to $\sim 0.1\sigma_{mz}$, (and the sign of σ_r is opposite that of σ_{mz}). Curve 2 corresponds to dense fiber packing for the ratio b/a = 1.25, which corresponds to ~60% fiber volumetric content. In this case, $\sigma_r = 0.05\sigma_{mz}$. Curve 1 was plotted for the limiting dense packing case, when the fibers are in contact and the matrix lies in closed regions between the fibers.

§2. Strength of Glass-Reinforced-Plastic Elements as a Regular Structure

Experimental studies [105] have shown that the polymer matrix must provide compatible functioning of the reinforcing fibers in the deformation process and monolithicity of the material [3, 103]. The limiting states of the glass-reinforced-plastics are determined by the stress state and strength of their elements. They depend to a considerable degree on the combination of the mechanical properties of the fibers and matrix.

On the basis of the properties of the composite elements, we can formulate the following limiting state criteria:

a) with respect to fiber strength for large matrix elongation and high adhesive strength in shear;

b) with respect to matrix strength (formation of the first crack) for small matrix elongation;

c) with respect to shear resistance of the matrix with progressive failure of the fibers after preliminary breaking of the fibers to an inoperative length, and also as a result of tangential stress concentration because of reinforcement imperfection;

d) with respect to resistance to progressive crack growth, here we must also bear in mind the residual structural stress state in the composite.

Resistance to Interlaminar Shear

The shearing strength of the adhesive bonds between the fiber and the matrix shows up in progressive breaking of the fibers, at the ends of which shearing failure of the matrix is possible.

The resistance to interlaminar shear depends on several factors — first of all, the mechanical characteristics of the matrix. The following conclusions can be drawn from the data of [183], in which the influence of matrix strength on shear resistance was examined. For low polymer matrix tensile strength (up to 400 kgf/cm^2) the resistance to interlaminar shear increases linearly with increase of the matrix strength. In this case, other conditions being the same, the composite strength is determined by the tensile strength of the matrix. Further increase of the matrix tensile strength does not lead to any significant increase of the limiting tangential stresses, whose growth terminates for a matrix strength of 650 - 800 kgf/cm^2. The maximal value of τ_{sh} is ~700 kgf/cm^2 (Figure 8), regardless of fiber type. The experimental data were obtained for E-glass and S-glass with surface treatment using the HTS preparation for a polymer matrix based on a combined epoxy-polyester resin. The specimens were fabricated from wound rings, and the shear resistance was determined in transverse bending of a specimen of dimensions l/h = 16/3 with resin weight content ~14%. The data on resistance to interlaminar shear for certain fiber and matrix combinations are shown in Table 1.

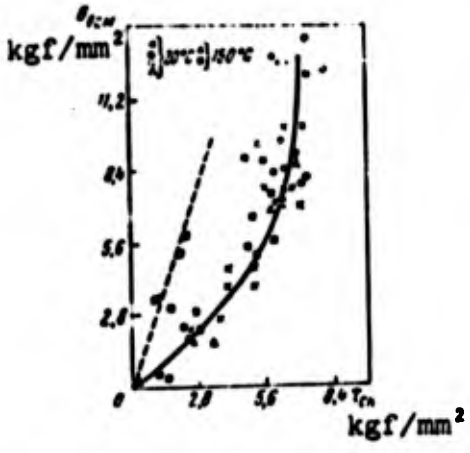

Figure 8. Limit tangential stresses of composite versus tensile breaking stress of epoxy (solid curve) and phenol resins.

TABLE 1

INTERLAMINAR SHEAR STRENGTH FOR SOME MATRIX AND FIBER COMBINATIONS

Matrix	Matrix Tensile Strength in kgf/mm²	Type of Glass Fiber	Shear Resistance in kgf/mm²	Resin Content by Weight in %	Voids in %
ME-1	7,7	E-HTS	5,6	—	—
			6,6	13,2	1,8
		E-801	5,0	12,0	2,0
ME-25	2,7	E-HTS	3,5	—	—
		E-801	3,1	12,5	1,9
ME-115	4,5	E-HTS	4,0	—	—
		E-801	3,0	12,0	1,3
ME-118	2,1	E-HTS	2,4	—	—
ME-144	4,5		4,6	11,8	2,2
ME-159	7,6		6,4	—	—
ME-160	10,0		7,2	13,3	2,1
			6,4	13	—
		E-801	5,5	11	2,9
ME-172	3,8	E-HTS	5,1	13,3	—
			4,0	11,8	—
ME-206	7,7	E-801	1,5	12,7	2,8
		E-HTS	7,0	14,3	2,3
		S-HTS	6,0	13,8	—
			6,6	—	—
ME-230	12,6	E-HTS	6,0	14,5	4,8
		E-801	5,0	15,3	5,0

The type of fiber surface treatment influences the interlaminar strength. The reduction of shear strength growth as a function of matrix strength is explained by the presence of voids, whose percentage content determines to a considerable degree the shear resistance (see §5).

Without touching on the physical and chemical processes taking place at the fiber-matrix interface and affecting the adhesion of the resins to the fibers, we note that according to the latest studies [104] of Trostyanskaya et al. failure of the glass-reinforced plastics takes place, not along the glass-resin interface, but rather in the binder layer near the fibers (at a distance of 1 - 2 μ), where weakening of the binder strength is caused by the inhibiting action of the fibers on the binder solidification process. The fiber surface structure and their chemical composition affect the mechanical properties of the binder around the fibers and thus affect the interlaminar shear strength of the composite.

For the Soviet butvarphenolic binders [3], it has been found that with increase of the resin tensile strength in the 340 - 540 - 570 kgf/cm^2 range the adhesive strength increases, taking values of 100, 210, 240 kgf/cm^2.

The data of Table 2 characterize the influence of glass fiber surface modification on the shear adhesion strength and shearing strength. The shearing resistance corresponds quite well to the adhesive strength. The strength of the composite in bending increases markedly with increase of the shearing resistance; however, the composite tensile strength increases less sharply, apparently because of initial curvature of the glass fibers.

TABLE 2

STRENGTH OF GLASS-REINFORCED TEKSTOLITE AS FUNCTION OF TYPE OF GLASS CLOTH SURFACE TREATMENT

Strength in kgf/cm^2	Paraffin Lubricant	Heat Treated to Remove Lubricant	Volan	Vinyl Trieth-oxysilane	Alumino-ethoxysilane
Adhesion in shear	260	295	317	402	400
Shear	290	370	420	500	—
Bending at 20° C	4800	5000	5500	6470	6450
100° C	2400	3000	3800	4300	—
Tension at 20° C	—	3800	4000	4200	—

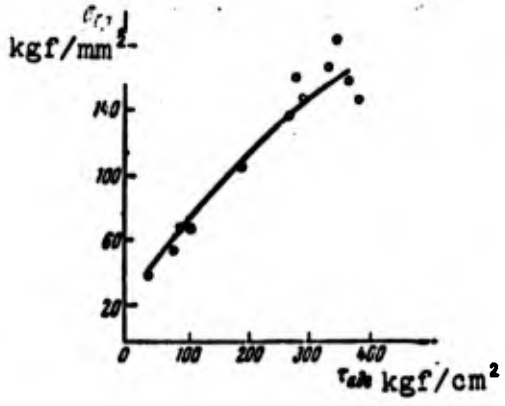

Figure 9. Adhesive strength versus tensile strength for composite.

For oriented composites without significant curvature of the fibers [38], the tensile strength increases with increase of the adhesion. Figure 9 shows a curve illustrating the relationship between the tensile strength of the oriented glass-reinforced plastics and the adhesive strength for different polymer matrixes. The magnitude of the adhesion of glass fibers which have not been treated with

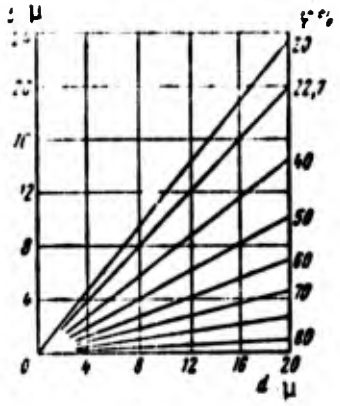

Figure 10. Polymer film thickness as function of fiber diameter and fiber content in material.

finishers depends on the resin type, and for the epoxy, epoxy-polyester, and phenol matrixes the average values of the adhesive strength are [4] 370, 300, and 190 kgf/cm^2. Glass fibers which differ in chemical composition have different adhesive strength in shear for the same matrix. For example, the alumoborosilicate, quartz, and quartzoid glass fibers with phenol-silicone matrix of the K-9F type have, respectively, an adhesive strength of 230, 170, and 136 kgf/cm^2, while for the phenol-formaldehyde matrix the strengths are 223, 217, and 148 kgf/cm^2.

The polymer film thickness influences the resistance to interlaminar shear, since the adhesion is determined by the thickness and continuity of the polymer film. Figure 10 shows the film thickness in an oriented glass-reinforced plastic as a function of glass fiber content and diameter [105]. We note that these values are approximate, since in reality there may be various defects and a disordered structure. For the glass-reinforced plastics with volumetric fiber content (~65%) the film thickness is 0.3 - 0.5d.

The results of bond joint shear tests [3] show that the bond strength in shear (in nominal stress units) decreases linearly with increase of the epoxy polymer film thickness (Figure 11).

One of the important factors determining the magnitude of the adhesion is the temperature. The temperature dependence of the resistance to interlaminar shear is quite marked, and apparently leads to the strong temperature sensitivity of reinforced plastic strength. The experimental data for an epoxy-polyester glass-reinforced plastic [160] and for adhesion of 10-micron-diameter fibers to a butvarphenolic matrix [3] are shown in Figure 12. The

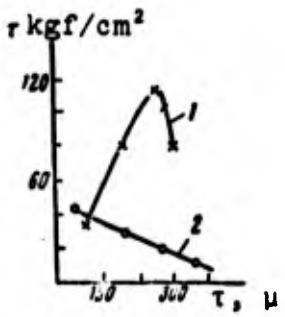

Figure 11. Tangential stresses τ(1) measured optically and shear strength τ_b(2) as a function of polymer film thickness.

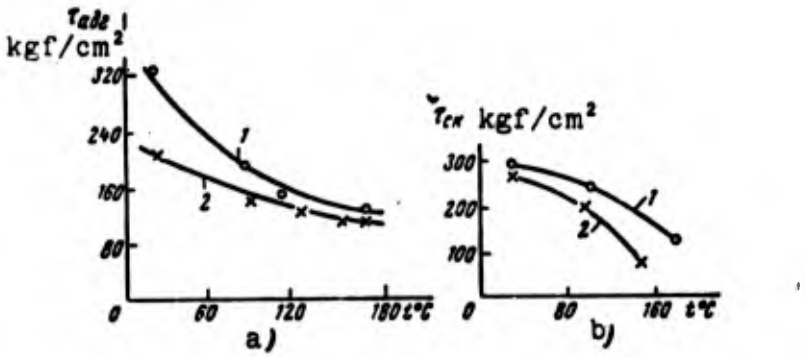

Figure 12. a — temperature dependence of adhesive strength of BF-4 matrix and nonalkali glass fibers for fiber diameter 10 - 12 microns, bond area $1 \cdot 10^{-2}$ mm²; 1 — from [105]; 2 — from [3]; b — temperature dependence of shear resistance for epoxy resins; 1 — solidification at 155° C for 3 hours [160]; 2 — at 100° C for 2 hours and 150° C for 2 hours [160].

weaker temperature dependence for the phenolic binder determines the higher thermal stability of the phenolic glass-reinforced plastics. The results of tests at high temperatures for an epoxy matrix and S-HTS fibers at 150° C, plotted on the curve of interlaminar shear resistance as a function of the matrix tensile strength, agree with the general relationship (see Figure 8).

The data characterizing adhesive and shear strength scatter in the case of composite delamination are limited. A curve of the breaking strength distribution (Figure 13) was presented in [4] for the adhesive strength of 10 - 15 μ diameter fibers. In laboratory tests, the coefficient of variation of the adhesive strength in shear for most of the polymer matrixes does not exceed 10 - 15% [4].

As a rule, the magnitude of the adhesion decreases with increase of the bond area [57]. It is difficult to evaluate the true stresses when testing speciments of existing structures in interlaminar shear; therefore, there is definite interest in examining this relationship on the basis of experiments with more uniform distribution of the stresses. When making bend tests of relatively short specimens using the transverse force loading scheme, shear failure takes place

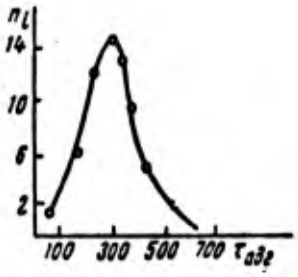

Figure 13. Adhesive strength probability density curve.

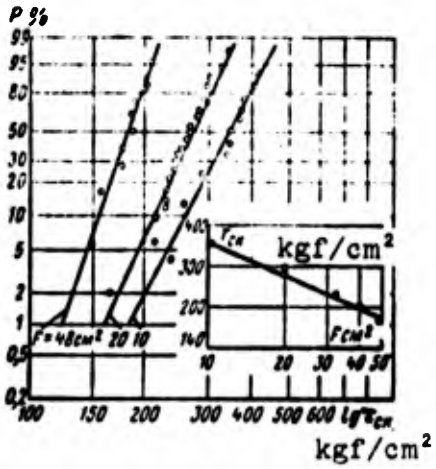

Figure 14. Integral curves of ultimate shear strength distribution for glass-reinforced plastic 33-18c (F = 48, 20, 10 cm²).

along a plane near the neutral axis. The magnitudes of the interlaminar shearing stresses as a function of area have been obtained for the AG-4c and 33-18c composites (Table 3). The ultimate stresses and coefficient of variation decrease with increase of the shear area.

TABLE 3

RUPTURE STRESSES FOR INTERLAYER SHEAR

Shear Area in cm²	Average Stress in kgf/mm²	Coefficients of Variation in %	l/h	b x h	Material
10	310	18.7	5		
20	260	28.7	10	20 × 10	
20	280	19.2	5		
33	230	19.0	10	20 × 20 30 × 10	33-18c
40	200	19.0	10		
48	180	10	12	20 × 20	
33	190	15	5		
41	170	10	11	30 × 20 20 × 20	AG-4c

The ultimate shear strength distribution curves (Figure 14) show the validity of the Weibull statistical distribution for describing resistance to fracture in interlaminar shear and its variability. The distribution parameters are: $m = 1.8$ $\tau_u = 135$ kgf/cm².

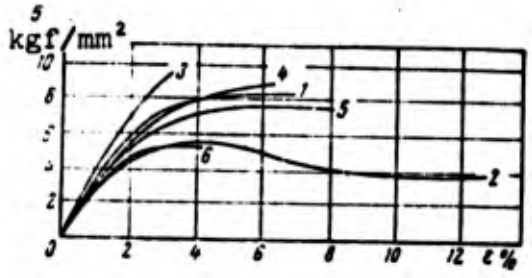

Figure 15. Polymer stress-strain curves.

1 — K-100; 2 — LMI-6; 3 — K-63; 4 — K-322; 5 — K-35-90; 6 — PN-1 ($\dot{\varepsilon}$ = 0.01/min).

Data were presented in [3] showing that upon transition to monofilaments the adhesive strength increases by 2 - 2.5 times in comparison with the adhesive strength for macrospecimens, determined for the case of interlaminar shear in the presence of tangential stress concentration at notch locations. The values of the ultimate stresses of the butvarphenolic binder for a bond area of 1 cm² are ~100 kgf/cm². The adhesive strength in shear of the 33-18 and AG-4 binders [4] is 338 and 210 kgf/cm², respectively. The latter values are close to the shear resistance values obtained in bending tests of short specimens.

Mechanical Characteristics of Certain Polymer Binders

These arguments show that definite requirements are imposed on the mechanical characteristics of the polymer matrixes. The strain curves of the polyester, epoxy, and phenolformaldehyde resins are shown in Figure 15. According to Polyakov [78], fracture of the PN-1 binder is brittle without necking. The temperature dependences of the PN-1 polymer binder elastic characteristics are presented in Figure 16.

Strain curves of the epoxy binders were analyzed by Bernatskiy [23], who showed that monotonically increasing curves and curves with transition through a load peak are characteristic for polymer matrixes of the types studied. In the first case, brittle fracture is observed, while in the second case, the fracture takes place after necking. Brittle fracture becomes dominant with increase of the strain rate.

The elastic constants and strength characteristics of the polymer binders are shown in Tables 4 and 5. The linearity of the relation σ_b - lg $\dot{\varepsilon}$ and the weak dependence of the elongation ε_b corresponding

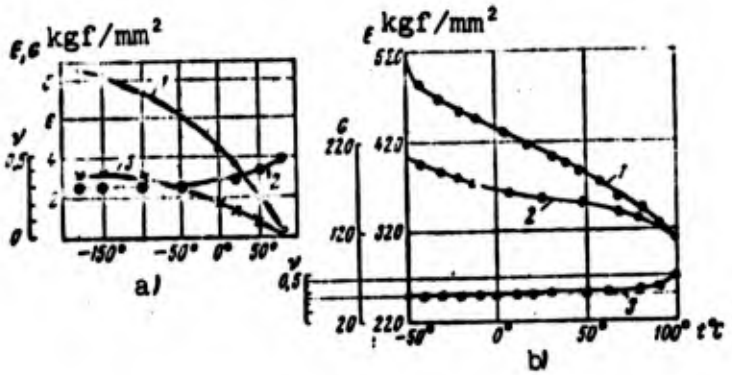

Figure 16. Temperature dependence of elastic characteristics of polymer binders.

a — PN-1; b — 6EI-60 (1 — E; 2 — ν; 3 — G).

TABLE 4

STRENGTH, ELONGATION AT FAILURE, AND VARIATION COEFFICIENT OF SOME BINDERS

Polymer Matrix	σ_b in kgf/mm²	v	ε_b	v	ε_{max}	v
		in %				
LMI-6	9.17	10.3	5.82	7.9	6.26	13
K-156C	9.63	9.9	5.84	24.4	7.7	31
K-63A	11.3	21.2	6.39	21.1	6.58	21
K-100	9.38	14.7	5.7	23.7	5.86	24.2
K-35-90	11.59	8.9	6.87	8.8	7.01	25.6

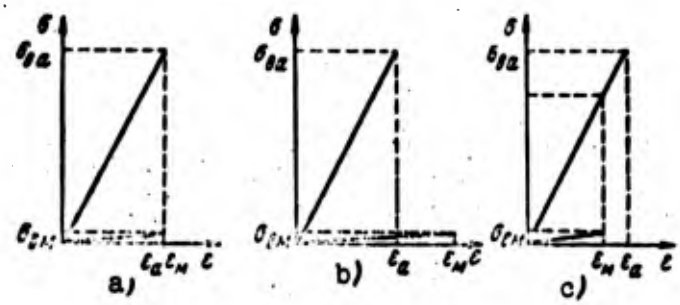

Figure 17. Influence of resin elongation at fracture on fiber strength utilization.

a — $\varepsilon_a = \varepsilon_m$; b — $\varepsilon_a < \varepsilon_m$; c — $\varepsilon_a > \varepsilon_m$.

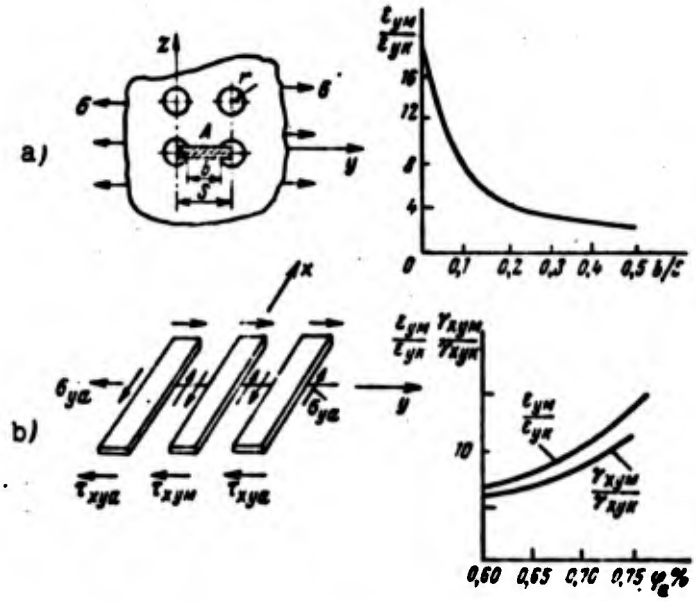

Figure 18. Influence of packing density (a) and fiber content (b) on required fracture elongation of the matrix.

to the stress α_b on the strain rate have been proved experimentally. Evaluation of the scatter of the binder characteristics showed that the dispersion of the strength limits increases with increase of the deformation rate. For a rate of about 20 min^{-1}, the scatter of the ultimate strength nd the strains ε_b and ε_{max} (strain at the moment of fracture) is characterized by data (Table 4) from which it follows that the dispersion of the binder rupture stresses is significantly less than the dispersion of the reinforcing fiber strength, which determined the composite strength.

Matrix Elongation at Fracture

A definite relationship between the fiber and matrix fracture elongations is necessary for complete utilization of the reinforcing fiber strength. Possible schemes for the case of tension along the fibers are shown in Figure 17. The fracture elongation of the matrix should be larger than that of the fiber $\varepsilon_{b_m} \geq \varepsilon_{b_a}$, since, if a matrix with small elongation fails earlier, the fiber strength cannot be utilized. However, this relationship is not sufficient in the presence of transverse layers.

TABLE 5*

ELASTIC CHARACTERISTICS OF SOME BINDERS

Binder	E	G	v
	in kgf/mm²		
LMI-6	339	129	0.31
K-156C	326	123	0.32
K-63A	490	168	0.46
K-100	335	123	0.36
K-3590	346	123	0.41
K-322	322	121	0.33
PN-1	380	120	0.30
6EI-60	410	150	0.32
E181	320	—	—

*The values of the elastic constants were obtained from the resonant oscillation frequencies [32].

It has been established [6, 65] for square and hexagonal packing of the fibers that under the action of forces perpendicular to the fibers, the stresses and deformations in the polymer matrix depend on the ratio of the matrix and fiber moduli E_m/E_a and the fiber packing density in the matrix. For square packing, Figure 18 shows the ratio of the matrix deformation in the direction of the y axis to the average deformation in this same direction for the element A for $E_m/E_a = 0.05$, which may be characterized by the relation

$$\frac{\varepsilon_{ym}}{\varepsilon_{yc}} = \frac{1}{\frac{2r}{s}\cdot\frac{E_m}{E_a}+\frac{b}{s}}. \tag{5}$$

The strain concentration in the polymer matrix increases with increase of b/s if $b/s \to 0$, $\varepsilon_{ym}/\varepsilon_{yc} \to 20$. More exact analysis leads to the relation [191]

$$\varepsilon_{ym} = \left[\frac{1}{\frac{2r}{s}\cdot\frac{E_m(1-\nu_a^2)}{E_a(1-\nu_m^2)}+\frac{b}{s}}\right]\times$$
$$\times\left[\varepsilon_{ya}+\varepsilon_x\frac{2r}{s}\left(\nu_a-\frac{E_m}{E_a}\cdot\frac{1-\nu_a^2}{1-\nu_m^2}\right)\right]; \tag{6}$$
$$\gamma_{xym} = \frac{1}{\frac{2r}{s}\cdot\frac{G_m}{G_a}+\frac{b}{s}}\gamma_{xya};$$
$$\varepsilon_{xm} = \varepsilon_{xa}.$$

Figure 18 [191] shows the ratio of the relative matrix elongation at fracture and the fracture deformation of the composite necessary for monolithicity of the composite versus reinforcement ratio. We took $E_a/E_m = 20$; $G_a/G_m = 17$; $\nu_m = 0.4$; $\nu_a = 0.23$; $\varepsilon_x = \varepsilon_y$. In the studied reinforcing density range, the resin elongation should be 6 - 15 times greater than the corresponding composite elongation.

It should be noted that, in the case of inelastic deformation of the polymer matrix, the stresses in the matrix are lower, and this leads to a still larger value of $\varepsilon_{ym}/\varepsilon_{yc}$.

Increase of the load-carrying ability of shells made from oriented glass-reinforced plastics as a result of eliminating cracking of the binder in layers with transverse fibers has been studied by Molodtsov [74]. According to his data, the relative elongation of a binder with a volumetric fiber content 30 - 70% should amount to 4 - 26%. For a composite based on the EDT-10 epoxy binder, failure with loading along the fibers began with cracking of the binder resulting from summation of the stresses from the external load and the axial residual stresses.

Analysis of the data of §3 shows that composite strength is basically approximately proportional to the number of reinforcing fibers (reinforcement ratio). This leads to a tendency to increase the reinforcement density when fabricating composites; however, when so doing it is not possible to provide uniform packing through the entire volume of the composite.

It follows from (6) that with decrease of E_m for fixed b the required elongation ε_{bm} increases. Upon the introduction of plastifiers this characteristic increases, but at the same time there is a reduction of the matrix elastic modulus E_m and increase of the inelastic deformations, which in turn leads to increase of the required value of ε_{bm}. Consequently, the use of nonrigid binders is not an effective way to increase the strength of composites.

More effective is the provision of an optimum fiber packing density parameter b/s. For a square pattern the glass content in percent of volume is described approximately by the relation [65]

$$\varphi_0 = 0{,}7879\left[\frac{1}{1+\frac{b}{r}}\right]. \qquad (7)$$

According to Figure 18, for ϕ_a = 0.64 - 0.71 the elongation of a polymer matrix should exceed by a factor of 7 - 10 the elongation of the glass fiber b/r = 0.22 - 0.11. The requirements on polymer matrix on relative elongation at fracture lead to the necessity for providing some interval between the reinforcing fibers and limiting the reinforcement ratio. This explains the existence of some optimum parameter b/s or reinforcement ratio (see Figure 18).

The properties of some types of polymer matrices are shown in Table 6. We see from these data that the epoxy binders satisfy the conditions of monolithicity better; however, it appears that the elongations at fracture are not adequate.

TABLE 6

MECHANICAL CHARACTERISTICS OF PRIMARY BINDER TYPES

Binder Properties	Polyester Resins	Phenolformaldehydes	Epoxides
σ_{bt} in kgf/mm^2	4.00 - 6.60	2.00 - 5.00	5.0 - 6.5
σ_{bc} in kgf/mm^2	16 - 11.0	8.00 - 11	10 - 12
σ_{bb} in kgf/mm^2	7.5 - 9.00	6	14
E in kgf/mm^2	290 - 320	250 - 350	460
γ in g/cm^3	1.15 - 1.28	1.2 - 1.3	1.1
ε_b in %	Up to 4	Up to 2	Up to 5

If the fiber content is excessive, large shrinkage stresses develop, and stresses resulting from the different Poisson ratios of the matrix and fibers are created during loading.

§3. Limiting States of Glass-Reinforced Plastic with Respect to Fiber and Matrix Strength

The reinforcing fiber content and orientation basically determine the level of the mechanical characteristics of the glass-reinforced plastics. The experimental data of various studies [69, 110, 115, 128, 139, 157, 159] show that the optimum fiber content is different

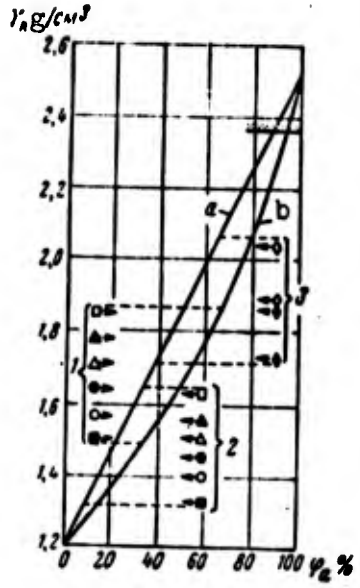

Figure 19. Composite specific weight versus reinforcement ratio for various fabrication techniques.

a — volume content in %;
b — weight content in %:
1 — cloth reinforcement;
2 — glass mat reinforcement;
3 — oriented structures;
■ — manual layup without pressure; 0 — vacuum methods; ● — fabrication by bag under pressure (molding); Δ — autoclave methods; ▲ — forming by rubber dies; ▽ — fabrication in press forms; ◆ — drawing of profiles; ◇ — winding, methods for obtaining oriented structures [173].

for binder materials of different types and depends on the type of reinforcing filler.

The relationship of the glass-reinforced plastic components is determined both by the requirements with regard to strength and stiffness and by technological factors. As a rule, the fabrication methods without pressure or with low values of the pressure yield a glass content up to 20%. With moderate pressure the glass content will be up to 30%, and with high pressures up to 40% by volume in the case when an unoriented filler is used.

The use of fillers with organized structure (glass cloth and oriented fibers) makes it possible to increase the volumetric glass content to 55 - 80% with corresponding increase of the strength and stiffness of the materials.

Figure 19 shows how the reinforcement ratio (glass fiber content) and density of glass-reinforced plastic varies as a function of the fabrication method. The calculation was made for a resin with specific weight 1.22 g/cm³ and glass fiber with specific weight 2.53 g/cm³. The three basic forms of reinforcing filler make it possible to obtain materials with a quite wide range of properties, including anisotropic materials. Within the limits of each group, the properties of the glass-reinforced plastics may differ as a function of number of filaments, filament degree of twist, structure (pattern) of the cloth, relationship of warp and woof filaments, etc.

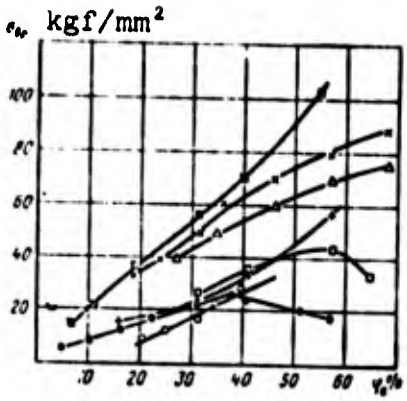

Figure 20. Tensile strength versus volumetric glass content.

• — polyester resin reinforced randomly with glass mat [111]; X — unidirectional prestressed fibers [110]; Δ — unidirectional fibers without tension, polyester resin [110]; — glass cloth, polyester resin [110]; Ø — unidirectional fibers, epoxy resin [115]; + — crossed reinforcement, epoxy resin [115]; 0 — polyester glass-reinforced plastic [157].

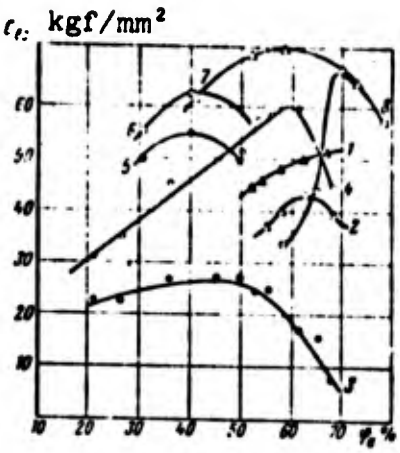

Figure 21. Compressive strength versus volumetric glass content.

1 — GRP based on ED-6 resin [69]; 2 — GRP based on BF-4 resin [69]; 3 — glass cloth plus polyester resin [157]; 4 — glass cloth in woof direction plus polyester resin [157]; 5 — glass cloth 32/24/19, 110 gf/m² [159]; 6 — glass cloth 39/19/12 [159]; 7 — glass roving [159]; 8 — epoxy resin plus E-801 glass fiber [139].

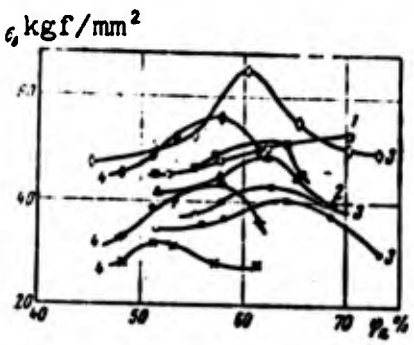

Figure 22. Compressive (Io□×), tensile (II●■▲) and bending (III○◆) ultimate strength versus volumetric glass content.

1 — ED-6; 2 — E-1200; 3 — BF-4; 4 — glass cloth 181 plus epoxy resin [128].

The variation of the strength in tension, compression, and bending is shown in Figures 20 - 22. For most cases, the tension strength increases nearly linearly with increase of the glass filler content; however, in structures with interweaving of the filaments we observe an optimum, after which the composite strength decreases, apparently as a result of mechanical damage of the glass fibers when forming the material or part.

The tension strength of structures based on oriented filler can be increased by increasing the reinforcement ratio through more dense packing of the fibers.

The strength in compression and bending changes similarly; however, the glass filler optimum depends more markedly on the type of binder. The optimum glass content is about 60% for polyester, 65% for phenol, and 70% for epoxy resins.

If we analyze the optimum filler content and the properties in tension, compression, and bending, we obtain the curves shown in Figure 22. For curves 3, the optimum glass content in bending is less than in tension and compression; for curves 4, the optima in tension and bending coincide. This is apparently explained by the fact that in [69] relatively short specimens ($l/h = 10$) were tested, yielding shear fracture along the neutral axis, which leads to a situation in which the breaking stresses expressed in terms of σ are not comparable. Tests of specimens with $l/h > 16$ [128], yielding failure from normal stresses, show that the bending strength is approximately 1.3 times the tensile strength.

Other conditions being the same, even such factors as the number of layers affects the strength characteristics for the relatively thin materials. Figure 23 shows experimental data [162] indicating the influence of the number of filler layers on material strength in tension and compression for flat-plate and tubular specimens. The variation of the elastic modulus in tension, compression, and bending for loading in the direction of the reinforcement is described by curves (Figure 24) constructed from the results of [39, 81, 115, 139, 173, 184]. These curves are close to linear and nearly parallel; thus, the form of binder and glass filler has very little effect on the nature of the function $E = f(\phi_a)$, altering only the initial values of the elastic properties. This relation has an asymptotic nature in the direction perpendicular to the axis of reinforcement (curve 8).

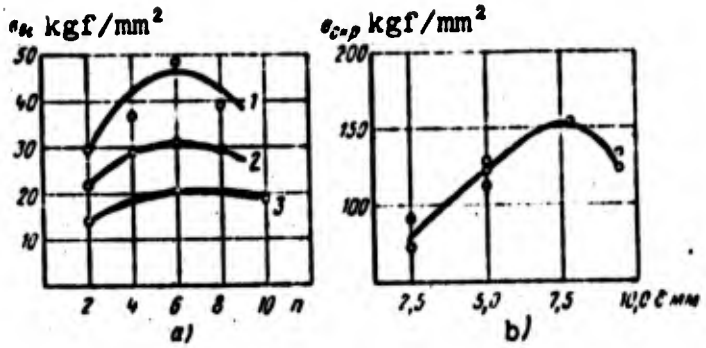

Figure 23.

a — influence of number of reinforcing cloth layers on tubular specimen strength: 1 — 38/19/12, 285 gf/m², 40% glass; 2 — 32/24/24, 110 gf/m², 110 gf/m², 40% glass (compression); 3 — 38/19/12, 285 gf/m²,30% glass (tension); b — influence of tubing thickness on tensile strength in circumferential direction (test under internal pressure) [162].

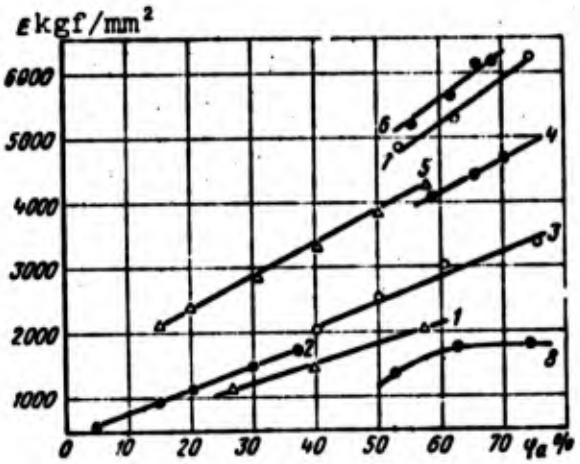

Figure 24. Modulus of elasticity in tension, compression, and bending versus volumetric glass content.

1 — epoxy resin with crossed reinforcement (bending) [108]; 2 — polyester resin (tension) [173]; 3 — SVAM 1:1 (tension) [81]; 4 — epoxy resin based on 801 fiber (compression) [139]; 5 — epoxy resin, winding (bending) [39]; 6 — roving from S-994 fibers, epoxy resin 826 [184]; 7 — epoxy resin, 12.5-micron diameter oriented fibers; 8 — same, tension perpendicular to the fibers.

An approximate calculation of composite properties was formulated in [131]. It was based on the assumption of ideal elasticity of the reinforcing fibers and matrix and also uniform loading of the parallel reinforcing elements. The composite characteristic has the form

$$\bar{x}_\alpha = \frac{1}{F_\alpha} \sum_1^n x_i F_i. \tag{8}$$

We see from formula (8) that the determining factor is the glass fiber content. A more detailed analysis [71] leads to the following relations for calculating composite strength as a function of the relative content of the components and their mechanical characteristics.

The cross sections of the composite are considered to consist of the regions F_a, corresponding to the fibers, and the region F_m, corresponding to the filled polymer matrix. The regions F_a are considered to be separate, and the characteristics of the components are known (fiber diameter d, elastic modulus E_a, Poisson's ratio ν_a; the polymer matrix has the corresponding characteristics E_m, ν_m, and is considered to be an elastic medium).

The reinforcing elements are connected with the polymer matrix along the interfaces, and there are no initial stresses in the composite.

Analysis of the solution obtained showed that the axial displacements are independent of the x and y coordinates (z axis is directed along the filament), and are the same in regions F_a and F_m (hypothesis of plane sections). The axial stresses σ_z are the largest in magnitude and constant within the limits of the regions F_a and F_m, but change stepwise at the interface.

The average modulus of elasticity is

$$E_к = E_м\left[\varphi_а\left(\frac{E_а}{E_м}+\frac{4\nu_м}{B}\right)+(1-\varphi_а)\right]. \tag{9}$$

where ϕ_a is the reinforcement ratio, the volumetric fiber content is

$$B=\frac{2(1+\nu_а)(1-2\nu_а)+\varphi_а\frac{E_а}{E_м}(1+\nu_м)}{\frac{E_а}{E_м}(\nu_а-\nu_м)}.$$

The relationship between the volumetric ϕ_a and weight ψ_a fiber contents has the form

$$\varphi_а=\frac{\psi_а\gamma_м}{\psi_а\gamma_м+(1-\psi_а)\gamma_а},$$

where γ_a and γ_m are the specific weights of the reinforcing fibers and the matrix.

For the ratio $E_a/E_m \to 20$, $|\nu_a - \nu_m| < 0.2$, we obtain the approximate relation

$$E_к \cong E_м\left[\varphi_а\frac{E_а}{E_м}+(1-\varphi_а)\right]. \tag{10}$$

For deformation $\varepsilon_c = \varepsilon_z$, the average axial stress in the composite is

$$\sigma_к=\varepsilon_z E_м\left[\frac{E_а}{E_м}\varphi_а+(1-\varphi_а)\right]. \tag{11}$$

In the linear stress state case, failure of the composite can take place at the moment the deformation ε_c reaches a value equal to the breaking strain for the fibers or matrix. Then we can write the approximate values of the composite strength limits (see Figure 17).

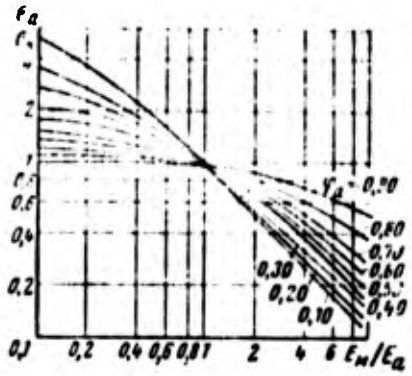

Figure 25. Ratio of stresses in fibers to stress in composite as a function of elastic properties of the matrix and fibers.

For the first case $\sigma_{bc} = \sigma_z$ with $\varepsilon_z = \varepsilon_{ba} = \sigma_{ba}/E_a$, since the fibers are elastic

$$\sigma_{oc} = \sigma_{om}\left[q_a + \frac{(1-q_a)E_m}{E_a}\right]. \qquad (12)$$

For the second case ($\varepsilon_{ba} > \varepsilon_{bm}$) the corresponding relation takes the form

$$\sigma_{oc} = \sigma_{om}\left[\varphi_a \frac{E_a}{E_m} + (1-q_a)\right]. \qquad (13)$$

These relations agree satisfactorily with the experimental data for comparatively low (up to 60%) reinforcement ratios. According to the experimental data, better agreement for the polyester composites is obtained under the assumption $\varepsilon_{ba} > \varepsilon_{bm}$ and calculation using (13). It follows from these relations that the modulus ratio E_a/E_m also influences composite strength (Figure 25).

The behavior of the polymer matrix in composites has not received adequate study; it is not clear whether there is pure yield of the resin or whether it is accompanied by fracture. As a result of the large values of the ratio of resin surface area to composite volume, this factor affects the resin yield point.

The GRP model in the form of two regions (matrix and filler) connected in parallel makes it possible to write — on the basis of the hypothesis of plane sections and for known properties of the components (F_a, σ_{ya}, E_a for the fibers and F_m, σ_{ym}, E_m for the matrix) — the relations between the stresses in the fibers and the matrix

$$\sigma_a = \frac{E_a}{E_m}\sigma_m = \frac{Q_c}{F_a}\left(1 + \frac{E_m}{E_a}\cdot\frac{F_m}{F_a}\right)^{-1}, \tag{14}$$

where σ_{ya} and σ_{ym} are the yield limits of the fibers and the matrix.

In all cases of reinforcement of existing matrices $\sigma_{ya}/\sigma_{ym} > E_a/E_m$, and yield occurs first in the matrix if we take $\sigma_m = \sigma_{ym}$ as the yield condition. In this case, the nominal stress in the composite reaches magnitudes

$$\sigma_{ky.n} = \frac{Q_k}{F_m + F_a} = \sigma_{mk}\left[1 + \frac{F_a}{F_k}\left(\frac{E_a}{E_m} - 1\right)\right], \tag{15}$$

where $F_c = F_a + F_m$.

The deformation in the limiting state with regard to yielding of the matrix is

$$\varepsilon_{ky.n} = \frac{\sigma_{mk}}{E_m}. \tag{16}$$

The force absorbed by the matrix without account for hardening is $Q_m \leq F_m \times Q_{ym}$, and the loading on the fibers will increase with increase of the load on the composite. The stresses in the fibers increase up to σ_{ba} with increase of Q_c

$$\sigma_a = \frac{Q_a}{F_a} = \frac{Q_k}{F_a} - \sigma_{mk}\frac{F_m}{F_a}, \tag{17}$$

and the nominal stress and strain in the composite at the moment of material fracture are

$$\begin{aligned}\sigma_{km} &= \frac{Q_k}{F_k} = \sigma_{mk} + \frac{F_a}{F_k}(\sigma_{ak} - \sigma_{mk}) = \\ &= \sigma_{mk}(1 - \varphi_a) + \varphi_a\sigma_{ak};\quad \varepsilon_{km} = \frac{\sigma_{ak}}{E_a}.\end{aligned} \tag{18}$$

Transition of the matrix into the plastic state can be determined from the strain diagram, where an inflection point will be observed at $\varepsilon_c = \sigma_{ym}/E_m$, and the slope of the diagram is characterized by the modulus

$$E' = \frac{\sigma_{km} - \sigma_{ky.n}}{\varepsilon_{km} - \varepsilon_{ky.n}} = \frac{F_a E_a}{F_k}. \qquad (19)$$

The inflection point is absent for $E_a/E_m = \sigma_{ba}/\sigma_{ym}$. However, because of nonuniformity of the loading of the individual segments and scatter of the matrix yield limits, as a rule the inflection is not clearly expressed on the diagram.

We see from this simple analysis that the matrix strength and yield characteristics should be quite high. As a rule, the mechanical characteristics of the composites improve with increase of the matrix tensile strength.

Reference 21 presents the results of calculating the effectiveness of the utilization of glass-fiber reinforced material strength and a comparison of the calculated strength $\sigma_{ba}\phi_a + \sigma_{bm}\phi_m$ and the experimental values for various filler types (Table 7).

Comparing the calculated and experimental relations (Figure 26) from [177], we can conclude that the experimental values are lower.

We see from these relations that the variation of strength with fiber content in percent by volume is linear. However, in this case the number of defects in the reinforcing filler increases and the fiber working conditions in the matrix degrade. These relations yield an estimate of the upper values of the strength without account for several of the considerations presented in §1 - 5. The existence of peaks on the $\sigma_{bc} - \phi_a(\psi_a)$ curves shows that for some reinforcement ratio, the experimental curve deviates from the theoretical curve as a result of the influence of defects in the fibers and matrix. These

TABLE 7

UTILIZATION OF GLASS FIBER STRENGTH IN VARIOUS COMPOSITES

Filler Type	Stress in Fibers in kgf/mm²	Utilization of Fiber Strength in %	Fiber Length	σ_{bc} in kgf/mm²		Effectiveness in %
				Theory	Experiment	
Filaments wound in one direction	164	58.5	Continuous	217	126	58
Fibers in two directions	190	68	Same	138	51	36
Glass cloth	113	40.5	Same	138	30	22
Layer of fiber mat	176	63	Same	138	40	29
Chopped fibers	92	33	Short	42.5	10.5	24.1
Glass floc	20	7.0	Same	116	14	12.1

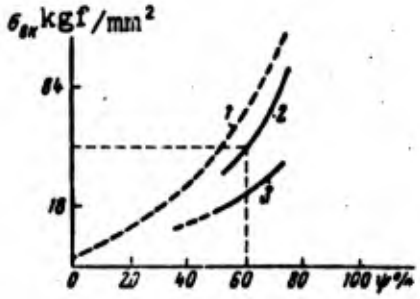

Figure 26. Calculated and experimental curves for composite strength versus glass weight content in %.

1 — theory; 2 — reinforced in one direction; 3 — cross reinforcement.

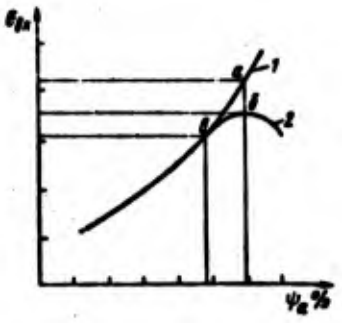

Figure 27. Relation $\sigma_{bc} - \psi_a$.

1 — theory; 2 — experiment; a,b — theoretical and experimental strengths with optimum glass content; c — limiting value of correspondence between theoretical and experimental strength without structural damage.

deviations have a statistical nature (see §1 - 3). Figure 27 shows the nature of the relation $\sigma_{bc} - \psi_a$ and the optimum values of the strength and reinforcement ratio corresponding to composites with damaged and undamaged fibers.

§4. Limiting States of GRP with Regard to Progressive Fiber Failure

The basic difference between the process of composite material failure and fiber bundle failure is that the failure of a fiber at any point of the bundle means weakening of the bundle and leads to increase of the effective stress, while failure of individual fibers in a composite (combined bundle), taking place at different sections, leads to redistribution of the load on the fibers located close to the failure zone. It has been proved experimentally that materials can be treated on the basis of resins and short parallel reinforcing fibers [3]. Final failure of the composite apparently takes place at stresses corresponding to the strength of a material based on short fibers with ends randomly positioned through the volume of the material.

Let us examine the failure model of a composite consisting of a binder strengthened by glass fibers oriented in a single direction. The strength of the glass fibers depends basically on the defects which are distributed randomly along the length of the fibers, as a result of which fiber failure takes place at different stress levels at different locations. In the case of tension of composite material specimens, the individual fibers fail at the locations of local defects, as a result of which shorter and stronger fibers are formed which are capable of accepting the load. At the fracture locations, the load is transmitted to the fiber by means of tangential stresses which arise on the surface between the fiber and binder. At the end of the failed fiber, we observe concentration of tangential stresses, while the normal stresses are equal to zero. With increase of the distance from the end of the fractured fiber, the tangential stresses in the polymer matrix decrease, while the normal stresses in the fiber increase to the value of the nominal stresses. With load increase, the progressive failure of the fibers continues until the

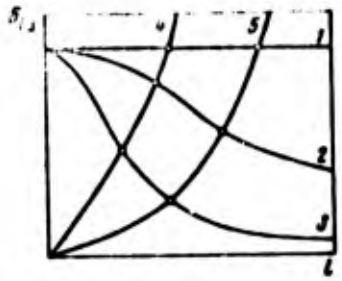

Figure 28. Fiber bundle strength versus length.

1 — defect free fibers; 2 — fibers with slight defects; 3 — highly damaged fibers; 4, 5 — bundle strengthening "force" for small and large diameters.

effective "working" length of the fibers becomes so short that further increase of the load is not transmitted to the fibers because of the tangential stresses in the matrix reaching the yield limits or shear failure of the matrix. After this, final failure of the composite material takes place.

Failure of fiber reinforced composites by breakup of the fibers was suggested by Parratt [180] and confirmed experimentally by Rabinovich, Malinskiy, and others [59, 72].

Figure 28 shows a qualitative picture of the strengthening effect for composites based on bundles with small (2) and large (3) defects and defect-free (1) fibers of different diameters (4, 5) as a function of fiber length.

For the transmission of a (nominal) stress of 140 kgf/mm^2, it is necessary that the critical fiber length be on the order of 400 fiber diameters, for 350 kgf/mm^2 the length must be 1000 d.

Malinskiy and Rabinovich [59, 72] studied the elementary acts of the GRP failure process. The stress state in the failure zone was evaluated using the polarization-optical method with movies taken in the process of loading specimens made from reticulate polymer binders (of the polyester and polyepoxy type) with 50 - 100-micron reinforcing elements. In this case, individual fractures occured, whose number gradually increased with load increase, stress concentration was observed in the fracture zone, and a sort of edge effect developed. The stress state in the fracture zone had a local nature and did not depend on the boundary conditions associated with force application.

A fiber segment protruding above the fracture surface formed at the fracture location, indicating rupture of the adhesive bond as a result of shearing failure before the model specimen failed through the entire cross section.

The length of the freed filter segment (failure region) depends on the extent of the edge effect zone and its decay rate (gradient). The zone of nonuniform tangential stress distribution is restricted to the segment l_a, whose relative magnitude is a linear function of the ratio of polymer layer thickness to fiber diameter.

The relative length of the nonworking fiber segment is determined [59, 72] as a function of the mechanical and geometric parameters of the components of the reinforced plate using the relation which follows from the conditions of equilibrium and the compatibility of the deformations of the fiber and the elasto-viscous matrix

$$\frac{l_a}{d} = \ln \frac{\tau_{max}}{\tau_c} \left(1 + \frac{G_m}{G_{m\infty}}\right)\left(\frac{E_a}{E_m}\right)(1-\beta)^{1/n}\left(\frac{t}{d}\right)^{1/n}, \qquad (20)$$

were d is the reinforcing fiber diameter; τ_{max} is the maximum shear stress; τ_c is a parameter having the dimensions of a stress; G_m and $G_{m\infty}$ are the moduli of elasticity and Mackian elasticity in shear for the matrix; E_a, E_m are the moduli of elasticity of the reinforcing element and matrix; β is a parameter which depends on the elastic constants and volume ratio of the composite components; t is the binder layer thickness.

The linear relationship between l_a/d and $\sqrt{t/d}$ is confirmed by the experimental data shown in Figure 29. Since specimen failure takes place at a section whose location is determined by the boundary of the tangential stress concentration zone at the fiber-resin interface, and the relationship between l_a/d and $\sqrt{t/d}$ is confirmed by

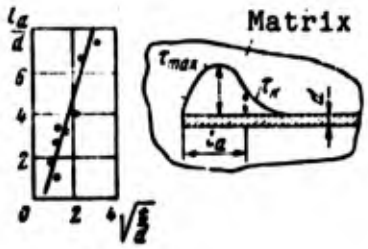

Figure 29. Curve of nonworking segment length as function of polymer layer thickness, fiber diameter, and tangential stresses in the failure zone after [59, 72] (PN-1 resin).

experiment, we can assume that the failure is caused by the overstress arising in the reinforcing fiber fraction zone. A crack develops at the fiber-matrix boundary, and in the central part of a specimen reinforced by a single fiber the surface which forms in the first fracture stage is mirror smooth, while at the peripheral part the fracture is rough, characteristic for "prefracture" of the section. With decrease of binder shrinkage and weakening of the adhesive bond, the overstress decreases. In all the experiments, failure takes place at deformations whose magnitude is less than the fracture deformation of the unreinforced binder.

Few experimental data are available on the failure of composites with high reinforcement ratio. In order to determine the conditions for delamination of a composite, Melvin [65] analyzed a model consisting of parallel rods with the outer rods being initially failed. In spite of the large rod diameters (d = 3 mm), the basic results characterize qualitatively the matrix operation, force redistribution, and the stress state of the neighboring rods in the failure zone.

The reinforcing rods and matrices were considered elastic, and at some distance from the fracture location all the fibers were loaded uniformly. The normal stress state of the binding matrix was taken equal to zero, since the ratio of the elastic moduli of the rods and matrix was 20; however, the matrix transmitted tangential stresses from the failed fibers to the unfailed ones. The results showed that the tensile and tangential stresses in the rods and in the matrix die out at a distance ~5K from the fracture point, where $K^2 = G_m t/bE_a f_a$; G_m is the shear modulus of the matrix; E_a, f_a are the modulus of elasticity and area of the fiber; t is the thickness of the polymer layer in the single-layer model; b is the distance between fibers.

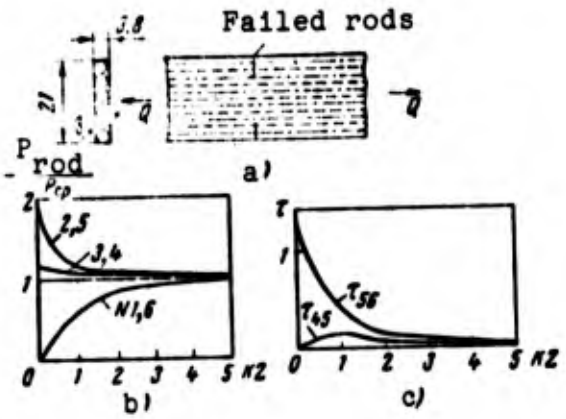

Figure 30. Model of composite reinforced by parallel fibers, two of which are fractured (a); variation of load in rods with distance to failed section in units of KZ (b); tangential stresses in the matrix between fibers 4,5 and 5,6 (c).

The curves (Figure 30) confirm the assumption that the stresses are concentrated in the neighboring fibers in the zone of the failed fibers, which increases the probability of failure of any of the neighboring fibers. The actual magnitude of the concentration in a real material is lower than in the Melvin single-layer model, the concentration also decreases as a consequence of incomplete elasticity of the properties. In this connection, there is an increase of the length of the segment with high stresses, basically determined by the modulus G_m and also by the ratio t/b. The stress concentration level in the fibers is independent of the component properties and model parameters.

The tangential stresses in the polymer matrix depend on K and the force acting Q, i.e., on the normal stress, characterizing the tendency of the material to delaminate. The maximum tangential stress is

$$\tau_{max} = C\frac{QK}{l} = C\sigma_a\sqrt{\frac{G_m}{E_a}\cdot\frac{F_a}{bl}}, \qquad (21)$$

where C is a constant, equal to 1.27 for six fibers. For composites with multi-layer structure with parallel pattern of round fibers $t \approx d$

$$\tau_{max} = C\sigma_a\sqrt{\frac{G_m}{E_a}\cdot\frac{d}{b}}, \qquad (22)$$

where C' = 0.1 - 1.0, depending on the fiber arrangement. The maximum tangential stress increases with increase of the level of the stresses σ_a, ratio G_m/E_a, and d/b. Creation of composites with high tensile strength requires higher shear strength of the polymer matrix with lower elastic properties of the resin (G_m). The ratio d/b, characterizing fiber packing geometry, is also of considerable importance. The quantity τ_{max} increases with decrease of the distance between fibers. Thus, it is necessary to maintain some finite distance between the fibers. For example, for b - 0.1d τ_{max} is twice as large as for d = b. The polymer layer thickness t is found on the basis of the uniform fiber arrangement (packing) scheme, if we consider that the matrix forms a cylindrical tube of thickness t around the fibers and fills the entire space between the fibers. For hexagonal and square packing schemes (grids), t can be found from the equations

$$\varphi_a = \frac{\pi d^2}{4(d+t)^2} \quad \text{and} \quad \varphi_a = \frac{\pi d^2}{3.48(d+t)^2},$$

where ϕ_a is the reinforcing fiber volumetric content.

For the plane stress state, the influence of fiber arrangement in the matrix on the tendency to delaminate becomes still more significant, since the concentration from the load perpendicular to the reinforcing fibers is superposed on the concentration from fracture of the fibers. As a result, numerous cracks form in the transverse layers and separate the composite into several individual fibers coated with binder.

The data characterizing the strength of fibers in composites [105] were obtained in the case in which fiber bundles and glass mat layers were tested. The number of fibers varied from five to several thousand and hardened and unhardened resins were used as the matrices. In the absence of matrices, if the binder is hardened (curves 1 and 2 in Figure 31) we observe considerable bundle strength reduction as a function of the number of fibers (the initial fiber strength is shown by the dash-dot lines, and the strength measured

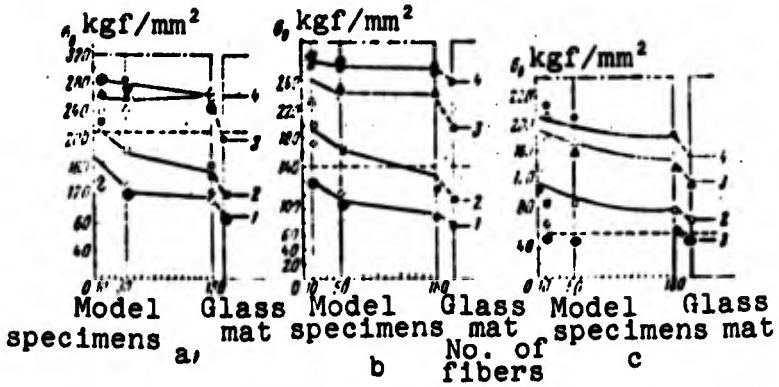

Figure 31. Strength of glass fibers in oriented GRP with unidirectional structure.

a — 10 μ diameter fibers; b — 15 - 17 μ diameter fibers; c — 50 μ diameter fibers; 1 — specimens without binders; 2 — based on unhardened ED-5; 3 — based on bakelite lacquer; 4 — based on ED-5 (specimen working length 10 mm (0) and 100 mm (•) .

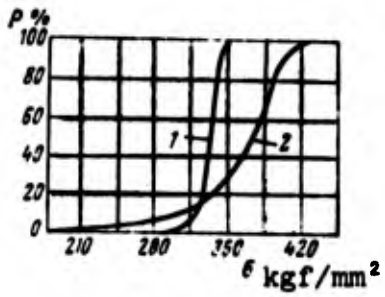

Figure 32. Statistical distribution of strength for monofilament (2) of E-glass and composite (1) based on epoxy resin reinforced by the same E-glass fibers.

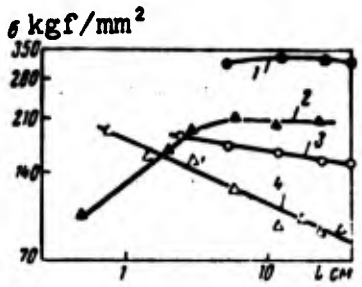

Figure 33. Variation of average strength of two types of yarn fibers and a yarn composite with epoxy resin as function of fiber length.

1 — E-glass, yarn in composite; 2 — S-glass, yarn in composite; 3 — E-glass yarn; 4 — S-glass yarn.

under normal conditions is shown by the dashed lines). In the presence of a hardened binder, this relation weakens somewhat; however, the breaking stresses in the fibers are less than the initial fiber strength and for a diameter of 10 microns amount to ~220 kgf/mm².

The strength of E-glass monofilaments and epoxy resin composites based on these fibers was analyzed by Korten [65]. Figure 32 shows that 20% of the monofilaments fail at a stress corresponding to the average strength of the composite. The distribution curves for the monofilaments and the composite cross at a point with ~15% failure (stress ~350 kgf/mm^2). If we assume that these fibers (15%) in the composite do not accept load, the average stress in the remaining fibers will be ~390 kgf/mm^2. About 70% of all the monofilaments fail at this stress, and the composite specimen could scarcely retain its load-carrying ability if there were no redistribution of the load at the points of fiber failure to the neighboring fibers, whose shorter segments are stronger.

Figure 33 shows the variation of the strength of yarns and yarns in a composite with length of the monofilaments comprising glass yarns of two types. While the strength of the yarns without resin decreases with increase of the fiber length, the strength of the yarns in the composite is independent of the length beginning at some value of the length. This length can apparently be considered the minimum critical length for the transmission of tensile forces to the fibers through the shear stresses in the matrix.

Figure 34 [180] shows the average fiber stresses as functions of fiber diameter d and the ratio l/d (a) for epoxy and polyester GRP with 50% fiber content by weight.

In [109] results are presented of tests of fiber yarns whose strength was calculated on the basis of monofilament strength distribution according to the Daniels scheme. The yarn lengths were 2.5; 12.5; and 25 cm. We see from these data that the strength of the yarn in the composite depends very weakly on length (Figure 35, Table 8).

The results of the monofilament tests were used to construct the deformation diagram for a fiber bundle. Figure 36 shows such a diagram for a bundle of 216 monofilaments. Let us examine the tension process for a constant strain rate. As the weak fibers break, the load decreases since the strain magnitude is fixed, but with increase of the deformation,

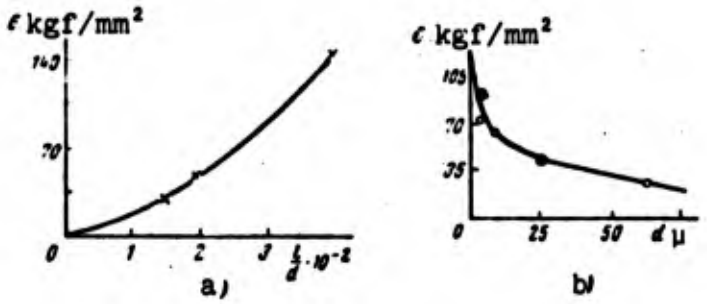

Figure 34. Average fiber stresses versus ratio l/d (a) and fiber diameter (b) for epoxy (•) and polyester (o) composites.

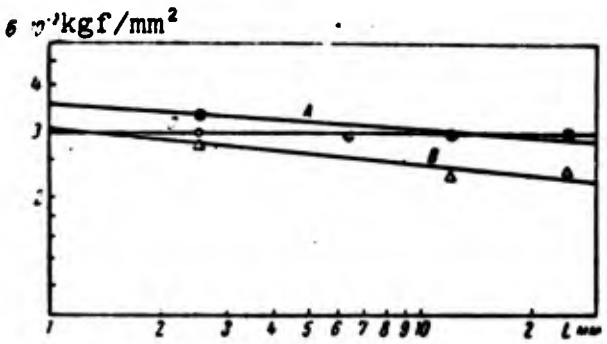

Figure 35. Average strength of monofilaments versus length.

A — monofilament; B — Fiber bundle (n = 112); C — coated bundle (n = 216).

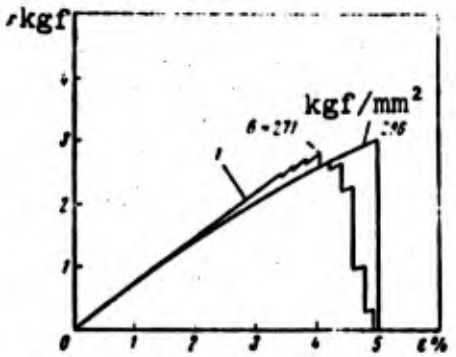

Figure 36. Deformation diagram for bundle (1) consisting of 112 E-glass fibers and yarn (2) consisting of 216 fibers coated with resin.

TABLE 8

STRENGTH OF MONOFILAMENT, BUNDLE OF MONOFILAMENTS, AND BUNDLE IN MATRIX AS A FUNCTION OF LENGTH

Monofilament Length in cm	$\bar{\sigma}_{bt}$ of Monofilaments	$\bar{\sigma}_{bt}$ (calc) of Monofilament Bundle	σ_{bt} of Bundle in Matrix
	in kgf/mm²		
2.5	326	271	294
12.5	287	228	295
25.0	298	231	296

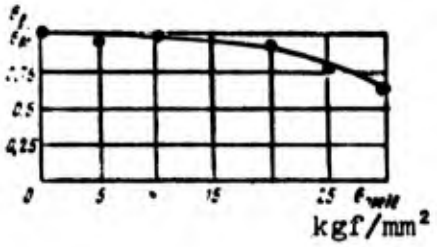

Figure 37. Variation of strength of 33-18c epoxy GRP with degree of prestressing and subsequent water soak (4500 hours).

the load increases until the next fibers break, and after reaching the peak point the load decreases. Also shown is a comparison with the deformation diagram for a bundle in a composite; this curve does not have the jumps caused by breaking of the fibers, since the load is transferred to the other fibers. The curvature of the diagram is associated with the manifestation of stiffness change because of gradual breaking of the fibers.

These experimental data give a basis for assuming that breaking occurs for fiber lengths considerably shorter than the length of the fibers tested.

In view of the variety of the factors affecting the monolithicity condition, it is important in practice to establish the crack formation bounds. Figure 37 shows the strength of 33-18c epoxy GRP as a function of the degree of prestress and subsequent soak in water for 4500 hours. A marked influence of moisture penetrating into the places where continuity is disrupted is observed for stresses $\geq 0.5\sigma_b$.

Figure 38 illustrates the breakdown voltage for polyester GRP plates 1.1 mm thick as a function of the degree of surface deformation, ($\varepsilon \equiv \delta/2\rho$ %), which makes it possible to establish the crack-formation boundary ($\varepsilon \approx 0.52\%$) [205]. Thus, in real composites there is marked disruption of the monolithicity of the structure at stresses and strains which are about half the ultimate values.

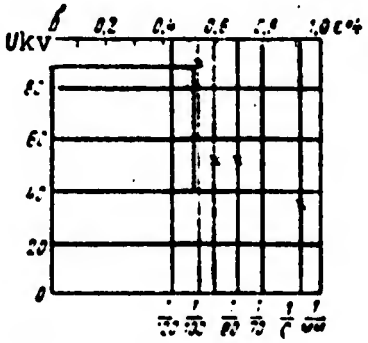

Figure 38. Breakdown voltage for polyester GRP plates as a function of degree of surface deformation.

§5. Limiting States with Regard to Matrix Resistance to Crack Growth

In real composites there are always larger numbers of differently oriented cracks. In this connection, the composite strength depends on the resistance of the polymer binder to crack growth. Therefore, it is of interest to analyze the conditions for transition of a matrix with initial cracks into the nonequilibrium state and the kinetics of macrofracture crack growth. The current ideas on rigid polymer fracture are given in a monograph by Bartenyev [15].

According to Griffith (see §1, Chapter 1), the material fracture condition leads to the relation $\sigma_c\sqrt{c} = \text{const}$, where σ_c is the nominal critical stress; c is the crack length, and we can obviously write $\sigma\sqrt{c_c} = \text{const}$, which defines the existence of cracks of the critical size. A crack of the critical length is unstable; if the crack length is greater than the critical value, it will grow spontaneously for a fixed stress from an external load.

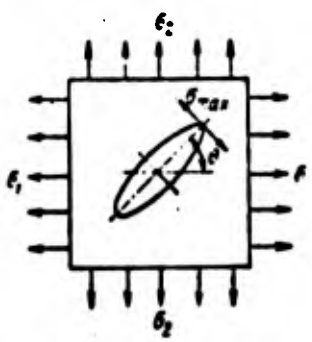

Figure 39. Stresses at tip of elliptic crack.

The submicroscopic cracks which arise in deformable specimens in the early fracture stages have been studied using optical and other methods by Zhurkov [48].

Griffith and Smecal examined microcracks of elliptic form (Figure 39).

The maximum stresses at the tip of an elliptic crack with semi-axes a and b ($b/a \ll 1$) are defined [147] in terms of the principal stresses σ_1 and σ_2

$$\sigma_{max} = (\sigma_2 - \sigma_1)\cos 2\theta + \frac{a}{b}[(\sigma_1 + \sigma_2) - (\sigma_2 - \sigma_1)\cos 2\theta] \qquad (23)$$

(see Figure 39), or in terms of the nominal stresses σ_n in the crack plane far from the crack

$$\sigma_{max} = (\sigma_2 - \sigma_1)\cos 2\theta + 2\frac{a}{b}\sigma_n. \qquad (24)$$

For a crack oriented perpendicular to the stress σ_2, so that $\theta = 0°$, for $a/b \gg 1$ the primary term in (23) is the second term, and the concentration effect for $\sigma_1 = 0$ and $\sigma_2 = \sigma$ is evaluated as

$$\sigma_{max} = \sigma\left[1 + 2\frac{a}{b}\right] \approx \sigma 2\frac{a}{b} \qquad (25)$$

($K = 2\ a/b$). For cracks of nonelliptic form, the quantity $2\ a/b$ is replaced by the ratio $(2c/\rho)^{1/2}$, where $c = 2a$ is the crack length and $\rho = b^2/a$ is the radius of curvature at the tip of the crack. In this case, the stress concentration is evaluated by the quantity $K = \sqrt{2c/\rho}$.

Smecal [194] suggested that an elementary volume with an elliptic crack fails if the maximum stress σ_{max} reaches the value of the theoretical strength with the correction $\sqrt{4/\pi} = 1.13$. *

$$\sigma_{max} = \sqrt{\frac{4}{\pi}}\sigma_m.$$

For $\theta = 0$

$$\sigma = \frac{\sigma_m}{K}\sqrt{\frac{4}{\pi}} = \sqrt{\frac{4E\alpha_{sur}}{\pi c}}\sqrt{\frac{\rho}{r_0}}. \qquad (26)$$

The theoretical strength is calculated from the energy balance condition for free surface formation as a result of elastic energy accumulation in a layer of thickness $2r_0$, r_0 is the equilibrium interparticle distance: $\sigma_y \approx \sqrt{2E\alpha_{sur}/r_0}$; $r_0 = 5\cdot10^{-8}$ cm. The ratio $\sigma_y/\sigma = \sqrt{\pi c/2\rho} \approx \sqrt{(\pi/2)(c/r_0)}$, if the crack width is $2r_0$, can be considered the stress concentration at the tip of a single crack.

---

*This coefficient is adopted for agreement with the Griffith criterion.

The Griffith fracture mechanism [143] is applicable to the athermal fracture process, in which the thermal motion of the body particles can be neglected. The energy balance condition (§1, Chapter 1) is valid for the equilibrium state, in which the crack growth rate is zero.

When the crack grows at a certain rate, as a result of interparticle bond breaking there is an energy dissipation; moreover, part of the energy is necessary for moving the crack walls apart. If the fracture energy is referred to a unit fracture surface, the Griffith formula will have the form [143]

$$\sigma_{кр} = \frac{2}{\sqrt{\pi}} \sqrt{\frac{T_{с.э} E}{c}}, \tag{27}$$

where $T_{c.e}$ is the characteristic energy of the fracture process; the other notations are the same as before. The magnitude of the characteristic energy exceeds considerably (by nearly four orders) the value of α_{sur} for the polymers. For example, for polymethyl methacrylate and polystyrene at 20° C, this energy amounts to $5 \cdot 10^5$ and $9 \cdot 10^5$ erg/cm^2.

According to Irwin [149, 207], a crack in a material advances by the distance α if the work on crack growth, including plastic deformation energy, reaches the value necessary for the formation of a new surface. The energy balance condition thus includes the plastic deformation energy

$$\frac{d}{dl}\left[\left(-\frac{\sigma^2 \pi l^2}{E} + 4l(\alpha_{пл} + \alpha_{sur})\right)\right] = 0. \tag{28}$$

Assuming that the energy released during crack growth is numerically equal to the work to close the crack, we can calculate the crack growth energy.

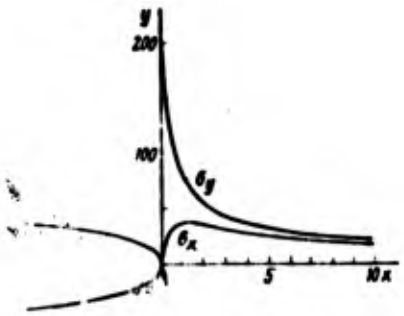

Figure 40. Stresses at crack tip [211].

The stress distribution in the crack vicinity for a point with coordinates θ and ρ is defined by the Westergaard equations

$$\left.\begin{aligned}\sigma_x &= \frac{K}{\sqrt{2\pi\rho}}\cos\frac{\theta}{2}\left(1-\sin\frac{\theta}{2}\sin\frac{3\theta}{2}\right);\\ \sigma_y &= \frac{K}{\sqrt{2\pi\rho}}\cos\frac{\theta}{2}\left(1+\sin\frac{\theta}{2}\sin\frac{3\theta}{2}\right);\\ \tau_{xy} &= \frac{K}{\sqrt{2\pi\rho}}\cos\frac{\theta}{2}\sin\frac{\theta}{2}\cos\frac{3\theta}{2},\end{aligned}\right\} \quad (29)$$

where $K = \sigma\sqrt{c}$ is a coefficient characterizing the stress intensity.

The displacement along the y axis, which is the crack opening, is described by the Equation (Figure 40)

$$v = \frac{K\sqrt{2\rho}}{(1-\mu)E}\left[(1-\mu)2\sin\frac{\theta}{2} - \frac{1}{2}\sin\theta\cos\frac{\theta}{2}\right], \quad (30)$$

and the energy for a plate of unit thickness is calculated with account for (29) and (30)

$$\Delta W = \int_0^a \frac{1}{2}\sigma_y v\,dx = \frac{\pi K^2 a}{E}.$$

The rate of elastic energy release is defined as dW/dF, where F is the crack area in a plate of unit thickness

$$\frac{dW}{dF} = \frac{\pi K^2}{E} = \frac{\pi\sigma^2 c}{E}. \quad (31)$$

With increase of σ, the quantity dW/dF increases to the critical value and a crack develops. Up to this value, each value of σ corresponds to a definite length of the equilibrium crack. When K reaches the value K_{cr}, the crack becomes unstable and grows spontaneously.

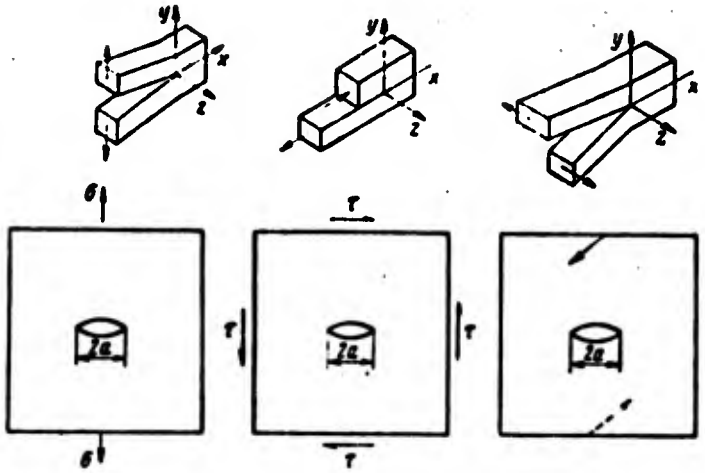

Figure 41. Basic forms of crack growth.

The material resistance to crack growth can be determined experimentally, since at the moment of crack growth initiation, the quantity $\pi K^2/E$ is equal to this resistance in the plane stress state case and $(1 - \nu^2)\pi K^2/E = dW/dF$ in the plane strain case. The influence of inelastic deformation, localized in a narrow region at the tip of the crack, is accounted for under the assumption that — in place of the crack of length 2c — we consider a crack of length $2(c + r_{pl})$, where $r_{pl} \approx K^2/2\sigma_y^2$.

The nominal stress at fracture is defined by the relation

$$\sigma = \sqrt{\frac{2E(\alpha_{n\omega} + \alpha_{n\delta})}{\pi c}}.$$

Direct application of these results to the reinforced materials is difficult. The complexity of the composite structure determines the great variety of crack forms, which affect differently the capability of the material to withstand cracking. The question of the determination of the crack growth energy magnitude has not received adequate study and quantitative data for matrices and composites are not available.

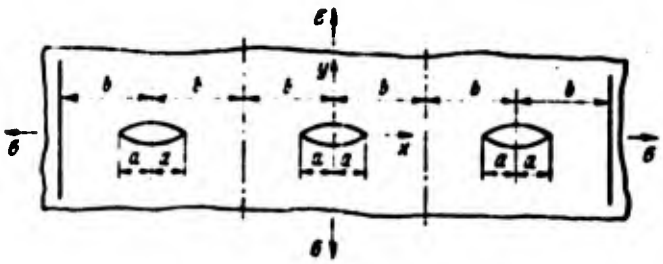

Figure 42. Schematic of periodic crack arrangement.

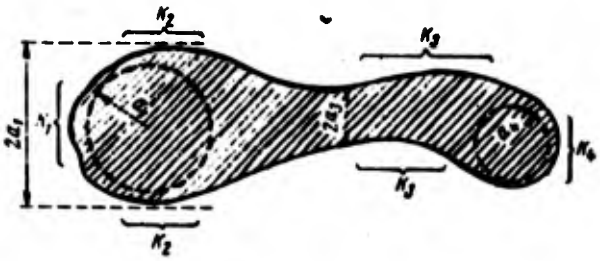

Figure 43. Crack of irregular form.

The basic crack growth modes are shown in Figure 41. The stress state for these cases was analyzed in detail in [179]. The values of the coefficients K_I, K_{II}, K_{III} (Figure 41) are

$$K_I = C_1\sigma\sqrt{c};$$
$$K_{II} = \tau(\pi c)^{1/2};$$
$$K_{III} = \tau(\pi c)^{1/2},$$

where C_1 is a constant, $K_{II} = K_{III} = 0$;

$$K_I = K_{III} = 0;$$
$$K_I = K_{II} = 0.$$

In the presence of a series of cracks arranged periodically (Figure 42), we have

$$K_I = \sigma(\pi c)^{1/2}\left(\frac{2b}{\pi c}\operatorname{tg}\frac{\pi c}{2b}\right)^{1/2},$$
$$K_{II} = K_{III} = 0.$$

For a crack of irregular shape (Figure 43), the value of K is determined by comparing the quantities

$$K_1 \approx 0{,}75\sigma(\pi c_1)^{1/2};$$
$$K_2 \approx 0{,}85\sigma(\pi c_2)^{1/2};$$
$$K_3 \approx 1{,}05\sigma(\pi c_3)^{1/2};$$
$$K_4 \approx 0{,}75\sigma(\pi c_4)^{1/2},$$

from which the largest value is taken. All these coefficients can be functions of the deformation rate [179].

Korten [65] made an approximate evaluation of the dependence of K on the matrix and fiber moduli ratio and the crack dimensions for the case of a single fiber breaking in a polymer matrix and a crack in the form of a disk with radius (r_a + c), where r_a is the radius of the fiber

$$\frac{K_{I\,cr}}{\sigma_a\sqrt{r}} = \frac{1}{\pi}\left[2\frac{E_m}{E_a}\sqrt{\frac{c}{r_a}+1} + \frac{1}{\sqrt{\frac{c}{r_a}\left(\frac{c}{r_a}+1\right)}}\right], \qquad (32)$$

where σ_a is the nominal stress in the fibers; r is the radius of the crack.

We have noted previously that the presence of such cracks was confirmed by the experiments of S. Zhurkov [48]; moreover, at the interface [104] a zone of binder disintegration develops because of incomplete hardening.

Analysis of (32) shows that, with an increase of the relative crack dimension c/r_a from 0 to 1, the quantity $K_{I\,cr}/\sigma_a\sqrt{r}$ decreases and is minimum for $c/r_a = 1$. In spite of the approximate nature of the equation, we can note certain characteristics.

For a given ratio E_m/E_a with an allowable c/r_a, some limiting value of $K_{I\,cr}/\sigma_a$ is required. The crack in the matrix around the broken fiber will be smaller, the higher the plasticity of the matrix and the smaller the product $\sigma_a\sqrt{r}$. Consequently, for a specific value of $K_{I\,cr}$ the allowable stress σ_a in the fiber is larger, the smaller the fiber diameter. Fibers of small diameters thus prevent cracking

of the matrix. The use of stronger fibers requires increase of binder plasticity to prevent its cracking.

Data from tests of plane epoxy matrix specimens with side notches are presented in [65]. The estimate of K_I was made using the relation of [149] with account for inelastic deformations ($\sigma_y = \sigma_{0,2}$ was assumed)

$$K_I = \sigma_m \left[\frac{b}{\pi} \operatorname{tg} \frac{\pi (c + r_{pl})}{b}\right]^{1/2}, \tag{33}$$

where σ_m — nominal stress in the matrix without account for the notch;

c — half the crack (notch) length;

b — specimen width;

r_{pl} — correction for the size of the plastic zone.

For the DER332 epoxy binder, the quantity $K_{I\,cr} = 56$ kg/cm$^2 \cdot$cm$^{1/2}$. For the same resin with the introduction of a plasticizer (40% x 26732) the value of K_I increases and reaches 179 kg/cm$^2 \cdot$cm$^{1/2}$.

Quite high resistance of the matrix binders to crack growth is necessary to obtain high-strength composites.

For the hard polymers, it has been established [14, 43, 46, 47, 49] that fracture occurs at stresses σ less than the critical value σ_c. Observation of crack growth shows that there are two fracture stages: the first is associated with slow growth of the initial crack, leading to the formation of a smooth, mirror-like surface (thermal phase), the second is the athermal phase with growth of the initial and secondary cracks with velocity close to the speed of sound, accompanied by the formation of a rough zone. In the first stage, the crack growth rate depends on the stress, temperature, and the medium. *

*The influence of atmospheric moisture on the hard polymers is not great. The temporal relations in air and in a vacuum practically coincide for the hard polymers.

The most frequently encountered type of hard polymer failure [15] is the growth of the initial crack from the most critical defect. When the stress in the remaining portion of the section exceeds σ_c, competing secondary cracks develop and cleavage lines form when the growth fronts of these secondary cracks meet. The form of these lines characterizes the crack growth kinetics.

In the fast loading case, the elastic strain growth velocity may exceed the speed of sound, and the breaking stresses may become higher than σ_c. Fracture takes place with simultaneous growth throughout the volume of a multitude of cracks, since if $\sigma > \sigma_c$ all defects are hazardous and the critical overstress is reached at the tips of many of these defects.

At the temperature of liquid air, the mirror-like portion on the fracture surface is absent and the time dependence of the strength does not show up. If the load is referred to the area of the rough zone, the same value of σ_c is obtained.

Experimental data [14, 42, 43, 46, 47, 49] have made it possible to formulate the basic temperature-time relationships of polymer resistance to static failure, based on the physical concept of the corresponding molecular mechanism.

The connection between the time-to-failure τ and the magnitude of the static stress σ is expressed by the exponential relation

$$\tau = A\exp(-\alpha\sigma) = A\exp\left(-\frac{U_0 - \gamma\sigma}{KT}\right), \qquad (34)$$

where A and α are constants; K is the Boltzmann constant; T is the temperature in °K; $U = U_0 = \gamma\sigma$ is the fracture process activation energy, which depends on the stress; U_0 is the fracture process activation energy in the absence of stress, close to the chemical bond energy for the polymers; γ is the structure coefficient. The formula is valid over a wide range of temperatures, and in semilog

coordinates σ - lg τ the straight lines form a bundle originating from the point (σ_c, lg τ_0). For relatively low temperatures and high loading rates, fracture of the hard polymers takes place at stresses close to the critical value σ_c.

If σ = const, the temperature dependence of the lifetime is defined by the relation

$$\tau = \tau_0 \exp \frac{U}{KT}, \tag{35}$$

where τ_0 is a constant, numerically close to the thermal vibration period of the atoms (10^{-12} - 10^{-13} sec).

Equation (34) may be reduced to the form

$$\lg \tau = \lg \tau_0 + \frac{1}{2.3KT}(U_0 - \gamma\sigma), \tag{36}$$

and the constants A and α in (34) will be equal to $A = \tau_0 \exp x$ U_0/KT, $\alpha = \gamma/KT$. For a stress $\sigma = U_0/\gamma = \sigma_c$, the life is independent of temperature and equal to τ_0.

Thus, the primary factors determining failure of the hard polymers are stress and temperature. On the basis of the molecular mechanism for the growth and closure of cracks [15], Bartenyev showed the existence of a stress level at which cracks do not grow

$$\sigma_m = \frac{2\alpha_{cp}}{2r_0 k} = \frac{\alpha_{cp}}{k\lambda_0}, \tag{37}$$

where k is the coefficient of stress concentration at the crack tip; r_0 is the equilibrium interparticle distance.

Examining crack growth rate with account for the actual stress at failure of part of the section, he determined the time to failure for a given stress as the sum of the time to failure in the first and second stages (see §3)

$$\tau = \int_0^{c_\kappa} \frac{dc}{v} - \tau_\kappa \frac{b - c_\kappa}{b} = b \int_0^{y_\kappa} \frac{dy}{v} + \tau_\kappa (1 - y_\kappa), \tag{38}$$

where c_c — critical crack length;

b — specimen width;

y_c — relative crack length;

v — crack growth velocity;

τ_c — specimen failure time with application of the critical stress.

If a crack is present in the material in the original state, the integration is performed not from zero but from y_0, and the actual initial stress is equal to $\sigma/(1 - y_0) = \kappa\sigma$. The scatter of the lifetimes for long-term loading is explained by the difference in the different specimens of the coefficient κ, whose value cannot be determined a priori. The random deviations in the crack growth process itself also affect this scatter significantly.

The generalized life curve with account for (34) is described [58] by the equation

$$\sigma - \sigma_\kappa = \frac{2.3KT}{\gamma} (\lg \tau_0 - \lg \tau), \tag{39}$$

since the σ - lg τ curves as functions of the temperature T form a bundle with the pole (σ_c, lg τ_0).

The crack growth phenomenon is also associated with development of elasto-viscous polymer deformations, which occur [87] even in the case of seemingly pure brittle fracture. The elasto-viscous deformation process accelerates in connection with crack formation, leading to further cracking. In the first stage, microcracks develop with nearly identical velocity, since the stress changes slowly for constant external load. The macrofracture crack grows with increasing velocity, which is facilitated by the growth of the actual stress. The formation of a system of microcracks always precedes macrofracture. The first stage occupies the majority of the fracture time, and the

laws governing strength temperature-time dependence are determined basically by this stage. The time dependences show up in resistance to fracture with impact loading.

According to the data of Perry [77], during impact loading of bonded joints the adhesive strength increases, following the same laws as polymer resistance to normal stresses.

The laws governing the strength and deformation of certain reticulate polymer binders have been examined [36] in connection with the deformation rate effect, and a linear dependence of the tensile and shear strength on the logarithm of the deformation rate has been established. The principal elongations at the instant of shear fracture correspond to the principal elongations in tension.

Because of the difficulties associated with generalized rheological models, we shall examine particular loading regimes $\sigma = f(\dot{\sigma})$ and $\sigma = f(\dot{\varepsilon})$.

The breaking stress is proportional to the logarithm of the loading rate $\dot{\sigma}$ for the regime $\dot{\sigma} = \text{const}$:

$$\dot{\sigma} = \frac{1}{A\alpha} e^{\alpha\sigma_0} \quad \text{or} \quad \sigma_0 = \frac{\ln A\alpha}{\alpha} + \frac{1}{\alpha} \ln \dot{\sigma}, \tag{40}$$

where A and α are the constants of the temporal strength relation.

For the constant deformation rate regime, the dependence of strength on strain rate $\dot{\varepsilon}$ is described by the relation

$$\sigma_0 = \sigma_0 - m \ln 10 \left(\lg \frac{\dot{\varepsilon}}{\dot{\varepsilon}_0} - \lg \frac{\sigma_0}{\sigma_0} \right). \tag{41}$$

where m is the rate modulus ($m = 1/\alpha$), the slope [37] of the straight line in the coordinates σ_b - ln τ or σ_b - ln $\dot{\varepsilon}$; σ_0 and $\dot{\varepsilon}_0$ are the magnitudes of the strength and the standard deformation rate.

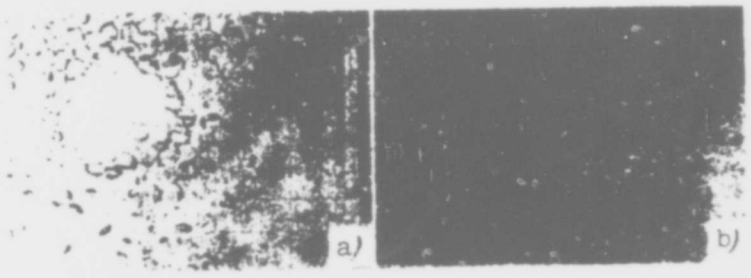

Figure 44. Structural voids in GRP.
a — large voids; b — voids in resin between fibers.

In determining hard polymer lifetime the condition of relative lifetime summation is valid

$$\sum \frac{\Delta\tau_i}{\tau_{\sigma_i}} = 1,$$

where $\Delta\tau_i$ is the time of action of the stress σ_i; τ_{σ_i} is the lifetime for fixed σ_i, which indicates the irreversible nature of the failure [44].

Examination of the model of an idealized composite material consisting of continuous reinforcing fibers and monolithic polymer material showed that material failure takes place as a result of fiber breaking and failure of the binder because of local tangential stress concentration. Defects of processing origin have a marked influence on composite strength and its variance.

Among the most frequently encountered matrix defects are voids, which have a considerable influence on composite material strength. The void dimensions in glass-fiber composites vary over wide limits. Figure 44a shows voids whose dimensions exceed by many fold the fiber dimensions; in Figure 44b the void dimensions are limited to the space between the fibers [118]. The void shape is quite varied and if they have small radii some of them are sources of high stress concentration, capable of fracturing the matrix or disrupting the adhesive bond between the fibers and the matrix.

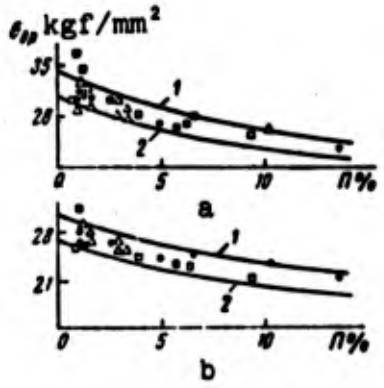

Figure 45. Tensile strength versus void content; composite based on 181-114 glass cloth.

a — dry material; b — wet material; 0 — closed press-form; • — open press-form, Plaskon resin; □ , ■ — same, Selektron resin (1 — upper, 2 — lower strength limit).

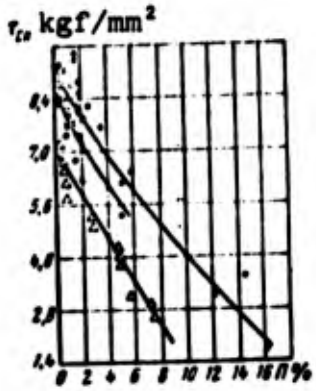

Figure 46. Influence of composite voids on strength in interlaminar shear.

0 — specimen thickness 6 mm; • — thickness 3 mm.

Small voids can be eliminated by using various additives — finishers — large voids can be eliminated by increasing the molding pressure, using a binder with low release of volatiles during hardening, improving impregnation of the filler by the binder, etc.

The volumetric void content is evaluated approximately using the formula

$$\Pi = 1 - \left[\frac{\psi_м}{\gamma_м} + \frac{\psi_в}{\gamma_в}\right]\frac{\gamma_к}{100}, \qquad (42)$$

where Π — volumetric pore content in the composite;

ψ_m, ψ_a — weight contents of the matrix and reinforcing fibers;

γ_m, γ_a — specific weights of the matrix and fibers;

γ_c — specific weight of the composite (ψ_a is usually determined by burning out the matrix).

According to the data of Veier and Pons [65], composite tensile strength decreases monotonically with variation of the porosity from 1 to 14%.(Figure 45). The test results average statistically the influence of the voids as structure defects. Let us examine the

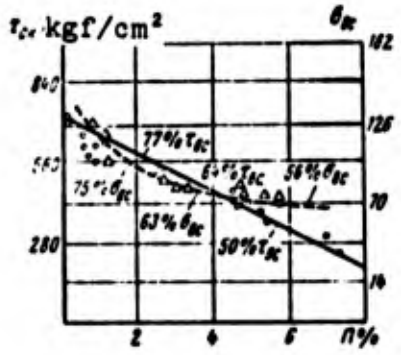

Figure 47. Variation of resistance to shear and compression with void content in composite.

Δ — compression; 0 — shear.

influence of voids on the resistance to interlaminar shear, since the tangential stresses in many cases are the cause of delamination of the composite.

Figure 46 shows the variation of the resistance to interlaminar shear for a composite based on S-glass fibers and epoxy resin, determined in bend testing of short beams, with void content. The interlaminar shear strength for 3-mm thick specimens varies from 8.4 to 5.6 kgf/mm² with increase of the void content in the composite to 5%. For specimen thickness of about 6 mm and variation of the void content from 0 to 15%, the interlaminar shear strength decreases from 9.0 to 2.0 kgf/mm². The lower curve is plotted [137] for epoxy resin and E-glass fibers and confirms the previous remarks. Figure 47 compares the relations for resistance to interlaminar shear and compression as a function of void content.

§6. Characteristics of Structure Defects. Qualitative Picture of Composite Fracture

Two groups of defects are characteristic for real composites [65]: defects near the ends of the fibers in materials reinforced by short fibers or at the location of breaks which arise after failure; disruption of monolithicity of the polymer matrix (surface scratches, gaseous inclusions, initial kinking of the fibers, local cracks at the ends of the reinforcing fibers, segments with failure of the adhesive bond, cracks in the polymer matrix at locations of inclusions of spherical, elliptical, cylindrical, and arbitrary shape, cracks in the binder resulting from stress concentration in the case of dense packing). In many cases, the existence of residual stresses in the binder may also lead to cracking of the binder.

Local failure resulting from structure defects leads to the appearance of cracks which lead to failure of the composite, and crack propagation takes place in various ways.

Microstructural analysis [65] showed that, during fiber fracture, delamination along the fiber over a length exceeding by many times the fiber diameter is possible, which reduces reinforcement effectiveness; fracture of the polymer binder from the ends of broken fibers in the direction toward neighboring fibers was observed. When the crack reaches the neighboring fibers, delamination of the binder from these fibers is observed, and this delamination either propagates to the fiber segment with fracture or is localized. Fracture of the fibers as a result of stress concentration at the tip of the crack is also possible.

Cracking of the polymer binder can take place around the neighboring fibers without their failure, as a rule, in materials with low fiber content and low binder plasticity. In this case, the crack grows perpendicular to the fibers, disrupting fiber adhesion in a limited zone. The binder failure is localized if the crack encounters segments with high resistance to fracture or segments with delamination. The ratio of the adhesive strength in shear to the fiber-matrix bond separation strength for the polyester composites is 1/5 [118]; for the epoxy composites, this ratio is 1/3 = 1/5. If the shearing adhesive strength is higher than the cohesive strength along the crack growth path, the fibers deflect the crack, but the adhesive bond of the fiber with the matrix outside the crack plane is not disturbed (Figure 48a).

If the shear strength of the glass-matrix bond is lower than the cohesive strength, the tensile stresses parallel to the crack front will cause disruption of the adhesive bond in the direction perpendicular to the crack plane. The growth of this second crack also depends on the residual stress at the glass fiber-matrix interface and the free surface formation energy.

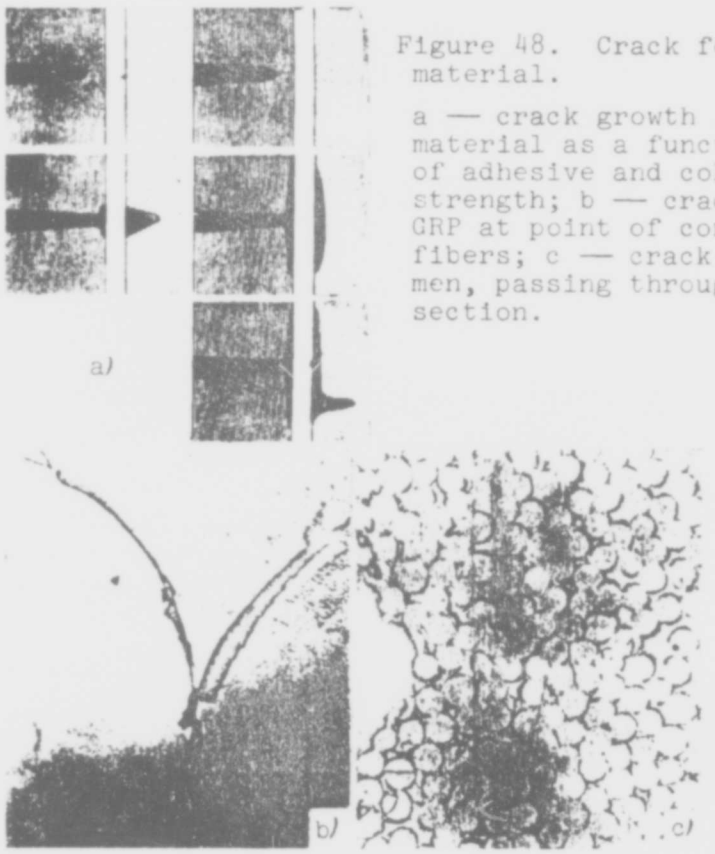

Figure 48. Crack forms in composite material.

a — crack growth in composite material as a function of ratio of adhesive and cohesive resin strength; b — crack onset in GRP at point of contact of two fibers; c — crack in GRP specimen, passing through the entire section.

Defects of processing origin in the matrix are also a source of binder failure. For even small stresses cracks develop as a result of the high stress concentration at the tips of the defects. The experimental data of Feltner [65] showed that cracks are observed in the binder around defects of the structure. The fracture surface of a binder specimen has a smooth zone around a small defect which arises during slow crack growth and a rough zone in the fast growth case. The nominal stresses, responsible for transition from slow to fast fracture, are inversely proportional to the area of the fracture surface smooth zone. For large defects, the smooth zone is small or disappears entirely if the defect has the critical dimensions (see §5).

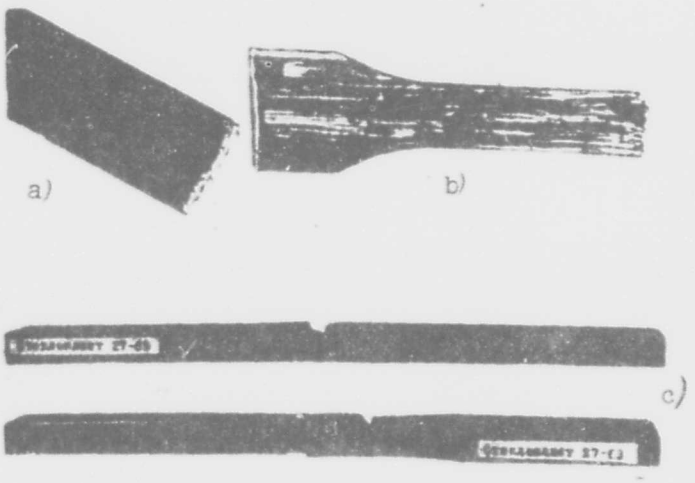

Figure 49. Types of GRP failure.
a — brittle fracture; b — delamination in composite structure as a result of random kinking of fibers; c — fibrous fracture.

Fibers which do not coincide in direction with the acting force cause significant strain concentration in the binder, whose level is determined by the ratio of the elastic moduli of the fiber and resin and the fiber packing density. In this case, the fracture in layers with cross reinforcement takes place at deformations significantly less than the breaking deformations for the pure binder, since the polymer binder volume capable of localizing large local deformations decreases. Figure 48b shows how a sharp corner formed when two fibers contact can serve as a crack site. The direction of a crack which passes through the entire section (Figure 48c) depends on the arrangement of the fibers and weak spots and also disruption of the adhesive bond. In the case of a good adhesive bond between the fibers and matrix and high fiber stiffness, periodic local stress and strain concentration develops through the entire volume of the composite, which is a source for crack formation in the matrix. In the case of a poor adhesive bond, concentration takes place at defect locations, so that in both cases, the presence of the reinforcement in composite materials reinforced by parallel fibers does not prevent crack propagation parallel to the fibers.

As a rule, on microsections of GRP with high fiber content we see a large number of cracks oriented parallel to the fibers. They open up access for moisture to reach the interior elements or lead to disruption of the structure continuity and separate the monolithic structure of the GRP into a series of regions made up of the polymer binder and fiber yarns. In this case, the material resists stresses only along the fibers.

Delamination of GRP can also take place as a result of random curvature of the fibers or of reinforcement consisting of fibrous cloth without pretensioning. In the process of loading of such composites along the fibers, the latter tend to straighten and stress concentration arises in the matrix [27]. Then there is failure of the matrix between the fibers or delamination of the fibers from the matrix. This sort of defect and failure resulting from fiber curvature is superposed on the previously described phenomena and complicates the fracture picture.

Two forms of fracture are observed in tensile tests of composite models: in specimens with a thick binder layer cracks in the polymer matrix lead to fracture of the fibers (the specimen separates into two parts), while for specimens with a thin binder layer fast serrated (fibrous) fracture resulting from failure of the fibers and delamination is characteristic. These two cases are also observed in testing multilayer composites. Failure of the first form takes place along an area oriented normal to the effective stresses, and is characteristic for materials with relatively brittle matrix and low fiber content, when fracture occurs prior to disruption of the adhesive bonds.

In failures of the second form, short segments of the fracture surface are also oriented perpendicular to the tensile stresses; however, they are joined with one another by large shear failure (delamination) segments. In this case, the binder has high adhesion to the fibers, and there is an accumulation of individual failure sites in the material; the fiber content will be considerably higher than in the first case.

The fracture types are shown in Figure 49a, b, c for phenolic and epoxy composites with the same degree of reinforcement and the same fiber arrangement.

In the case when a very thick layer of binder is applied to the surface of the specimen or upper layers are applied with transverse fibers, it is possible to observe cracking of the binder at loads and deformations considerably below the ultimate values. The network of parallel cracks becomes "denser" with load increase and propagates across the entire width of the specimen. The load is taken by the glass fibers of the neighboring layer, and their strength determines the strength of the entire specimen.

In the case of fracture of specimens with a thin layer of binder on the surface or when testing unidirectional composites, the failure of several fibers leads to the onset of longitudinal cracks whose length depends on the defect distribution among the neighboring fibers. These fibers fail when the stresses with account for concentration in the delamination crack exceed the fiber strength of their weak spot. After the failure of one or more fibers, delamination again takes place, and as a result of growth of the process a fracture of fibrous nature is obtained. As a result of delamination, the fracture travels to the other weak spots in the material.

However, in both cases, the role of binder strength or, more precisely, the ratio of tensile strength and adhesive shear strength is obvious. In the case of fracture of the binder from normal stresses brittle fracture dominates; in the case of shear failure of the matrix, the fracture will be ductile-fibrous.

Here we should also bear in mind the directional nature of the binder. For example, as a rule materials with regular fiber yield fibrous fractures, which is explained by shear failure at points when the fibers curve. The binder cracks, and on the tension diagram we

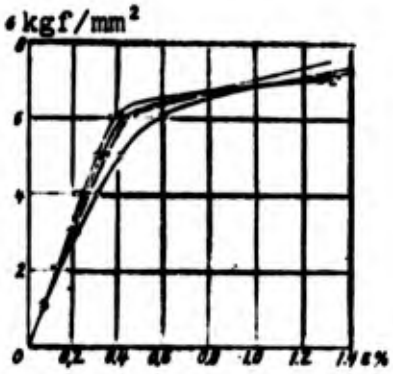

Figure 50. Deformation diagram for material with fibrous fracture.

see a large "pseudo-plasticity" segment as a result of spreading apart of material, working in the last stage as a bundle of separate fibers (Figure 50).

Chapter 6

STATIC STRENGTH OF GRP AS REINFORCED COMPOSITES IN THE STATISTICAL ASPECT

§1. Statistical Concepts of Progressive Fracture

The assumption of fibrous material failure upon reaching the breaking strain in the individual fibers should be examined in the statistical sense, since the breaking deformation is not a deterministic quantity for a bundle of fibers. On the basis of the statistical characteristics of reinforcing fiber strength, the failure of a reinforced plastic in tension can be described by successive breakdown of the fibers to the point of formation of fibers of the critical length, which are not capable of transmitting normal stresses because of shear failure of the matrix.

Let us assume that:

1) the composite material consists of equally loaded reinforcing fibers and a matrix, which are monolithically connected with one another;

2) the fibers contain randomly distributed defects; therefore, their fracture takes place at different stress levels;

3) the tensile stresses in the matrix are lower than those in the reinforcing fibers, and the shear deformations in the fibers are negligibly small in comparison with those in the matrix;

4) near an internal fiber break in the composite, the axial load taken by the fiber is transmitted to the neighboring fibers by shear stresses in the matrix;

5) accumulation of such random fractures in the composite materials leads to the appearance of a large number of nonoperating fiber segments at one spot and the formation of a weak section, which leads to fracture of the composite as a whole.

At some distance from the point of internal fiber fracture, the stress in the fiber constitutes some fraction θ of the nominal stress in a continuous fiber. This fraction of the average stress can be determined by assuming that the segment of length δ, within the limits of which the stress $\sigma < \theta\sigma_{ao}$, can be considered [93] (Figure 1a) "nonworking."

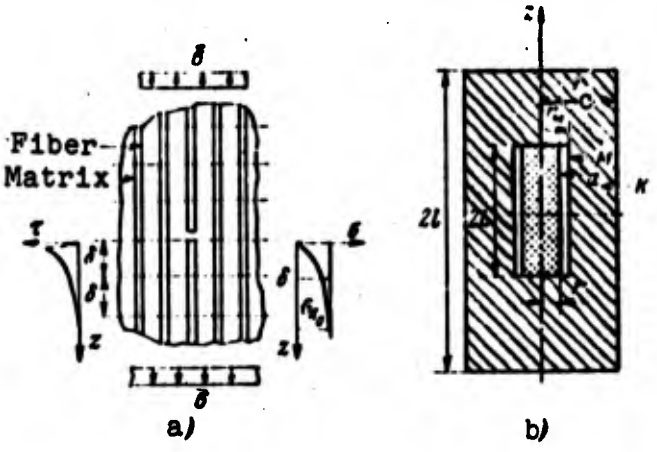

Figure 1. Tangential stress concentration and stress transmission during failure of a composite material (a) and the material model (b). K denotes the composite; M denotes the matrix; and a denotes the fiber.

Consequently, a reinforced material can be considered to consist of several layers of thickness 2δ. Each fiber which fails within the limits of this layer not only cannot transmit the load to the neighboring layers, but even within the layer limits it cannot accept stresses larger than $\theta\sigma_{ao}$. We consider that the applied load is uniformly distributed over all the unfractured fibers of each layer. The segment corresponding to a single layer can be considered a link in the chain forming the fiber. Then each layer is a bundle of links, and the composite material is a sequential connection of layers (bundles). The composite material fails as soon as any layer fails, and the material strength thus depends on the reinforcing fiber characteristics within the limits of the layer and the matrix characteristics.

The strength of fibers of length L which reinforce a material can be examined as the strength of a chain consisting of L/δ links. The length 2δ of the "nonworking" segment is determined by the tangential stress distribution on the fiber-matrix contact surface. This model is shown in Figure 1b. It consists of a fiber surrounded by matrix, which in turn interfaces with the composite, considered as an averaged material. If an axial load acts on the model, the stresses are evaluated as follows. The stresses are not transmitted in the axial direction from the end of a fiber to the "averaged" material. The tensile stresses in the matrix are neglected. The shear deformation in the fiber and in the "averaged" material decays at a small distance from the corresponding surfaces of contact with the matrix [102, 176, 210].

From the condition of fiber element equilibrium in the axial direction, we write the relation

$$\tau + \left(\frac{r}{2}\right)\frac{d\sigma_a}{dz} = 0, \tag{1}$$

where τ is the shear stress in the matrix; σ_a is the axial stress in the fiber; r is the radius of the fiber.

For the definition of r_c and r_m see Figure 1b. From the condition of composite equilibrium in the axial direction we have

$$\left(\frac{r}{r_a}\right)^2 \sigma_a + [(r_a^2 - r_a^2)/r_a^2]\sigma_a = \bar{\sigma}; \tag{2}$$

where σ_c is the average axial stress in the composite; $\bar{\sigma}$ is the uniformly distributed tensile stress (see Figure 1a).

We denote displacements in the fiber by u_a and in the averaged material by u_c. Then the shear deformations of the matrix are

$$u_c - u_a = (r_m - r)\gamma. \tag{3}$$

Differentiating (3) and using the relation between the stresses and strains, we obtain

$$\frac{1}{E_c}\cdot\frac{d\sigma_c}{dz} - \frac{1}{E_a}\cdot\frac{d\sigma_a}{dz} = \frac{r_m - r}{G_m}\cdot\frac{d^2\tau}{dz^2}, \tag{4}$$

where E_c, E_a are the moduli of elasticity of the composite and fibers; G_m is the shear modulus of the matrix.

Differentiating (1) and substituting the result into (2) and (3), we obtain

$$\frac{d^2\tau}{dz^2} - \eta^2\tau = 0, \tag{5}$$

where

$$\eta^2 = \frac{2G_m}{E_a(r_m - r)r}\left[1 + \frac{E_a}{E_c}\left(\frac{r^2}{r_a^2 - r^2}\right)\right].$$

Equation (5) has a solution in the form

$$\tau = A \operatorname{sh} \eta z + B \operatorname{ch} \eta z. \tag{6}$$

For the boundary conditions $\tau_{z=0} = 0$; $\sigma_{a_{z=L}} = 0$, we obtain the values B = 0 and

$$A = \frac{G_m \bar{\sigma} r_a^2}{\eta E_a (r_m - r)(r_a^2 - r_m^2) \operatorname{ch} \eta l}.$$

Hence, the tangential stresses

$$\tau = \frac{G_m \bar{\sigma} \operatorname{sh} \eta z}{\eta E_a (r_m - r)(r_a^2 - r_m^2) \operatorname{ch} \eta l}. \tag{7}$$

According to (2) and (7), the normal stresses

$$\sigma_a = -\frac{\bar{\sigma} r_a^2 E_a}{E_a (r_a^2 - r_m^2) + E_m r_m^2} \left(\frac{\operatorname{ch} \eta z}{\operatorname{ch} \eta l} - 1 \right). \tag{8}$$

For $r_c \gg r_m$

$$\eta^2 \approx 2G_m / r E_a (r_m - r); \tag{9}$$

$$\sigma_a = -\frac{\bar{\sigma} E_m}{E_a} \left[\frac{\operatorname{ch} \eta z}{\operatorname{ch} \eta l} - 1 \right], \tag{10}$$

and we define the maximum axial stress as

$$\sigma_{a\,max} = -\bar{\sigma} \frac{E_m}{E_a}. \tag{11}$$

Let us estimate the value of the quantity $\theta = \sigma(\delta)/\sigma_{a0}$. The stress at the distance δ from the end of the fiber is

$$\sigma_a(L-\delta) = -\frac{\eta E_a}{E_a}\left[\frac{\operatorname{ch}\eta(L-\delta)}{\operatorname{ch}\eta L} - 1\right] \tag{12}$$

and

$$\theta = \frac{\sigma_a(L-\delta)}{\sigma_a(\delta)_{L=\infty}} = 1 - \operatorname{ch}\eta\delta + \operatorname{th}\eta L \operatorname{sh}\eta\delta. \tag{13}$$

For large values of L th ηL = 1; therefore

$$\theta = 1 - \operatorname{ch}\eta\delta + (\operatorname{ch}^2\eta\delta - 1)^{1/2}. \tag{14}$$

Hence, ch $\eta\delta$ = [1 + (1 - θ)^2]/2(1 - θ) and the relative length of the nonworking segment is

$$\frac{\delta}{d} = \frac{1}{2}\left[(\eta_a^{-1/2} - 1)\frac{E_a}{G_m}\right]^{1/2} \operatorname{ch}^{-1}\left[\frac{1 + (1-\theta)^2}{2(1-\theta)}\right]. \tag{15}$$

Figure 2 shows the "nonworking" segment lengtns versus the ratio of the component moduli for different reinforcement ratios. We write the ratio of the tangential stresses to the nominal axial stress in the fiber

$$\frac{\tau}{\sigma_{a0}} = \frac{1}{2}\left(\frac{G_m}{E_a}\right)^{1/2}\left(\frac{\eta_a^{1/2}}{1-\eta_a^{1/2}}\right)^{1/2}(\operatorname{ch}\eta z - \operatorname{sh}\eta z), \tag{16}$$

where

$$\eta^2 = \frac{G_m}{E_a}\left(\frac{\eta_a^{1/2}}{1-\eta_a^{1/2}}\right)\left(\frac{1}{r}\right)^2.$$

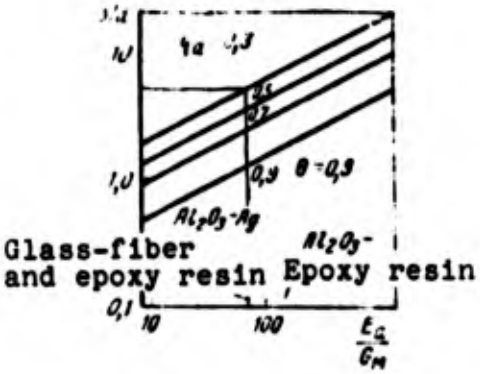

Figure 2. Length of "nonworking" segment in composite materials as function of fiber and matrix properties.

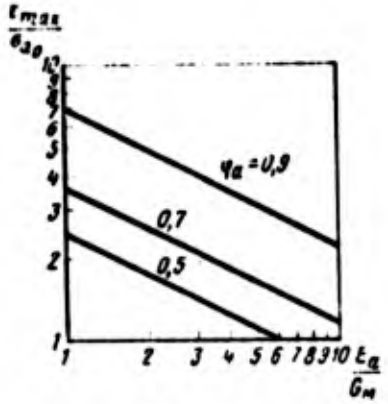

Figure 3. Maximum tangential stresses at fiber-matrix contact surface.

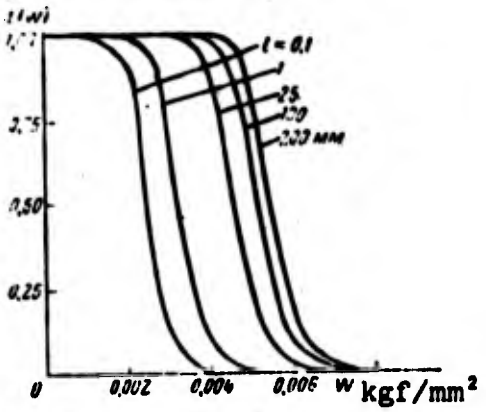

Figure 4. Strength distribution of fibers of different length.

Figure 3 shows the variation of the maximum tangential stresses at the surfaces of contact of the fiber with the matrix as a function of the ratio of the component moduli for different reinforcement ratios. Now let us examine the fracture conditions in connection with variance of the fiber strength characteristics. The distribution curves of the reciprocal strength for fibers of different length are shown in Figure 4. The values of w_{cr} correspond to the reciprocal of the maximum fiber stress at which fast fracture of the bundle begins.

Assuming that the strength distribution of fibers of length δ is defined by the probability density curve $p_\delta(\sigma)$, where $p_\delta(\sigma)d\sigma$ is the probability that the strength of a given elementary fiber lies between σ and $\sigma + d\sigma$, the probability that the fiber strength is higher than σ is $\int_\sigma^\infty p_\delta(\sigma)d\sigma$, and the probability that the links from 1 to $n = L/\delta$ have a strength lying between σ and $\sigma + d\sigma$ is $np_\delta(\sigma)d\sigma$. The probability that none of the elementary fibers fail for the stress σ will be

$$\left[\int_{\sigma}^{\infty} p_0(\sigma)\,d\sigma\right]^{n-1}.$$

Let us determine the probability that the breaking load for a chain consisting of n links lies between σ and σ + dσ

$$p(\sigma)\,d\sigma = np_0(\sigma)\times \times\left[\int_{\sigma}^{\infty} p_0(\sigma)\,d\sigma\right]^{n-1} d\sigma. \tag{17}$$

With account for the fact that $\int_0^{\sigma} p_0(\sigma)d\sigma = P_0(\sigma)$, we obtain $\int_{\sigma}^{\infty} p_0(\sigma)d\sigma = 1 - P_0(\sigma)$ and (17) can be written as

$$p(\sigma)\,d\sigma = = np_0(\sigma)\,[1 - P_0]^{n-1}\,d\sigma. \tag{18}$$

Then the statistical fiber strength distribution function in integral form is

$$P(\sigma) = \int_0^{\sigma} p(\sigma)\,d\sigma = \int_0^{\sigma} np_0(\sigma)\,[1 - P(\sigma)]^{n-1}\,d\sigma, \tag{19}$$

and after integrating

$$P(\sigma) = 1 - [1 - P_0(\sigma)]^n. \tag{20}$$

Weibull [206] proposed writing the function $P_0(\sigma)$ in the form of a power-law dependence on the stress

$$P_0(\sigma) = \left(\frac{\sigma - \sigma_u}{\sigma_0}\right)^m, \tag{21}$$

where σ_0 is a parameter having dimensions of a stress; σ_u is the lower breaking strength; m is a parameter characterizing the degree of nonuniformity of the properties and in the present case, it defines the glass fiber surface defects.

Then the fiber strength statistical distribution function

$$P(\sigma) = 1 - \left[1 - \left(\frac{\sigma - \sigma_u}{\sigma_0}\right)^m\right]^n. \tag{22}$$

For small values of $(\sigma - \sigma_u)/\sigma_0$ the right side of the equation is approximated by the expression

$$P(\sigma) \approx 1 - e^{-n\left(\frac{\sigma - \sigma_u}{\sigma_0}\right)^m}. \tag{23}$$

Following [188, 28], we define the average strength of monofilaments having such a strength distribution function as

$$\bar{\sigma} = \sigma_0 n^{-1/m} \Gamma\left(\frac{m+1}{m}\right) + \sigma_u, \tag{24}$$

and the mean square deviation

$$\bar{s} = \sigma_0 n^{-1/m} \sqrt{\Gamma\left(\frac{m+2}{m}\right) - \Gamma^2\left(\frac{m+1}{m}\right)}, \tag{25}$$

where Γ is the gamma function.

For n = 1, we obtain from (23) - (25) the parameters for the strength distribution of a single element (elementary volume) and the distribution curve which characterize the microstructure property distribution.

We can also use the Gauss, Pearson, Maxwell, and other curves to describe the strength distributions of the elementary volumes. After several simplifications, we calculate in final form the mean values and variances of the macrovolumes (Table 1).

TABLE 1

Probability Density Function	Most Probable Value	Mean Value	Mean Square Deviation
Laplace	$\sigma_0\left[\alpha-\ln\frac{V}{V_0}\right]$		$\frac{\pi}{\sqrt{6}}\sigma_0$
Gauss	$\sigma_0\left[\alpha-\sqrt{2\ln\frac{V}{V_0}}\right]-\frac{\ln\ln\frac{V}{V_0}+\ln 4\pi}{2\sqrt{2\ln\frac{V}{V_0}}}$		$\frac{\sqrt{3}\sigma_0}{2\sqrt{3}}\cdot\frac{1}{\sqrt{\ln\frac{V}{V_0}}}$
Weibull	$\left[1-\frac{1}{m}\right]^{\frac{1}{m}}\sigma_0\times\left(\frac{V_0}{V}\right)^{\frac{1}{m}}$	$\sigma_0\left(\frac{V_0}{V}\right)^{\frac{1}{m}}\times\Gamma\left(1+\frac{1}{m}\right)$	$\sigma_0\left(\frac{V_0}{V}\right)^{\frac{1}{m}}\times\sqrt{\Gamma\left(1+\frac{2}{m}\right)-\Gamma^2\left(1+\frac{1}{m}\right)}$

Figure 5 shows the strength distribution curves for the elementary volumes and the calculated curves for macrovolumes with ratio V/V_0 up to 1000.

For the Laplace distribution, the dispersion remains constant, the mean value decreases, the curves for $V/V_0 > 0$ have left asymmetry, the skewness of the distribution is constant. In case b (Gauss distribution) the mean value and the dispersion decrease, the curves for $V/V_0 > 1$ have left asymmetry, which increases with increase of V. For the Weibull distribution (Figure 5), depending on the exponent m, either left or right asymmetry is possible and for values of m close to 3 the distribution is symmetric, close in form to the Gaussian distribution. With increase of V/V_0, the mean value and variance decrease. For m = 3 (Figure 5d), the right asymmetry decreases with increase of V.

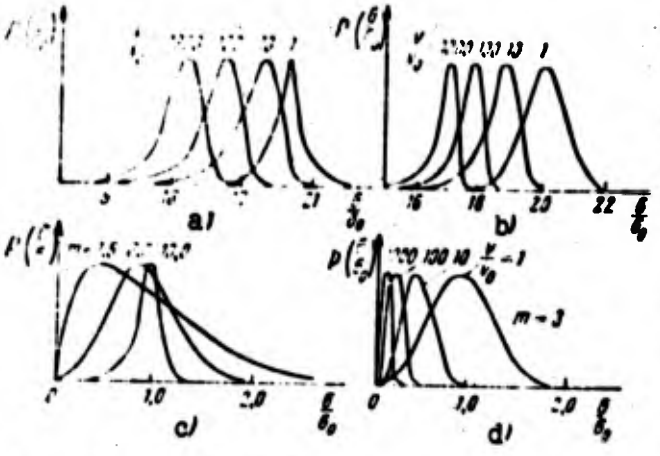

Figure 5. Microstructure strength distribution according to Laplace (a), Gauss (b), Weibull (c) and (d).

Since there is not adequate experimental information on defect distribution in materials and substantiation of the parameters of the material breaking strength distribution functions in connection with defects in the macrovolumes, the macrostructure probability density curves must, generally speaking, be taken on the basis of statistical analysis of the experimental data.

However, in application to fibers, the available results of large-scale tests show (see §1, Chapter 5) that we can use the Weibull distribution, whose advantage lies in the fact that it permits obtaining several estimates of the mechanical properties in finite form. The presence of three constants makes this distribution more flexible and acceptable for a wide range of materials. The power-law nature of the damage accumulation function, adopted a priori by Weibull, variation with increase of the stress has been confirmed by the experiments of Rosen (Figure 6). The values obtained are approximated by a relation of the form $(\sigma/\sigma_0)^m$; $m = 5.25$ (for simplification σ_u is taken equal to zero).

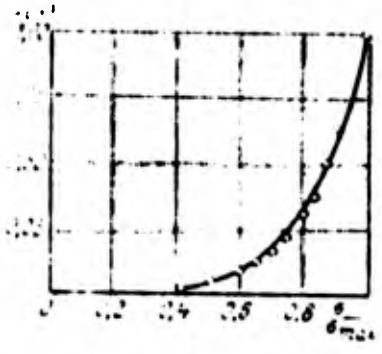

Figure 6. Power-law nature of damage accumulation function for short-term loading of fiber-base composite.

The load on a bundle of fibers of equal diameters with the same tensile stress is [65]

$$Q = \sigma_i F_i.$$

where Q is the load applied to a bundle of N fibers, r of which remain unfailed; σ_r are the stresses in the unfailed fibers, and $r/N = F_r/F_N$; here F_r is the area of the unfailed part of the section; F_N is the initial section area.

We then obtain

$$Q = \sigma_r F_N \tag{26}$$

where the ratio r/N characterizes (for large N) the probability of fiber nonfailure. Using (23), we transform the expression for the load

$$Q = \sigma_r F_N e^{-a\left(\frac{\sigma_r - \sigma_u}{\sigma_0}\right)^m}. \tag{27}$$

since for $N \to \infty (r/N) \approx 1 - P(\sigma)$.

From the load maximization condition $dQ/d\sigma_r = 0$ and taking $\sigma_u = 0$ which for a probability close to 0.5 does not affect significantly the magnitude of the load, we obtain the following relation for the stress in the bundle fibers at the moment of failure

$$(\sigma_r)_{max} = \sigma_0 \left(\frac{1}{mn}\right)^{1/m}, \tag{28}$$

where $n = L/2\delta$.

The maximum load for the fiber bundle is then determined as

$$Q_{max} = \sigma_0 F_N \left(\frac{1}{mn}\right)^{1/m} e^{-1/m}. \tag{29}$$

The strength of a bundle of N parallel fibers for $\sigma_u = 0$ (in nominal stresses) is

$$\bar{\sigma}_0 = \frac{Q_{max}}{f_K} = \sigma_0 \left(\frac{1}{mn}\right)^{1/m} e^{-1/m}. \tag{30}$$

It then follows that the stresses in the fibers at bundle failure are higher than the nominal stresses in accordance with the relation

$$(\sigma_i)_{max} = \bar{\sigma}_0 e^{1/m}. \tag{31}$$

Therefore, the strength of a fiber bundle is directly proportional to the fiber parameter σ_0, decreases with bundle length as $n^{-1/m}$, and depends on the exponent m.

Comparison of the strength of a fiber bundle with the mean strength of a group of fibers when tested separately shows that the ratio $\bar{\sigma}_b/\bar{\sigma}_a$ decreases (for $\sigma_u = 0$) with reduction of m according to the expression

$$\frac{\bar{\sigma}_0}{\bar{\sigma}_a} = \frac{(mn)^{-1/m}}{\Gamma(1+1/m)}. \tag{32}$$

Thus, the realization of the mean fiber strength in a bundle is determined by the exponent m, and the strength of nonuniform bundles is lower than the strength of bundles of uniform fibers. Because of the progressive nature of the failure, the strength of a fiber bundle is always lower than the mean strength of the fibers forming the bundle. The influence of the parameter m on the realizable strength of monofilaments in a bundle, characterized by the ratio $\bar{\sigma}_b/\bar{\sigma}_a$, is shown in Figure 7.

Experimental substantiation of the progressive failure model was obtained in a study by Rosen [93], who analyzed composite material strength using a function of the type (21) in the form

$$p(\sigma) = L\alpha\beta\sigma^{\beta-1}\exp(-L\alpha\sigma^{\beta}), \tag{33}$$

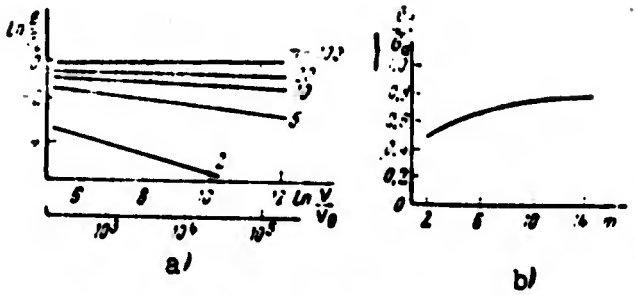

Figure 7. Influence of defect parameter (m) and bundle dimensions (V/V_0) on bundle strength (a); influence of quantity m on ratio of bundle strength to mean strength of group of fibers (b).

Hence, the microstructure strength distribution

$$p_{\sigma}(\sigma) \quad \alpha\beta\delta\sigma^{\beta-1}(-\alpha\delta\sigma^{\beta}), \tag{34}$$

where $\delta = L/n$ is the specific length, and the constants α and β are defined on the basis of the length dependence of the glass fiber ultimate strength. The average glass fiber strength is described as a function of length

$$\bar{\sigma}_{\sigma} = \int_0^{\infty} \sigma p(\sigma)\, d\sigma = (L\alpha)^{-1/\beta}\Gamma\left(1 + \frac{1}{\beta}\right). \tag{35}$$

which yields a linear relation in log-log coordinates. The parameter $\alpha^{-1/\beta}$ has dimensions of a stress and corresponds to some characteristic fiber strength level.

Daniels showed that for any monofilament strength distribution the bundle strength distribution approaches the normal law with mathematical expectation

$$\sigma_{\sigma} \quad \sigma_{\max}[1 \quad P(\sigma_{\max})] \tag{36}$$

and mean square deviation

$$s \quad \sigma_{\max}\sqrt{P(\sigma_{\max})[1 \quad P(\sigma_{\max})]/n}. \tag{37}$$

as $n \to \infty$ the bundle ultimate strength probability density

$$p_n(\sigma_a) = \frac{1}{\sqrt{2\pi}s} \exp\left[-\frac{1}{2}\left(\frac{\sigma_a - \bar{\sigma}_a}{s}\right)^2\right]. \tag{38}$$

Bundles with the distribution (38) are considered sequentially connected links, and the probability density of the fiber stress σ_a corresponding to failure of the material, is

$$\varphi(\sigma_a) = n p_n(\sigma_a)\,[1 - P_n(\sigma_a)]^{n-1}. \tag{39}$$

The quantity $\phi(\sigma_a)d\sigma_a$ is obtained by multiplying the probability of single bundle failure for a stress in the interval from σ_a to $\sigma_a + d\sigma_a$, equal to $[p_n(\sigma_a)d\sigma_a]$, by the probability that the breaking stresses of the remaining n - 1 elements exceed $\sigma_a + d\sigma_a([1 - P_n(\sigma_a)]^{n-1})$. Here failure is possible in any bundle.

The most probable breaking stress σ_c^* is obtained from the condition

$$\frac{d\varphi(\sigma_a)}{d\sigma_a} = 0; \tag{40}$$

$$\sigma_c^* = \bar{\sigma}_a - s(2\ln n)^{1/2} + s\frac{\ln\ln n + \ln 4\pi}{2(2\ln n)^{1/2}}. \tag{41}$$

For $n \gg 1$, $\bar{s} \to 0$

$$\sigma_c^* = (\alpha\lambda\beta e)^{1/\beta}$$
$$(\beta = 7.7;\ \alpha = 1.1\cdot 10^{-13};\ \alpha^{1/\beta} = 21.1\ \text{kgf/mm}^2). \tag{42}$$

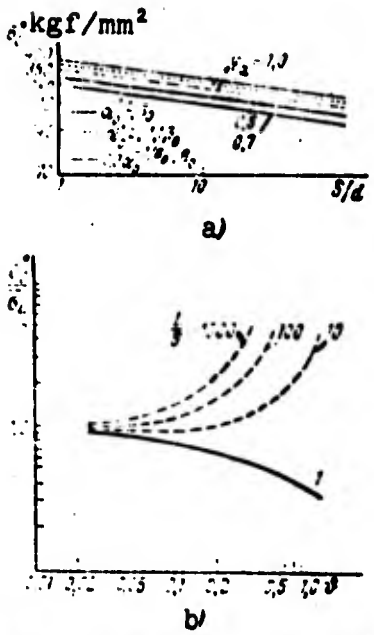

Figure 8. Most probable value of GRP breaking strength (a) [93]; influence of the coefficient of variation and relative fiber length on the ratio of composite strength to mean strength (b) [188].

The breaking stress for the composite is found by multiplying the value of σ_c^* obtained for glass fiber volumetric content equal to 1 by the actual reinforcement ratio ϕ_a. Figure 8a shows the calculated values of the most probable breaking stress of a composite material for values of the "nonworking" segment lengths varying from one to hundreds of fiber diameters; also shown is the influence of increase of the variance (defined by a 10% change in β) and reduction of the maximum strength level (defined by a 10% change in the quantity $\alpha^{-1/\beta}$).

Figure 8b shows the ratio of the most probable breaking stress in the fibers during composite failure to the mean monofilament strength

$$\frac{\sigma_c^*}{\sigma_m} = \left(\frac{\delta}{L}\right)^{-1/\beta} \frac{(\beta e)^{-1/\beta}}{\Gamma\left(1-\frac{1}{\beta}\right)} \tag{43}$$

versus the monofilament strength variation coefficient

$$\frac{\sigma_c^*}{\sigma_m} \quad \frac{\sqrt{\Gamma\left(1+\frac{2}{\beta}\right) - \Gamma^2\left(1+\frac{1}{\beta}\right)}}{\Gamma\left(1+\frac{1}{\beta}\right)} \tag{44}$$

for $L/\delta = 1 - 1000$.

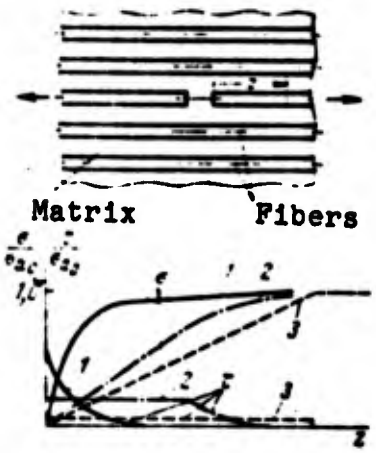

Figure 9. Distributions of normal and tangential stresses for elastic (1), elastoplastic (2), and plastic (3) matrix states.

Stress transfer from the matrix to the fibers for an ideally plastic matrix was examined by Cotrell [127]. In this case, the tangential stresses are constant along the fiber and equal to τ_T. The normal stress increases linearly to the maximum value

$$\sigma_a = \tau_T \frac{\delta}{d}.$$

The presence of plastic deformations of the matrix displaces the boundary of shear fracture crack formation and tends to increase the length 2δ of the "nonworking" fiber segments. In this case, a large region of the tangential stress diagram develops for transmission of the forces. A comparison of the distribution diagrams of the normal and tangential stresses in the fiber rupture zone for the elastic, elastoplastic, and plastic material states is given in Figure 9, where σ_a is the stress in the fibers far from the point of failure [93, 83, 119].

The stress distribution on the surface of contact of the polymer matrix with a fiber with account for elastoviscous deformations of the matrix was examined by Rabinovich [83, 84]. The temporal effects reduce the tangential stresses; therefore, the normal stresses in the fiber increase over a relatively long distance.

As a consequence of tangential stress relaxation, the length 2δ of the nonworking fiber segments increases, which leads to reduction of composite strength, since the probability that random fractures will occur in a large volume increases.

§2. Statistical Estimate of the Limiting State in the Case of Static Tension Failure

Failure of GRP under short-term static loading was examined in [97] on the basis of the dispersion of the properties of elementary cells forming the composite. The unidirectional GRP was represented in the form of individual cells consisting of a glass fiber and the binder surrounding it. Here it was assumed that the stresses acting on each cell are equal in magnitude; the strength of the elementary cells in the section is distributed in accordance with a normal law which is bounded symmetrically on the left and right in the limits

$$a - \varkappa\bar{s} \text{ and } a + \varkappa\bar{s}, \tag{45}$$

where a is the average value of the strength of the elementary cells; $\varkappa$ is a coefficient characterizing the truncation of the distribution and is equal to 1/v; $\bar{s}$ is the mean square deviation.

When the effective stress exceeds the strength level of the elementary cell after cell failure, the load is redistributed over the remaining part of the section and the average stress in the unfailed cells increases

$$\sigma_x = \frac{\sigma_n}{1 - D_x}, \tag{46}$$

where σ_x is the average stress with account for the failed part of the section; σ_n is the average initial stress in the section; D_x is the relative fraction of the failed part of the section.

The strength of the elementary cells has a normal distribution

$$p(\sigma) = \frac{1}{\sqrt{2\pi}\bar{s}} e^{-\frac{(\sigma - a)^2}{2\bar{s}^2}}. \tag{47}$$

The relative magnitude of the area remaining unfailed prior to the final fast fracture is

$$(\Psi_x)_\kappa = 1 - (D_x)_\kappa = 1 - \frac{1}{\sqrt{2\pi}\,\bar{s}} \int_{a-n\bar{s}}^{\sigma_x} e^{-\frac{(\sigma-a)^2}{2\bar{s}^2}} d\sigma = \frac{1}{\sqrt{2\pi}\,\bar{s}} \int_{\sigma_x}^{a+n\bar{s}} e^{-\frac{(\sigma-a)^2}{2\bar{s}^2}} d\sigma. \tag{48}$$

The breaking strength σ_b in terms of the nominal stress

$$\bar{\sigma}_0 = (\Psi_x)_\kappa (\sigma_x)_\kappa. \tag{49}$$

Since the magnitude of the load on the material must be a maximum at the moment of fast fracture initiation, the quantity $(\Phi_x)_c(\sigma_x)_c$ should also be considered maximal.

Using (48), we obtain the connection between the breaking strength and effective stress in the cells

$$\bar{\sigma}_0 = (\sigma_x)_\kappa \frac{1}{\sqrt{2\pi}\,\bar{s}} \int_{(\sigma_x)_\kappa}^{a+n\bar{s}} e^{-\frac{(\sigma-a)^2}{2\bar{s}^2}} d\sigma \tag{50}$$

or

$$\bar{\sigma}_0 = (\sigma_x)_\kappa \frac{1}{\sqrt{2\pi}\,\bar{s}} \left[\int_{(\sigma_x)_\kappa}^{a} e^{-\frac{(\sigma-a)^2}{2\bar{s}^2}} d\sigma + \int_{a}^{a+n\bar{s}} e^{-\frac{(\sigma-a)^2}{2\bar{s}^2}} d\sigma \right]. \tag{51}$$

Both integrals in the right side of (51) are calculated as functions of the Laplace Φ

$$\bar{\sigma}_0 = (\sigma_x)_\kappa \left[\Psi\left(\frac{(\sigma_x)_\kappa - a}{\bar{s}} \right) + \Phi(n) \right]. \tag{52}$$

For the two given stressed areas F_1 and F_2, we can write

$$\bar{\sigma}_{0F_1} = (\sigma_{1F_1})_\alpha \left[\Phi\left(\frac{(\sigma_{xF_1})_\alpha}{s_{F_1}} - \frac{a_{F_1}}{s_{F_1}}\right) + \Phi(x)\right];$$
$$\bar{\sigma}_{0F_2} = (\sigma_{1F_2})_\alpha \left[\Phi\left(\frac{(\sigma_{xF_2})_\alpha}{s_{F_2}} - \frac{a_{F_2}}{s_{F_2}}\right) + \Phi(x)\right]. \tag{53}$$

From similarity of the static fracture conditions it follows that

$$(\sigma_{xF_2})_\alpha = (\sigma_{xF_1})_\alpha \frac{\bar{\sigma}_{0F_2}}{\bar{\sigma}_{0F_1}} \tag{54}$$

characterizes the proportionality between the average strengths of the cells and the specimens with sections F_1 and F_2

$$\frac{a_{F_2}}{a_{F_1}} = \frac{\bar{\sigma}_{0F_2}}{\bar{\sigma}_{0F_1}}. \tag{55}$$

Assuming that the coefficient of variation depends on the area F (which follows from the weak-link hypothesis in the first approximation), we obtain

$$\left[\Phi\left(\frac{(\sigma_{xF_1})_\alpha}{s_{F_1}} - \frac{a_{F_1}}{s_{F_1}}\right) + \Phi(x)\right] =$$
$$= \left[\Phi\left(\frac{(\sigma_{xF_2})_\alpha}{s_{F_2}} - \frac{a_{F_2}}{s_{F_2}}\right) + \Phi(x)\right] = \kappa = \text{const}$$

and

$$\Phi\left(\frac{(\sigma_{xF_1})_\alpha}{s_{F_1}} - \frac{a_{F_1}}{s_{F_1}}\right) - \Phi\left(\frac{(\sigma_{xF_2})_\alpha}{s_{F_2}} - \frac{a_{F_2}}{s_{F_2}}\right) =$$
$$= \Phi\left(\frac{(\sigma_{xF})_\alpha}{s_F} - \frac{a_F}{s_F}\right) - \kappa - \Phi(x). \tag{56}$$

Denoting the argument of the Laplace function by λ_c

$$\left|\frac{(\sigma_{xF})_\alpha - \bar{a}_F}{\bar{s}_F \quad \bar{s}_F}\right| = \lambda_\alpha, \tag{57}$$

we write the magnitude of the effective stresses at the instant of failure as

$$\begin{aligned}(\sigma_{xF})_\alpha &= a_F - \lambda_\alpha \bar{s}_F = a_F - v\lambda_\alpha a_F = \\ &= a_F(1 - v\lambda_\alpha).\end{aligned} \tag{58}$$

With account for this expression

$$\begin{aligned}\bar{\sigma}_\theta &= (\sigma_x)_\alpha (\Psi_x)_\alpha = \bar{\sigma}_{\theta F} = \\ &= a_F(1 - v\lambda_\alpha)[\Phi(\lambda_\alpha) + \Phi(\kappa)].\end{aligned} \tag{59}$$

In order for the load to reach the maximum value, the product $(1 - v\lambda_c)[\Phi(\lambda_c) + \Phi(\kappa)]$ must be maximal.

For the AG-4c, 33-18c, 27-63c, and SVAM [anisotropic glass fiber material] GRP's, the coefficients of variation were taken equal to their values for the specimen strength distribution. This was used as the basis for determining the parameters of the elementary cells and calculating the degree of damage prior to the beginning of the avalanche fracture process (Table 2)

$$(D_x)_\alpha = 1 - [\Phi(\lambda_\alpha) + \Phi(\kappa)]. \tag{60}$$

TABLE 2

PARAMETERS CHARACTERIZING PROGRESSIVE FRACTURE OF CERTAIN COMPOSITES

Material	m	λ_c	v in %	$(D_x)_c$ in %
E-1200	2,85	1,09	0,2	13,8
27-63C	2,7	1,09	0,2	13,8
33-18C	7,55	1,23	0,18	10,9
AG-4C	3,76	1,48	0,12	6,91

Hence it follows that, with decrease of the coefficient of variation, the magnitude of the damage prior to fast fracture initiation decreases.

To simplify and speed up the calculation of the degree of critical damage, the following interpolational relation was proposed in [97]

$$(D_*)_\kappa = 0{,}437v + 1{,}26v^2,$$

found on the basis of statistical analysis of results of trial and error calculations.

§3. Influence of Stressed Volumes on GRP Strength for Uniform Stress State

The limiting GRP states with regard to fracture as a composite reinforced material should be examined in the longitudinal tension case in light of the statistical concepts of sequential breaking of the glass fibers into segments of minimal length, which depend on both the fiber strength characteristics and the matrix shear strength, and also on the possible processes of stress relaxation at the ends of the broken fibers and crack growth in the matrix. For the formation of a primary macrofracture crack, it is necessary to have in the stressed volume zone — which is on the order of two minimal broken fiber lengths — a concentration of the number of breaks and accompanying microcracks sufficient for fast macrofracture growth with maximal value of the load achieved.

As was shown in §1, statistically the limiting state for a bundle fibers which are not bonded by a matrix, corresponding to this maximal load, is described with the aid of the parameters of the fiber breaking stress distribution density function. The process of fiber breaking along their length and disruption of their connection with the matrix as a result of shear failures, which precede the main failure, becomes important for the limiting state of the composite. This process is affected by defects which arise in the matrix during

composite formation (§5, Chapter 5), fiber arrangement defects, and the residual stresses in the composite (§1, Chapter 5). Thus, the crack growth conditions in the matrix, both after partial breaking of the fibers and prior to this breaking, are of considerable importance for composite fracture strength if this breaking of the fibers results from a combination of deformations and mechanical properties of the fibers and the matrix (§2, Chapter 5).

The mechanical properties of the matrix are very important in determining the magnitude of the composite resistance to interlaminar shear. In this case, the fracture conditions are affected by both the average values and the random deviations from the average values associated with matrix defects (§4, Chapter 5).

As will be shown later in this section, the dispersion of composite static strength in longitudinal tension is determined basically by the variation of the fiber breaking strength, since this is apparently the principal factor which determines the equilibrium conditions in the initial fracture stages prior to formation of the limiting state corresponding to the maximum load, after reaching which fast fracture occurs through the entire section. The breaking load distribution density reflects not only the variance of the fiber breaking strength but also the influence on this variance of the matrix surrounding the fiber and the matrix defects, which lead to both reduction of the average values and increase of the scatter in comparison with the variance for bundles with a large number of fibers.

It was shown previously (§4, Chapter 5) that fast fracture of a fiber bundle occurs upon reaching some critical damage (number of broken fibers) $a(w)_{max}$. Increase of the initial number of fibers in the bundle leads to reduction of both the average values of the breaking load and reduction of its variance, as follows from the weak link hypothesis. The function $P_s(\sigma)$, characterizing microstructure strength, may be used to evaluate the portion of failed specific volumes for the stress σ. In this connection, depending on the

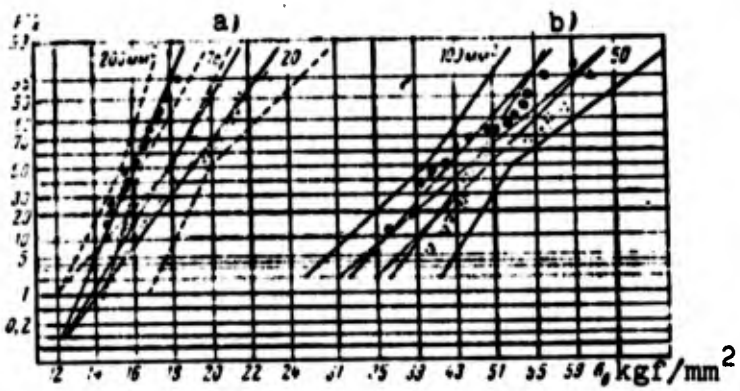

Figure 10. Integral curves of breaking strength distribution in tension of AG-4c(a), 33-18c (b) composites for different areas.

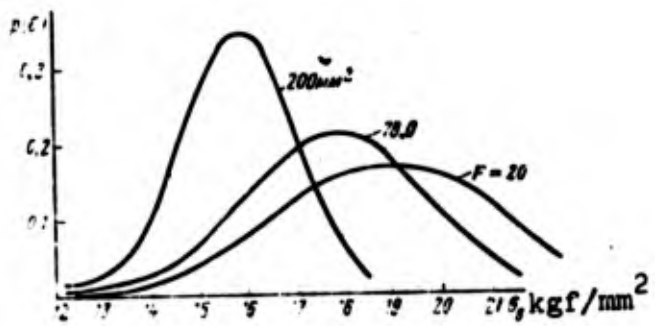

Figure 11. Tensile breaking strength probability density curves for the AG-4c phenol composite.

stressed volumes, the reinforced composite strength changes with exclusion of all the technological factors (degree of damage, void content, polymerization temperature and time), which have a definite influence on the subject effect.

In order to eliminate the influence of processing, we tested specimens of different sections of a single plate, which made it possible to characterize the scale effect and analyze the strength of the phenol, epoxy, and epoxy-phenol composites based on nonalkaline 7 - 10-micron diameter fibers.

The experimental data [98] showed that GRP static strength depends very little on the part (object) size, and is determined by the dimensions of the loaded element or specimen. The influence of the absolute dimensions on the strength is associated with dispersion of the mechanical properties and can be characterized statistically. Figure 10 shows the relationship between the breaking strength values and failure probability on the normal distribution scale for the AG-4c and 33-18c materials. Figure 11 shows the probability density curves for AG-4c specimens of different areas. Tests of other GRP showed the quite general nature of scale effect manifestation [31].

The basic data are summarized in Table 3 [66]. By analyzing the data for a volume of 25,000 mm³, we find that for both composites (particularly for the same thickness) the strength is practically independent of the length and width variation. The influence of thickness on the scale effect manifestation is apparently associated with the influence of technological factors (degree of hardening, for example), since the thickness effect shows up most markedly. For a fixed length and no technological effects, we can take as the basic dimensional parameter the area of the specimen cross section, in light of the statistical concepts concerning the fracture mechanism.

TABLE 3

INFLUENCE OF ABSOLUTE DIMENSIONS ON STRENGTH OF AG-4b AND AG-4c COMPOSITES

Composite	Width x Thickness x Length of Specimen Working Section in mm	Volume of Working Section in mm	σ_b in kgf/mm²	$\bar{s}$ in kgf/mm²	v in %
AG-4b	10×5×50 100×10×100 100×5×50 10×50×50 10×5×50	2 500 5 000 25 000	4.27 3.21 3.66 3.18 3.65	0.814 0.521 0.694 0.752 0.691	19.1 16.2 18.9 21.6 18.9
AG-4c Equistrength	10×5×50 100×10×100 100×5×50 10×50×500 10×5×500	2 500 5 000 25 000	25.01 19.21 22.86 17.01 22.99	4.926 2.224 2.482 4.092 2.408	14.4 11.6 10.4 18.2 10.5

With increase of the area, we observe marked reduction of the strength (see Figures 10 and 11). In the phenol GRP, which has a typical brittle fracture, the dispersion also decreases with increase of the cross section area. For the 33-18c GRP, the tendency toward reduction of the dispersion with increase of the dimensions is less, and apparently the manifestation of the scale factor is also associated with the fracture process, since the fracture of the 33-18c GRP is mixed (brittle and fibrous).

An averaged relationship of the form $\sigma_{b_1}/\sigma_{b_2} = (F_2/F_1)^{1/m}$ agrees satisfactorily with the experimental data and can be used for approximate evaluation of the absolute dimension effect with use of graphs or values of the absolute dimension influence coefficient $\varepsilon_\sigma = \sigma_b F_i/\sigma_b F_0$, where $\sigma_b F_0$ is the strength of the standard specimen, as adopted in design practice. The coefficients ε_σ have similar values for various materials. The exponent m is determined either from the $\sigma_{b_1}/\sigma_{b_2} - (F_2/F_1)^{1/m}$ relation or from the lg σ_b - lg F plot. The resulting values of m show that the GRP are more nonhomogeneous materials than the metals. Therefore, in calculating the static strength we must consider the influence of the dimensions on the magnitude of the breaking stresses. The exponent m has a statistical nature, since the reinforcing glass fibers have considerable scatter of their properties.

In order to obtain the breaking strength distribution parameters, we tested a large number of specimens of the same section (100 units). Specimens of other sections were tested to verify the agreement between the calculated and experimental values. As a rule, it was found that the GRP breaking strength distributions were bounded by some stress value σ_u by a minimum strength boundary $\sigma_b > \sigma_u$. The data obtained, plotted on a probability grid in the coordinates ln ln 1/1 - P(σ) — ln ($\sigma - \sigma_u$), show that the distribution can be linearized (Figure 12).

Thus, the GRP can be considered a brittle body with defects distributed throughout the volume, which determine the GRP structure element strength scatter, which for tension follows the Weibull distribution

$$P(\sigma) = 1 - \exp \int_V \left[\frac{\sigma - \sigma_u}{\sigma_0}\right]^m dV. \qquad (61)$$

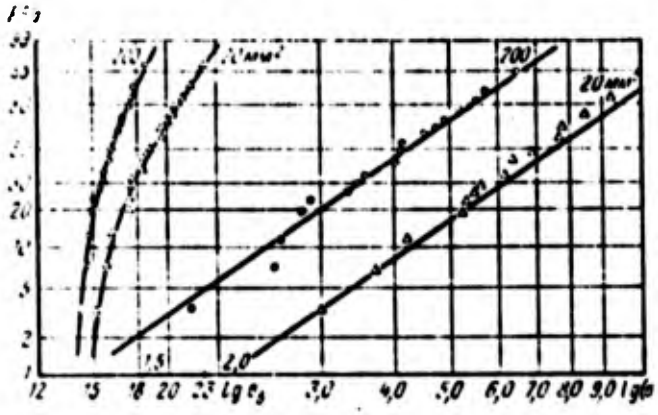

Figure 12. Linearization of limit tensile strength distribution curves of the AG-4c composite and introduction of the left-hand strength bound.

For uniform stress distribution, it is written as

$$P(\sigma) = 1 - \exp\left[-\frac{V}{V_0}\left(\frac{\sigma - \sigma_u}{\sigma_0}\right)^m\right], \quad (62)$$

where V is the stressed volume; V_0 is a quite small stressed volume containing a defect; σ_u is the left-hand strength bound; σ_0 is a parameter having the dimensions of stress; m is an index of homogeneity, characterizing the degree of damage and scatter of the local material strengths.

In the first approximation, V_0 is taken equal to one; however, change of this parameter has no effect on the values of m. The accumulation of damages which can lead to fracture must take place in a thin layer of length 2δ; therefore, in place of the volume V we can examine the cross section area F and the specific area F_0. We can assume that F_0 is the area bounding a hexagonal cell consisting of seven neighboring fibers, since it is the strength of these fibers at the break location which determines the growth or retardation of the progressive fracture. For the AG-4c and 33-18c composites the cell element size is approximately equal to 0.0033 mm^2.*

*If an experimental strength distribution curve is available, we can write for some stress $\ln [1 - P(\sigma, V)] = (1/V_0)n(\sigma)V$, where $n(\sigma)$ is a function of the microstructure. For known V for each σ, we find, without dividing out, $n(\sigma)/V_0$. Then for any V we determine for the same σ the fracture probability. Thus, the quantity V_0 can be excluded.

Thus,

$$P(\sigma) = 1 - \exp\left[-\frac{F}{F_0}\left(\frac{\sigma - \sigma_u}{\sigma_0}\right)^m\right]. \qquad (63)$$

Taking the logarithm of (63), we obtain

$$\ln\ln\frac{1}{1-P(\sigma)} = m\ln(\sigma - \sigma_u) - m\ln\sigma_0 + \ln\frac{F}{F_0}. \qquad (64)$$

which is the equation of a straight line in the logarithmic coordinates ln ln 1/[1 - P(σ)] - ln (σ - σ_u), and m defines the slope of this line. With increase of the stressed volume, the line shifts into the region of lower strength values, with all the parameters retaining their values.

The parameters of the composite breaking strength distribution function can be determined [101] by solving the system of equations

$$\left.\begin{aligned}\sigma'_{50} &= \sigma_u + \sigma_0 q'_{50};\\ \sigma'_5 &= \sigma_u + \sigma_0 q'_5;\\ \sigma''_{50} &= \sigma_u + \sigma_0 q''_{50};\\ \sigma''_5 &= \sigma_u + \sigma_0 q''_5.\end{aligned}\right\} \qquad (66)$$

where σ′, σ″ are the stresses corresponding to two sections and fracture probabilities of 5 and 50%; $q_p = \left(\ln\frac{1}{1-P(\sigma)}\right)^{1/m}$ is determined for the same sections and fracture probabilities.

The values of the breaking strength distribution function parameters are shown in Table 4 for some composites.

Let us evaluate the microstructure strength distributions considering the GRP as a bundle of fibers and establish those elementary cell strength distributions which correspond to the strength of the real composites. We take $F_0 = 0.0033$ mm^2. Then we find that the microstructure of the AG-4c composite is described by the strength distribution $n(\sigma) = \left(\frac{\sigma - 12}{90}\right)^{3.76}$; for 33-18c $n(\sigma) = \left(\frac{\sigma - 16}{112}\right)^{7.35}$.

TABLE 4

COMPOSITE BREAKING STRENGTH DISTRIBUTION FUNCTION PARAMETERS

Composite	m	σ_u	σ_b for F_0 = 1 mm^2	σ_b for F_0 = 0.0033 mm^2
AG-4c Equistrength	3.76	12	17	90
AG-4c Unidirectional	—	—	—	—
33-18 Equistrength	7.55	16	50	112
27-63	2.70	31.5	103	—
E-1200	2.90	39	74	—
AG-4b	2.5	2.1	13.8	—

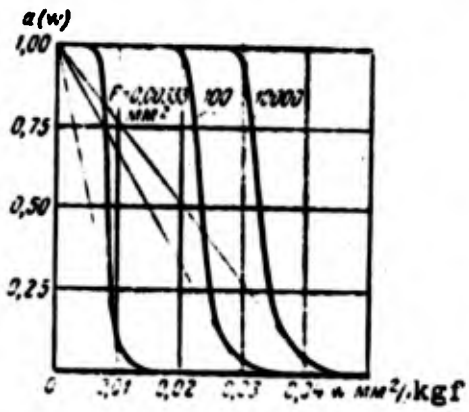

Figure 13. Weibull tensile strength limit distribution for 33-18c composite specimens with different areas.

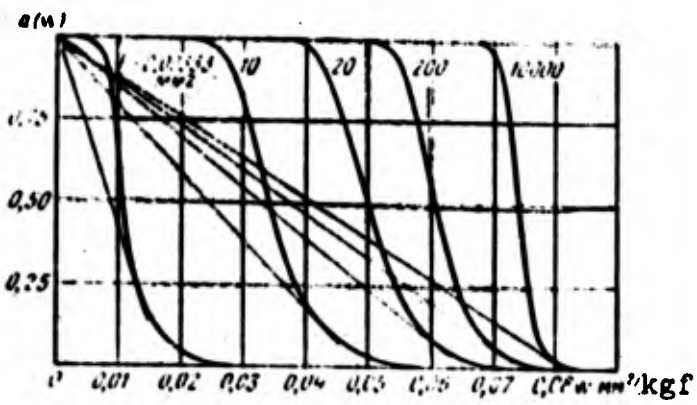

Figure 14. Weibull tensile strength limit distribution for AG-4c GRP specimens with different cross-section areas.

Comparing the distribution parameters with the corresponding data for glass fibers (§2, Chapter 5), we find that the nonuniformity of the fiber properties does not increase in the 33-18c composite (exponent m for the fibers is 5 - 9), while the value of m for the AG-4c composite indicates increase of the reinforcing fiber nonuniformity. Thus, the polymer matrix type has a significant influence on the value of m for the real composite. The decrease of m for AG-4c shows that the phenol matrix is more brittle, and has a tendency toward cracking. The parameter σ_0, which characterizes indirectly

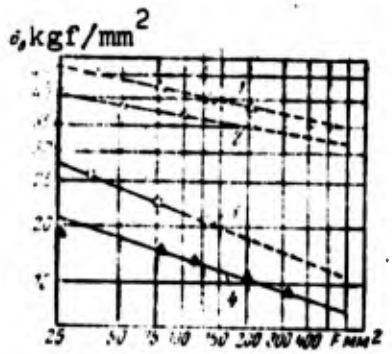

Figure 15. Composite tensile strength as a function of area in log-log coordinate system
1 — P-49c (heat treated); 2 — 33-18c; 3 — P-49c (not heat treated); 4 — AG-4c.

the utilization of the fiber strength in the composite, is smaller for the phenolic composite. The composite strength distribution curves (Figures 13 and 14) make it possible to characterize the critical degree of damage, which depends on the section area; this is quite logical since the strength dispersion decreases with increase of the area. If σ_u = 0, the coefficient of variation is independent of the stressed volumes, and the critical degree of damage is constant [97].

Figure 15 shows GRP tensile strength as a function of specimen cross-section area (l = const) in a log-log coordinate system. Since the average tensile breaking strength is

$$\bar{\sigma}_e = \sigma_u + \frac{\sigma_0}{F^{1/m}}\Gamma\left(1+\frac{1}{m}\right), \tag{67}$$

then

$$\lg(\bar{\sigma}_e - \sigma_u) = \lg\sigma_0\Gamma\left(1+\frac{1}{m}\right) - \frac{1}{m}\lg F. \tag{68}$$

For the P-49c (heat treated), 33-18c, and AG-4c (1:1) GRP, these functions have the following form, respectively, (the parameter σ_u is taken equal to zero)

$$\left.\begin{array}{l} \lg\sigma_e = 1{,}8050 - 0{,}0952\lg F; \quad \lg\sigma_e = 1{,}6980 - 0{,}0645\lg F; \\ \lg\sigma_e = 1{,}695 - 0{,}178\lg F; \quad \lg\sigma_e = 1{,}548 - 0{,}1509\lg F \end{array}\right\} \tag{69}$$

and can be used for approximate estimation of the average strength values as a function of section area. The experimental data agree well with the theory. The quantity q_p [197] connects the fracture

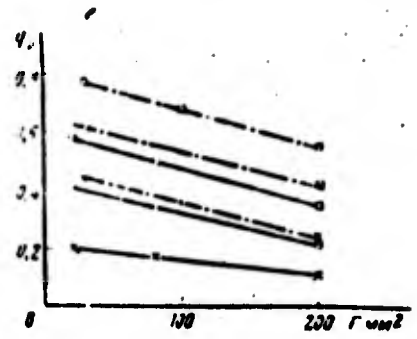

Figure 16. Criterion q_p as a function of absolute dimensions and fracture probability for AG-4c (solid curves) and 33-18c specimens:
—— P = 95%; O — 50%; X — 5%.

probability, stressed material volume, and the exponent m, i.e., all the factors on which the breaking stress depends, and characterizes the statistical effect of the absolute dimensions. The variation of the quantity $q_p = (\sigma_p - \sigma_u)/\sigma_0$ with cross-section area for different fracture probabilities is shown in Figure 16. The reduction of the slope of the curves for low fracture probabilities indicates weakening of the scale effect in this region.

Equations of the type

$$\sigma_p = f\,[P(\sigma_b),\ F,\ \sigma_0,\ m,\ \sigma_u]. \qquad (70)$$

obtained on the basis of the Weibull statistical distribution, can be used to construct short-term static strength probability diagrams which characterize the breaking strength dependence on the constructional element area F, the fracture probability $P(\sigma_b)$, and the material constants σ_0, m, σ_u, determined on the basis of statistical analysis of test results. The calculated breaking strength values are shown in Figure 10 (denoted by the symbol 0).

The strength variability and the scale effect are a consequence of the material microstructure defect statistical distribution, and can be described within the framework of statistical theory [28].

For a distribution of the type (61), the mean square deviation is defined by the formula

$$s = \frac{\sigma_0}{F^{1/m}} \sqrt{\Gamma\left(1 + \frac{2}{m}\right) - \Gamma^2\left(1 + \frac{1}{m}\right)}. \qquad (71)$$

stress field may be coordinated with the reinforcement in the concentration zone; however, we shall examine the influence of the usual sources of concentration on GRP strength, since highly overstressed material volumes may be present in the concentration zones.

The scale effect and the stress state nonuniformity factor have not been separated in the analysis of the results obtained in published studies.

For the experimental studies of stress concentration influence on the short-term static strength of the phenolic (AG-4c) and epoxy (33-18c) GRP, we took as the stress concentration source a two-sided hyperbolic notch, approximated by a circle and two tangents, which makes it possible to vary the magnitude of the theoretical concentration factor α_σ over wider limits (than in the hole case). The notch parameters were selected so that the relative stress gradient

$$\bar{G}_N = \frac{d\sigma}{dy} \cdot \frac{1}{\sigma_{max}}, \qquad (65)$$

remained constant for specimen cross section areas of different magnitude and different stress concentration factors, which establishes similarity of the specimen loading in the notch zone. The stress gradient varied from 0 to 10. The tests were made on a testing machine with mechanical drive at a strain rate of ε_p = 0.005 1/sec.

The specimen area was varied in the range 20 - 200 mm^2. The number of specimens of each type and size was sufficient for statistical analysis.

Analysis of the data shows that the increase of GRP sensitivity to stress concentration with increase of the dimensions is comparatively small (Table 6).

TABLE 6

VALUES FOR EFFECTIVE STRESS CONCENTRATION FACTORS FOR GRP

Specimen Area in mm^2	Theoretical Concentration Factor	Average Breaking Strength in kgf/mm^2	Effective Concentration Factor	Specimen Area in mm^2	Theoretical Concentration Factor	Average Breaking Strength in kgf/mm^2	Effective Concentration Factor
AG-4c; t = 20° C				33-18c; t = 20° C			
20	1.0	19		25	1.0	44.1	
78	1.0	18.0		50	1.0	43	
112	1.0	17.21		100	1.0	42.5	
200	1.0	15.9		25	1.5	39.4	1.12
314	1.0	14.6		50	1.75	35.40	1.22
78	2.8	16.0	1.13	100	2.3	34.06	1.25
78	3.3	14.8	1.30	25	2.0	41.04	1.10
78	5.5	12.7	1.42	50	2.75	33.4	1.29
200	3.3	10.7	1.48	100	3.6	29.1	1.46
200	4.0	10.5	1.51	25	4.0	39.85	1.13
200	6.7	9.8	1.62	50	6.1	31.2	1.25
				100	7.4	27.24	1.56
				33-18c; t = 150°			
25	1.0	19.55	1.0	25	2.0	19.96	0.982
50	1.0	19.6	1.0	50	2.75	17.65	1.1
100	1.0	15.51	1.0	100	3.6	14.83	1.04
25	1.5	17.44	1.1	25	4.0	18.83	1.14
50	1.75	18.5	1.06	50	6.1	18.88	1.04
100	2.3	15.29	1.01	100	7.4	12.93	1.19

Considering the linearity of the GRP strain diagrams, we can assume that an elastic stress distribution is maintained up to the beginning of fracture at the root of the notch. Depending on the stress gradient at the stress concentration location, the over-stressed material volume in which the stresses are higher than the minimum material strength limit σ_u will vary. Consequently, fracture in the concentration zone is determined not only by the maximum stress, but also depends on the stress distribution.

Comparison of the variation of σ_{max} with the relative gradient $\bar{G}_N$ and section area indicates similarity of the influence of these two factors on GRP fracture, and the similarity indices depend on

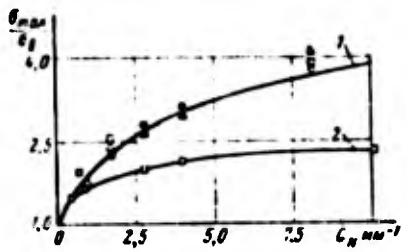

Figure 17. Experimental (1) and calculated (2) curves of maximum breaking stresses versus relative stress gradient for AG-4c (● — 80 mm²; ▲ — 200 mm²); and 33-18c (o — 25 mm²; Δ — 50 mm²; □ — 100 mm²).

the fracture probability. In this connection the subject dependences can be written as the product of two functions

$$\sigma_{max} = f(\bar{G}_N)\,\psi(F). \qquad (74)$$

When we divide the effective maximum stresses ($\alpha_\sigma\sigma_n$) by the average breaking strengths of smooth phenolic and epoxy material specimens, we obtain values which agree well. The relation $\sigma_{max} = f(\bar{G}_N)$ makes it possible to separate the concentration effect and the absolute dimension effect (Figure 17, curve 1).

The incomplete sensitivity of oriented GRP to stress concentration is apparently associated with the statistical nature of the fracture process, since individual fibers fail in the concentration zone at loads far below the breaking loads, and there is redistribution of the stresses (the load at which cracking begins is approximately half the breaking load).

However, even for the very largest gradients, calculating the maximum stresses in terms of the theoretical concentration factor and the nominal stresses, we obtain the values of σ_{max} smaller than the breaking strength of the glass fibers.

Linearization of the stress diagram in the concentration zone and calculation of the fracture probability integral

$$P(\omega) = \begin{cases} 1 - \exp\left[-\int_F \left(\frac{\sigma - \sigma_u}{\sigma_0}\right)^m dF\right] & \text{for } \sigma \geq \sigma_u \\ 0 & \text{for } \sigma \leq \sigma_u \end{cases} \qquad (75)$$

for the AG-4c GRP gives the values of the maximum breaking stresses in the concentration zone in comparison with the calculated maxima, shown in Table 7.

TABLE 7

COMPARISON OF EXPERIMENTAL AND CALCULATED VALUES

(Calculated Values in Numerator)

FOR THE AG-4c COMPOSITE WITH 200 mm² SECTION

Relative Gradient mm^{-1}	Fracture Probability in %		
	5	50	95
0	13/12,9	16/15,9	18/17,9
2,7	18,5/30	23/35	29/40
4,0	19,5/35	24/42	32/47
11,5	21/55	29/65	40/75

The equation of the tanget to the stress diagram is

$$\sigma = \sigma_{max} - G_N(a - y), \quad G_N = \frac{d\sigma}{da}. \tag{76}$$

We integrate from a_0 to a over the area, where $\sigma \to \sigma_u$

$$\int_F \left(\frac{\sigma - \sigma_0}{\sigma_0}\right)^m dF = \frac{2b}{m+1}\left(\frac{\sigma_u}{\sigma_0}\right)^m \frac{1}{G_N}\left(\frac{\sigma_{max}}{\sigma_u} - 1\right)^{m+1} \times \frac{1}{\frac{\sigma_{max}}{\sigma_u}} = -2{,}3\lg|1 - P(\sigma)|. \tag{77}$$

The calculated data are shown in Figure 17 (curve 2).

Small stress gradients can be obtained in bending. In this case the stress diagram is linear. We calculate the probability integral directly, and obtain the following relation between the breaking stresses in bending and tension [206]

$$\frac{\sigma_{eu}}{\sigma_{ep}} = (2m + 2)^{\frac{1}{m}}. \tag{78}$$

When testing GRP specimens of different dimensions in bending and tension, the breaking stresses are different and increase in bending with reduction of the thickness, and the quantity $\bar{G}_N$ increases in this case. For AG-4c with $\bar{G}_N = 2/h = 0.07; 0.1; 0.2; 0.3$, the ultimate strength in bending is, respectively, 21, 22.5, 25.5, 31 kgf/mm^2. Referring these values to the ultimate strengths in tension for equal sections, we obtain 1.54 - 1.60. For m = 6.48, the ratio is 1.52; thus, the experimental and theoretical values agree quite well.

In determining the ratios $(\sigma_{max}/\sigma_{b\ pr}) = \alpha_\sigma(\sigma_{bc}/\sigma_{b.pr})$ for different areas, we obtain the same values (with 50% probability for the AG-4c and 33-18c materials). A relation of the form $(\sigma_{max}/\sigma_b) = 1 + B(\bar{G}_N)^k$ describes satisfactorily the experimental data (B = 1.098, k = 0.487 for phenolic and B = 1.32; k = 0.384 for epoxy GRP). From analogous relations, we can determine the breaking stresses for nonuniform stress states, specifically for bending, if the solution of the elastic problem for the corresponding part shape is known.

For a linear stress distribution with account for the difference in the compression and tension elastic moduli for AG-4c, we obtain

$$\sigma_{max} = \sigma_n \frac{1+\alpha}{\alpha}, \text{ where } \alpha = \sqrt{\frac{E_c}{E_p}}; \qquad \bar{G}_{Np} = \frac{2}{h_p} = \frac{1+\alpha}{h\alpha}. \tag{79}$$

From the known dimensions of the element being bent, we determine $\sigma_{b\ pr}$ with account for the scale factor and then σ_{max} in terms of the gradient from the curve (see Figure 17). For example, for a beam b x h = 30 x 9 (AG-4c) $h_p = 4.5$ mm; $\bar{G}_N = 0.21$; $F_p = 135$ mm^2; $\alpha = 1.15$, the nominal breaking stress is (from experiment) $\sigma_n = 27$ kgf/mm^2. For $\bar{G}_N = 0.21$ (see Figure 17) $(\sigma_{max})_{calc} = 1.4\ \sigma_{b\ pr}$, where

$$\sigma_{b.pr} = \sigma_{bF_0}\left(\frac{F_0}{F_p}\right)^{1/m} \approx 17 \text{ kgf/mm}^2.$$

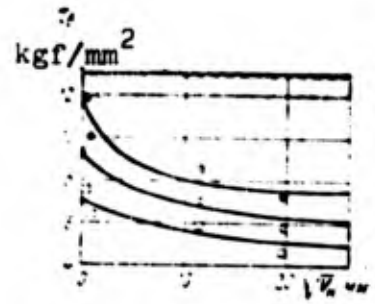

Figure 18. Breaking strength in torsion of AG-4b GRP as function of stressed volume V_s for different cumulative fracture probabilities $P(\tau < \tau_1)$, equal to 0.95 (•); 0.50 (o); 0.10 (□).

Then

$$(\sigma_{max})_b = 1.4 \cdot 17 = 24 \text{ kgf/mm}^2,$$

$$(\sigma_{max})_{torsion} = \sigma_b \frac{1+\alpha}{2\alpha} = 25 \cdot 0{,}98 = 24{,}5 \text{ kgf/mm}^2,$$

and the agreement of the results is satisfactory.

The influence of scale factor on GRP breaking strength in torsion was investigated in [31]. On the basis of the Weibull brittle strength theory, formulas were obtained for calculating the shear strength and dispersion with account for the left-hand bound

$$\tau_u = \tau_u + \left(\frac{m+2}{2}\right)^{1/m} \frac{\tau_u}{\Gamma^{1/m}\left(\frac{2}{3}\right)} \Gamma\left(1+\frac{1}{m}\right);$$

$$s(\tau_u) = \frac{\tau_u}{\Gamma^{1/m}\left(\frac{m+2}{2}\right)} \left(\frac{1}{\frac{2}{3}}\right)^{1/m} \times \left[\Gamma\left(1+\frac{2}{m}\right) - \Gamma^2\left(1+\frac{1}{m}\right)\right]. \tag{80}$$

For small volumes, these formulas yield values which are high in comparison with the experimental values.

Figure 18 shows the torsional breaking strength of the AF-4b GRP as a function of the stressed volume for various fracture probabilities. The theoretical relation was calculated using the formula

$$\tau_1 = \tau_u + \left(\frac{m+2}{2}\right)^{1/m} \times \frac{\tau_u}{\Gamma^{1/m}\left(\frac{2}{3}\right)} \times \ln^{1/m} \frac{1}{1-P(\tau < \tau_1)}. \tag{81}$$

Thus, for small stress gradients, the similarity condition can be expressed in terms of the relative stress gradient. For large gradients, the similarity condition in the form (77) does not describe the experimental data because of the progressive nature of the fracture in the concentration zone.

Analysis of the maximum fracture stress distributions for different concentration levels and areas showed that the maximum stresses depend more weakly on the gradient in the region of low fracture probabilities.

The concentration effect diminishes with increase of the gradient, and with increase of the temperature the dispersion of the breaking stresses also decreases.

§5. Statistical Characteristics of GRP Mechanical Properties

As a rule, in testing specimens and components of GRP structures, we find considerable scatter of the experimental data. The dispersion of the GRP properties is explained, on the one hand, by imperfect fabrication technology, variations of the resin and glass fiber chemical composition and their chemical and mechanical properties, the polymerization chemical reaction process conditions, the precision in placing the reinforcing fibers, and so on, and, on the other hand, by the fact that because of the statistical nature of the fracture process the force transmission and redistribution processes are not the same for different specimens.

Therefore, statistical data analysis methods should be used in determining GRP properties. The accumulation and analysis of GRP strength data are also of practical importance, since the use of materials with significant property variability in structures requires a probabilistic approach to determining strength margins and allowable stresses.

In the statistical treatment of data, it is important to determine the required number of tests for evaluation of the material characteristics with a given degree of reliability, and also the form of the distribution curve of the quantity being investigated and its parameters on the basis of a comparatively small number of observations which will be acceptable for practical use.

Examining a particular type of material as a general population, containing an infinite set of specimens and their limited number n as a random sample, the number of specimens necessary for determining the mechanical property characteristics with the reliability α can be found from the formula [99]

$$n = \frac{z_\alpha^2 v_x^2}{\gamma^2}, \qquad (82)$$

where the parameter z_α is found from the equation $2\Phi(z_\alpha) = \alpha$ using a table of the Laplace function; $v_x = \sigma/a$ is the coefficient of variation (σ is the mean square deviation for the general population); $\gamma = \Delta a/a$ is the maximum relative error. The reliability α means that the inequality $|\bar{x} - a| < \Delta a$ is satisfied with probability no less than α, $\bar{x}$ is the arithmetic mean value for a sample of limited size; a is the arithmetic mean value for the general population; Δa is the upper limit of the error in determining a from $\bar{x}$.

Figure 19 shows the nomogram of sufficiently large numbers, constructed using (82), which relates the property variation coefficient v_x, reliability α, and maximum relative error γ with the number n of specimens. The nomogram is constructed for $\gamma = 0.05$ and consists of three scales: A is the probability, B defines the number of specimens, scale C shows the coefficient of variation v_x. If the coefficient of variation v_x of the material is known, and the reliability α is specified or selected, then by connecting the corresponding points on the A and C scales by a straight line, we obtain at the point where it crosses the B scale the value of n, i.e., the number of

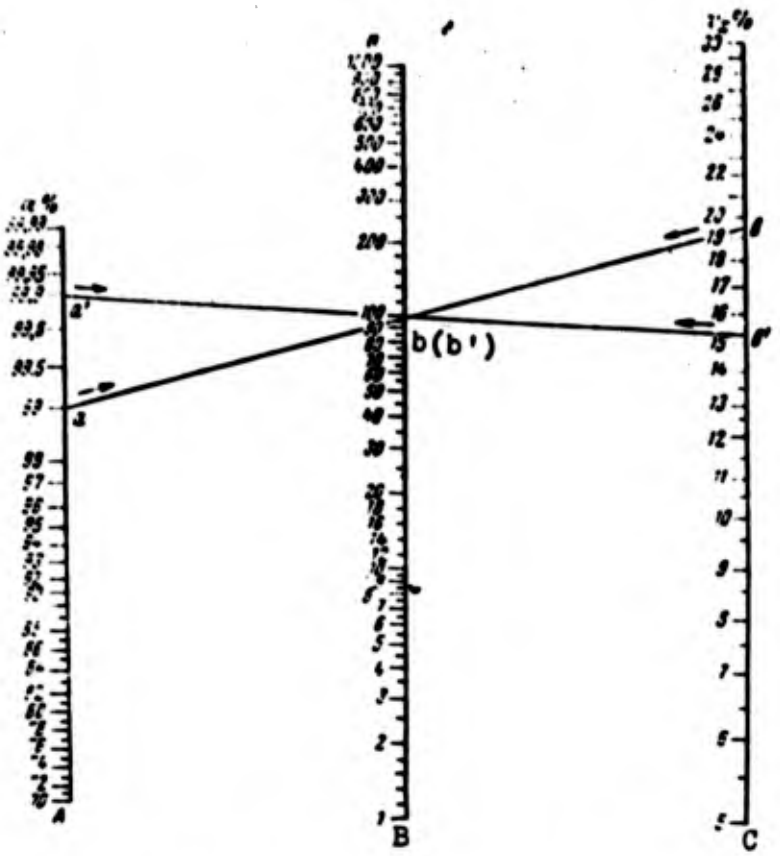

Figure 19. Nomogram of sufficiently large number of tests ($\gamma = 0.05$).

specimens which must be tested to obtain the specified reliability in determining a.

Since it is difficult to note any pattern in the values of a random quantity obtained directly from observation, the test results are arranged in an ascending variational series, and we determine the sample arithmetic mean value $\bar{x}$ and the sample mean square deviation $\bar{s}$ from the formulas

$$\left.\begin{aligned} \bar{x} &= \frac{\sum x_i}{n}; \\ \bar{s} &= \sqrt{\frac{1}{n-1}\left[\sum x_i^2 - \frac{(\sum x_i)^2}{n}\right]}. \end{aligned}\right| \qquad (83)$$

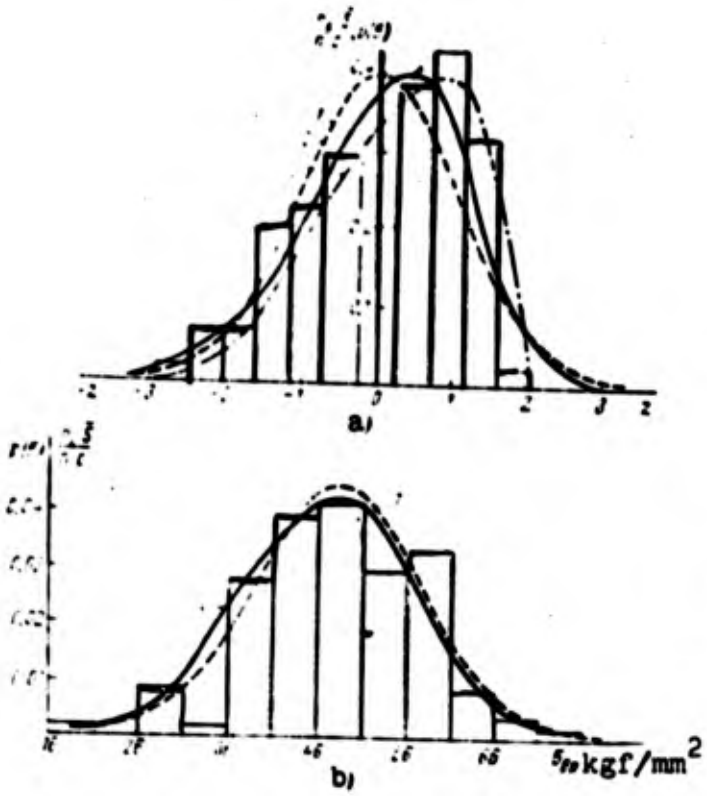

Figure 20. Histograms of maximum tensile strength distribution for 33-18c (a) and AG-4c 1:0 (b) GRP.

1 — normal distribution curve;
2 — type A distribution curve;
3 — Sedrakyan (four-parameter) curve.

where x_i is any obtained value of the random quality X; n is the sample size.

Then we find the coefficient of variation $v_x = \bar{s}/\bar{x}$ and refine the sample size.

In order to determine the type of distribution curve, the data obtained are represented with the aid of a histogram, characterizing the frequency of the quantity in question in the given interval. The range of values obtained is usually divided into 10 - 12 intervals. Figure 20 shows the 33-18c GRP ultimate strength histogram (a), which has assymetry, and the nearly symmetric AG-4c histogram (b).

Most common is the normal distribution law, according to which the probability density is defined as

$$n(x, a, \sigma) = \frac{1}{\sqrt{2\pi}\sigma} \exp -\frac{1}{2}\left(\frac{x-a}{\sigma}\right)^2. \qquad (84)$$

where a is the mathematical expectation of the quantity in question; σ^2 is the variance.

These parameters characterize the general population. The mean value $\bar{x}$ and the mean square deviation $\bar{s}$ are the experimental estimates of the parameters.

Thus, $\bar{x} \approx a$, $\bar{s}^2 \approx \sigma^2$. We make a statistical evaluation of the closeness approximateness of these equalities by finding the confidence intervals for the experimental values of $\bar{x}$ and $\bar{s}$, i.e., the smallest intervals in which a and σ are defined with the specified reliability. We calculate the confidence interval for the mean value of the general population as

$$\bar{x} - \frac{\bar{s}}{\sqrt{n-1}} t_{q,n-1} \leq a \leq \bar{x} + \frac{\bar{s}}{\sqrt{n-1}} t_{q,n-1}. \qquad (85)$$

Specifying the confidence coefficient $P = 1 - q/100$, we find from statistical tables the Student criterion $t_{q \cdot n-1}$ as a function of q and $k = n - 1$.

The confidence interval for the mean square deviation of the general population is defined by the inequality

$$\bar{s} \sqrt{\frac{n-1}{n}} z_1 \leq \sigma \leq \bar{s} \sqrt{\frac{n-1}{n}} z_2.$$

The values of z_1 and z_2 are calculated as functions of the specified reliability and sample size using statistical tables. Using these characteristics, we find the equalizing frequencies and obtain the theoretical distribution curves (Figure 20). We can assume that the distribution histograms characterize the sample population patterns, and the theoretical curve characterizes the general population.

The validity of the normal law in the first approximation is checked on special probability paper, where the ordinates are the cumulated frequencies on the probability scale, and the abscissas are the values of the random quantity. For the normal distribution, the

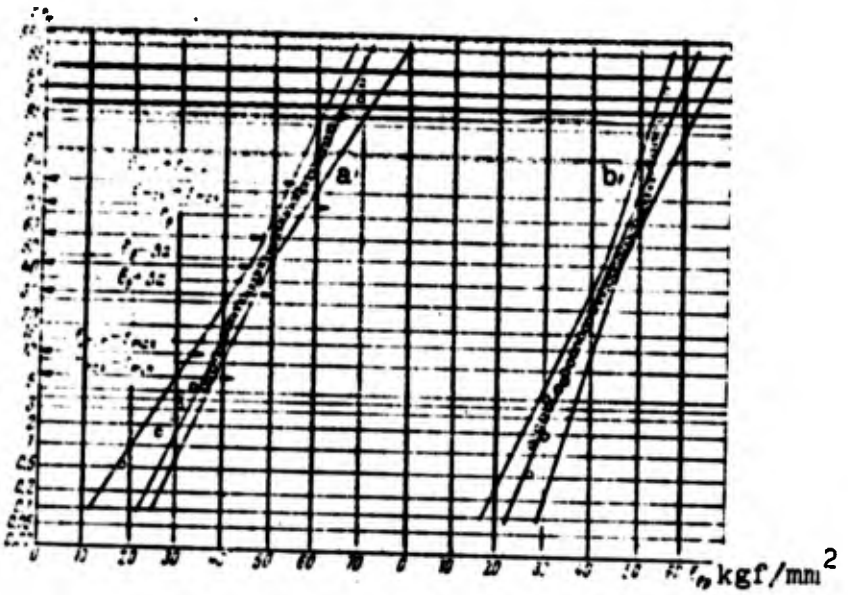

Figure 21. Integral curves of maximum tensile strength distribution of AG-4c (a) and 33-18c (b) GRP.

points fall on a straight line with slope $1/\bar{s}$, passing through the points ($\bar{x}$, P = 50%) and ($\bar{x} + \bar{s}$, P = 84%), and have random deviations from this line. Shown as illustrations of such distributions are those of the maximum strength of AG-4c (reinforced in one direction) and 33-18c (reinforced in mutually perpendicular directions). The values of P were determined from the formula P = (i - 0.5)/n, where i is the sequential number of the random quantity in the ascending variational series; n is the sample size (Figure 21), and the light lines show the 95% confidence region.

The symmetry of the probability density curves is evaluated by the dimensionless index S_k (skewness), which is equal to 0.547 for the 33-18c composite curve; the flatness of the curve is evaluated by the index E_k (excess), equal to 0.32 for 33-18c. The skewness and excess of the normal distribution are equal to zero.

The asymmetric histograms agree poorly with the normal distribution law. The theoretical distribution curve for such histograms can be a type-A distribution curve, which is a generalization of the normal distribution law. The probability density for the type-A

distribution is determined from the formula [73]

$$f_A(x) = f(x) - \frac{r_3}{6} f^{(3)}(x) + \frac{r_4 - 3}{24} f^{(4)}(x), \tag{86}$$

where f(x) is the normal probability density function; $f^{(3)}_{(x)}$, $f^{(4)}_{(x)}$ are its third and fourth derivatives; r_3, r_4 are the third- and fourth-order basic moments.

The first term of this equation yields the normal distribution, the second term reflects the influence of skewness (asymmetry) of the curve, and the third reflects the influence of steepness (excess).

A four-parameter distribution curve was proposed in [94], whose probability density is found as follows

$$p(R) = \frac{\gamma m}{R_{max} - R_{min}} \left[1 - \left(\frac{R - R_{min}}{R_{max} - R_{min}}\right)^m\right]^{\gamma - 1} \times \left(\frac{R - R_{min}}{R_{max} - R_{min}}\right)^{m-1}, \tag{87}$$

where R_{min} and R_{max} are the lower and upper values of the random sample quantity; R is the current value of the random quantity; γ and m are constant parameters.

This distribution curve is defined through the parameters m, γ, and the sample span limits. This is important in practical calculations, since the other distributions usually allow strength values of $\pm\infty$, which are not physically realistic.

The correspondence between the theoretical and empirical distributions is evaluated by the Pearson goodness of fit criterion κ^2. We consider that the empirical curve agrees with the theoretical curve, if the agreement probability is greater than 0.05. If the agreement probability is greater than the adopted level, we assume that the empirical distribution agrees with the theoretical distribution. Evaluation of the correspondence of the theoretical curves for the 33-18c composite maximum strength histograms (see Figure 19)

gave the following results: the probability of experimental distribution agreement with the normal distribution curve is 0.02 (< 0.05). The Sedrakyan and type-A distribution curves can be considered to correspond to the empirical distribution, since the probability of agreement in both cases is 0.1 (> 0.05). For the AG-4c composite, the level of agreement for the normal distribution is characterized by the probability 0.47.

The parameters of the Weibull distribution curve were examined previously. We note that the probability density for this distribution function is written in the form

$$p(x) = \frac{m}{x_0} \cdot \frac{V}{V_0} \left(\frac{x - x_u}{x_0} \right)^{m-1} \exp \left[- \frac{V}{V_0} \left(\frac{x - x_u}{x_0} \right)^m \right] \qquad (88)$$

and for the AG-4c and 33-18c composites the probability of agreement is 0.53 and 0.61.

Most convenient for practical calculations is the normal distribution, which has been tabulated and for which the parameter estimates have been worked out. Therefore, we should analyze the possibility of "rectifying" the distribution which deviates from the normal form by replacing the quantity x by some variable which is associated with it by a simple relationship (change of scale along the abscissa axis). As such quantities use is made of lg x, $\lg(x - x_u)$, $(x - x_u)/(x_n - x)$, $\lg (x - x_u)/(x_n - x)$, the last being used for distribution which is truncated on the left and right.

For parameters characterizing the GRP, this distribution gives results close to the log-normal law. At the same time, the Weibull distribution is better justified physically, since it does not include negative strength values nor values smaller than x_u. The parameters x_0, m, x_u make this distribution more flexible in comparixon with the two-parameter, normal, and log-normal distributions.

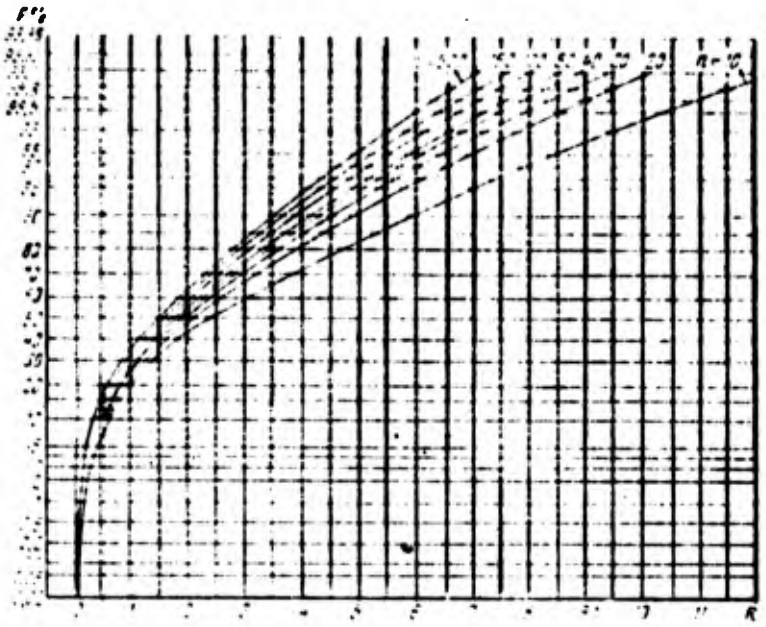

Figure 22. Curves for determining the left bound of a distribution with given reliability.

In certain cases, it is necessary to determine the minimum (left-hand) strength values. In the normal distribution case, we can find from the sample characteristics those limits $u_1 = \bar{x} - k\bar{s}$ and $u_2 = \bar{x} + k\bar{s}$ within which probability γ we can guarantee that a fraction of the population no smaller than the given limit P will fall. The value of k, which is a function of P and γ, is approximately [41]

$$k = k_\infty \left(1 + \frac{x_\gamma}{\sqrt{2n}} + \frac{5x_\gamma^2 + 10}{12n}\right), \tag{89}$$

where k_∞ corresponds to the general population characteristics a and σ and is determined as follows

$$\begin{gathered} \frac{1}{\sqrt{2\pi}} \int_{-k_\infty}^{k_\infty} e^{-\frac{t^2}{2}} dt = 2\Phi(k_\infty) = P; \\ \frac{1}{\sqrt{2\pi}} \int_{x_\gamma}^{\infty} e^{-\frac{t^2}{2}} dt = 0{,}5 - \Phi(x_\gamma) = 1 - \gamma; \\ \Phi(x_\gamma) = \gamma - 0{,}5. \end{gathered} \tag{90}$$

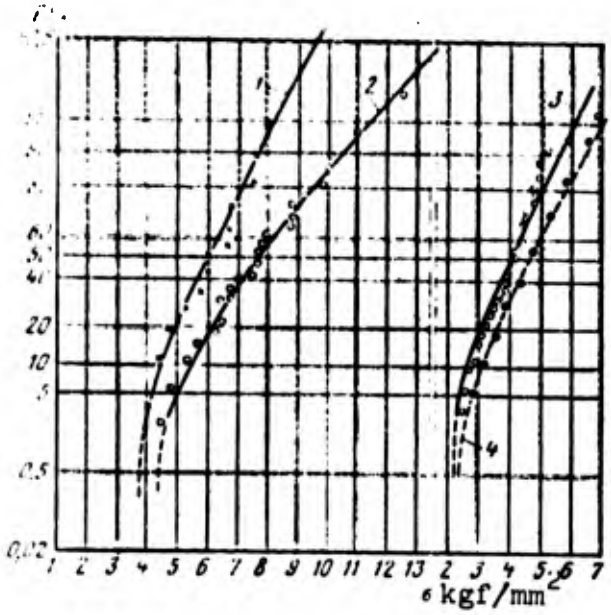

Figure 23. Results of tensile tests.

1 — M20 bolt; 2 — M14 bolt; 3 — tubing; 4 — specimen.

The general population span is $2k\bar{s}$ and the normed span is $R = 2k$. For the confidence level $\gamma = 99\%$, Figure 22 shows the dependence of the normed span on sample size n and probability P. For these curves we can determine the span for constructing the type-A distribution curve using (86).

For example, determination of the minimum strength values for the AG-4c composite with probability 0.9973 yields the following values of the breaking stresses for areas of 200, 78 and 20 mm^2, calculated as $x - 3s$: 12.4; 12.3; 12.0 kgf/mm^2, which gives results close to the left strength bound x_u in the Weibull distribution, since for $m = 3.7$ the Weibull distribution is close to the symmetric normal distribution.

The configuration of a GRP part predetermines the macrostructure of the composite, which to a considerable degree determines the material strength. Therefore, a strength calculation using the mechanical properties presented in handbooks is not always possible, and we need data from tests of specimens or detail parts.

Figure 23 shows the results of tensile tests of specimens cut from tubing (AG-4b) and full scale tests of large-diameter tubing under internal pressure, and also results of M14 and M20 bolt tests. The results of detail part tests are characterized by large scatter, and the breaking stresses are distributed following a law which is close to the normal law in its parameters. Comparison of the results showed that the material strengths in the specimens and parts based

on their left bounds were similar, although the scale influence does show up in the mean.

Comparison of the data from tests of bolts and tubing indicates that their strengths differ markedly, apparently because of glass filler orientation during molding of the bolts.

The agreement in the minimum breaking stresses for tubes of small curvature and different sizes, and for bolts of different diameter, and the difference in the strength of these different types of parts made from GRP shows that we should test typical details (cylinder, plate, cone, bolt) and the corresponding process samples, since the similarity conditions depend on the shape of the part and the stress state.

§6. Variability of GRP Properties and Allowable Stresses

The determination of the allowable stresses and stress margins when designing GRP parts and the normative requirements on the material must be established with account for the scatter of their strength characteristics resulting from random deviations, which depend on several structural and processing factors. Thus, for strength calculations it is not enough to know the average ultimate strength, since determination of the allowable stresses on the basis of the average value does not ensure integrity of the component if there is any variance of the properties. In this case, it is more correct to determine the probability with which the subject structural component will have an ultimate strength equal to or less than the effective stress, i.e., we need to have the integral ultimate strength distribution functions of the structural component and the loads acting on the component.

The scatter of the experimental data in the GRP tests corresponds to the scatter characteristic for brittle materials. For a first estimate of the properties, we can use the normal distribution law. Examining the property scatter characteristics (Tables 8 and 9), we see that the variability of the properties varies over a wide range even for a single type of composite.

TABLE 8

STRENGTH AND ITS VARIABILITY FOR AG-4b MOLDING COMPOSITE

Part Type	Part Wall Thickness in mm	Molding Temp in °C	Molding Time in min/mm	Specific Molding Pressure P_{sp} in kgf/cm²	Bending Ultimate Strength in kgf/cm²	Coefficient of Variation in %
Cylinder	6	130	1.0	300	13.0	31
			3.0		16.5	29
	12	130	1.0	150	13.0	23
				200	13.5	30
	6	130	1.0	300	13.2	21
			3.0		11.2	18
Cone	12	130	1.0	300	14.0	21
Plate	6	130	1.0	100	16.5	18.0
				200	22.3	20
	12	130	1.0	100	17.5	17
				200	16.5	17
Bolt	M-14	130	1.0	300	13.2	16
			1.5		10.8	17
	M-20	130	1.0	300	8.4	29
				400	8.2	23
Standard	—	130	1.0	200	22.1	8
			2.0		23.0	14
Tubing ∅ 500 mm	20	—	—	-	4.4	11
Tubing ∅ 100 mm	10	—	—	—	6.0	18

Fracture probability is the probability of the existence of negative values of the difference between the strength of the structural element and the stress acting on the element [91] and can be determined by integrating the probability density function of the magnitude of this difference over the region of negative values

$$V_{(R)} = V(\sigma_{oi} - \sigma_{ei} < 0) = \int_{-\infty}^{0} \varphi(R)\,dR. \qquad (91)$$

For a normal distribution of the breaking and effective stresses $p(\sigma_b)$ and $p(\sigma_e)$ with the parameters $\bar{\sigma}_b$, $\bar{s}_{\sigma_b}$, $\bar{\sigma}_e$, $\bar{s}_{\sigma_e}$ the probability density is

TABLE 9

COMPARISON OF STRENGTH VARIANCE OF GRP COMPOSITES AND SOME STRUCTURAL MATERIALS

Material	σ_b in kgf/mm²	v in %	σ_{bu} in kgf/mm²	v in %	σ_{bc} in kgf/mm²	v in %
AG-4c (1:0)	60	11	57	13	39	27
33-18c (1:0)	86	10	75	14	40	19
33-18c (1:1)	43	13	45	14	39	17
27-63 (1:1)	103	9	79	11	41	22
27-63 (1:1)	44	12	65	14	42.6	7
St.3	27	5.5	—	—	—	—
St.0c	30	8.6	—	—	—	—
ABT	39	0.4	—	—	—	—
ML-12	15.8	0.6	—	—	—	—
ML-5	10.7	6.6	—	—	—	—

$$q(R) = \frac{1}{\sqrt{2\pi}\, s_R} \exp\left[-\frac{1}{2}\left(\frac{R-\bar{R}}{s_R}\right)^2\right], \qquad (92)$$

where

$$\bar{R} = \bar{\sigma}_a - \bar{\sigma}_\partial; \quad s_R = \sqrt{s_{\sigma_a}^2 + s_{\sigma_\partial}^2 - 2r s_{\sigma_a} s_{\sigma_\partial}},$$

and we can assume that the strength and the effective load are independent and the correlation coefficient r = 0.

We write the fracture probability in the form

$$F(R) = \frac{1}{\sqrt{2\pi}\, s_R} \int_{-\infty}^{0} \exp\left[-\frac{1}{2}\left(\frac{R-\bar{R}}{s_R}\right)^2\right] dR. \qquad (93)$$

We convert to the normed function

$$F(R) = \frac{1}{\sqrt{2\pi}} \int_{-\frac{\bar{R}}{s_R}}^{\infty} \exp\left(-\frac{t^2}{2}\right) dt, \qquad (94)$$

where $(R - \bar{R})/\bar{s}_R = t$; $dt = dR/\bar{s}_R$ and the value of the probability integral can be calculated from Laplace function tables presented in probability theory courses.

The limit of integration can be expressed through the characteristics of the strength and load distribution functions

$$\frac{\bar{R}}{\bar{s}_R} = \frac{1}{v_R} = \frac{\bar{\sigma}_e - \bar{\sigma}_b}{\sqrt{\bar{s}^2_{\sigma_e} + \bar{s}^2_{\sigma_b}}} = \frac{\bar{n} - 1}{\sqrt{v^2_{\sigma_b} + v^2_{\sigma_e}\bar{n}^2}}, \tag{95}$$

where $\bar{n} = \bar{\sigma}_b/\bar{\sigma}_e$ is the average strength margin corresponding to 50% fracture probability. The fracture probability V thus depends on the strength margin $\bar{n}$, which is usually used in engineering calculations, and on the coefficients of variation of the mechanical properties v_{σ_b} and the loading v_{σ_e}.

If we initially take $v_{\sigma_e} = 0$, the fracture probability integral is calculated in terms of the limit of integration for this particular case, defined by the coefficient of variation v_{σ_b}, and the role of material mechanical property nonuniformity becomes obvious. The limit of integration

$$\frac{\bar{R}}{\bar{s}_R} = \frac{\bar{n} - 1}{\bar{n} v_{\sigma_b}} = \frac{1}{v_{\sigma_b}}\left(1 - \frac{1}{\bar{n}}\right). \tag{96}$$

The reliability of a structural element is characterized by the safety factor $\bar{n}$ and the corresponding fracture probability. Specification of the factor $\bar{n}$ does not yield an estimate of the reliability of different parts made from different materials, since for the same fracture probability the strength margins are different, depending on the relation between the load and strength variance characteristics (if the loading scatter is small, then material nonuniformity has a marked influence and vice versa).

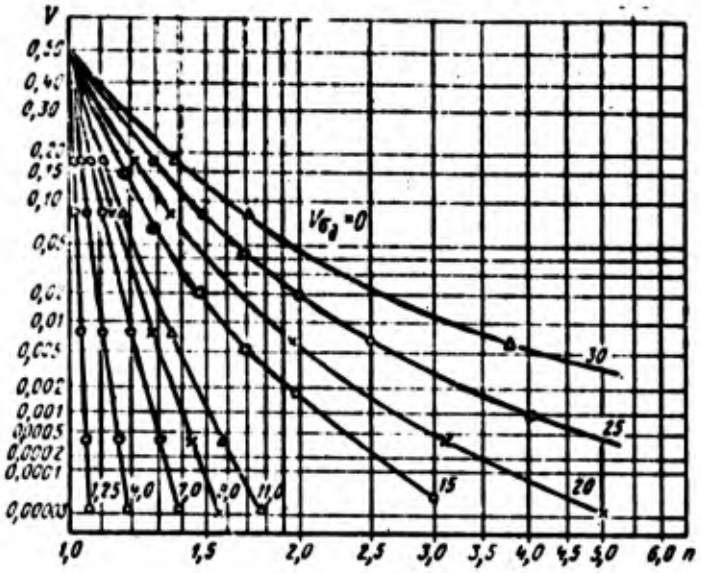

Figure 24. Influence of strength variance on fracture probability as function of average safety factor.

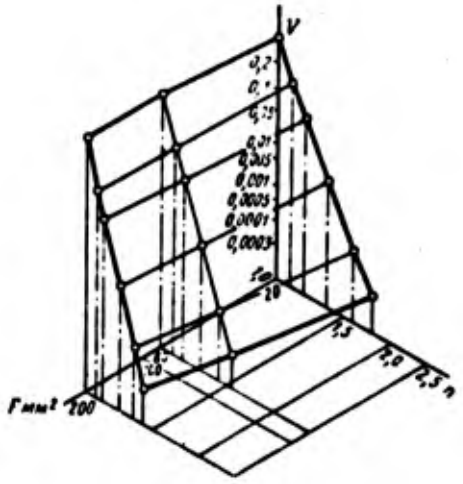

Figure 25. Fracture probability as function of safety factor and stressed area.

Figure 24 shows the fracture probability as a function of the safety factor $\bar{n}$ for different coefficients of variation which are characteristic for the mechanical properties of composites. The variation of fracture probability as a function of the safety factor for different areas in tension for the AG-4c material is shown in Figure 25.

A similar approach [95] can be used in calculating the fracture probability for long-term loading of components. In this case, we need to know the load variation function and the long-term static strength limits for a definite time base.

The fracture probability in the long-term static loading case is determined as

$$V = \int_0^{\sigma_{max}} P(\sigma_{0_i})\, p(\sigma_{0_i})\, d\sigma \approx \sum_1^n p(\sigma_{0_i})\, P(\sigma_{0_i}). \qquad (97)$$

CHAPTER 7

FRACTURE RESISTANCE UNDER LONG-TERM STATIC AND CYCLIC LOADING

§1. Statistical Laws Governing Temporal Dependence of Strength

Stochastic Picture of Fracture Process

In analyzing the strength of fiber bundles in §4, Chapter 4, it was shown that in the case of constant nominal stresses, a stage of quasi-equilibrium states is possible in which the number of fractured fibers varies from $a(w_I)$ to $a(w_{II})$. It was previously assumed that the stress increases continuously, and fracture occurs at the instant of reaching the maximum magnitude of $\sigma\int_{\sigma}^{\infty}p(\sigma)d\sigma$ for some fiber strength distribution function $p(\sigma)$. In the case of a fixed load (long-term strength regime) the stress on the fibers can increase only as a result of fracture of part of the fibers in the long-term static loading process. Failure occurs when the stress

$$\sigma_{np} = \frac{\sigma_n}{1 - a(w_{II})}, \tag{1}$$

is reached, where $a(w_{II})$ depends on the stress level and the kinetics of the long-term static fracture process. With lower initial stress, it follows from the bundle fracture scheme that occurrence of the condition $(\sigma_{cr})_{lt} > (\sigma_{cr})_{stat}$ is possible. Experiment shows, however,

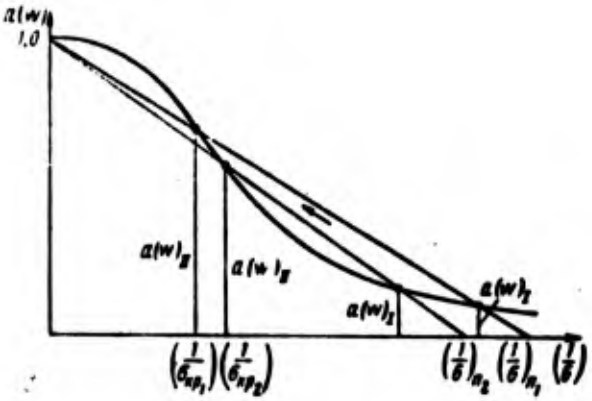

Figure 1. Scheme of fiber bundle failure in the long-term loading case.

that the long-term static failure fracture process can stagnate in the case of low initial stresses.

Let us examine how the process of transition from the state $a(w_I)$ into the state $a(w_{II})$, whose scheme is shown in Figure 1, takes place. We assume that the fibers in a quite large bundle of N fibers are equally loaded, and the tensile stress is the same function of time t for all the unfailed fibers. We denote the bundle breaking time by t_b, the number of unbroken fibers by n(t). The life is determined by the time for reduction of n(t) to n_{cr} (the magnitude of the life obviously changes only slightly when replacing n_{cr} by 0, since the duration of the fast-fracture segment is short in comparison with the segment of slowly progressing fracture up to $n(t) = n_{cr}$). The stresses in the fibers are independent of the initial number of fibers and at the time t are equal to $\sigma N/n(t)$, since the broken fibers do not accept any load. The fiber bundle can be considered an assemblage of thin plates (regions 2δ), whose boundaries are planes perpendicular to the bundle axis. When the bundle fails, the crack is entirely in an individual layer S_1. At the initial instant of time, each layer has the same number of fibers (for $t = 0$ $N_i = \text{const}$, N_{ti} can be determined with account for the initial damage which arises at the instant of load application).

For the sake of simplification, it is advisable to assume [123] that the only possible transitions for the given region 2δ are the transitions

$$\varepsilon_{N,N} \to \varepsilon_{N,N-1} \to \varepsilon_{N,N-2} \to \cdots \varepsilon_{N,n} \cdots \to \varepsilon_{N,0}, \tag{2}$$

where, for example, the constants $\varepsilon_{N,\,n}$ mean that in the region S_i the number of unfailed fibers at the time t is n(t). We can further assume that for constant stress the probability of occurrence of the transitions $\varepsilon_{N,n} \to \varepsilon_{N,n-1}$ remains unchanged so long as the region S_i is in the condition $\varepsilon_{N,n}$, regardless of the state of the neighboring regions S_{i+1}, S_{i-1}, and so on. Fiber fracture at constant stress obeys activation theory, and the probability of the $\varepsilon_{N,n} \to \varepsilon_{N,n-1}$ transition, which takes place after short time intervals, is equal to nkdt, where $k = f[\sigma N/n(t)]$ is a function which depends only on the stress, increasing monotonically with decrease of n(t). We neglect the possible stress concentration effects at the fiber fracture location. The function k can be taken in the form [122, 123]

$$k\left[\frac{\sigma N}{n(t)}\right] = a\exp\left[\frac{b\sigma N}{n(t)}\right], \tag{3}$$

where the parameters a and b depend only on the temperature.

Thus, it is necessary to determine the probability that the bundle of fibers will fail after the time interval t_b. The probability that the region S_i will be the state $\varepsilon_{N,\,n}$ at the time t for a known stress σ is denoted by $P_{N,\,n}(t, \sigma)$, and the probability of the transition $nk(\sigma N/n)dt$ is denoted by $\lambda_{N,\,n}dt$. These assumptions essentially mean that the behavior of the region S_i obeys the laws of a stochastic process [68] with the following levels for the partial derivatives of the probabilities $P_{N,\,n}$ with respect to time

$$\left.\begin{aligned} P'_{N,N} &= -\lambda_{N,N}P_{NN};\\ P'_{N,n} &= -\lambda_{N,n}P_{N,n} + \lambda_{N,n+1}P_{N,n+1};\\ P'_{N,0} &= \lambda_{N,1}P_{N,1}. \end{aligned}\right\} \tag{4}$$

where for all n and t the following relations are satisfied

$$\begin{gathered} 0 \leq P_{N,n}(t, \sigma) \leq 1,\\ \text{for } n \neq N\ P_{N,n}(0, \sigma) = 0 \text{ and } P_{N,N}(0, \sigma) = 1. \end{gathered} \tag{5}$$

Recovery of the failed fibers is thus not provided for.

The quantity $1 - P_{N,\,0}(t, \sigma)$ is the probability that the region S_i has longer lifetime than t at the stress σ. The number of regions in the bundle is $M = L/2\delta$. Then the probability $1 - Q_\sigma(t_b)$ that the fiber bundle has a life longer than t_b corresponds to the probability of occurrence of M independent cases of each probability $1 - P_{N,\,0}(t_b, \sigma)$:

$$1 - Q_\sigma(t_b) = [1 - P_{N,0}(t_b, \sigma)]^M. \tag{6}$$

Consequently, the fiber bundle fails at that cross section which has the shortest lifetime for the load $f(\sigma)$, and kinetic theory is compatible with the weak link hypothesis.

Determination of the mean life [122, 123] and its scatter has shown that the lifetime distribution for long-term static loading is not normal; the asymmetry approaches a constant magnitude. A bundle of N fibers, for which (3) is valid, has the mean life

$$\bar{t}_\sigma = \Gamma\left(1 + \frac{1}{N}\right) M^{-1/N} a^{-1} \exp\left(-b\sigma \sum_{n=1}^{N} \frac{1}{n}\right),$$

which as $N \to \infty$ becomes

$$\bar{t}_\sigma = M^{-1/N} a^{-1/N} N^{-b\sigma} \exp(-\gamma b\sigma) = Ae^{-\alpha\sigma}, \tag{7}$$

where

$$\gamma = \lim_{N \to \infty}\left(\sum_{n=1}^{N} \frac{1}{n} - \ln N\right).$$

It follows from (7) that the logarithm of the life is a linear function of the stress σ. The variance is described by the relation $S_{t_b} = (\pi/\sqrt{6})N^{-1}\bar{t}_b$, i.e., the coefficient of variation of the life is constant.

The distribution of the long-term static strength limits for a fixed life is characterized by the mean value

$$\bar{\sigma}_{\vartheta_*} = (\gamma + \ln N)^{-1} b^{-1} [-\ln(\bar{t}_* a) - N^{-1} \ln M]$$

and the variance

$$s^2_{\sigma_{\vartheta_*}} = \frac{\pi}{6} \gamma^2, \text{ where } \gamma = b \sum_{i=1}^{N} \left(\frac{1}{n}\right). \tag{8}$$

It is noted in [124] that (7) is the solution of a deterministic equation of the form

$$\frac{dn}{dt} = n\kappa\left(\frac{\sigma N}{n}\right).$$

Account for damage accumulation in the long-term static fracture case under the assumption of power-law damage accumulation can be made using the equation

$$\frac{dw}{dt} = w^{\beta} B \sigma^{\kappa}, \tag{9}$$

where $\sigma = \sigma_0/1 - w$; w is the degree of damage (cracking), characterized by the fractured section area [87, 96]. We write the brittle fracture condition in the form [87]

$$\int_0^t (1 + \kappa) B \sigma_0^{\kappa} dt = \int_0^1 (1 - w)^{\kappa} w^{-\beta} dw = 1, \tag{10}$$

where the limits of integration with respect to w were taken as 0 and 1 for simplification. According to (10), for a constant stress σ_0 and $\beta = 0$, the life

$$t^*_{(\sigma_0)} = \frac{1}{(1 + \kappa) B \sigma_0^{\kappa}}. \tag{11}$$

For variable long-term stress and $\beta = 0$, (10) expresses the linear damage summation condition.

In the case of damage accumulation at low stress levels, the experimental data [96] and the results of life calculation using linear and nonlinear damage summation conditions are similar.

In the case in which the major damage (~70%) is accumulated at high stress levels during loading with markedly differing stress levels, calculation using the nonlinear summation condition gives results which are closer to the experimental data.

For a sinusoidal isothermal stress cycle

$$\sigma(t) = \sigma_m + \sigma_a \sin \omega t, \tag{12}$$

where $\sigma_m > \sigma_a$ (the fracture processes in compression and tension are not equivalent). Calculation of the life yields the following magnitude of the mean cyclic life [123]

$$t(\sigma_m, \sigma_a) = \frac{a^{-1}\exp(-b\sigma_m)}{I_0(b\sigma_a)} = \frac{t(\bar{\sigma}_m)}{I_0(b\sigma_a)}, \tag{13}$$

where $\bar{t}(\sigma_m)$ is the life with constant stress $\sigma = \sigma_m$; $I_0(b\sigma_a)$ is the Bessel function of zero order.

Long-Term Static Strength. Experimental Data

The time dependences of the fiber and polymer matrix strength determine the effect of loading duration during composite fracture. The experimental data [100, 103, 142] show that significant reduction of the strength in the long-term loading process is characteristic for the GRP. Thus, in tests lasting for ~10^3 - 10^4 hours in air and at normal temperatures, GRP strength is half that obtained in short-term tests.*

*Questions of creep are not considered here. (Table 1).

TABLE 1

LONG-TERM STRENGTH LIMITS OF SOME COMPOSITES

Resin	Filler	Test Duration in Years	°C	$\frac{\sigma_{lt}}{\sigma_b}$
Epoxy	Glass cloth	1000*		0.66
Phenolic	Atlas weave	1000*	23	0.57
Silicone				0.50
Phenol formaldehyde	Asbestos	5		34/18.5
	Paper	5		35/21.5
	Cloth	5	23/75	36/19.5
	Cotton waste	5		25.6/15.0

*In hours

The resistance to long-term static fracture depends on the form of glass filler and binder and the type of stress state. The GRP based on oriented glass fibers have the highest long-term strength limits; the chopped fiber glass mats have the lowest strength (0.33 σ_b for $t = 10^4$ hours). As a rule, the time dependence of the strength shows up more markedly in compression and bending, which is apparently associated with the greater role of the binder shear strength when the material works in compression and bending [177].

The variance of composite long-term static strength leads to scatter of the time required for fracture. Tests under identical conditions have shown the validity of the normal distribution law for the logarithms of the lifetimes with deviations in the region of low fracture probabilities, which indicates the existence of a left-hand lifetime bound. We can take as the transform for equalizing the distribution the function $\lg (t - t_0)$, where t_0 is the left-hand life bound (sensitivity threshold). Plotting of the experimental points on probability paper corresponding to the Weibull statistical distribution shows that this distribution also describes quite well the lifetime scatter (Figure 2). However, for parameters characteristic of the materials studied the two distribution types are close in the probability range studied.

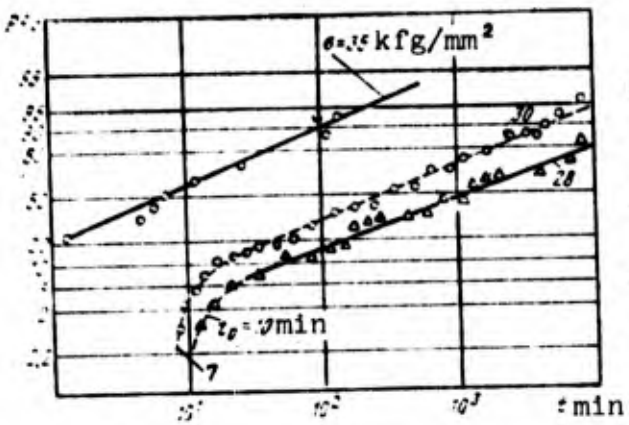

Figure 2. Long-term loading life distribution curves for 33-18c composite.

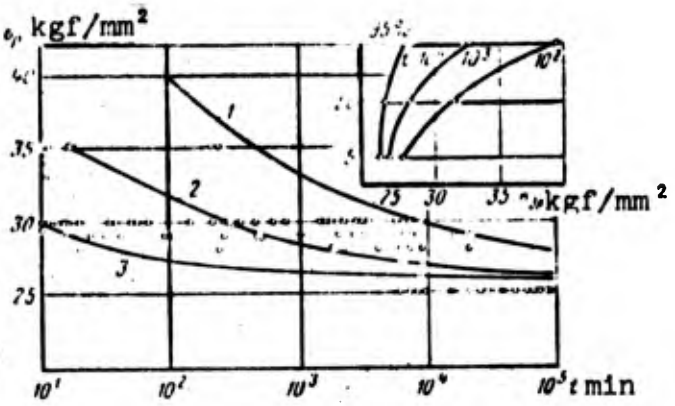

Figure 3. Long-term strength curves for the 33-18c composite (section 25 mm² t = 20° C):
1 — P = 95%; 2 — 50%; 3 — 5%.

According to the experimental data, the lifetime scatter depends very weakly on the stress level in the region $\sigma_{lt} > 0.75\sigma_b$ (see Figure 2).

The resistance to long-term static fracture is described by the long-term stress-rupture curves in terms of the fracture probability parameter (Figure 3). After specifying the probability, we can determine the long-term strength limit corresponding to the base τ and can obtain the distribution of the long-term static strength limits for a fixed time base.

Figure 3 shows that the long-term strength curve in the coordinates σ - lg t for 50% probability is linear in the region of stresses higher than $0.6\sigma_b$, and deviates from the linear dependence for lower stresses. The weak dependence of the lifetime variance on the stress level makes it possible to use linear correlation analysis for statistical processing of the results of long-term static GRP tests. The correlation coefficient for stresses $\sigma_{lt} > 0.6\sigma_b$ and the corresponding lifetimes are close to -0.9, i.e., the exponential equation for the long-term strength curve, which follows from the

stochastic fracture process relations, is valid for these stress levels. However, the nature of the experimental relation σ - lg t indicates the existence of some stress level which the material withstands infinitely long without fracturing.

The existence of a long-term strength limit for the composites based on glass fiber is associated in [192] with the GRP creep process. It was shown experimentally that if the creep has a decaying nature, the damage accumulation for $\sigma_{lt} \leq 0.5\sigma_b$ decays without leading to fracture.

Structural analysis [24] shows that long-term static fracture begins at the fiber-matrix interface, and is primarily a disruption of the adhesive bond. Damage accumulation leads to the formation of the main cracks, and to final failure.

In analyzing the experimental data, it was found that a power-law equation for the long-term strength curve in the form $\sigma^k t = C$ could also be used, particularly for the thermosetting composites with high fiber content and in the presence of aggressive media. For values of the exponent k characteristic of GRP, the difference in the correlation coefficients for the semilogarithmic and power-law relations is not significant (comparison of the power-law and semilogarithmic relations in the form $t = Ae^{-\alpha\sigma}$ and $t = Ce^{-k \ln \sigma}$ yields exponents $\alpha\sigma$ and $k \ln \sigma$ for the GRP which are similar in magnitude).

We note that the power-law equation is more convenient than the exponential equation, particularly when summing the lifetimes. For glass-fiber-base composites, neglecting inelastic deformations, the equation $\sigma^k t = C$ can be written in the form

$$t = B\tilde{E}^{-b}\varepsilon^{-b}. \tag{14}$$

From the condition $\int_0^{t_b} \frac{dt}{t_{(\sigma)}} = 1$ we obtain, for example, for a monotonic loading process following the law $\varepsilon = \varepsilon_0 + \dot{\varepsilon}t$

$$\frac{E^*}{B}\int_0^{t_b} (\varepsilon_0 + \dot{\varepsilon}t)^k dt = 1$$

and then

$$\sigma = [BE(1+b)\dot{\varepsilon}]^{\frac{1}{1+b}} + \sigma_0.$$

In the case of loading from $\sigma_0 = 0$

$$\lg\sigma = C_0 + C_1 \lg\dot{\varepsilon}, \qquad (15)$$

where

$$C_0 = \frac{1}{1+b}\lg[(1+b)EB],\ C_1 = \frac{1}{1+b}.$$

The following values of the exponents k were obtained from the composites studied: 19 for AG-4c reinforced in two directions; 26 for AG-4c reinforced in a single direction; 24, 37, 27 respectively for 33-18c, E1200, 27-63c, reinforced in two directions.

Figure 4 shows the long-term strength curves for the AG-4c and 33-18c materials as a function of the cross section area.

The scale effect also shows up in the long-term static loading case (see Table 2). Determination of the breaking stresses corresponding to different fixed failure times t^* showed that in the long-term static loading case, the scale effect can be estimated using the relation

$$\left(\frac{\sigma_{F_1}}{\sigma_{F_2}}\right)_{t^*=\text{const}} = \left(\frac{F_2}{F_1}\right)^{1/m}, \qquad (16)$$

i.e., the similarity relation is valid for fracture in the short-term loading case.

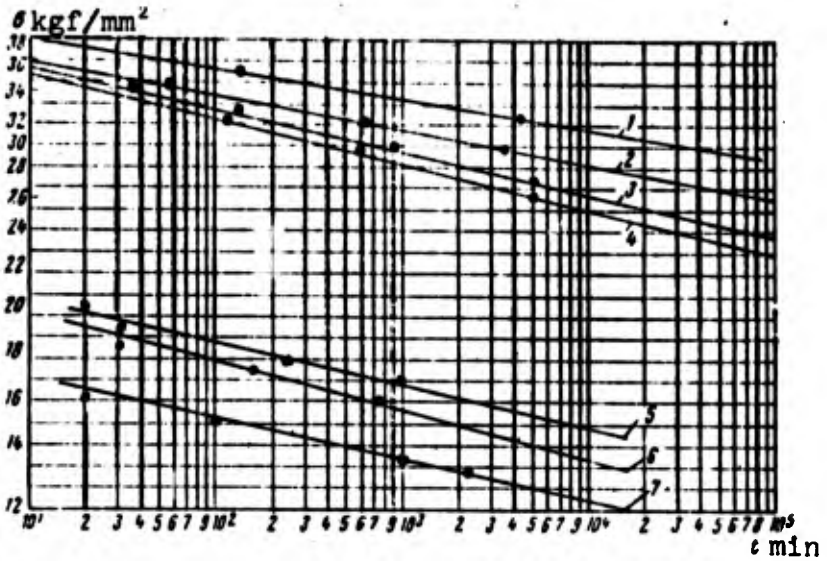

Figure 4. Curves of long-term strength for:

1 — unidirectional AG-4c (section 50 mm²); 2, 3, 4 — equistrength 33-18c (section 25, 50, 100 mm²); 5, 6, 7 — equistrength AG-4c (section 25, 50, 120 mm²).

TABLE 2

LONG-TERM STRENGTH LIMITS OF 33-18c AND AG-4c COMPOSITES

Material Specimen	σ_b in kgf/mm² (short-term)	σ_{lt} in kgf/mm² (1000 hours)	$\frac{\sigma_{lt}}{\sigma_b}$
33-18c			
100 мм², 20° C	42,0	24	0,57
50 мм²	41,0	24,8	0,56
25 мм²	46,0	26,5	0,57
φ = 30°, 100 мм²	16,5	9,0	0,54
φ = 45°, 100 мм²	14	8,4	0,60
33-18c			
50 мм², 150° C	20	12	0,60
200° C	21,5	10	0,46
25 мм² 100° C	30	18	0,60
AG-4c			
120 мм², 20° C	16,5	11,9	0,72
50 мм², 20° C	18,2	12,8	0,70
25 мм², 20° C	20,0	14,0	0,70
25 мм², 100° C	13,0	9,0	0,69

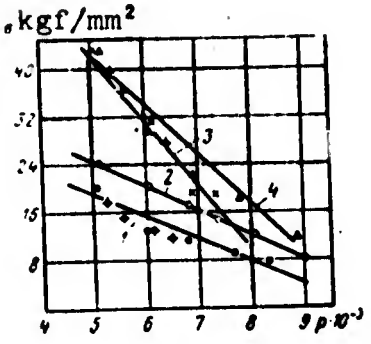

Figure 5. Parametric relations for the materials:

1 — AG-4c; 2 — P-25c; 3 — 33-18c; 4 — R-49c (× indicate points of long-term strength curve).

The linearity of the stress dependence on the logarithm of the time makes it possible to use parametric relations of the Larson-Miller type with a precision adequate for practical applications

$$\sigma = a - bp, \qquad (17)$$

where

$$p = T(C + \lg t),$$

for estimating GRP life under operational temperature and stress conditions (Figure 5). Using the parametric relation (C = 20), we can determine from the results of the short-term static tests at different temperatures the coefficients of the parametric equation and construct the parametric relations for approximate evaluation of the lifetime.

Tests at elevated temperatures show that the long-term strength curves do not cross at a single point, as follows from the concept of time dependence of the strength for the hard polymers. This is apparently explained by the marked change of the shear characteristics of the polymer matrix when heated, particularly if heated above the vitrification temperature of the binding matrix. At temperatures of ~100°C, the matrix softens to the degree that the glass reinforced plastic becomes a weakly bound bundle of parallel glass fibers, for which the laws governing static failure differ markedly.

The static long-term strength limit for a base up to 500 hours varies considerably with increase of the temperature and decreases by a factor of two at temperatures of 200° C. For temperatures in the 100 - 300° C range, the inclination to the time axis of the left part of the long-term strength curve is steeper and the break in the curves occurs at low time values, which is apparently determined by the rate of the relaxation processes in the matrix, which increases with

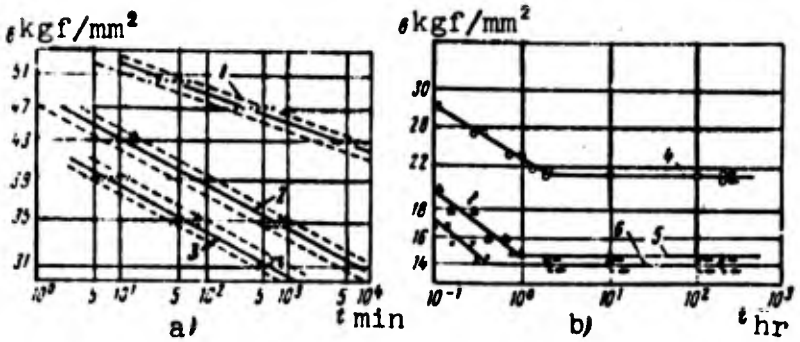

Figure 6. Long-term strength curves for the composites: E1200 (1 — t = 20° C) and 27-63c (2 — t = 20° C; 3 — t = 60° C; 4 — t = 100° C; 5 — 200° C; 6 — 300° C).

increase of the temperature (Figure 6a, b), as a result of which the stresses are transferred entirely to the glass fibers, and also by the possible physical and chemical changes in the material with long-term heating.

Results of Tests Under Quasi-Static and Impact Loading

The time dependence of the strength was studied experimentally in the deformation rate range from 2 sec^{-1} to $3 \cdot 10^{-8}$ 1/sec. Short-term loading was accomplished on a hydropneumatic rig, the quasi-static deformation regime was conducted on a machine with mechanical drive, and the low rates were obtained during tests in the long-term strength regime [63]. The deformations in the course of the tests and at fracture were recorded.

The variation of the breaking stresses with time is shown in Figure 7 for the 27-63c material. Statistical analysis showed that the correlation coefficient between the values of σ - lg t is -0.927, i.e., the dependence is linear.

Also shown is the breaking stress curve for tests in the regime σ = const, which falls below the curve of strength time dependence for the regime $\dot{\varepsilon}$ = const, crossing this curve at a point close to the composite short-term static strength limit obtained at the rate $45 \cdot 10^{-4}$ 1/sec (Figure 8).

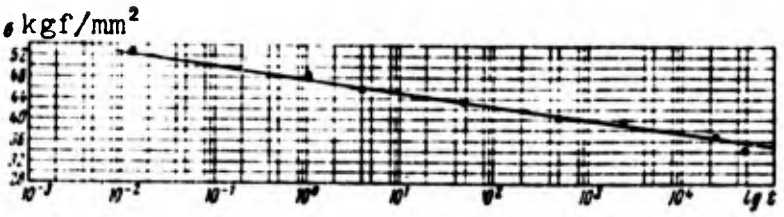

Figure 7. Time dependence of the breaking stresses for the composite 27-63c (ε = const).

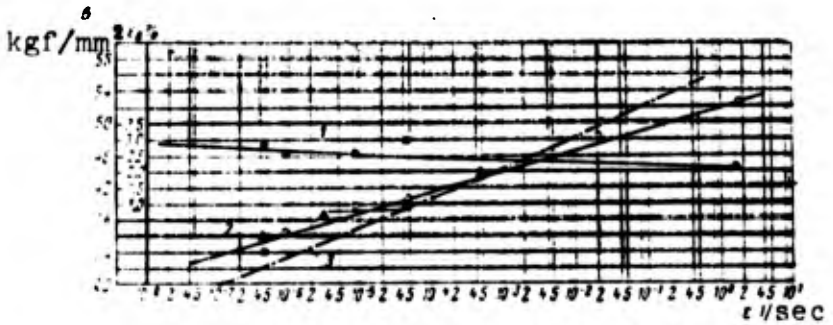

Figure 8. Time dependence of breaking stresses and deformations for 27-63c:

1 — ε_b; 2 — $\dot{\varepsilon}$ = const; 3 — σ = const.

The resulting dependence of the deformation at composite fracture on the rate $\dot{\varepsilon}$ (see Figure 8) indicates the weak influence of deformation rate on its magnitude. The breaking deformation for 27-63c decreases monotonically, varying from 2.8 to 2.3% with increase of the rate by 10^7 times. For a deformation of about 2%, we observed cracking of the matrix in the layers with fibers oriented perpendicular to the force. As a rule, with increase of the rate the fracture had a fibrous nature. In the case of lower rate and quasi-static loading, the magnitude of the fracture deformation increases somewhat and the progressive fracture segment is more marked. Generalizing the experimental data obtained, we can assume that the magnitude of the breaking deformation in uniaxial tension in the first approximation depends very little on deformation rate.

Similar results were noted in [86].

The test results show that the breaking stress dependence on deformation rate is linear and is described by an equation of the form

$$\sigma - \sigma_0 = m^* \lg \frac{\dot{\varepsilon}}{\dot{\varepsilon}_0},$$

where σ and $\dot{\varepsilon}$ are the strength and deformation in the test regime $\dot{\varepsilon}$ = const, and σ_0 and ε_0 are the strength and deformation for some standard test regime; $m^* = m \ln 10$ is the rate modulus [81], characterizing the slope of the curve σ - lg $\dot{\varepsilon}$.

Assuming the breaking deformation to be independent of the rate, we can convert to the equation connecting stress and time to fracture

$$t_* = t_0 \exp\left[-\frac{\sigma - \sigma_0}{m}\right],$$

where t_0 is the time to fracture for the standard rate $\dot{\varepsilon}_0$.

For the composite 26-63c σ_0 = 43.2 kgf/mm^2, $\dot{\varepsilon}_0 = 45 \cdot 10^{-4}$ 1/sec and m^* = 109 kgf/cm^2.

Conversion of the results of long-term static loading using the regime σ = const under the assumption that the longest-duration long-term static fracture process takes place at (approximately) constant deformation rate (steady-state creep) leads to agreement of the data based on the relation σ - lg t with the data for the regime $\dot{\varepsilon}$ = const.

This shows that the relation σ - lg $\dot{\varepsilon}$ is valid over a wide range of time to fracture.

§2. GRP Fracture Under Cyclic Loading

Characteristics of Low-Cycle Fatigue Process

In the process of GRP cyclic loading with relatively high amplitudes, we observe self-heating of the specimens as a result of energy dissipation. The nature of the material self-heating can be explained by analyzing the strain diagram in the cyclic loading case. Figure 9 shows the strain diagrams for the 33-18c (a) and 27-63c (b) composites, characterizing the presence of elastic hysteresis and the amount of energy absorbed by the material per cycle. As a rule, the curves of temperature rise during cyclic loading have three zones: initial zone with decaying heating rate, which corresponds to stabilization of the strain diagram in the first loading cycles and of the width of the hysteresis loop; zone of steady-state heating at a rate which varies little (loop width does not change); zone of temperature rise of increasing rate prior to fracture. In this last segment, the hysteresis loop broadens and specimen stiffness decreases markedly. For the 33-18c and 27-63c GRP specimens the modulus of elasticity changes in the cyclic loading process from 2800 to 1500 kgf/mm² for a maximal cycle stress of 28.2 and 44.6 kgf/mm² with a lifetime of 200 cycles.

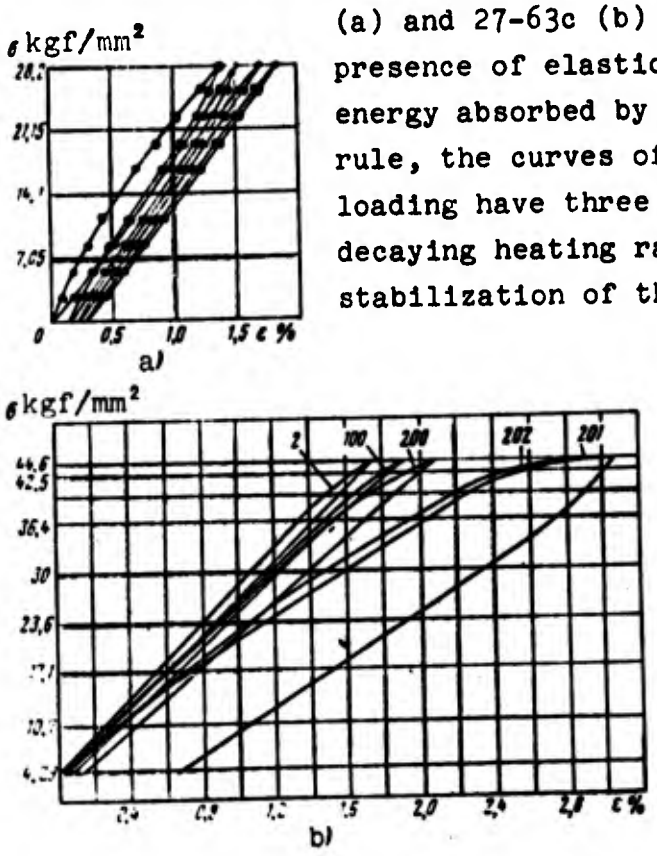

Figure 9. Strain diagram for cyclic loading:
a — 33-18c; b — 27-63c.

In the sinusoidal load variation case ($\sigma = \sigma_0 \sin \omega t$), the equation for the deformation of a composite made from elastic fibers and the viscoelastic binder takes the form

$$(-\tau_0 E_0 \omega_i + E_\infty)\,\varepsilon_0 \sin(\omega t + \delta) = \sigma_0 (t + \omega\tau), \tag{18}$$

where τ_0 is the relaxation time; E_0 is the instantaneous modulus of elasticity; E_∞ is the long-term modulus of elasticity; ω is the loading frequency; σ_0 and ε_0 are the stress and strain amplitudes; δ is the phase shift angle between the stress and strain.

The deformation process can be described more exactly with introduction of the relaxation time spectrum into the strain equation. Depending on the strain rate (frequency), a definite portion of the spectrum shows up. In the simplified treatment, we take the relaxation time τ_0 as the determining factor for a given test frequency. Thus, the strain equation can be written for each frequency ω with its relaxation time τ_{0_ω}. The connection between the quantities ε_0 and σ_0 is written in the form [92]

$$\varepsilon_0 = \sigma_0 \left(\frac{1 + \omega^2 \tau^2}{E_\infty^2 + E_0^2 \tau^2 \omega^2} \right)^{1/2}. \tag{19}$$

In this case,

$$\operatorname{tg} \delta = \frac{\omega\tau (E_\infty - E_0)}{E_\infty + E_0 \tau^2 \omega^2}. \tag{20}$$

Consequently, the strain amplitude ε_0 and the tangent tg δ of the phase shift angle depend on the relaxation time and loading frequency. The strain amplitude varies as a function of the parameter $\tau\omega$, taking values in the interval $(\sigma_0/E_\infty) - (\sigma_0/E_0)$ (Figure 10), while the phase shift angle has a maximum for $\tau\omega = \sqrt{E_\infty/E_0}$ and is equal to

$$\operatorname{tg} \delta_{max} = \frac{E_\infty - E_0}{2\sqrt{E_0 E_\infty}}. \tag{21}$$

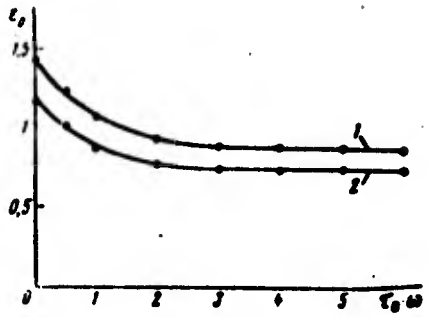

Figure 10. Strain amplitude versus the parameter $\tau_0\omega$: 1 — σ = 30 kgf/mm^2; 2 — σ = 25 kgf/mm^2.

It follows from this relation that tg δ is always negative. For the 33-18c material with E_0 = 350,000 and E_∞ = 210,000 kgf/cm^2, the relaxation times are on the order of 0.6 sec, characteristic for test frequencies of 10 - 400 cpm; the maximum of tg δ is obtained at a frequency of 80 cpm and amounts to 0.26.

An oscillographic record was made of the cyclic deformation process for an experimental check of the assumed equation. In determining the parameters characterizing energy dissipation, the cyclic strain resistance can be evaluated by the elastic modulus

$$E = E' + iE'', \tag{22}$$

where E' is the real modulus, coinciding in phase with the strain; E'' is the imaginary modulus, 90° out of phase with the strain, or in terms of the corresponding compliances

$$J = \frac{1}{E} = J' - iJ'', \tag{23}$$

where J' is the elastic compliance; J'' is the loss compliance.

The elastic compliance characterizes the energy accumulation and release during unloading, and the loss compliance is associated with the energy dissipated in the material.

From the results of the oscillographic study tg $\delta = E''/E'$, and for the quantitative estimate of the energy dissipation, we can use the magnitude of the specific energy stored per cycle and increasing during a quarter period

$$U'_{acc} = \int_0^{\varepsilon_0} E'\varepsilon\, d\varepsilon = \frac{E'\varepsilon_0^2}{2}. \tag{24}$$

The energy dissipated is measured during the time of a complete cycle. Since the stored energy increases during a quarter period, it is advisable to compare it with the energy dissipated during a quarter period

$$U_{пог} = \int_0^{\varepsilon_0} \frac{E''\varepsilon}{\omega} d\varepsilon = \frac{\pi E''}{4} \varepsilon_0^2. \tag{25}$$

The ratio of the dissipative loss energy to the stored energy is

$$\alpha = \frac{U_{пог}}{U_{зап}} = \frac{\pi}{2} \operatorname{tg}\delta \tag{26}$$

and is proportional to tg δ.

With increase of the maximum cycle stress, the phase shift between the stress and strain increases and the energy absorption intensity increases. For the same stress, the heating rates of different specimens differ significantly, with a shorter life corresponding to the higher rate. Characteristic for high stresses is less variance of the heating rate. Specimens tested under different stresses but with lifetimes which are close in magnitude have similar heating curves. Table 3 presents test results for the 33-18c GRP for different loading levels and frequencies of 200 and 400 cpm in pulsating tension.

TABLE 3

INFLUENCE OF STRESS LEVEL ON TANGENT OF PHASE SHIFT ANGLE AND ENERGY ABSORPTION FOR THE 33-18c MATERIAL

Maximum Cycle Stress in kgf/mm^2	Tangent of Phase Shift Angle	Ratio of Dissipated and Stored Energies	Increase of Energy Absorption in %
20	0.111 (0.087)	0.174 (0.141)	9 (9)
25	0.124 (0.099)	0.195 (0.159)	12 (13)
30	0.133 (0.119)	0.209 (0.186)	20 (31)

NOTE: Values in parentheses are for 400 cpm frequency.

The role of the frequency for a constant pulsating cycle stress level (σ = 25 kgf/mm^2) is characterized by the data shown in Table 4.

TABLE 4

INFLUENCE OF LOADING FREQUENCY ON TANGENT OF PHASE SHIFT ANGLE AND ENERGY ABSORPTION FOR THE 33-18c GRP

Frequency in cpm	Tangent of Phase Shift Angle	Ratio of Dissipated and Stored Energies	Change of Energy Absorption in %
200	0.132	0.207	0
300	0.128	0.200	−3.5
400	0.111	0.174	−16
600	0.089	0.154	−24

With increase of the frequency, the values of tg δ decrease, and therefore the ratio of the dissipated energy to the cycle energy decreases. The energy release per second can be estimated, considering heat exchange between the specimen and the surrounding medium, by the quantity

$$\dot{U} = \kappa \frac{\omega J'' \sigma_0^2}{2}. \qquad (27)$$

If we take $\frac{\kappa\sigma_0^2}{2} = \lambda$, we can determine the heat release dependence on frequency. The reduction of tg δ and J'' is offset by the frequency effect, as we see from the values of $\dot{U}/\lambda$ for frequencies of 200, 300, 400, and 600 cpm, equal to 0.436; 0.645; 0.735; and 0.910. Consequently, GRP self-heating increases with increase of the frequency and its life shortens. Figure 11 shows the results of 33-18c composite tests, and also tests of an epoxy GRP [145] at different stress levels and different frequencies.

The coefficient k depends on the specimen shape, conditions of heat exchange with the surrounding medium, and so on, and also takes into account any possible change of the compliance in the cyclic loading process resulting from increase of lg δ with increase of the

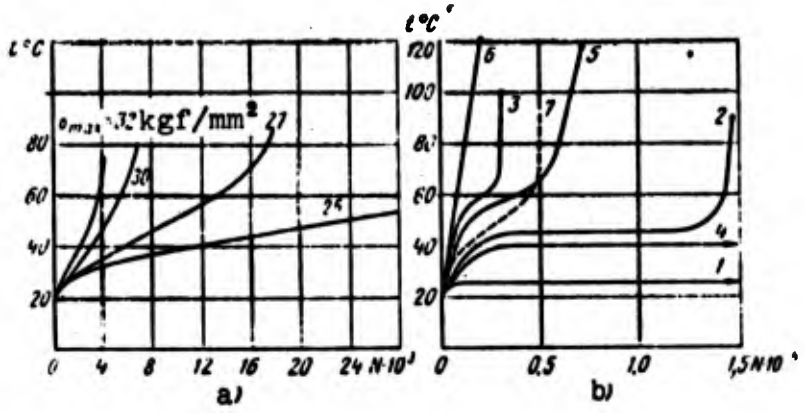

Figure 11. Curves of dissipative heating in pulsating tension for epoxy GRP as function of stress level (a) and loading frequency (b):

Curve	$\frac{\sigma_{max}}{\sigma_b}$ in %	ω in 1/min
1	31.5	1000
2	40	
3	50	
4	31.5	—
5	40	2000
6	50	—
7	50	200

temperature, reduction of the elastic modulus during heating, and damage accumulation. Experimental data have shown that $k \approx 49/(\sigma - 24.3)$ and decreases with increase of the stress.

The temperature rise curves also depend on the GRP resin damping properties and the loading mode. Figure 12a shows curves of temperature rise for epoxy and polyester GRP for pulsating tension with amplitude 5±5 and for symmetric bending with amplitude ±10 kgf/mm^2.

The data of Figure 12a show that for the same maximum cycle stresses, the heating during tension-compression takes place far more intensely than in the bending case, when the high stress zone is limited as a result of the stress gradient.

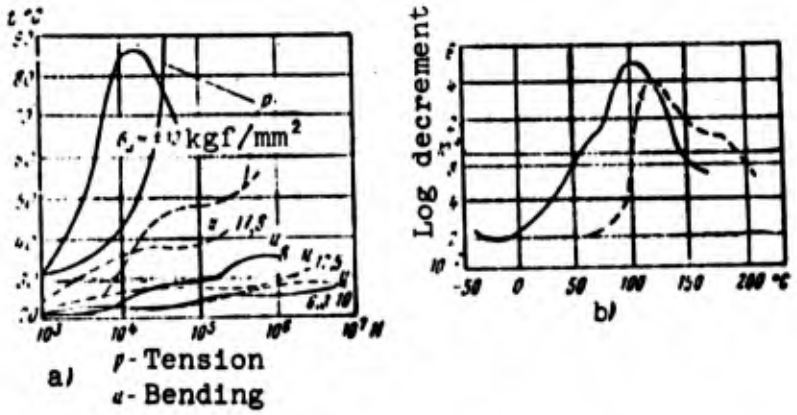

Figure 12. Influence of loading mode (a) and damping properties (b) of polyester (dashed curves) and epoxy (solid curves) resins on temperature rise.

The results of tests with asymmetry of the loading cycle showed that specimen heating decreases markedly. This leads to a noticeable increase of the lifetime for the same maximum cycle stress. The lifetimes in cycles and time for different frequencies and in the presence of loading cycle asymmetry are shown for the 33-18c GRP in Table 5.

TABLE 5

LIFETIME UNDER DIFFERENT TEST CONDITIONS

Frequency in cpm	Cycle Asymmetry	*Lifetime at Maximum Stresses in kgf/mm²						
		32	30	28	27	26	25	20
10	0,1	—	—	236 23,6	920 92	3640 364	6460 646	—
200	0,1	3900 19,5	6820 34	—	18 100 91	—	55 400 277	700 000 3500
200	0,5	23 820 119	26360 132	—	4000 200	—	120 000 600	—
400	0,1	2200 5,5	3400 8,5	—	7200 18	—	14 000 35	600 000 1500

*Numerator is life in cycles; denominator is life in minutes.

The cyclic tests of GRP specimens at high temperatures confirm indirectly the presence of self-heating. For the phenolic and polyester GRP at temperatures of 23 and 150° C, the fatigue limits based on 10^6 cycles are similar (Figure 13), which apparently indicates the existence of a temperature field inside the specimen.

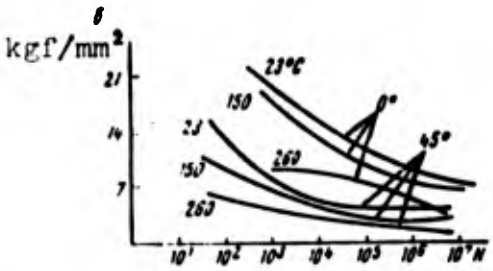

Figure 13. Influence of temperature on life of polyester GRP.

The results of tests of three GRP types at different temperatures (stress level $0.4\sigma_b$, pulsating tension, frequency 16 Hz) were presented in [166] (Table 6).

Thus, the lifetimes differ very little, and the imposition of an external temperature field in the indicated limits does not influence the number of cycles to failure.

TABLE 6

Temperature in °C	Life in 10^4 Cycles for Resin		
	Polyester	Epoxy	Phenolic
−20	3	1,3	2
20	4	1,4	2
80	1	1,1	1,5

In the theoretical estimation of plastic life, in most studies [18, 90] it is considered that the summation condition is valid

$$\int_0^{t_b} \frac{dt}{t(\sigma)} = 1, \tag{28}$$

where t_b is the lifetime; σ is the stress, which varies following some law.

If for pulsating tension with constant loading rate (for simplification) we take the time dependence of the strength in the form

$$t(\sigma) = A \exp(-\alpha\sigma), \tag{29}$$

we obtain the relation between the cyclic life and the life under long-term static loading

$$t_{\text{цикл}} \approx \alpha\sigma_{\max} t(\sigma), \tag{30}$$

where $t(\sigma)$ is the life under long-term static loading at σ_{max}, determined from the long-term strength curve; α is a parameter of the long-term static strength curve.

Comparison of the calculated and actual lifetimes without account for heating shows a significant difference [18, 90]. If the maximum stresses are the same, the lifetime under cyclic loading is considerably shorter than in the case of long-term static loading, and with increase of the frequency this difference increases. Thus, we can assume that not only the loading time but also the cyclic nature of the loading, associated with the heating, affects the lifetime.

Since the temperature changes continuously in the low-cycle fracture process, $t(\sigma)$ should be calculated by summing the lifetimes for σ = const and a temperature which is variable through the entire cyclic loading process. In the pulsating tension cycle case, the temperature field in the specimen working zone is quite uniform. In the first approximation, in the calculation we can take the lifetime from the long-term strength curve for some arbitrary average temperature, corresponding to the heating process for the given stress, considering the thermal state of the specimen to be quasi-uniform

$$t(\sigma) = A \exp(-\alpha\sigma)_{T=T_{cp}}. \tag{31}$$

If there are no long-term strength curves available for the limited range of times and temperatures (Figure 14a) characteristic for the low-cycle tests, we can use the parametric relation of the Larson-Miller type P = T(20 + lg t) for calculating the long-term static life, which agrees with the experimental data in the range of parameter values p = 5000 - 7000.

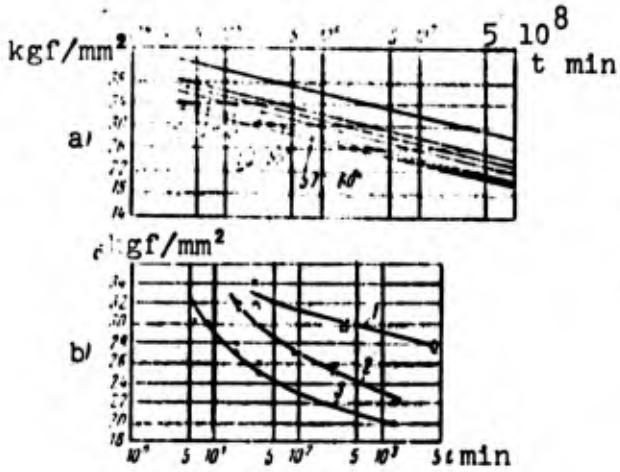

Figure 14. Curves of 33-18c GRP long-term strength for different temperatures (a) and comparison of the calculated (x) and actual (•) lifetimes (b) for frequencies 10(1), 200 (2), and 400 (3) cpm.

Figure 14b shows, for the 33-18c material, the calculated and actual lifetimes (in terms of time) for frequencies of 10, 200, and 400 cpm. We see that introduction of the temperature correction yields better agreement with the experimental data than does determination of the lifetime from the long-term strength curve without heating.

In performing the temperature correction of the lifetime summation condition, we should bear in mind that the long-term strength and fatigue curves should be statistically valid, since an error in determining the slope of their left-hand segments can lead to errors, since the slope index α appears as a factor in (30) and as an exponent in the lifetime formula.

Linearization of the self-heating curve has been used [76] for an approximate estimate of the lifetime under cyclic loading. However, the tests were conducted in a narrow range of stress amplitudes, and this apparently led the authors to conclude that the temperature was constant at the moment of fracture, while the final temperature depends on the magnitude of the variable stresses and other factors [25].

Thus, internal damping is the primary factor determining GRP cyclic life. The decrement depends on the resin type, reinforcement type, fiber orientation, loading level, and degree of fatigue (damage). Here the temperature dependence of the decrement and the presence of maxima (see Figure 13) determine the temperature range of GRP operation. The epoxy GRP are used in the range of small decrements (with low stresses). For high stresses, the heat release

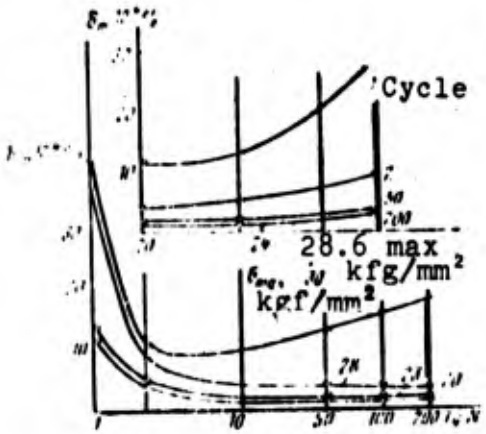

Figure 15. Kinetics of loop width change as function of the number of cycles for different stress amplitudes for the 33-18c composite.

increases; however, a higher temperature is required to reach the maximum decrement than for the other types of GRP. It was noted in [166] that in the case of cyclic loads it is preferable to use the epoxy composites at 20 - 30° C and polyester resin composites from -10 to -20° C.

Apparently we should differentiate two fatigue fracture mechanisms: at high stresses and frequencies the fracture process is determined by energy dissipation in the material; at low stresses and frequencies the absorbed energy is not large or is dissipated. In the first case, the purely mechanical nature of the fracture may not be manifest. Tests at low frequencies made it possible to trace the fracture process kinetics. The strain diagrams (see Figure 9) for loading with a frequency of 10 cpm for the 27-63c composite show that there is a monotonic increase of the maximum cycle deformation in the cyclic loading process. The width of the loop (Figure 15) initially decreases, then either stabilizes (up to 0.6 σ_b) or increases (above 0.6 σ_b). At the instant of fracture, the maximum strain differs little from the strain for short-term static loading.

For comparatively low stresses in the fatigue fracture region and cycle frequencies $>10^5$, the effects associated with dissipative losses are not strong, and fracture takes place as a consequence of damage accumulation in the cyclic loading process.

Cyclic Life Scatter and Fatigue Curve Equations

The results of fatigue testing of a large number of specimens at the same stress amplitude show that there is a considerable scatter of the GRP cyclic lifetime values. Therefore, it is necessary to

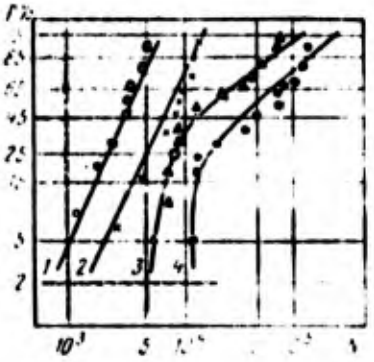

Figure 16. Lifetime distribution curves for the 33-18c composite in pulsating tension.

Curve	$N_0 \cdot 10^{-3}$	β
1	1	2.18
2	2	2.08
3	5	0.98
4	14	1.1

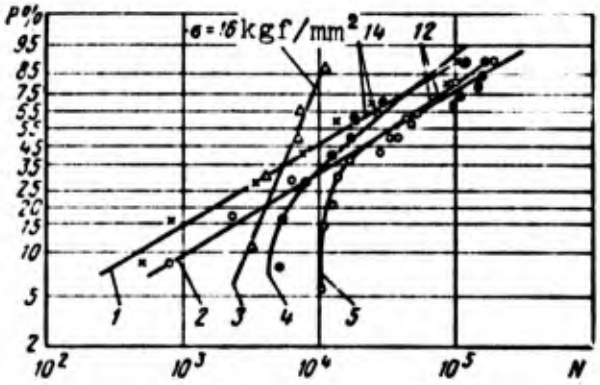

Figure 17. Lifetime distribution curves for the AG-4c composite in pulsating tension:

1, 2 — rectified distribution curves for σ = 14 and 12 kgf/mm²; 3, 4, 5 — lifetime distribution for stresses σ = 16, 14, and 12 kgf/mm², respectively.

conduct a large number of tests, use statistical analysis of the results, and establish the shape of the lifetime distribution curve.

Figures 16 and 17 show lifetime distribution curves for the 33-18c and AG-4c GRP at different stress levels for pulsating tension. If we plot the values of lg ($N - N_0$) along the abscissa axis, the distribution curves linearize (see curves 4 and 5 and curves 1 and 2 in Figure 17). This indicates that the lifetime distribution can be described with the aid of a Weibull function whose parameters are selected on the basis of the experimental data

$$P_N = 1 - \exp\left[-\left(\frac{N - N_0}{N_a}\right)\right]^{\beta}, \qquad (32)$$

where P_N is the probability of failure at the number of cycles N; N_0 is the number of cycles corresponding to low fracture probability, taken for the probability 0.02% ("cycle sensitivity threshold"); N_a

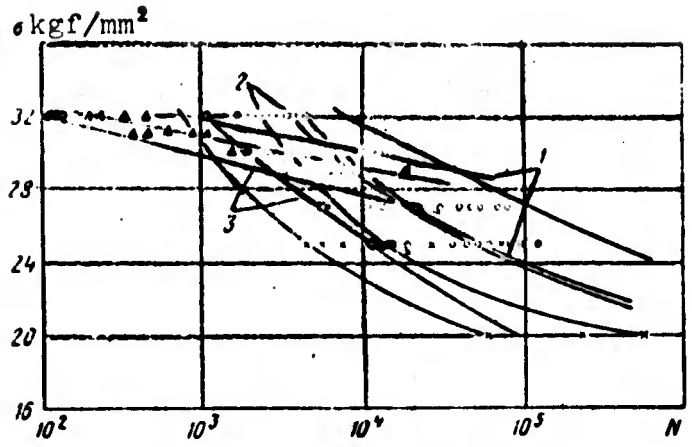

Figure 18. Fatigue curves of 33-18c composite for different probability levels for frequencies 10 (Δ), 200 (O), and 400 (X) cpm (r = 0.1):
1 — P = 95%; 2 — 50%; 3 — 5%.

is the number of cycles corresponding to a probability of 63.2%; β is the slope of the lifetime distribution curve.

Statistical analysis yields the following parameters of the lifetime distribution curves for the 33-18c and AG-4c materials at a frequency of 200 cpm (Table 7). After linearization, the lifetime distribution curves become parallel. For distribution parameters characteristic of the GRP data, use of the log-normal distribution law with account for the threshold N_0 is possible [192]. The sample size does not permit drawing definite conclusions on the type of lifetime distribution. From the statistical lifetime distributions for different stress levels, we can construct the fatigue curve based on the fracture probability parameter (Figures 18 and 19).

TABLE 7

PARAMETERS OF CYCLIC LIFETIME DISTRIBUTION CURVES FOR PULSATING CYCLE

Maximum Cycle Stress in kgf/mm²	Material			Maximum Cycle Stress in kgf/mm²	Material		
	β	$N_0 \cdot 10^{-3}$	$N_a \cdot 10^{-3}$		β	N_0	$N_a \cdot 10^{-3}$
32	2,18	1	38	16	2.2	2	8
30	2,08	2	90	14	0.56	4.5	25.3
27	0,98	5	95	12	0.56	11.6	35.4
25	1,10	14	400				

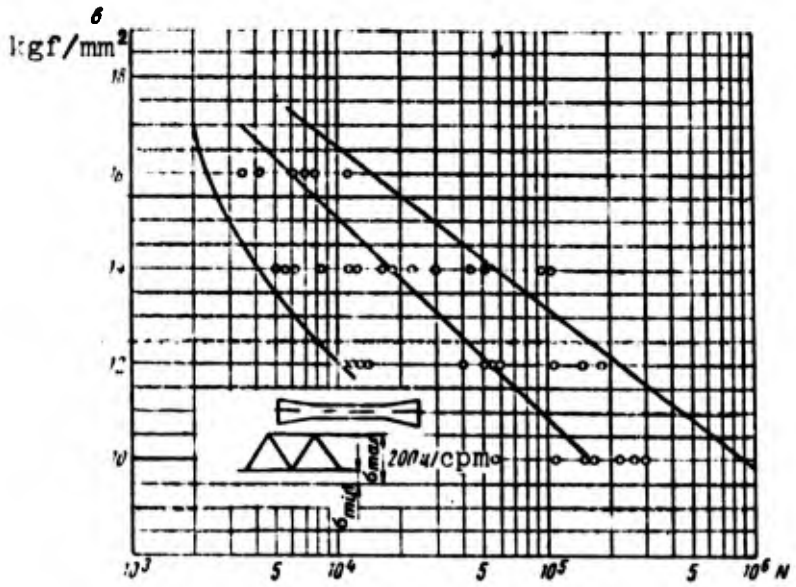

Figure 19. Fatigue curves of AG-4c composite for different probability levels.

In analyzing the test results, we usually plot curves of σ - lg N or lg σ - lg N. If the dependence of the lifetime variance on the stress level is weak, we can use correlation analysis to find the parameters of the fatigue curve equation. The correlation equation in semilog coordinates is written in the form

$$\lg N = \overline{\lg N} + r_{1/1} \frac{s_{\lg N}}{s_\sigma} (\sigma - \bar{\sigma}), \tag{33}$$

where $r_{1/1}$ is the coefficient of correlation between the quantities σ, and lg N and is found from the formula

$$r_{1/1} = \frac{\sum_{i=1}^{n} (\lg N_i - \overline{\lg N})(\sigma_i - \bar{\sigma})}{(n-1)\, s_{\lg N} s_\sigma}; \tag{34}$$

Here $s_{\lg N}$ is the mean square deviation of the quantity lg N; s_σ is the mean square deviation of the quantity σ; n is the number of tests; $\bar{\sigma}$, $\overline{\lg N}$ are the average stress and average lifetime.

For the logarithmic dependence, we write the analogous equation relating the stress and lifetime

$$\lg N = \overline{\lg N} + r_{1/1} \frac{s_{\lg N}}{s_{\lg \sigma}} (\lg \sigma - \overline{\lg \sigma}), \tag{35}$$

where $s_{\lg \sigma}$ is the mean square deviation of the quantity lg σ; $r_{1/1}$ is the correlation coefficient of the quantities lg σ and lg N; $\overline{\lg \sigma}$ is the mean logarithm of the stress.

Table 8 presents results of the determination of the basic parameters characterizing the GRP fatigue curves for various loading modes and regimes [79, 126]. Results of statistical analysis are given for the power-law and semilog fatigue curve equations.

We see from Table 8 that we obtain a closer correlation for the power-law dependence; therefore, the equation of the fatigue curve for the 50% probability level for glass fiber composites should be taken in the form $\sigma^{11}N = \text{const}$.

In many cases for composites with large strength scatter, the fatigue curve equation is written for the relative stress amplitudes. Statistical analysis of the results of fatigue tests [79] of GRP based on the PN-1 polyester resin and the ASTT(b)-C_2 glass cloth yields a correlation coefficient for the relation $\lg N - \lg (\sigma_a/\sigma_b)$ which is close to -1, while for the relation $\lg N - \lg \sigma$, $r_{1/1} \approx -0.87$. The existence of a fatigue limit for a number of cycles up to 10^7 is observed for pulsating tension, while for tension-compression and bending the resin shear strength has a higher value, and inflection of the fatigue curve is not found for this number of cycles.

Fracture Process with Cyclic Loads

The results obtained by various investigators make it possible to assume that fracture of the filler under cyclic loading occurs after failure of the adhesive bonds between the reinforcing fibers

TABLE 8

EQUATIONS OF FATIGUE CURVES FOR SOME COMPOSITES

Loading Mode and Regime, Material	Power Relation Exponent	Correlation Logarithmic Equation	Correlation Coefficient for Logarithmic Relation lg N - lg σ	Coefficient of Correlation for Semilog Relation
Axial Compression, Pulsating Cycle				
Hollow fiber + E787 resin	25,6	$\lg N = 28,3610 - 14 \lg \sigma$	-0,53	--
Glass roving S994 + E787 resin	11,5	$\lg N = 22,0843 - 12,2 \lg \sigma$	-0,894	-0,70
Glass cloth S994 + E787 resin	15,7	$\lg N = 21,814 - 10,9 \lg \sigma$	-1,0	-0,46
E-glass + 20% E787 resin	33,3	$\lg N = 47,4 - 24,7 \lg \sigma$	-1,0	--
Loading of Cylinder by External Pulsating Pressure				
E-glass + 20% E787 resin	21,8	$\lg N = 23,5 - 12,34 \lg \sigma$	-1,0	--
Symmetric tension-compression Cycle				
UM31A glass + Epon 828C resin	5,87	$\lg N = 12,6832 - 6,9 \lg \sigma$	-0,795	--
E-glass + 1002 epoxy resin, layer orientation 0° and 90°	8,0	$\lg N = 17,1607 - 9,6 \lg \sigma$	-0,940	--
Symmetric Bending Cycle				
Glass cloth ASTT(b) + PN-1 resin	10,3	$\lg N = 33,8540 - 10,8 \lg \sigma$	-0,87	--

and the matrix. The damage susceptibility of the composites under cyclic loading has not received adequate study, and clear-cut criteria for fatigue fracture (including cases with hard and soft loading) are not available.

Boller [112], studying the effect of overloads by cyclic preloading, found that short-term overloads reduce the lifetime (sum of the relative lifetimes for different ratios σ_{na}/σ_a varied from 0.56 to 0.8) for a material based on fibers at an angle of ±5° to the axis of the specimen, which leads to the appearance of tangential stresses at the glass-resin interface. For a GRP based on fibers arranged at an angle of 90°, the preliminary overload effect is less marked and, moreover, an aging effect is observed.

Control of the specimen stiffness is accomplished more easily in the bending tests; therefore, the damage susceptibility during cyclic bending, evaluated on the basis of loss of stiffness, found better experimental confirmation.

Using the hypothesis of plane sections, we write the following equations for the stresses in the glass fibers and in the resin [200]

$$\left.\begin{aligned} \sigma_a &= \sigma_c \left[\varphi_a + (1-\varphi_a)\cdot\frac{E_a}{E_m}\right]; \\ \sigma_m &= \sigma_c \left[(1-\varphi_a) + \varphi_a\cdot\frac{E_a}{E_m}\right]. \end{aligned}\right\} \qquad (36)$$

where σ_c is the nominal stress in the GRP; E_a and E_m are the filler and binder moduli of elasticity; ϕ_a is the volumetric glass content.

For parallel arrangement of the glass cloth layers, the stresses in the fibers and resin during bending are

$$\left.\begin{aligned} \sigma_a &= \frac{M}{\frac{n}{6}(n+1)(\delta+\delta')\delta\left[1+\frac{n^2+3n+2}{n^2-1}\cdot\frac{E_m}{E_a}\cdot\frac{\delta'}{\delta}\right]b}; \\ \sigma_m &= \frac{M}{\frac{n-1}{6}(n+1)(\delta+\delta')\delta\left[\frac{E_m}{E_a}+\frac{n^2+3n+2}{n^2-1}\cdot\frac{\delta'}{\delta}\right]b}. \end{aligned}\right\} \qquad (37)$$

where n is the number of layers; δ is the thickness of the reinforcing layer; δ' is the thickness of the matrix layer; b is the specimen width.

In deriving (37), the section moment of inertia is defined as the sum of the moments of inertia of the reinforcing cloth layers and the matrix.

The fracture process (in the macro-sense) in the laminated reinforced plastic can be considered to be sequential fracture of the cloth layers and resin, developing from an initial crack. The fatigue curve equation is written in the form $\sigma = A + B \lg N$; the parameters A and B are determined from the experimental data.

Denoting the crack depth after several cycles by ξ, the stresses in the reinforcing layer along the crack edge in the case of hard loading by a moment in the plane of the layers, when the neutral layer is perpendicular to the glass cloth layers, will be

$$\frac{\sigma_\xi}{\sigma_0} = \left(\frac{P_\xi}{P_0}\right)\left(\frac{t}{t-\xi}\right)^2 \qquad (38)$$

and in the case of hard loading by a moment when the reinforcing layers are parallel to the neutral layer

$$\frac{\sigma_\xi}{\sigma_0} = \frac{P_\xi}{P_0}\cdot\frac{n(n+1)}{n'(n'+1)}\cdot\frac{\left(1+\frac{n^2+3n+2}{n^2-1}\cdot\frac{E_м}{E_в}\cdot\frac{\delta'}{\delta}\right)}{\left(1+\frac{(n')^2+3n'+2}{(n')^2-1}\cdot\frac{E_м}{E_в}\cdot\frac{\delta'}{\delta}\right)}, \qquad (39)$$

where σ_ξ is the bending stress in the glass fiber layer for crack depth ξ; P_ξ is the value of the load when the crack depth is ξ; P_0 is the initial load; t is the specimen thickness

$$n' = n - \frac{\xi}{\delta + \delta'}.$$

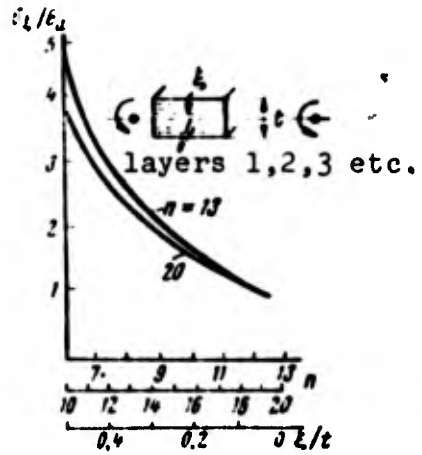

Figure 20. Ratio of actual and average stresses in fibers during fatigue crack growth.

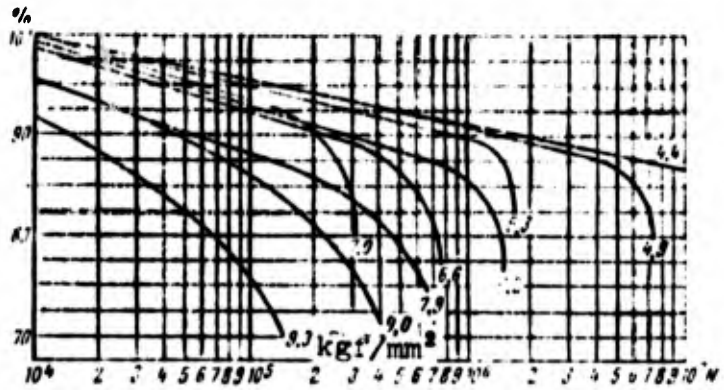

Figure 21. Variation of bending stiffness of polyester GRP specimens for different stress levels in the fatigue process.

For soft loading, the ratio σ_ξ/σ_a is shown in Figure 20 for specimens with 19 and 20 layers as a function of the number of failed layers and relative crack depth. The number of cycles to failure when testing with constant loading is determined by use of the fatigue curve equation and (38)

$$N = \sum_{i=0}^{\infty} \left| 10^{\frac{1}{k}} \left| \sigma_i \left(\frac{t}{2} \right)^2 - 1 \right| \right|, \qquad (40)$$

In the case of volumetric fiber content ~40% and moduli ratio $E_a/E_m = 10$, the calculated and actual lifetimes agree quite well for soft loading.

Failure of the specimen in bending [167] begins from numerous cracks which are oriented differently and arise as a result of fracture of the adhesive bond at the fiber-resin interface; in this case, there is marked increase of the volume of the material. The glass fibers have not yet failed and static strength is retained, while the bending stiffness drops off markedly. This can be seen by fatigue testing of specimens in bending and hard loading. Figure 21 shows the variation of the relative stiffness of polyester GRP

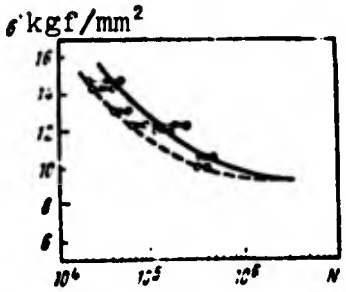

Figure 22. Beginning and end of specimen fracture for pulsating tension of polyester GRP.

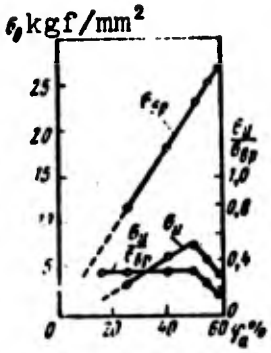

Figure 23. Relationship between short-term strength limit and fatigue limit for different reinforcement ratios.

specimens for different stress levels. The period between the instant of crack onset and failure for the polyester GRP amounts to 10 - 20% of the overall lifetime for hard loading (Figure 22) and is very small for soft loading, since the stresses in the remaining layers increase rapidly in the soft loading regime. According to the data of Figure 21, in the hard loading case the tests should be terminated when the stiffness decreases by 15 - 20%.

The fracture process in the variable loading case takes place as follows. In the first stage many fine cracks develop at the fiber-resin interface, at small stress concentration sources (voids, fiber kinks, failed fiber segments, and so on), and also at places where the cloth warp and woof fibers cross. Confirmation of the fact that fatigue fracture begins in the binder is given by comparison of the strength in short-term and cyclic loading versus degree fiber content, shown in Figure 23. The fatigue limit optimum is reached with a smaller glass fiber content. This is apparently explained by the fact that in the case of more dense packing of the fibers, the binder is more highly stressed and fails. In this case, the fibers are not broken, and static strength is maintained. However, the bending stiffness, characterizing the mutual influence of the layers and fibers, shows the presence of damage. After microcrack formation, the individual binder segments separate from the

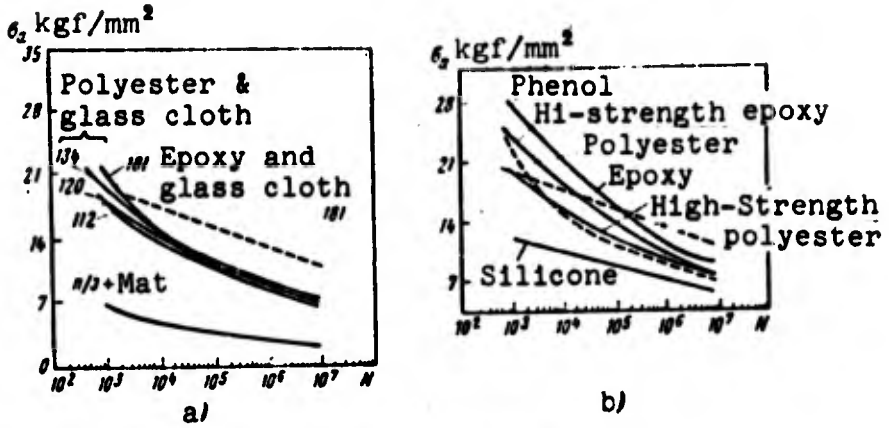

Figure 24. Fatigue curves for composites.

a — based on 181, 184, 120, and 112 cloths and glass mat (frequency 900 cpm, symmetric tension-compression cycle, temperature 24° C, humidity 50%); b — based on 181 cloth and different resins (frequency 900 cpm, t = 24° C, humidity 50%).

fibers because of disruption of the adhesive bond, partially break, material volume at the damage site increases, and the failed resin cannot provide connection between the fibers. After complete disruption of the adhesive bond, failure of the filler takes place: failure of the most highly stressed or most highly damaged fibers.

The two-phase nature of the GRP structure predetermines their behavior in the cyclic deformation process and the characteristics of the fracture process. An estimate of the influence of the individual structure components was first made by Boller [113], who studied the influence of the form of the reinforcing glass filler and the polymer matrix on the fatigue properties of composites. Boller showed that reinforcement in glass cloth form has very little influence on composite strength in the variable stress case, while the mechanical characteristics of the matrix have a large influence (Figure 24).

The small influence of cloth form for the same type of matrix can apparently be explained by the fact that fatigue damage occurs and develops at points of reinforcing fiber curvature, since the parameters of these kinks are similar for the different cloth types. Composites based on fibers have random fiber curvatures.

It was later established [126] in the process of studying the fatigue resistance of composites based on oriented fibers, hollow fibers, and glass cloth made from the same type of glass that the type of reinforcing filler also influences the fatigue resistance. The amplitude of the variable stresses for any number of cycles is larger for the composites based on oriented fibers.

The filler content has a large influence on the fatigue resistance of the composites. The influence of the volumetric glass fiber content on the fatigue strength of polyester GRP in symmetric bending and pulsating tension was investigated in [199, 200]. The satin weave glass cloth was treated with a "volan" coating. The experimental data for pulsating tension show that the fatigue limit of the composite increases with increase of the glass filler content from 0 to 50% by volume. With further glass filler saturation, the fatigue characteristics of the material decrease because of reduction of the stressed resin volume, which leads to increase of the polymer binder stress level. The bending tests were conducted with constant load and constant deformation (soft and hard loading). In both cases, the fatigue resistance in bending increased with increase of the glass volumetric content (Figure 24). Figure 25 shows Boller's data [113], indicating that for a symmetric tension-compression cycle, the optimum fatigue properties of a composite based on 181 glass cloth and epoxy resin correspond to 60% glass content by volume. The cyclic strength in axial compression varies similarly (see curves 1 and 2 in Figure 25 [126]). Increase of the degree of reinforcement has the most marked influence in the low-cycle fatigue region. The strength of the composite based on E-glass fibers with HTS coating and the Scotchply-1002 and 1009 resins increases for 10^2 cycles by 30% with increase of the filler content by 15% [126].

Anisotropy of GRP strength also influences its fatigue characteristics [8]. Fatigue curves of a polyester GRP based on 181 - 112 cloth with symmetric tension-compression cycle are shown in Figure 26. The stress amplitudes for the same number of loading cycles for specimens cut along the warp are approximately twice as

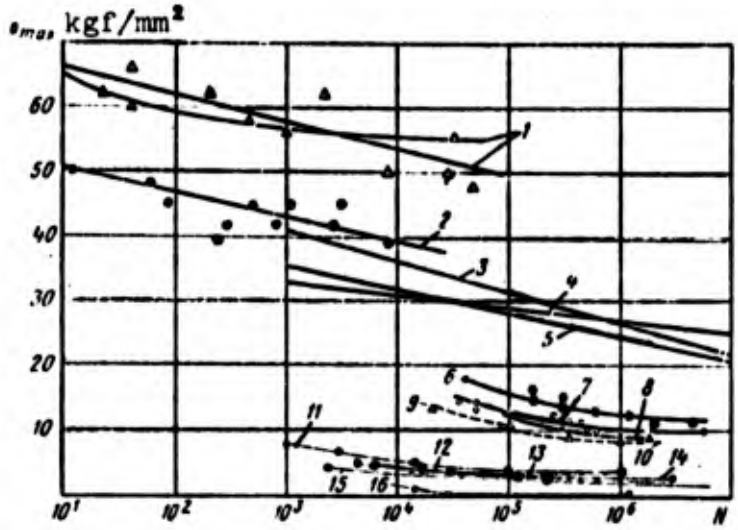

Figure 25. Influence of filler content on fatigue strength of composites.

1, 2 — pulsating compression with glass weight content 80% (resin 1009) and 85% (resin 1002) [126]; 3, 4, 5 — symmetric tension-compression cycle with glass weight content, respectively, 74, 68, and 80-63%, epoxy resin [113]; 6, 7, 8 — fatigue curves in bending, constant deformation and glass (AN-1 resin) content by volume, respectively, 60, 41, and 26% [199]; 9, 10 — fatigue curves in bending, constant stress and glass filler (PN-1 resin) content by volume 41 and 26% [199]; 11, 12, 13, 14, 15, 16 — pulsating tension with glass filler (PN-1 resin) volume content, respectively, 51, 55, 39, 58, 25, and 0% [200].

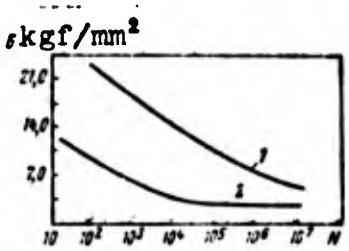

Figure 26. Influence of anisotropy on fatigue strength of polyester GRP based on 181 glass cloth [specimens cut along warp (1) and at 45° angle to warp (2)].

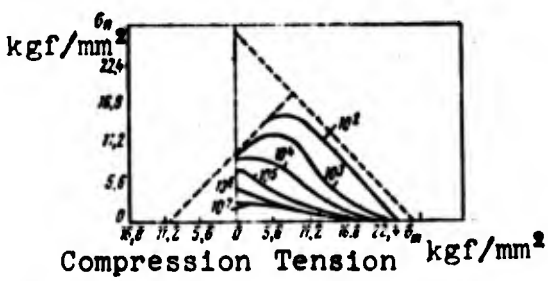

Figure 27. $\sigma_a - \sigma_m$ diagram for temperature 260° C (frequency 900 cpm).

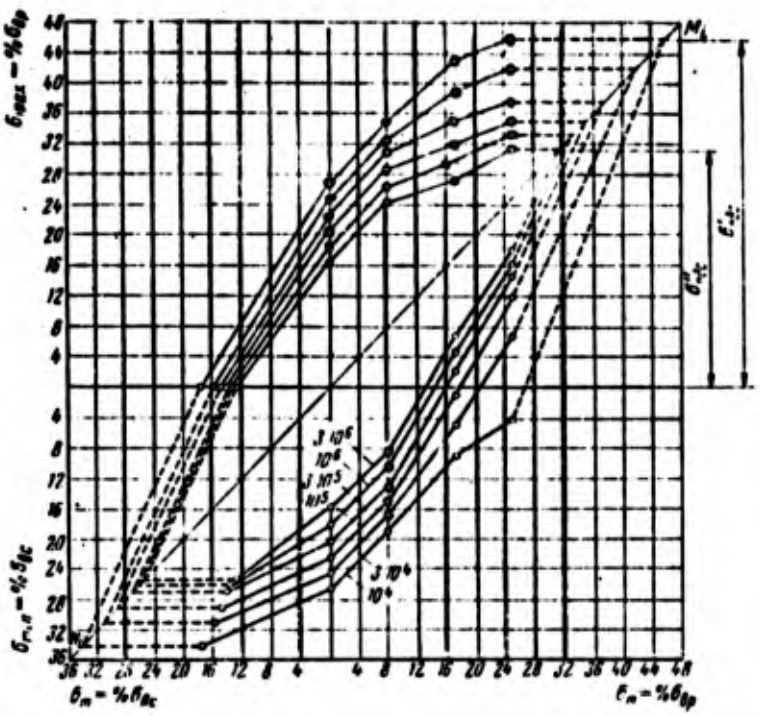

Figure 28. Diagram of maximum stresses for epoxy GRP with asymmetric cycle.

large as for specimens cut at a 45° angle to the warp direction, and correspond approximately to the anisotropy of the short-term static strength limits.

Among the other structural and operational factors which determine fatigue strength, of interest are the influences of cycle asymmetry, absolute dimensions, and temperature. According to the data of [114], fracture usually takes place during the compression cycle from the tangential stresses. The low shear strength influence is particularly marked with temperature increase (Figure 27). Characteristic for the GRP are asymmetric diagrams of the maximum variable breaking stresses with a smaller zone in the compression region (Figure 28). On the diagram of maximum stresses with account for the influence of the time factor, the points M_i and N_i should correspond to values of the long-term strength limits in tension and compression obtained as a result of long-term tests using the same number of cycles as for the fatigue limit [22].

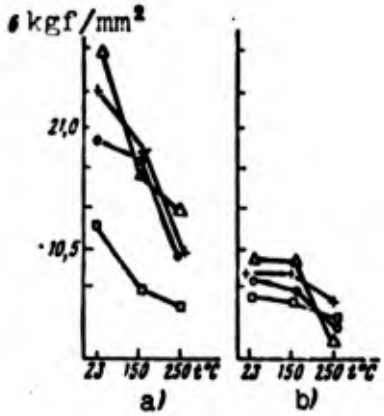

Figure 29. Influence of temperature on fatigue limit for $N = 10^3$ (a) and 10^7 (b) cycles.

Δ — phenolic GRP; + — epoxy GRP; 0 — polyester GRP; □ — silicone GRP.

The scale factor influence increases with growth of the number of test cycles. Determination of the exponent m for fixed numbers of cycles 10^4, 10^5, 10^6 from the data of tests [88] for specimens with sections 78, 115, and 200 mm² yields values of the uniformity index $\left(\frac{\sigma_1}{\sigma_2}\right)_N = \left(\frac{F_2}{F_1}\right)^{1/m}$ 4.25; 3.60; 2.0, respectively. The influence of temperature for different binder types on the magnitude of the fatigue limit decreases with increase of the number of cycles (Figure 29).

If the branches of the maximal stress diagram are represented by straight lines, the finite fatigue limit can be found from the formula

$$\sigma_r = \sigma_{-1} + \sigma_m\left(1 - \frac{\sigma_{-1}}{\sigma_{n.b.c}}\right), \tag{41}$$

the corresponding amplitude in this case will be

$$\sigma_a = \sigma_{-1}\left(1 - \frac{\sigma_m}{\sigma_{n.b.c}}\right), \tag{42}$$

where r is the cycle asymmetry coefficient.

The values of σ_{max} for 10^4 and $3 \cdot 10^6$ cycles are bounded by the stress rupture limits $\sigma'_{s.r.l}$ and $\sigma''_{s.r.l}$.

CHAPTER 8

STATIC STRENGTH OF GRP AS A FUNCTION OF STRESS STATE AND STRESS CONCENTRATION*

§1. Basic Mechanical Properties of the Subject Material

The GRP based on polyester resins have high strength, but at the same time have a relatively low modulus of elasticity. Because of this, structures made from these plastics may experience large deformations, and failure as a result of loss of stability occurs more frequently than for metal parts. Therefore, the shape of structural parts and components made from GRP must be selected with account for the maximum stiffness requirement. Favorable in this regard are structures in the form of thin-wall hollow profiles of closed cross section and thin-wall shells. Consequently, parts made from these plastics operate most frequently under biaxial stress state conditions.

With regard to strength, the GRP are an advanced type of composite material with polymer matrix and strong elastic filler fibers. Theoretically, for optimum interaction of the components of such a material in load transmission, it is necessary that the reinforcing fibers occupy a definite portion of the overall cross section area and have an adequate length. In the case of either ordered or random distribution of the fibers, some strength increase of the composite

*This chapter was written by I. Kabelka.

material in the direction of the effective stresses and comparatively low sensitivity to temperature and loading conditions are achieved. A material of this type has moderate sensitivity to defects and stress concentration. Suitable reinforcement provides certain additional advantages, particularly in connection with the fact that the strength in the complex stress state increases differently in the directions of action of the different stress components. A large number of small defects are distributed in the reinforced material, and under certain deformation conditions they may have a marked influence on the strength. In order to determine this influence, we need to study the behavior of the reinforced plastics in the complex and nonuniform stress state.

An advantage of the laminated plastics, particularly the GRP, is the simplicity of fabrication of parts of large size and complex shape, in which however there may be a complex stress state with high local stresses. The necessity for joining individual parts of composite structures by bonding or using bolts and rivets leads to the appearance of new zones of stress concentration. In view of this, along with providing strength in the complex state state, we need data on GRP sensitivity to stress concentration.

The investigations described below were made on a polyester plastic whose properties were studied sufficiently completely to permit reducing and analyzing the experimental results. The specimens were prepared in the GRP contact molding laboratory from glass cloth of the Iplast-35 type and the ChS polyester 104 resin, produced in Czechoslovakia. Iplast-35 is a glass cloth of density 5.8/6, strength in the warp direction 276 kgf/5 cm, specific weight 0.287 kgf/m^2, thickness 0.4 mm, and fiber diameter 9 microns.

The resin composition included 30% styrene and 70% polyester, prepared from 2.5 moles ethylene glycol, 1 mole malein anhydride, and 1.5 moles phthalic anhydride. The RU1 catalyzer with cobalt naphthanate was prepared in the form of a 10% solution in toluene as an accelerator in a ratio 100:2:1.

Molding and hardening of the specimens were performed at room temperature. Twenty-four hours after molding, the specimens were subjected to final hardening for 48 hours at a temperature of 80° C, followed by hardening under natural conditions for 21 days. The glass fiber content in the composite by weight was 48 - 55%. The basic characteristics of the material in the plane stress state are presented below [155].

The glass cloth used gives the GRP orthotropic properties in the macrovolumes. The elastic deformations of a plate made from GRP depend on three elastic constants: the elastic modulus $E_x = E_y$, the shear modulus G_{xy}, and Poisson's ratio ν_{xy}, referred to x, y axes of elastic symmetry of the material, one of which is aligned in the cloth warp direction, the second in the woof direction. We assume that the elastic moduli in tension and compression are the same. Since the technical literature presents a considerable amount of contradictory data, we need to confirm the equality of these moduli. The relevant measurements were made on composite beams fabricated by building up the GRP on a thin steel plate. The thickness of the steel and plastic parts of the section was selected so that the neutral line of the specimen in bending passed through the plate. When loading the described specimens by a bending moment in the plane perpendicular to the steel plate, the plastic portion of the beam was loaded as a single unit by a tension or compression force. Comparing the specimen deflections under bending moments which are the same in absolute magnitude and opposite in sign, we can determine the relationship between the elastic moduli in tension and compression (Figure 1) [155], whose magnitude depends on the temperature. Within the limits of the temperature range investigated, the difference between the elastic moduli in tension and compression does not exceed 7%. Thus, in the solution of practical problems, we can consider these moduli to be the same.

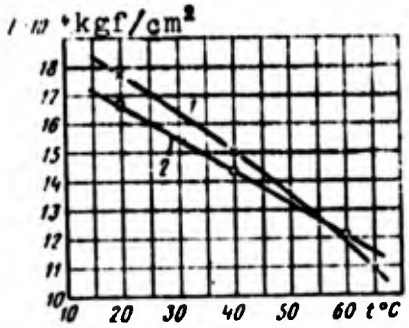

Figure 1. Glass cloth elastic modulus in warp direction versus temperature: in compression (1) and tension (2).

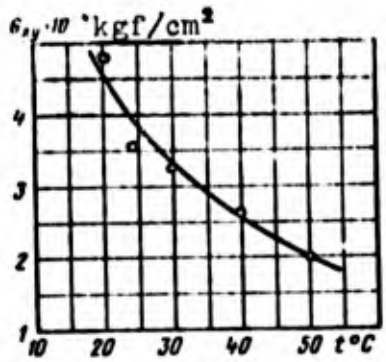

Figure 2. Shear modulus G_{xy} versus temperature.

The modulus of elasticity in shear G_{xy} characterizes the elastic deformations of the GRP plate under the action of paired shear stresses acting in the cloth warp and woof directions. The temperature dependence of G_{xy} from the thin-wall tube test data is shown in Figure 2.

The Poisson's ratio was determined using strain gages to measure the resistance to deformation of specimens in the form of ribbons made up from four layers of glass cloth. The temperature dependence of the Poisson's ratio found is shown in Figure 3. The magnitude of the deformation of the plastic, even in the elastic region, depends on the exposure duration under a load. In view of this, all the measurements made in determining the elastic constants were made so that readout of the deformation was made at the end of one minute after loading the specimen. The values obtained were thereafter considered to correspond to short-loading duration.

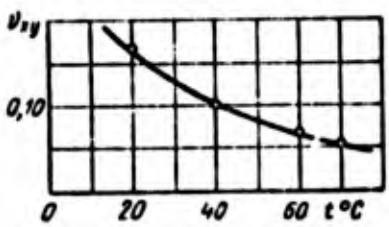

Figure 3. Temperature dependence of Poisson's ratio ν_{xy}.

The elastic constants are the components of a fourth-order tensor, whose values for an arbitrary system ξ, η of rectangular coordinates, whose axes form the angle ϕ with the axes of the basic x, y

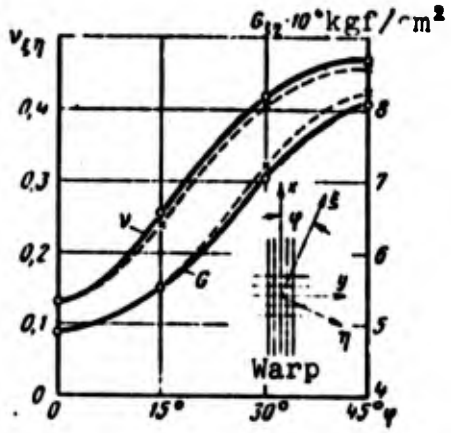

Figure 4. Dependence of shear modulus and Poisson's ratio on loading direction from experimental data (solid curves) and theory (dashed curves).

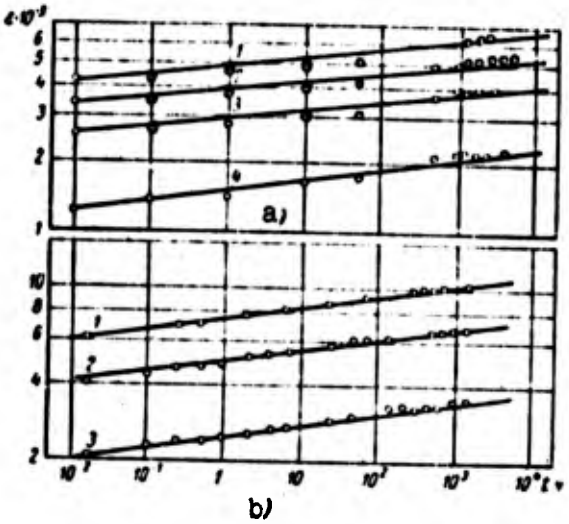

Figure 5. Creep diagram for tension in the glass cloth warp direction. a — for a temperature of 18° C and stresses: 1 — 755 kgf/cm^2; 2 — 623 kgf/cm^2; 3 — 475 kgf/cm^2; 4 — 221 kgf/cm^2; b — for a temperature of 60° C and stresses: 1 — 900 kgf/cm^2; 2 — 600 kgf/cm^2; 3 — 300 kgf/cm^2.

coordinate system, can be obtained with the aid of equations of transforming the tensor components to a new coordinate system. Figure 4 shows the variation of the elastic constants $G_{\xi\eta}$ and $\nu_{\xi\eta}$ as a function of the angle ϕ according to the results of calculation using the coordinate transformation formulas and direct measurements; the theoretical and experimental data agree quite well.

The deformation characteristics of a material in the long-term loading case are most often presented in the form of creep curves for constant load and temperature. Since these characteristics are among the basic values of a material, in the following some of them are presented to describe the material examined as a representative of the laminated plastics in studying strength and sensitivity to stress concentration.

Figure 5 shows the deformation time dependence for temperatures of 18 and 60° C for several values of the tensile stress acting in the reinforcing glass cloth warp direction. In logarithmic coordinates,

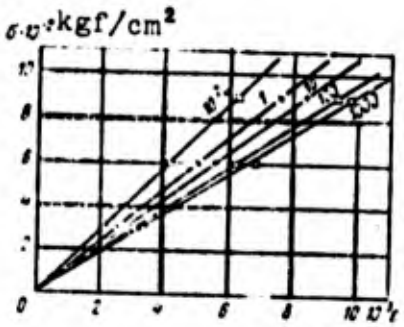

Figure 6. Creep deformation as function of stress for a temperature of 45° C.

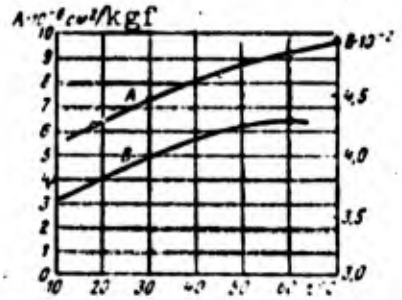

Figure 7. Parameters A and B of creep equation versus temperature.

this dependence is nearly linear, which corresponds to a power-law deformation-time dependence. Similar relations were obtained for temperatures of 30, 45, and 68° C. Figure 6 shows the stress-strain relation for a temperature of 45° C. In the stress variation range studied, this relation is linear. This means that the deformation can be represented in the form of the following function of temperature, time, and stress

$$\varepsilon(\sigma, t, T) = A(T)\,\sigma\left(\frac{t}{t_0}\right)^{B(T)},$$

where A(T) and B(T) are functions of the temperature T only; the quantity t_0 is taken equal to one hour, t exceeds one minute. The temperature dependence of the parameters A and B is shown in Figure 7.

Although it has been shown that the elastic moduli of the subject material in tension and compression are practically the same, the deformations as a function of time, determined on the basis of the yield rate, can be considered the same only for relatively low stresses. The results of the relevant measurements, also performed in the warp direction on specimens of tubular form, are shown in Figure 8.

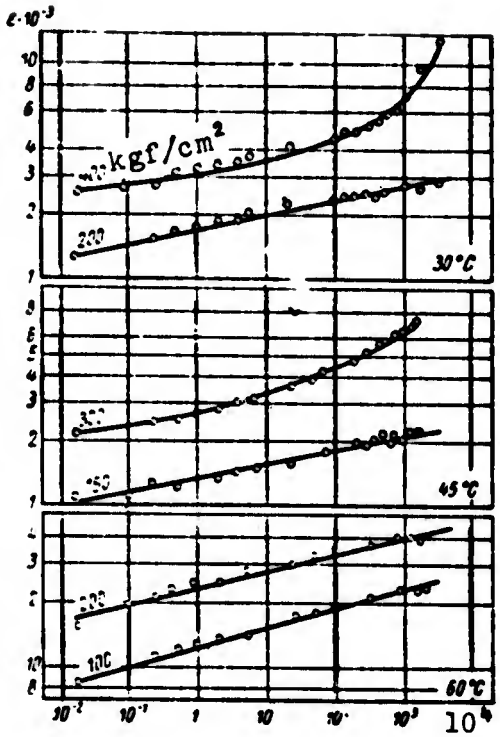

Figure 8. Creep diagrams of polyester GRP in compression in the glass cloth warp direction.

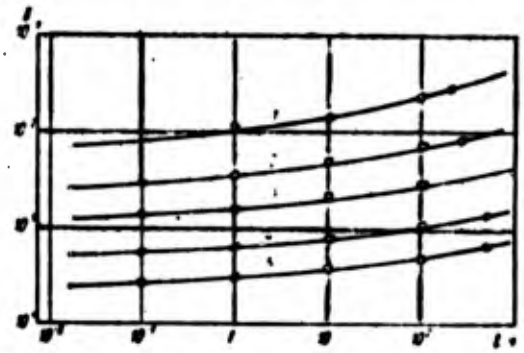

Figure 9. Shear deformation γ versus loading time for different values of the shear stress acting in the glass cloth warp direction:

1 — 207 kgf/cm²; 2 — 100 kgf/cm²; 3 — 50 kgf/cm²; 4 — 25 kgf/cm²; 5 — 8.8 kgf/cm².

When loading the material by normal stresses in the direction of the reinforcing glass-cloth fibers the material strength and deformations are determined primarily by the characteristics and number of the fibers. In contrast, when loading the material by tangential stress in the fiber direction, the resin characteristics have a considerable influence on the material properties, and in this case the deformation changes markedly depending on the loading duration (Figure 9).

§2. Static Strength of Polyester Resin GRP in the Complex Stress State

The questions of laminated plastic strength in the complex stress state have been studied in recent years, and several strength criteria have been formulated [7, 35, 54, 55, 165, 193]. However, these studies were made from the purely phenomenological viewpoint, and they do not yet permit clarification of the physical nature of material failure, nor the influence of the structure of the composite material and the properties of its component parts. Measurements have

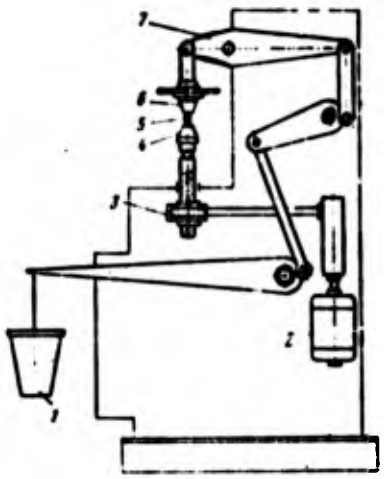

Figure 10. Schematic of fixture for tensile force loading.

1 — tank for liquid serving as variable weight; 2 — electric motor for setting system to equilibrium position; 3 — worm drive; 4, 6 — lower and upper grips; 5 — test specimen; 7 — contactor.

been made basically only under short-term loading, without account for the influence of temperature on strength, although in the plastics with ordered arrangement of the reinforcing elements, the relationship between the strength in shear and tension (compression) may alter markedly as a function of temperature.

The strength of the laminated plastics in the complex stress state has been studied [214] on specimens made from polyester resin GRP, for which certain mechanical data were presented in §1. The specimens were tested under the action of tension and shear on compression and shear stresses at temperatures of -20; 0, 20 and 45° C. In order to investigate the influence of loading duration, the tests at a temperature of 20° C were conducted with three values of the loading rate, corresponding to loading durations to failure of 1 min, 30 min, and 10 hours.

A Matra testing machine with 1000 kg maximum force was adapted for the tests in simultaneous tension and torsion. This machine provides a constant loading rate by means of a tensile load determined by the weight of water poured at a constant rate into a tank hung on the loading arm (Figure 10). The water flow rate entering the tank can be varied over a wide range by means of interchangeable nozzles.

Torsion loading is accomplished by means of a cable loading device (Figure 11). A reversing device was constructed for combined loading by compressive load and twisting moment.

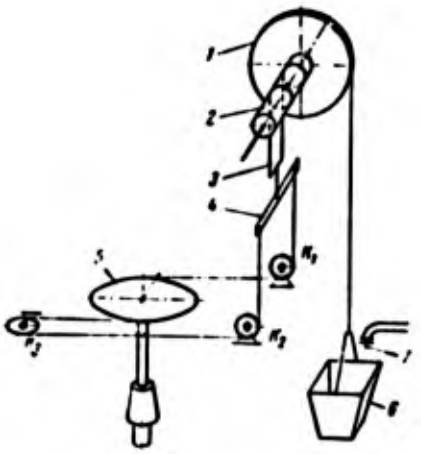

Figure 11. Schematic of fixture for torsional loading.

1, 2 — pair of pulleys on common shaft; 3 — strap; 4 — lever; 5 — pulley coupled with upper grip; 6 — tank for liquid serving as variable weight; 7 — pump; K_1, K_2, K_3 — rollers.

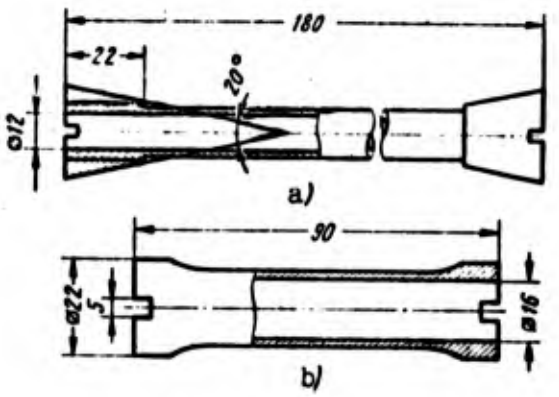

Figure 12. Specimens for testing with simultaneous loading by tensile force and twisting moment (a) and by compressive force and twisting moment (b).

Study of strength with simultaneous action of shear and tensile stresses is most conveniently carried out on thin-wall tubes. Such specimens were prepared by winding two layers of Iplast-35 glass cloth on a wax mandrel with simultaneous impregnation of the cloth with polyester resin and a catalyzer; the specimen axis was parallel to the glass cloth woof direction. Upon termination of winding, the mandrel with the specimen was mounted in a special adapter for hardening under natural conditions. After this, the wax mandrel was melted out and the specimen was maintained for 48 hours at a temperature of 100° C for final hardening.

Particular attention was devoted to ensuring axial loading of the specimens. Conical adapters made from Epoxy 1200 epoxy resin were cast on both ends of each specimen for this purpose. After hardening, the conical surfaces of both adapters were machined on a lathe in a single pass. Then keyways were made in the adapters to prevent the possibility of rotation in the testing machine grips when loading the specimen in torsion. Specimens with a short working section were prepared for determining the strength limit in shear at a

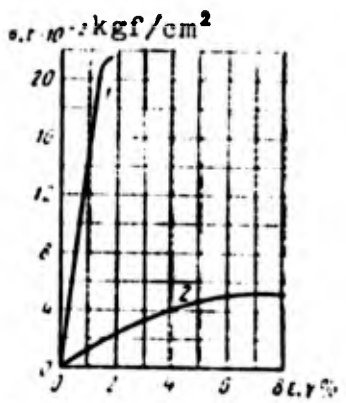

Figure 13. Deformation of laminated plastic with polyester resin in tension (1) and shear (2) in the warp direction.

temperature 45° C, since the longer specimens failed under these conditions because of wall buckling. For the tests with simultaneous loading by compressive force and twisting moment, specimens were fabricated with larger inside diameter (16 mm), whose wall was obtained by winding three layers of glass cloth. The ends of the specimens were reinforced. After hardening, performed just as in the preceding case, both end surfaces of each specimen were machined to obtain flat and parallel ends (Figure 12).

In order to provide the required temperature, the specimens were placed in a special chamber inside which the specified temperature was maintained automatically to within ±0.1° C.

The influence of specimen temperature and loading rate was studied in the tests under the simultaneous action of tensile force and twisting moment. The specimen deformations were measured only for completeness of the data. We see in Figure 13 that the limit deformations of the GRP with polyester resin as binder are very small. In view of this, we can neglect the specimen section change during deformation and consider that for a constant load variation rate the stress variation rate is constant.

The limiting tensile and shear stresses were calculated on the basis of the values of the maximum tensile force P and the maximum twisting moment M using the formulas

$$\sigma = \frac{P}{F} \text{ and } \tau = \frac{MD}{2J_p},$$

where F is the specimen cross section area; D is the outside diameter; J_p is the polar moment of inertia of the section. The limiting stresses were determined in all cases in simple tension and simple torsion and, in addition, for no less than three different combinations of tensile and shear stresses. The ratio of the tensile stress to the shear stress was held constant, i.e., the loading trajectory was a straight line. Only in certain cases, considered later, was a different loading method used.

The tables present the average values of the limiting stresses and the deviation δ of the measurement results, determined statistically on the basis of a 95% probability confidence level. If we denote the average value of a series of measured σ_i values by $\bar{\sigma}$, then the probability that σ_i falls in the interval $\bar{\sigma} \pm \delta$ will be 95% [34]. Consequently,

$$\delta = t_{n-1} \frac{\bar{s}}{\sqrt{n}},$$

where t_{n-1} is a coefficient determined by the given 95% probability; n is the number of measurements; and $\bar{s}^2$ is a quantity determined from the formula

$$\bar{s}^2 = \left(\frac{1}{n} \sum_{i=1}^{n} \sigma_i^2 - \bar{\sigma}^2 \right) \frac{n}{n-1}.$$

The results of GRP strength measurements with the simultaneous action of tensile and shear stresses at temperatures -20, 0 and 45° C are shown in Table 1. The loading rate was selected so that specimen failure in pure tension and pure torsion took place approximately 30 minutes after loading initiation. The table also shows the number of specimens and the average value of the loading time to failure.

Figure 14 shows the dependence of the limit strength in static tension on loading duration, determined in tests of specimens of the strip type with the longitudinal axis oriented in the glass cloth warp direction. The dependence of the maximum strength in compression

TABLE 1

RESULTS OF GRP TESTS IN SIMULTANEOUS TENSION AND SHEAR AS A FUNCTION OF TEMPERATURE

Temperature in ° C	Loading Rate in kgf/cm²·sec		Loading Duration to Failure in min	No. of Specimens Tested	Max Stress in kgf/cm²		Deviation δ in kgf/cm²	
	$\dot{\sigma}$	$\dot{\tau}$			σ	τ	σ	τ
0	0,949	—	40	7	2270	—	125	—
	0,841	0,111	35	8	1930	253	92,4	10,7
	0,892	0,187	32	9	1791	385	61,8	16,4
	0,674	0,096	39	5	1559	501	142	36
	0,527	0,192	41	10	1353	496	215	66
	0,858 *	0,174	43	5	1200	453	—	33,6
	0,858 *	0,181	43	5	800	473	—	77,7
	0,858 *	0,174	41	6	400	426	—	20
	—	0,206	39	10	—	462	—	40
−20	0,894	—	37	6	2045	—	184	—
	0,628	0,112	36	5	1968	267	155	37
	0,843	0,226	30	10	1590	427	48,4	44
	0,496	0,208	42	6	1264	530	115	55
	—	0,195	41	6	—	500	—	44,6
45	0,843	—	39	6	1939	—	62	—
	0,843	0,026	41	6	2085	64	15,5	5,1
	0,817	0,106	39	6	1918	249	90	19,6
	0,494	0,095	55	6	1653	325	82	17,7
	0,782	0,199	29	5	1390	382	26,5	68,3
	—	0,186	28	7	—	320	—	30,4

*Tensile force increase was halted after reaching the specified tensile stress.

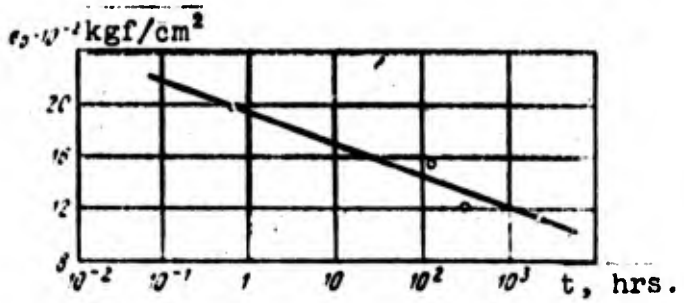

Figure 14. Dependence of limit tensile strength on static load duration (t = 20° C).

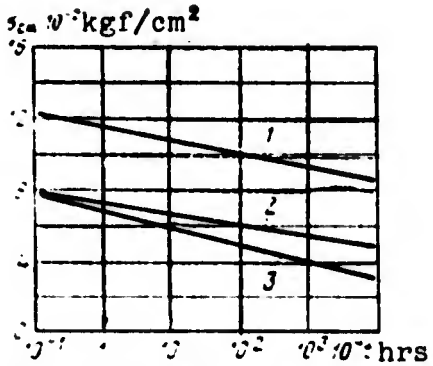

Figure 15. Limit compressive strength versus loading duration.

1 — 20° C; 2 — 33° C; 3 — 40° C.

on loading duration was determined by testing specimens in the form of tubes with the longitudinal axis parallel to the glass cloth warp direction at temperatures of 20, 33, and 40° C (Figure 15). These data show that the maximum strength in the uniaxial stress state depends significantly on the time of specimen exposure to load. However, no conclusion can be drawn on the basis of these results with regard to the influence of loading duration in the case in which the stress acts in a different direction, nor in the combined stress state case. Some data on this problem were obtained by testing specimens under the simultaneous action of tensile and shear stresses for three values of the loading rate, selected so that specimen failure occurred 1 min, 30 min, and 10 hours after loading initiation (Table 2).

At the present time, the limit strength of the subject GRP with the simultaneous action of compression and shear stresses has been determined only for a temperature of 20° C and loading rate corresponding to specimen failure 30 minutes after loading initiation (Table 3).

The variation of the limit strength as a function of temperature for simultaneous tension and shear action is shown in Figure 16. We see that the limit strength in shear is considerably lower than in simple tension. This is associated with the fact that, for the selected glass cloth orientation in the specimens, the resin transmits the tangential stress, while the tensile strength is essentially determined by the glass cloth fiber strength, since in the latter case the long, effective glass cloth fibers are aligned in the direction of tensile stress action. In shear, the transmission of the stresses to the glass cloth fibers is ineffective. We note that for stresses which reach half the value of the limiting strength in

TABLE 2

RESULTS OF GRP TESTS IN SIMULTANEOUS TENSIONN AND SHEAR AT t = 20° C

Loading Rate in kgf/cm²·sec		No. of Specimens Tested	Max Stress in kgf/cm²		Deviation δ in kgf/cm²	
σ̇	τ̇		σ	τ	σ	τ
15,96	—	6	2194	—	72,4	—
15,96	7,8*	10	2070	110	208	3
15,96	7,8*	10	2013	214	210	53,6
15,96	7,8	5	1980	389	201	36
1,8	7,8	5	1227	542	122	43,3
0	7,8	5	—	513	—	29
1,125	0	15	2169	—	187	—
1,125	0,317*	9	1992	159	122	19,6
1,125	0,317*	10	1833	242	121	13,6
0,96	0,317	10	1679	383	79	24
1,125	0,317	8	1906	399	100	35
1,125	0,432	8	1250	503	61,4	23,8
0,027	0,317	7	551	468	78,8	71
0	0,317	5	—	464	—	22
0,068	0	8	2199	—	214	—
0,068	0,011*	5	2122	124	217	5,4
0,068	0,011*	9	1875	241	105	22,3
0,068	0,011	10	1781	321	172	21,3
0	0,011	7	—	403	—	57,2

*Twisting moment increase was halted after reaching the specified shear stress value.

TABLE 3

RESULTS OF GRP TESTS IN SIMULTANEOUS COMPRESSION AND SHEAR AT t = 20° C

Loading Rate in kgf/cm²·sec		Loading Duration to Failure in min	No. of Specimens Tested	Max Stress in kgf/cm²		Deviation δ for 95% Probability in kgf/cm²	
σ̇	τ̇			σ	τ	σ	τ
0,69	—	22	7	974	—	81	—
0,61	0,12	23	8	861	169	91,2	10,7
0,64	0,25	20	8	736	286	66,4	31,8
0,33	0,25	25	8	567	405	44,9	48,3
—	0,25	35	6	—	524	—	44,4

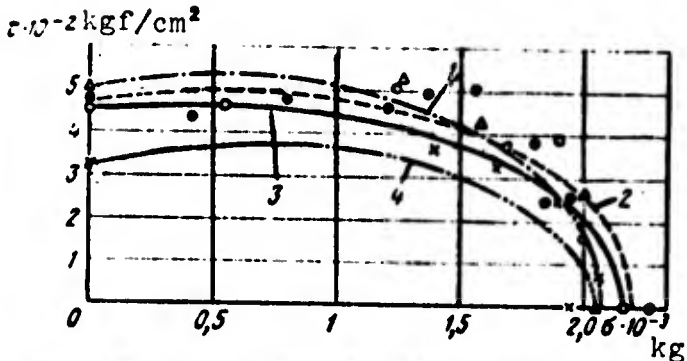

Figure 16. Limit stresses for laminated plastic with polyester resin in simultaneous tension and shear for various temperatures:

1 — 20° C; 2 — 0° C; 3 — 20° C; 4 — 45° C.

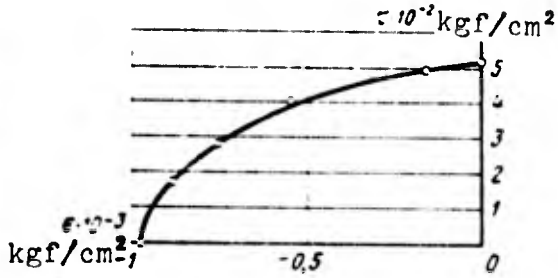

Figure 17. Limit stresses for laminated plastic with polyester resin in simultaneous compression and shear in the warp direction (t = 20° C).

tension, the strength is determined by the limiting tangential stress. The tensile stress determines the material strength only in the case of higher values. With increase of the tensile stresses, the limiting shear stress initially increases somewhat, which is apparently associated with the different limiting strengths in tension and shear. This phenomenon is not observed in the case of the simultaneous action of compression and shear (Figure 17). In this case, the limiting shear stress decreases monotonically with increase of the compressive stress from the axial force. The measurement results agree well with one another, and the limiting state diagram is nearly elliptic in form. Accordingly, the limiting strength conditions can be defined by a quadratic stress function. This condition for anisotropic materials was derived by Gol'denblat and Kopnov [35] on the basis of results of their studies and measurements performed by Zakharov [54, 55]. Considering only the quadratic terms, we write the strength condition in the form

$$\Pi_{ik}\sigma_{ik} + \Pi_{pqrs}\sigma_{pq}\sigma_{rs} \leqslant 1, \qquad (1)$$

where Π_{ik} and Π_{pqrs} are the strength tensor components, which are symmetric relative to the indices i - k, p - q, r - s, pq - rs. If we denote by σ_{ti} the absolute value of the strength limit in tension

in the direction i, by $\sigma_{c\,i}$ the absolute value of the strength limit in compression in the direction i, and by τ_{ij} the strength limit in shear in the directions i, j, then in the plane stress state case, when the stresses act along the direction of the material elastic symmetry axes, (1) takes the form

$$\Pi^{\circ}_{11}\sigma_1 + \Pi^{\circ}_{22}\sigma_2 + \sqrt{\Pi^{\circ}_{1111}\sigma_1^2 + \Pi^{\circ}_{2222}\sigma_2^2 + 2\Pi^{\circ}_{1122}\sigma_1\sigma_2 + 4\Pi^{\circ}_{1212}\tau_{12}^2} = 1. \tag{2}$$

where Π°_{ij} and Π°_{pqrs} are the strength tensor components in the basic coordinate system. In view of the material anisotropy, the value of the strength limit in shear may depend on the signs of the stresses acting, except for the case in which, in accordance with the Gol'denblat-Kopnov condition,

$$\frac{1}{\sigma_{p1}} - \frac{1}{\sigma_{c1}} = \frac{1}{\sigma_{p2}} - \frac{1}{\sigma_{c2}}. \tag{3}$$

Since for the glass cloth used in fabricating the specimens the strength values are practically the same in the warp and woof directions, for the GRP studied we can take $\sigma_{p_1} = \sigma_{p_2}$ and $\sigma_{c_1} = \sigma_{c_2}$, where the subscripts 1 and 2 denote, respectively, the warp and woof directions. Then condition (3) is satisfied, and the tensor components are expressed by the following formulas

$$\left.\begin{aligned} \Pi^{\circ}_{11} \quad \Pi^{\circ}_{22} \quad & \frac{1}{2}\left(\frac{1}{\sigma_{p1}} - \frac{1}{\sigma_{c1}}\right); \\ \Pi^{\circ}_{1111} \quad \Pi^{\circ}_{2222} \quad & \frac{1}{4}\left(\frac{1}{\sigma_{p1}} + \frac{1}{\sigma_{c1}}\right); \\ \Pi^{\circ}_{1122} \quad & \frac{1}{4}\left[\left(\frac{1}{\sigma_{p1}} + \frac{1}{\sigma_{c1}}\right)^2 - \frac{2}{(\tau^{\circ}_{45})^2}\right]; \\ \Pi^{\circ}_{1212} \quad & \frac{1}{4}\cdot\frac{1}{(\tau^{\circ}_{45})^2}. \end{aligned}\right\} \tag{4}$$

where τ_{45° is the strength limit in shear (the tangential stress forms a 45° angle with the axes of the basic coordinate system).

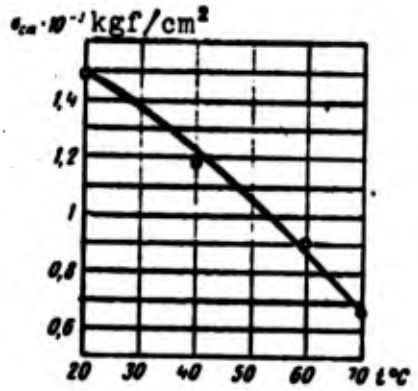

Figure 18. Strength limit in compression in warp direction versus temperature.

The equation of the limit curve for the case of simultaneous action of tension and shear after some transformations may be written in the form

$$\frac{\left(\sigma_1 - \frac{\sigma_{p1} - \sigma_{c.w1}}{2}\right)^2}{\sigma_{p1}\sigma_{c.w1} - \left(\frac{\sigma_{p1} - \sigma_{c.w1}}{2}\right)^2} + \frac{\tau_{12}^2}{(\tau_{12}^0)^2\left[1 + \frac{(\sigma_{p1} - \sigma_{c.w1})^2}{4\sigma_{p1}\sigma_{c.w1}}\right]} = 1. \qquad (5)$$

This is the equation of an ellipse with the center shifted in the direction of the higher of the strength limits σ_{t_1} and σ_{c_1}. The shift of the center of the ellipse is larger, the larger the difference $\sigma_{t_1} - \sigma_{c_1}$. The strength limit in tension in the direction of the glass cloth fibers for short-term and long-term loading depends less on temperature [106, 204] than on compression, as we see in Figure 18, which shows the corresponding relation obtained from test data of specimens in thin-wall tube form. The tests were conducted under short-term loading. the machine grip speed was 5 mm/min, and the loading time to specimen failure was on the order of 30 sec. In view of this, the limit strength values presented for compression (temperature 20° C) are considerably higher than the values (see Figure 17) corresponding to the long-term loading time to failure of 23 min.

Comparing the limit curves shown in Figure 19 for different loading rates, where the highest rate is three orders of magnitude greater than the lowest rate, we find that the nature of the curves is the same in all cases. In the tests under simple loading conditions, the loading duration has no influence on the form of the limit curve, although the strength limit in shear and long-loading duration decreases by nearly 20%. A marked decrease of the strength

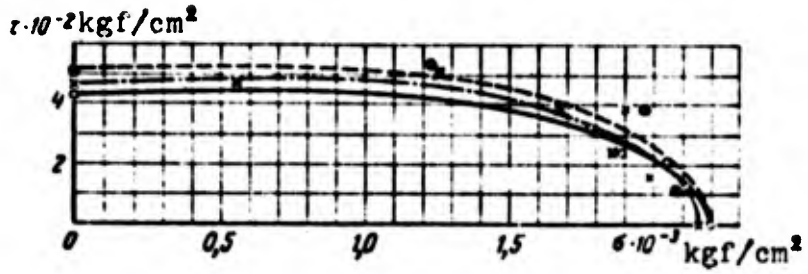

Figure 19. Limit stresses for simultaneous tension and shear (t = 20° C, for rate values see Table 2).

in shear also occurs in the combined loading case. This leads to a situation in which the entire limit curve is located lower for a long loading duration. The data presented in Figures 14 and 15 show the same influence of loading duration on the strength limit in tension and compression.

On this basis, we can consider that the Gol'denblat-Kopnov hypothesis is also valid for long-term loading. In order to use this hypothesis for the biaxial stress state, we need to know the six constants of the material characterizing the strength in the primary directions, which (if we do not take into consideration aging of the material and influence of the ambient medium) depend on the temperature and loading duration. The dependence of the strength on loading duration for static loading can be represented in the form (see Chapter 2)

$$t_f = Ae^{-c\sigma}, \qquad (6)$$

where t_f is the loading duration to failure, and A and c are constants whose values depend on the temperature. Hence it follows that, under the given assumptions, for the general study of the problem we need to know for each material 12 functions of the temperature, whose determination requires considerable time and high experimental precision. In view of this, it is advisable to study the laminated plastic structure properties, since the well-known peculiarities of the interaction between the glass cloth and the resin may lead to considerable simplification of the phenomenological

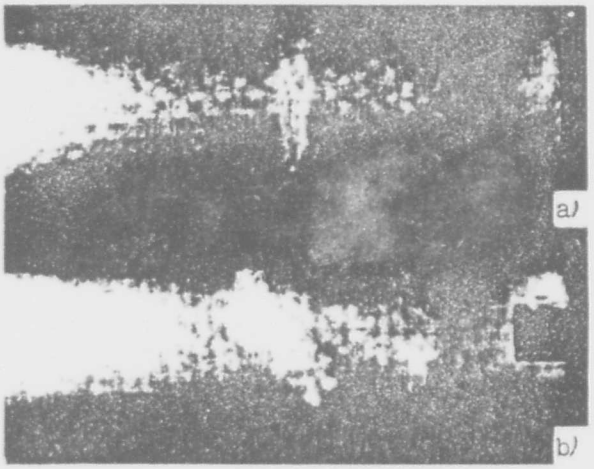

Figure 20. Typical specimen fracture in compression (a) and shear (b).

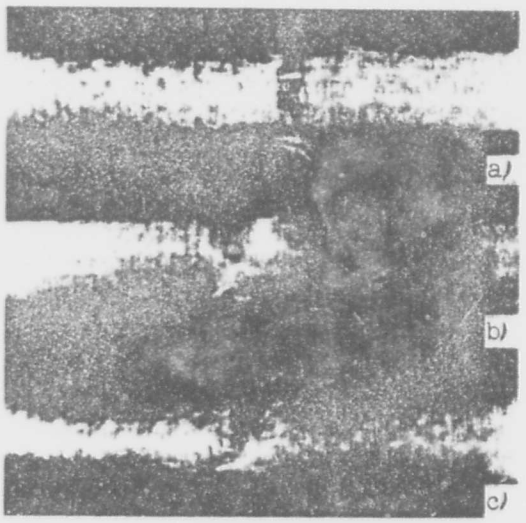

Figure 21. Typical specimen fracture in tension (a), torsion (b), and simultaneous action of tension and shear stresses (c).

strength theories. For the GRP in question, taking into account its equiaxial orthotropy, it is necessary to determine four strength characteristics. The strength limit in tension and compression in the warp direction and the strength limit in shear are obtained in the measurements described above. In addition, we also need to know the strength limit $\tau_{12}^{\bullet}$ when the material is loaded by a shearing stress acting at a 45° angle to the basic coordinate system. This characteristic was determined under the same conditions used in testing specimens under simultaneous compression and torsion (Table 4, Figures 20 and 21).

Let us examine the results of strength characteristic measurements for the laminated plastics under combined loading. We assume that there were no factors causing systematic errors in the measurements. Then the distribution of the stress limit values should be normal, which makes it possible to establish the magnitude of the permissible stress which the material can withstand with given probability.

TABLE 4

RESULTS OF TESTING IN SHEAR ($\tau_{4,5}^{\circ}$) AND COMPRESSION IN THE DIRECTION $\phi = 45°$

Loading Mode	Time of Loading to Failure in min	No. of Specimens Tested	Limit Stress in kgf/cm²		Deviation for 95% Probability in kgf/cm²	
			σ	τ	σ	τ
Compression	19.5	7	724	—	46.9	—
Torsion	46	9	—	707	—	82.5

If we evaluate the strength safety factor n using the formula

$$n = \frac{\sigma_0}{\sigma_{per}},$$

where σ_{per} is the left-hand (minimum) strength bound, determined for the required probability, then as a result of calculation using the data from tests in tension and shear we obtain

$$n_\sigma \geqslant 1{,}8; \quad n_\tau \geqslant 2{,}25.$$

This means that the scatter of the limit shear stress values is greater than the scatter of the limit tensile stress values, and the permissible shear stress will be correspondingly lower. The results of the tests conducted show that, in the design of detail parts made from the laminated plastics working under short-term loading conditions, the strength safety factor should not be less than 2.5

§3. Influence of Notches on Strength of Laminated Plastics Under Combined Static Loading

(The test results in this section were obtained by K. Zikesh.)

In thin-wall GRP units, we often encounter sharp transitions, local reinforcements, metallic inserts, holes for bolts or rivets, and other stress concentrators. The influence of stress concentration on the static strength depends on the notch shape and position

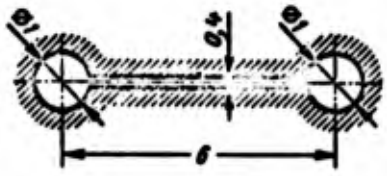

Figure 22. Dimensions of figure-eight cutout.

of the notch root in relation to the effective stress direction and the reinforcing cloth fiber direction. In view of this, the marked influence of a notch on specimen strength is observed in certain tests and not in others. In the general case, with a combined stress state the notch effect shows up more strongly, since some components always have an unfavorable direction. However, large nonlinear resin deformations which do not coincide with the glass fiber cloth directions reduce the stress concentration in the short-term loading case in comparison with the value obtained using linear anisotropic homogeneous medium theory.

The influence of stress concentration on laminated plastic strength has been studied by many authors [101, 133, 134, 196]. All the known studies were made with uniaxial loading, although in connection with the complex geometric shape of the structures for which the laminated plastics are most suitable the most important problem is that of the influence of notches on the strength of the plastic in the combined stress state. Therefore, in studying laminated plastic strength in the combined stress state, we also tested specimens with notches.

As in the preceding cases, we used thin-wall cylindrical specimens (see Figure 12) with round holes and cutouts in figure-eight form (Figure 22). This shape was used because of the fact that it is possible to obtain high values of the stress concentration and reproduce the cutouts exactly in all the specimens by drilling two holes at exactly the prescribed distance from one another and then cutting the web between them with a jig saw. Two cutouts were made in each specimen, located symmetrically relative to the longitudinal axis.

The specimens were tested in tension, torsion, and two combinations of tensile and shear stresses, with constant loading rate and constant ratio of the nominal tensile and shear stresses (no less

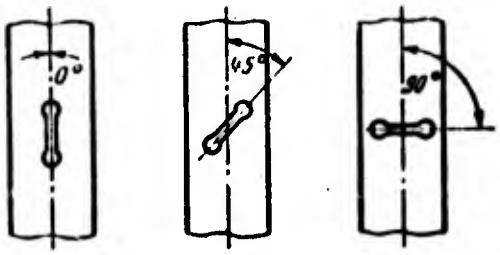

Figure 23. Different cutout orientations in specimen.

than three specimens for each combination). To study the influence of notch orientation, we prepared three series of specimens in which the longitudinal axis of the cutouts formed 0, 45, and 90° angles with the specimen longitudinal axis (Figure 23). The loading rate was selected so that fracture occurred 20 - 40 min after loading initiation, and so that the results could be compared with the test data for specimens without cutouts.

Specimens with two 1-mm diameter round holes located at the midpoint of the specimen length and symmetric with respect to the longitudinal axis were tested in tension, shear, and the simultaneous action of tension and shear stresses ($\omega_1 = \sigma/\tau = 2.7$; $\omega_2 = 3.0$). In all cases, four specimens were tested.

We shall compare the results of these tests (Table 5) and theoretical calculations made under the assumption that the material is elastic, homogeneous, and equiaxially orthotropic. For the sake of simplicity, we examine the solution for an orthotropic plate with a circular hole, i.e., we do not consider the curvature of the hollow cylindrical specimen wall. The stress concentration factor for the wall of a hollow cylinder with a hole is higher than for a flat plate with a hole, and the values of the concentration factor for the two cases are connected by the relation $\alpha_{cyl} = \alpha_{pl} + f(d/\sqrt{Dh})$. However, since the quantity $d/\sqrt{Dh}$ is close to one, in analyzing the test results we can ignore the indicated difference in the values of this concentration factor. Far more important is the fact that the hole cuts through the glass cloth fibers. Thus, the stress distribution near the hole differs from that obtained using continuous anisotropic medium theory. The theoretical determination of the actual stress concentration in the GRP model presents great difficulty. However, there is no need for doing this, since in practical strength studies, it is not possible to examine all notch orientations in a material

TABLE 5

TEST RESULTS OF SPECIMENS WITH FIGURE-EIGHT CUTOUTS*

Cutout Orientation	Loading Mode	Loading Duration to Failure in min	Nominal Stress at Failure in kgf/cm²		Nominal Stress at Delamination Initiation in kgf/cm²	
			σ_b	τ_b	σ_n	τ_n
Parallel to specimen axis	Tension	40	1780	–	525	–
	Shear	24,5		400		278
	ω = 2.41	21	992	575	474	195
	ω = 1.36	21	521	385	386	286
At 45° to specimen axis	Tension	30	1068	–	780	–
	Shear	19		340		260
	ω = 2.2	19,5	690	314	472	215
	ω = 1.35	21,5	480	355	280	200
Perpendicular to specimen axis	Tension	22	753	–	321	–
	Shear	20	–	335	–	287
	ω = 2.41	17,5	667	280	438	190
	ω = 1.39	22	482	346	425	305

*Three specimens were tested in each case.

of complex structure. We need only examine the local stress field, and in evaluating the notch effect we start from simplified stress distribution concepts.

Since in the subject case the stresses act in the direction of the axes of elastic symmetry, we obtain the stress function F(x, y) by solving the differential equation

$$\frac{1}{E_1}\left(\frac{\partial^4 F}{\partial x^4}+\frac{\partial^4 F}{\partial y^4}\right)+\left(\frac{1}{G_{12}}-\frac{2\nu_{12}}{E_1}\right)\frac{\partial^4 F}{\partial x^2\partial y^2}=0 \qquad (7)$$

with account for the edge conditions.

The characteristic equation has the form

$$\lambda^4-\left(\frac{E_1}{G_{12}}-2\nu_{12}\right)\lambda^2+\frac{E_1}{E_2}=0. \qquad (8)$$

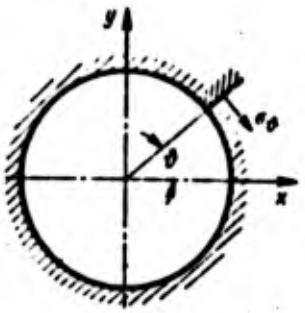

Figure 24. Notation for stress at circular hole.

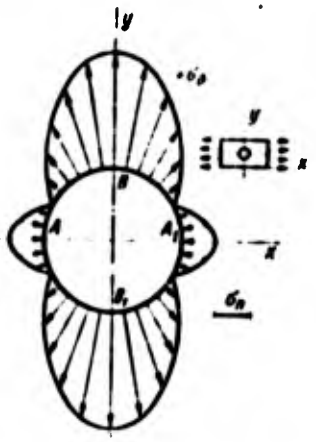

Figure 25. Stress distribution at circular hole in laminated plastic plate subject to tension.

After substituting the values of the elastic moduli $E_1 = E_2 = 1.65 \cdot 10^5$ kgf/cm^2, $G_{12} = 4.8 \cdot 10^4$ kgf/cm^2 and Poisson's ratio $\nu_{12} = 0.135$, we obtain the imaginary roots of the characteristic equation

$$\lambda_1 = 0.6i \text{ and } \lambda_2 = 1.67i.$$

We take a rectangular coordinate system with the origin at the center of the hole and axes parallel to the axes of elastic symmetry of the material, and we examine the tensile stress σ_ϑ at the edge of the hole as a function of the angle ϑ between the radius vector of a contour point and the x-axis (Figure 24). Then the tensile stress in the x-axis direction will be expressed by the formula

$$\sigma_\vartheta = \sigma_n \frac{E_\vartheta}{E_1} [-k \cos^2 \vartheta + (1 - n) \sin^2 \vartheta]. \qquad (9)$$

where

$$k = -\lambda_1 \lambda_2 = 1; \; n = \sqrt{2(1 + \nu_{12}) + \frac{E_1}{G_{12}}} = 2.27;$$

σ_n is the nominal tensile stress; λ_1, λ_2 are the roots of the characteristic equation (8); and E_ϑ is the modulus of elasticity in the direction of the tangent to the hole contour at the point in question.

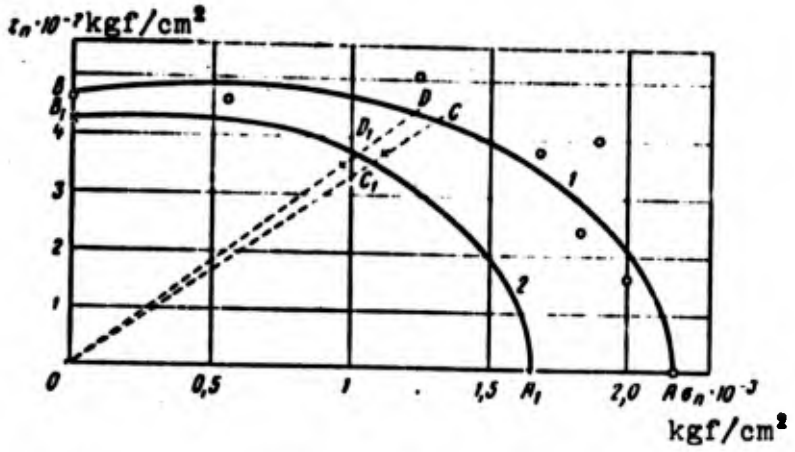

Figure 26. Limit stresses for simultaneous tension and shear:

1 — specimens without cutouts and holes; 2 — specimens with circular holes.

Taking into account the equiaxial orthotropy of the material properties, we find

$$\frac{1}{E_\phi} = \frac{1}{E_1}\left[1 + \left(\frac{E_1}{G_{12}} - 2\nu_{12} - 2\right)\frac{1}{4}\sin^2 2\phi\right]. \tag{10}$$

After substituting this expression into (9), we obtain

$$\sigma_\phi = \sigma_n \frac{-k\cos^2\phi + (1 + n)\sin^2\phi}{1 + \left(\frac{E_1}{G_{12}} - 2\nu_{12} - 2\right)\frac{1}{4}\sin^2 2\phi}, \tag{11}$$

and with account for the numerical values

$$\sigma_\phi = \sigma_n \frac{3.27\sin^2\phi - \cos^2\phi}{1 + 0.293\sin^2 2\phi}. \tag{12}$$

The stress distribution at a circular hole in a flat GRP specimen loaded by tensile stress is shown in Figure 25. The maximum stress occurs at point B for $\phi = 90°$ and is $\sigma_B = 3.27\ \sigma_n$. Thus, the theoretical stress concentration factor is 3.27.

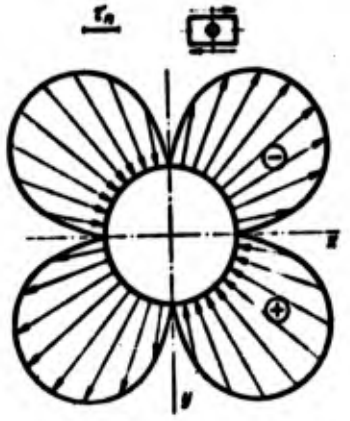

Figure 27. Stress distribution at circular hole in flat laminated plastic plate loaded by shear stress.

Figure 26 shows the limit stress curves for specimens with and without holes. The ratio of the limit stresses for uniaxial tension yields a value of the effective concentration factor of 1.3, which agrees with the results of Fel'd's studies [134] conducted on flat (strip) specimens.

In the shear case with stresses acting in the directions of the axes of elastic symmetry, the normal stress at the edge of the hole is determined from the formula

$$\sigma_\phi = -\tau_n \frac{E_\phi}{E_1}(1 + k + n)\, n \sin 2\phi, \tag{13}$$

where τ_n is the nominal shear stress. After substituting (10) for E_ϕ, we obtain

$$\sigma_\phi = -\tau_n \frac{(1 + k + n)\, n \sin 2\phi}{1 + \left(\frac{E_1}{G_{12}} - 2\nu_{12} - 2\right)\frac{1}{4}\sin^2 2\phi}, \tag{14}$$

and with account for the numerical values

$$\sigma_\phi = -\tau_n \frac{4{,}85 \sin 2\phi}{1 + 0{,}293 \sin^2 2\phi}. \tag{15}$$

The stress variation as a function of the angle ϕ is shown in Figure 27. The maximum value of σ_ϕ is equal in absolute magnitude to 3.8 τ_n. Theoretically the specimen should fail at a value of σ_ϕ equal to the limit strength of the material. The maximum stress occurs at the point $\phi = 45°$, where the material strength in tension is minimum. The weakest point is located in the compression zone, since the strength limit is considerably lower than in tension. The strength limit of the material in compression in the direction

forming a 45° angle with the axes of elastic symmetry is equal to 715 kgf/cm², according to the test data for a loading rate of 0.66 kgf/cm²·sec. Thus, the theoretical value of the limit shear stress for specimens with holes is $\tau_n = 715/3.8 = 188$ kgf/cm². The specimen with holes actually fails at $\tau_n = 425$ kgf/cm².

The effective concentration factor in shear is $\beta = OB/OB_1 = 1.1$ (see Figure 26), while the theoretical concentration factor for this case is 2.26. The difference is obviously explained by the fact that in this direction (45°) the material also has the smallest modulus of elasticity in tension, and therefore after partial local damage of the material there is equalization of the stresses with the adjacent, less loaded zones. This also explains the fact that during the tests the fracture surface in some cases bypassed the hole. In this case, the influence of internal material defects (for example, air bubbles) was greater than that of the artificial stress concentrator.

In studying the complex stress state, we assume that the stress σ_ψ from the shearing load has no effect on the distribution of the stresses from the tensile load and, conversely, that these stresses can be summed algebraically. In this case we obtain

$$\sigma_\theta = \sigma_n \frac{-\kappa\cos^2\theta + (1+n)\sin^2\theta - \frac{1}{\omega}(1+\kappa+n)n\sin 2\theta}{1+\left(\frac{E_1}{G_{12}} - 2\nu_{12} - 2\right)\frac{1}{4}\sin^2 2\theta}, \qquad (16)$$

where ω is the ratio of the tensile stress to the shear stress and is a constant quantity for the subject tests.

Figure 28 shows the distribution of the stress σ_ψ for $\omega = 2.7$. The action of the shearing stress leads to a shift of the point of maximum stress in the direction of the smaller modulus of elasticity of the material. This shift is favorable with regard to material strength, and therefore, the theoretical value of the stress concentration factor is somewhat lower. However, even in this case, the theoretical factor is higher than indicated by the experimental data.

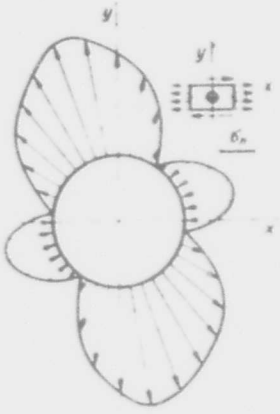

Figure 28. Variation of σ_v with simultaneous tension and shear ($\omega = 2.7$).

If we take as the effective concentration factor the ratio OC/OC_1 (see Figure 26), we obtain the value 1.21, while for the ratio OD/OD_1, the factor equals 1.14. This implies that the secondary shear stress reduces the stress concentration factor in comparison with the uniaxial tension case, for which the effective concentration factor is equal to the ratio $OA/OA_1 = 1.31$. Characteristic fractures of specimens with circular holes are shown in Figures 29 and 30.

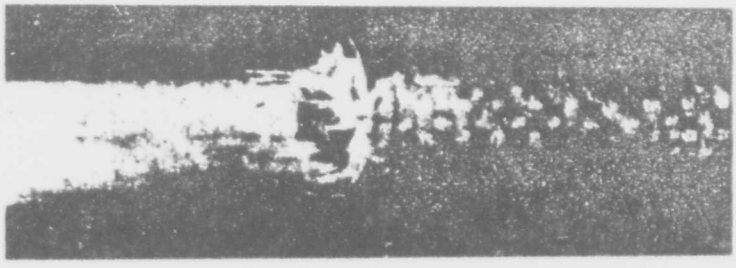

Figure 29. Typical tension fracture of specimen with circular holes.

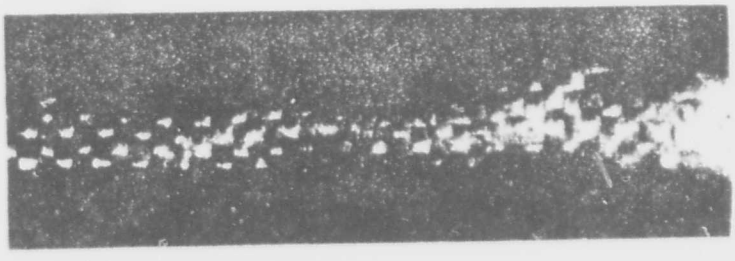

Figure 30. Typical torsion fracture of specimen with circular holes.

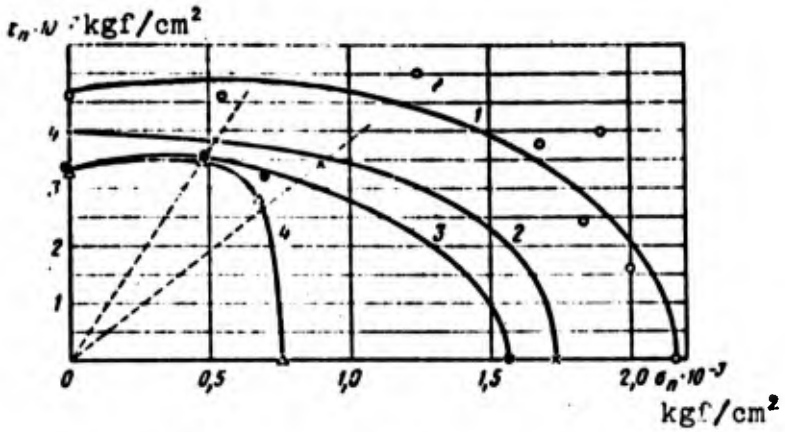

Figure 31. Limit stresses for simultaneous tension and torsion.
1 — specimen without cutout; 2 — (ϕ = 0°); 3 — (ϕ = 45°);
4 — (ϕ = 90°) specimens with figure-eight cutouts.

We see from (11) and (14) that the magnitude of the stress σ_ϑ at the circular hole is independent of the hole radius. However, individual internal defects may have a considerably more complex form, and are characterized by a larger stress concentration factor. Therefore, we also tested specimens with figure-eight cutouts in the wall, which cause greater stress concentration. The stress concentration factor at cutouts of this form depends on the orientation of the "8" relative to the axes of elastic symmetry of the material. The tests were conducted for three different cutout orientations (Table 5). The limit stress curves are shown in Figure 31, which also shows for comparison the values of the limit nominal stress for specimens without holes. The maximum stress values are obtained when the cutout is parallel or perpendicular to the specimen axis of symmetry. Therefore, we shall examine only two cutout orientations.

To simplify the calculation, we replace the actual cutout shape by an approximate shape given by the equations

$$\left.\begin{aligned} x &= a(\cos\theta - \varepsilon\cos 3\theta); \\ y &= a(\varepsilon\sin\theta - \varepsilon\sin 3\theta). \end{aligned}\right\} \qquad (17)$$

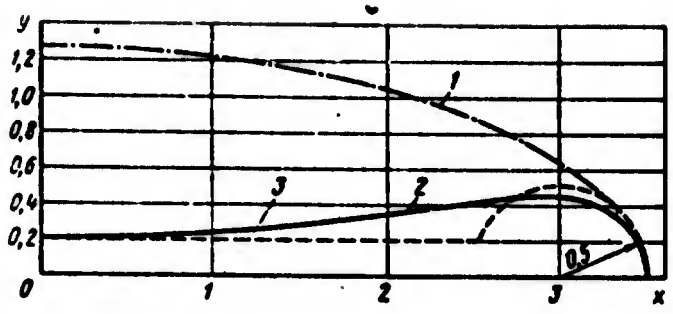

Figure 32. Approximation of cutout contour by analytic curve. 1 — ellipse; 2 — curve specified by (17); 3 — actual contour.

We take the equation parameters so that the radii of curvature at the point $\vartheta = 0$ of the simplified and actual cutout contour will be the same $\rho = 0.5$ mm. In accordance with the expression for the radius of curvature, we have

$$\frac{(\dot{x}^2 + \dot{y}^2)^{\frac{3}{2}}}{|\dot{y}\ddot{x} - \dot{x}\ddot{y}|} = 0{,}5 \quad \text{for} \quad \vartheta = 0, \tag{18}$$

where $\dot{x}$, $\ddot{x}$, $\dot{y}$, and $\ddot{y}$ are, respectively, the first- and second-order derivatives of the coordinates x and y with respect to the parameter ϑ.

We substitute into (18) the cutout contour point coordinates and their derivatives. Then

$$\frac{a(c - 3\varepsilon)^3}{(2\varepsilon - 1)(c + 3\varepsilon)} = 0{,}5.$$

To determine the constants in (17), we require as additional conditions that for $\vartheta = 0$ $x = 3.5$ and for $\vartheta = \pi/2$ $y = 0.2$. We then obtain the following value of the constants: $a = 3.7$; $c = 0.108$; $\varepsilon = 0.054$. The actual and approximate cutout contours are shown in Figure 32, on the basis of which we can conclude that the calculation made for the approximate contour provides a quite correct picture of the stress distribution around the contour of the actual cutout.

The distribution of the stresses σ_ϑ in a flat plate of large dimensions with a cutout whose contour is specified by (17), oriented parallel or perpendicular to the direction of the uniformly distributed tensile stress, can be determined by an approximate method. The distributions of the stress σ_ϑ obtained by this method for the two cutout orientation cases considered are shown in Figure 33a, b. These data show that, for a cutout orientation perpendicular to the tensile stress direction, we obtain a very high stress concentration factor, equal to $\alpha = 9.7$ at the point $\vartheta = 0°$. When the cutout is oriented parallel to the tensile stress direction, the maximum stress σ_ϑ is obtained at point $\vartheta = 35°$ and $\alpha = 2.3$. The secondary shear stress causes a secondary stress σ_ϑ which is equal to zero for $\vartheta = k\pi/2$, where k is an arbitrary integer.

As in the case when the hole is circular, the secondary shear stress causes a shift of the σ_ϑ stress peak. Figure 33c shows the distribution of the stress σ_ϑ in a flat plate made from the subject GRP with an elliptic hole, loaded by shear stress. The maximum value of the σ_ϑ stress occurs for $\vartheta = 18°$, and amounts to $3.3\ \tau_n$. The elliptic hole semiaxis $a = 3.5$ mm; the contour radius of curvature at the point $\vartheta = 0$ is 0.5 mm. The contour of the elliptic hole approximately coincides with the actual hole up to the angle $\vartheta = 25°$. On this basis, we can consider that in the region near the end of the cutout, which is of most interest in the present study, the distribution of the stress σ_ϑ for a shearing load does not differ very markedly from the stress distribution at the end of an elliptic cutout with the same contour radius of curvature. The approximate distribution of the stress for the subject case is shown in Figure 33d.

Figure 33e, f shows the stress distribution for combined tensile and shear loading with stress ratio, respectively, $\omega = 1.36$ and $\omega = 2.41$. In Figure 33f we see that for $\omega = 2.41$ the influence of shear stress on the stress distribution at the cutout perpendicular to the

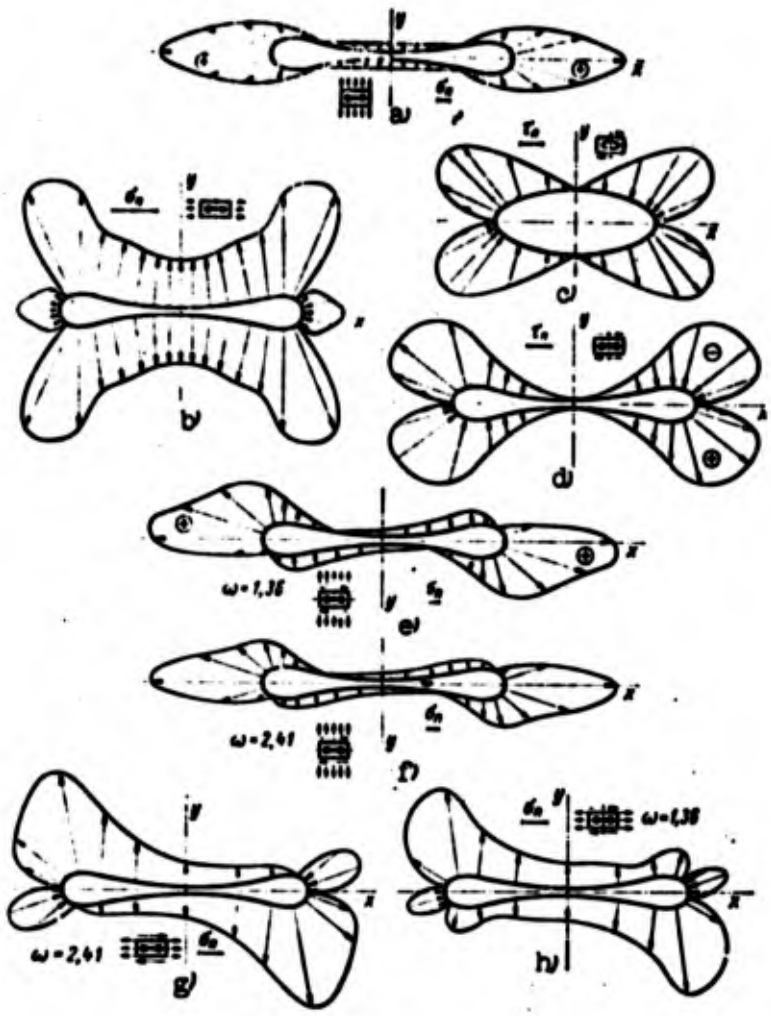

Figure 33. Stress distribution around cutout contour for different loading versions.

specimen longitudinal axis is negligible. The tensile stress concentration factor is several times higher than in shear, and therefore the σ_y maximum does not shift perceptibly. In the tests, this shows up in the fact that the fracture of specimens under the influence of tensile loading and combined tensile and shear loading with stress ratio $\omega = 2.41$ takes place at nearly the same tensile stress, which in the present case plays a decisive role (see Figure 32). If the stress ratio $\omega = 1.36$, the shift of the stress peak and the stress increase in the tensile zone are more marked, and the limit state is reached at a smaller value of the tensile stress. However, the stress

peak shift occurs in the direction of a region with lower elastic modulus, which leads to equalization of the stress peaks and reduction of the resultant stress concentration.

This phenomenon was observed during combined loading (tension and shear) tests of specimens with cutout oriented parallel to the specimen longitudinal axis (Figure 33g, h). Since the stress concentration factors in tension and shear are practically the same, the influence of the two loading modes shows up to the same degree. As a result of this, the limit stress diagram has the same form as for specimens without stress concentrators (see Figure 31, curve 2).

On the basis of the assumptions adopted, we can expect that specimen failure will occur at the nominal stress τ_n, corresponding to the moment when the material strength limit is reached at the most highly stressed point. In the present case, the,maximum value of σ_ϑ occurs at the point $\vartheta = 18°$ (see Figure 33f). The tangent to the cutout contour at this point forms an angle of 42° with the x-axis. The stresses first reach values equal to the strength limit in the compression zone. For the indicated direction, the strength limit in compression is 715 kgf/cm^2, and therefore this value corresponds to the calculated nominal shear stress $\tau_n = 715/3.3 = 217$ kgf/cm^2. However, the specimen actually fails in the case in which the cutout is oriented parallel to the specimen longitudinal axis at the nominal stress 401 kgf/cm^2 or for a perpendicular cutout at the stress 335 kgf/cm^2. The theoretical stress concentration factor $\alpha = 470/217 = 2.16$, while the effective factor from the experimental data in one case is $\beta = 1.175$ and in the other case $\beta = 1.4$. Thus, the effective stress concentration factor is considerably smaller than the theoretical value, particularly if we consider that — when the cutout is oriented perpendicular to the specimen longitudinal axis — its cross-section area is reduced considerably (by approximately 30%).

In the tensile load case, the effective stress concentration factor is again considerably smaller than the theoretical value. When the cutout is oriented perpendicular to the specimen longitudinal axis $\beta = 2.9$, while $\alpha = 9.7$. If we take into consideration the cross-section area reduction and take as the nominal stress the average stress in the weakened section, then $\beta = 1.9$, i.e., close to the value established in tests of specimens with circular holes.

If the cutout is oriented parallel to the longitudinal axis of a specimen loaded by a tensile load, then from the experimental data $\beta = 1.25$, while $\alpha = 2.3$.

Comparing the values of the theoretical and effective concentration factors, we see that notches and initial defects have considerably less influence on the strength of the laminated plastics than when testing specimens made from the quasi-homogeneous brittle resins which serve as the binder for these plastics (see Chapter 1). This difference is explained by the presence of the reinforcing glass-cloth fibers. Composite materials made from strong filler fibers and a soft binding matrix usually have low sensitivity to stress concentration, which is an important advantage in their industrial application. This is associated with the following factors:

1. A defect or sharp notch becomes stable if it reaches a definite critical value, which for the composite materials is usually less than the distance between the reinforcing material fibers.

2. In the case of relatively small critical defect size and propagation in the material of a brittle fracture crack, its growth is retarded strongly near the system of fibers.

3. Local stress concentration at the surface of contact between the glass-cloth fibers and the resin under the action of an external load usually leads to reduction of the stress at the edge of the defect and reduction of the effective stress concentration factor.

4. Upon failure of part of the reinforcing fibers, the length of the latter will usually be sufficient for transmission of the stresses to some distance from the location of the failure. This condition will not be satisfied only for very short fiber length or comparatively high density of the defects or fiber damages.

Results of specimen tests show that the laminated plastics have low notch sensitivity. In the process of loading parts made from such materials, particularly in the presence of creep, the stress peaks rapidly equalize. In a material with a weak bond between the filler and the binder, typical representatives being the GRP, there is partial or complete delamination in the most highly stressed zone prior to failure. In this case the material loses the properties of a continuous medium, for which the theoretical formulas were derived. The nature of specimen fracture for the different stress state types is shown in Figures 34 - 36. In accordance with the nature of the material behavior prior to fracture, the stress in the concentration zones increases to a certain level, at which the bond between the glass-cloth fibers and resin begins to fail. Typically, the material failure process during specimen tests is accompanied by characteristic cracking (Tables 5 and 6). At the edge of a hole, there can act only a normal stress (Table 7), which usually corresponds to the material strength limit in tension or compression in the corresponding directions. Deviation from this relationship was noted only in the case of specimens with figure-eight cutouts oriented perpendicular to the specimen longitudinal axis, during the testing of which it was apparently not possible to note material fracture initiation. The low values of the limit tensile stress for specimens with figure-eight cutouts oriented parallel to the specimen longitudinal axis can be explained

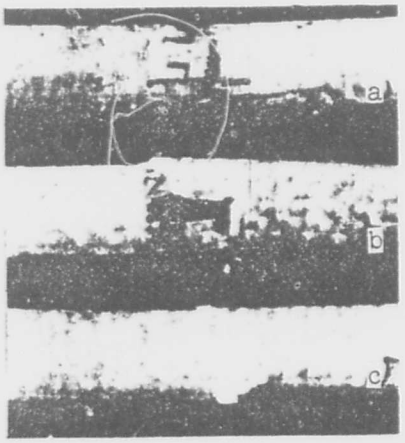

Figure 34. Typical fracture of specimens with figure-eight cutouts ($\varphi = 0°$) in tension (a) and torsion (b) and simultaneous tension and torsion (c).

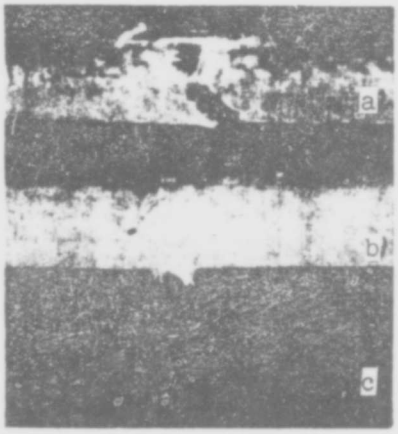

Figure 35. Typical fracture of specimens with figure-eight cutouts ($\varphi = 45°$) in tension (a), torsion (b) and simultaneous tension and torsion (c).

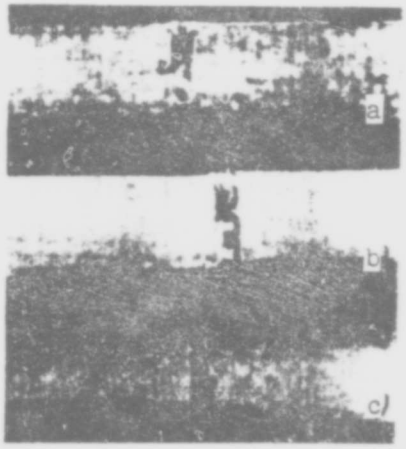

Figure 36. Typical fracture of specimens with figure-eight cutouts ($\varphi = 90°$) in tension (a), torsion (b) and simultaneous tension and torsion (c).

TABLE 6

TEST RESULTS OF SPECIMENS WITH CIRCULAR HOLES

Loading Mode	Loading Duration to Fracture in min	Nominal Stress at Failure in kgf/cm²		Nominal Stress at Delamination Initiation in kgf/cm²	
		σ_b	τ_b	σ_n	τ_n
Tension	46	1652	—	745	—
$\frac{\sigma}{\tau} = 3{,}0$	43	1124	372	564	155
$\frac{\sigma}{\tau} = 2{,}7$	43	971	349	493	—
Shear	34	—	425	—	352

by the fact that the approximate cutout contour has a small curvature at the critical section, which corresponds to a low value of the calculated stress concentration factor.

TABLE 7

THEORETICAL LIMIT STRESS VALUES AT INITIATION OF MATERIAL DELAMINATION

Stress Concentrator	Cutout Orientation	Loading Mode	Maximum Theoretical Stress Concentration Factor	Direction of Maximum Stress in Deg	Limit Stress in kgf/cm²	
					Tension	Compression
Circular hole		Tension	3,27	0	2440	—
		Shear	3,8	45	—	1300
		ω = 3	3,7	80	1825	—
		ω = 2.7	3,7	82	2080	—
Cutouts in Figure-Eight Form	Perpendicular to specimen axis	Tension	9,7	0	3140	—
		Shear	3,2	48	—	920
		ω = 2.41	9,75	3	4300	—
		ω = 1.39	9,8	5	4000	—
	Parallel to specimen axis	Tension	2,33	0	1210	—
		Shear	3,2	48	—	890
		ω = 2.41	3,5	16	1650	—
		ω = 1.36	4,3	14	1665	—

CHAPTER 9

EXAMPLES OF STRENGTH CALCULATIONS

§1. Thin-Wall Tube Under Short-Term Internal Pressure

For several GRP, the limit curve for the positive principal stresses and the plane stress state is described satisfactorily by and equation of the form [164]

$$\sigma_\theta^2 + \kappa_1\sigma_z^2 + \kappa_2\sigma_\theta\sigma_z + \kappa_3\sigma_\theta + \kappa_4\sigma_z = \kappa_5, \tag{1}$$

where k_i are determined by the relationships between the strength limits in different directions for the simple loading modes (tension, compression, and shear).

The strength margin can be characterized by the ratio of the limit stresses to the working stresses

$$n = \frac{\sigma_{\theta\,пред}}{\sigma_{\theta\,раб}} = \frac{\sigma_{z\,пред}}{\sigma_{z\,раб}}, \tag{2}$$

since the stresses σ_θ and σ_z at each point increase in proportion to the same parameter — the internal pressure. However, depending on the reinforcement form [85] the relationships between the strength limits $\sigma_{b\,z}$ and $\sigma_{b\theta}$ may change, and we can find the strength margins

$$n_z = \frac{\sigma_{bz}}{\sigma_{z\,раб}} \text{ and } n_\theta = \frac{\sigma_{b\theta}}{\sigma_{\theta\,раб}}. \tag{3}$$

In this case, the limit curve equation, in which the left side is numerically equal to the right side if we take $\sigma_\theta = \sigma_{\theta\ lim}$ and $\sigma_z = \sigma_{z\ lim}$, is written in the form

$$n^2 n_z^2 \sigma_{\theta\theta}^2 + \kappa_1 n^2 n_\theta^2 \sigma_{zz}^2 + \kappa_2 n^2 \sigma_{zz} \sigma_{\theta\theta} n_\theta n_z + \kappa_3 n n_\theta n_z^2 \sigma_{\theta\theta} + \\ + \kappa_4 n n_z n_\theta^2 \sigma_{zz} = \kappa_5 n_\theta^2 n_z^2. \tag{4}$$

For a thin-wall tube made from the 33-18c composite with reinforcement by an equal number of fibers in the σ_θ and σ_z directions, the limits $\sigma_{b\ z}$ and $\sigma_{b\theta}$ are equal and (4) simplifies to

$$n^2 n_z^2 + \kappa_1 n^2 n_\theta^2 + \kappa_2 n^2 n_z n_\theta + \frac{\kappa_3}{\sigma_{z\theta}} n n_\theta n_z^2 + \\ + \frac{\kappa_4}{\sigma_{z\theta}} n n_z n_\theta^2 = 0{,}87 n_\theta^2 n_z^2. \tag{5}$$

In this case, we can determine the individual safety factors if we know the working stresses. In the case of plane deformation of a tube with restrained ends [2, 70]

$$\left.\begin{aligned} \sigma_r &= \frac{p c^{\kappa+1}}{1-c^{2\kappa}} \left(\frac{r}{b}\right)^{\kappa-1} - \frac{p c^{\kappa+1}}{1-c^{2\kappa}} \left(\frac{b}{r}\right)^{\kappa+1}; \\ \sigma_\theta &= \frac{p c^{\kappa+1}}{1-c^{2\kappa}} \left(\frac{r}{b}\right)^{\kappa-1} + \frac{p c^{\kappa+1}}{1-c^{2\kappa}} \kappa \left(\frac{b}{r}\right)^{\kappa+1}; \\ \sigma_z &= -\frac{1}{a_{33}} (a_{13}\sigma_r + a_{23}\sigma_\theta). \end{aligned}\right\} \tag{6}$$

where

$$\kappa = \sqrt{\frac{a_{11}a_{23} - a_{13}^2}{a_{22}a_{33} - a_{23}^2}} = \\ = \sqrt{\frac{E_\theta}{E_r}\left(\frac{1-\nu_{zr}\nu_{rz}}{1-\nu_{r\theta}\nu_{\theta r}}\right)}.$$

The coefficients defining the stress distribution and the limit curve for the composite 33-18c (1/c = b/a = 100/55) are $k = 3.22$; $k_1 = 1$; $k_2 = -2$; $k_3 = k_4 = -6$; $k_5 = 1600$ (Figure 1).

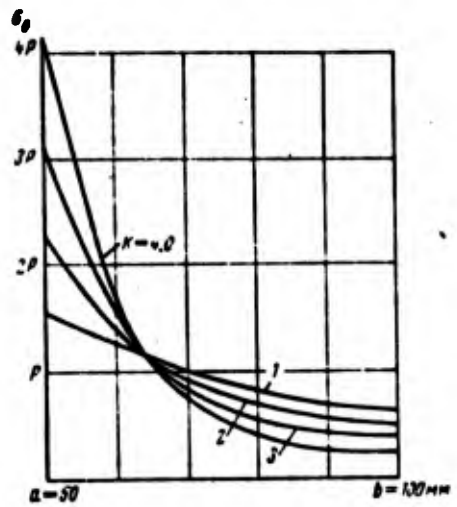

Figure 1. Distribution of circumferential stresses in thin-wall tube for different $k[(d\sigma_\theta/dr)(1/\sigma_{\theta\ max}) \approx 0.05]$.

The tangential stress diagrams are nonuniform, and in calculating the short-term strength the breaking stresses can be calculated if the actual diagrams are replaced by linear diagrams (See Figure 1). In the present case, linearization yields a stressed ring thickness ~20 mm. For a tube 500 mm long, we obtain the stressed area 10^4 mm^2. Using the Weibull approach (§3, Chapter 6) and relation (66) (Chapter 6), we find $\sigma_{b\theta}$ with account for the stress distribution nonuniformity for m = 7.55

$$\frac{\sigma'_{e0}}{\sigma_{e0}} = (15,1 : 2)^{0,132} = 1,45 \text{ and } \sigma'_{e0} = 1,45\sigma^{*}_{e0}.$$

We calculate the stresses $\sigma_{b\theta}$ and $\sigma_{b\,z}$ with account for the scale effect

$$\sigma_{e0} = 15,8 + \frac{43,8}{10\,000^{0,132}} = 29,7 \text{ kgf/mm}^2 (\sigma'_{e0} = 43 \text{ kgf/mm}^2);$$

$$\sigma_{ez} = 15,8 + \frac{43,8}{1800^{0,132}} = 32 \text{ kgf/mm}^2.$$

Let the pressure equal 500 at, then

$$\sigma_{\theta\,max} = 1700 \text{ kgf/cm}^2; \quad \sigma_{r\,max} = -500 \text{ kgf/cm}^2;$$

$$\sigma_z = -\frac{1}{3,572 \cdot 10^{-6}} 0,75 \cdot 10^{-6}(-400) + 0,572 \cdot 10^{-6}(1600) =$$

$$= -160 \text{ kgf/cm}^2.$$

*Calculating the relative gradient, we obtain $\bar{G} = d\sigma_b/dr\sigma_{\theta\ max} \approx 0.053$; $\sigma_{b\theta} = 40$ kgf/mm^2 (see Figure 17, Chapter 6).

We calculate $n_z = 3200/160 = 20$ and $n_\theta = 4300/1700 = 2.53$ and find the overall safety factor n from (4), $n = 2.0$. We note that in evaluating failure probability we must consider the dispersions of the quantities $\sigma_{b\,z}$ and $\sigma_{b\theta}$, which in the general case are not equal and have definite confidence limits.

§2. Calculation of Solid Orthotropic Disk

The basic equations for the stresses in a solid orthotropic rotating disk are [96]

$$\left.\begin{aligned}\sigma_r &= \rho\omega^2 r^2 \frac{3+\nu_\theta}{9-\kappa^2}\left[\left(\frac{r}{b}\right)^{\kappa-3}-1\right];\\ \sigma_\theta &= \rho\omega^2 r^2 \frac{3+\nu_\theta}{9-\kappa^2}\left[\left(\frac{r}{b}\right)^{\kappa-3}\kappa-\frac{\kappa^2+3\nu_\theta}{3+\nu_\theta}\right].\end{aligned}\right\} \tag{7}$$

The maximum values which the stresses σ_r reach for $r = b\sqrt[\kappa-3]{\frac{2}{\kappa-1}}$, are determined by the formula

$$\sigma_{r\max} = \rho\omega^2 b^2 \frac{3+\nu_\theta}{9-\kappa^2}\left[\left(\frac{2}{\kappa-1}\right)^{\frac{\kappa-1}{\kappa-3}}-\left(\frac{2}{\kappa-1}\right)^{\frac{2}{\kappa-3}}\right]. \tag{8}$$

The maximum θ_θ stress arises for $r = b\sqrt[\kappa-3]{\frac{2(\kappa^2+3\nu_\theta)}{\kappa(3+\nu_\theta)(\kappa-1)}}$ and is equal to

$$\sigma_{\theta\max} = \rho\omega^2 b^2 \frac{3+\nu_\theta}{9-\kappa^2}\left\{\left[\frac{2(\kappa^2+3\nu_\theta)}{\kappa(3+\nu_\theta)(\kappa-1)}\right]^{\frac{\kappa-1}{\kappa-3}}\kappa-\right.$$
$$\left.-\frac{\kappa^2+3\nu_\theta}{3+\nu_\theta}\left[\frac{2(\kappa^2+3\nu_\theta)}{\kappa(3+\nu_\theta)(\kappa-1)}\right]^{\frac{2}{\kappa-3}}\right\}, \tag{9}$$

where $k = \sqrt{\frac{E_\theta}{E_r}}$. For the epoxy-phenol composite 27-63c, $k = 4.00$, $\nu_\theta = 0.23$. With account for this, we obtain for the disk ($b = 150$ mm, $h = 7.5$ mm)

$$\sigma_{r\,max} = 0{,}0658\rho\omega^2 b^2 \quad (r = 0{,}817b);$$
$$\sigma_{\theta\,max} = 0{,}596\rho\omega^2 b^2 \quad (r = 0{,}874b);$$
$$\sigma_{\theta} = 0{,}555\rho\omega^2 b^2 \quad (r = b).$$

Hence it follows that $\sigma_{\theta\ max}/\sigma_{r\ max} = 9.06$ and the tangential stresses are definitive.

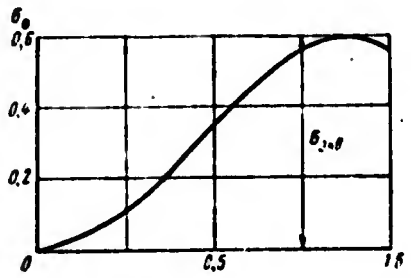

Figure 2. Distribution of σ_θ stresses in rotating disk as fractions of $\rho\omega^2 b^2$.

In the zone of maximum circumferential stresses, the ratio $\sigma_\theta/\sigma_r = 13.9$. The stress distribution is shown in Figure 2. The most highly stressed part of the disk is in the segment r = 0.75 — 1, and failure is most probable in this zone. The real σ_θ diagram can be replaced by the stress σ_{eq}. In this case, F = 0.25, $bh_{disc\ a}$ = 280 mm², $\bar{\sigma}_b$ = 42.6 kgf/mm² (see §4, Chapter 4), v_{σ_b} = 11.0%.

For the probabilities (see Figure 24, Chapter 6) 0.03; 0.003; 0.0003, and 0.00003 (v_σ = 11%), the required safety factors are approximately 1.25, 1.30, 1.50 and 1.80, and therefore $\sigma_{\theta\ eq}$ = 34.4, 32.5, 28.0, 24 kgf/mm². The limiting speeds for short-term operation are 34, 33, 30.7, $28 \cdot 10^3$ rpm.

If the disk operates under conditions of steady long-term loading (n = const), it is necessary to determine its service life or the working stress level (rpm). For example, let the speed of the same disk be $32 \cdot 10^3$ rpm. Then $\omega = 3.3 \cdot 10^3$ 1/sec and, using the equations for determining the stresses, we obtain

$$\sigma_{\theta\,max} = 30{,}3\ \text{kgf/mm}^2; \quad \sigma_{\theta r=0} = 26{,}2\ \text{kgf/mm}^2.$$

We take on the segment 0.75 b — 1.0 b

$$\sigma_{\theta_{ave}} = 0{,}588 p_{ave} b^2 = 30 \text{ kgf/mm}^2.$$

From the long-term strength curve, this yields an average lifetime of $60 \cdot 10^3$ min for m = 25. The possible lifetime scatter zone is also evaluated on the basis of the long-term strength curve constructed using the failure probability parameter.

In the case of stepwise long-term static loading with the following stress sequence $\sigma_{\theta_1} = 5.25$ kgf/cm², $\sigma_{\theta_2} = 40.4$ kgf/mm², and $\sigma_{\theta_3} = 30$ kgf/mm² with durations $\tau_1 = 15$ min, $\tau_2 = 1.6$ min, $\tau_3 = 600$ min, the lifetime determined for the condition $0 \leq D_x \leq 1$ (see §2, Chapter 6) amounts to 20 blocks (about 205 hours). Refinement of the damage boundaries $D_i \leq D \leq D_f$ yields a lifetime of 16.3 blocks (about 165 hours), which is apparently within the limits of the usual lifetime scatter in long-term static tests.

§3. Calculation of Long-Term Static Failure Probability

Let us examine the failure probability calculation for components which are loaded for long time periods. In this case, we must have the load variation and long-term static strength limit functions for a definite time base. For example, let us estimate the failure probability of a tank made from the 33-18c composite working under pressure for 10^5 min with an average wall stress of $\bar{\sigma}_e = 18$ kgf/mm² with coefficient of variation 11.0% ($\bar{s}_{\sigma e} = 2.0$ kgf/mm²). The distribution curves of the long-term static strength limits as functions of loading time correspond (see Figure 3, Chapter 7) to the following equations (normal distribution law):

Base 10^2 min

$$P(\sigma_{e,\tau}) = \frac{1}{\sqrt{2\pi}\,0{,}91} \int_0^{\sigma} \exp\left[-\frac{1}{2}\left(\frac{\sigma - 33}{0{,}91}\right)^2\right] d\sigma;$$

Base 10^3 min

$$P(\sigma_{e3}) = \frac{1}{\sqrt{2\pi}\cdot 0{,}86}\int_0^{\sigma}\exp\left[-\frac{1}{2}\left(\frac{\sigma-29}{0{,}86}\right)^2\right]d\sigma;$$

Base 10^5 min

$$P(\sigma_{e5}) = \frac{1}{\sqrt{2\pi}\cdot 0{,}71}\int_0^{\sigma}\exp\left[-\frac{1}{2}\left(\frac{\sigma-26{,}5}{0{,}71}\right)^2\right]d\sigma.$$

The failure probability under long-term static stress (§6, Chapter 6) is

$$V = \int_{\sigma=0}^{\sigma=\sigma_{max}} P(\sigma_e)\,p(\sigma_e)\,d\sigma,$$

where $P(\sigma_b)$ is the integral fracture stress (long-term strength limit) probability; $p(\sigma_e)$ is the probability density of the effective stresses. We calculate the probabilities V using the scheme shown in the table.

$$V = \sum_{1}^{18} p(\sigma_e)\,P(\sigma_e) = 6{,}5\cdot 10^{-5}.$$

Thus, the strength of a tank made from the 33-18c GRP is guaranteed for 10^5 min for the given failure probability.

CALCULATION OF FAILURE PROBABILITY FOR LONG-TERM LOADING

$\sigma_e = \bar{\sigma}_e + 2\bar{s}_{be}$	z	$p(\sigma_e)$	$P(\sigma_b)$	$p(\sigma_e) \cdot P(\sigma_b)$
20	1	0,24197	—	—
20,5	1,25	0,18265	—	—
21	1,50	0,12952	—	—
21,5	1,75	0,08628	—	—
22	2,00	0,05399	—	—
22,5	2,25	0,03174	—	—
23,0	2,50	0,01753	—	—
23,5	2,75	0,00909	—	—
24,0	3,0	0,00443	—	—
24,5	3,25	0,00203	—	—
25,0	3,50	0,00087	—	—
25,5	3,75	0,00035	0,00043	$0,01505 \cdot 10^{-5}$
26,0	4,00	0,00013	0,04846	$0,62900 \cdot 10^{-5}$
26,5	4,25	0,00007	0,50000	$3,5 \cdot 10^{-5}$
27	4,50	0,00002	0,95154	$1,90308 \cdot 10^{-5}$
27,5	4,75	0,000005	0,99957	$0,49978 \cdot 10^{-5}$
28	5,00	0,00000	1,0000	0,0000
28,5	5,25	0,00000	1,0000	0,00000
				$6,57465 \cdot 10^{-5}$

REFERENCES

1. Александров А. П. и Журков С. Н. Явление хрупкого разрыва. М., Гостехтеоризлат, 1933.
2. Амбарцумян С. А. Теория анизотропных оболочек. М., Физматгиз, 1961.
3. Андреевская Г. Д. Высокопрочные ориентированные стеклопластики. М., «Наука», 1967.
4. Андреевская Г. Д. и др. Влияние модифицированной поверхности стеклянных волокон на адгезию и механическую прочность стеклопластиков. «Механика полимеров», 1965, № 1.
5. Асланова М. С. Волокна, нити и ткани из стекла. М., Гизлегпром, 1945.
6. Армированные стеклопластики. Сб. трудов, 1966, № 55 (ЛМИ).
7. Ашкенази Е. К. Вопросы анизотропии прочности. «Механика полимеров», 1965, № 2.
8. Ашкенази Е. К. и Позднияков А. А. Испытание стеклопластиков на усталость. «Заводская лаборатория», 1961, № 10.
9. Баренблатт Г. И. О равновесных трещинах, образующихся при хрупком разрушении. Прямолинейные трещины в плоских пластинках. «Прикладная математика и механика», 1959, № 4.
10. Баренблатт Г. И. «Прикладная математика и механика», 1961, № 2.
11. Баренблатт Г. И., Энтов В. М., Салганик Р. Л. О кинетике распространения трещин. Замечание о правиле суммирования повреждаемостей. «Механика твердого тела», 1967, № 1 и № 2.
12. Бартенев Г. М. и Бовкуненко А. Н. Прочность стеклянных волокон и влияние на нее различных факторов. ЖТФ. Т. 26. Вып. 11, 1956.
13. Бартенев Г. М. и Бовкуненко А. Н. Структура стекла и прочность стеклянных волокон. ЖФХ. Т. 29, Вып. 3, 1955.
14. Бартенев Г. М. Зависимость прочности от времени действия нагрузки при хрупком разрыве. Т. 71. Изд. ДАН СССР, 1950, № 1.
15. Бартенев Г. М. и Зуев Ю. С. Прочность и разрушение высокоэластичных материалов. М., «Химия», 1964.
16. Бартенев Г. М. К вопросу о прочности нитей из аморфного материала ЖТФ. Т. 21. Вып. 5, 1951.
17. Бартенев Г. М. О природе высокой прочности стеклянных волокон. «Пластические массы», 1960, № 1.
18. Бартенев Г. М. и Паншин Б. И. О долговечности органического стекла при циклических нагружениях. «Известия АН СССР. Механика и машиностроение», 1960, № 6.
19. Бартенев Г. М. и Сидоров А. Б. Статистическая прочность стеклянных волокон. «Механика полимеров», 1966, № 1.

20. Бартенев Г. М. Статистическая теория прочности системы параллельных стержней в частности, стеклянных волокон Сб. научно-технических докладов совещания по статистическим методам прочности в машиностроении. Вып. 1. Изд. НТО Машпром, 1964.

21. Бела А. Влияние расположения стеклянных волокон на прочность армированных материалов. «Ракетная техника», т. 31, 1961, № 9.

22. Белянкин Ф. П., Яценко В. Ф., Дыбенко П. П. Прочность и деформативность слоистых пластиков. Киев, «Наукова думка», 1964.

24. Бершадский А. Л. Диаграммы растяжения и зависимость предельных характеристик некоторых стеклянных связующих от скорости деформации. «Физико-химия и механика ориентированных стеклопластиков». М., «Наука», 1967.

24. Бершейн В. А. и Гликман Л. А. Длительная прочность и ползучесть стеклопластиков как существенная материалов. Труды ЦНИИМФ, 1963, № 53

25. Бершейн В. А. и Гликман Л. А. Методика испытаний стеклопластиков на усталость при чистом изгибе плоских образцов с плавным моментом. «Заводская лаборатория», 1963, № 7.

26. Бершейн В. А. и Гликман Л. А. О механизме замедленного разрушения полимерных стеклопластиков. ФТТ, Т. 5. Вып. 8, 1963.

27. Болотин В. В. Основные уравнения теории армированных сред. «Механика полимеров», 1965, № 2.

28. Болотин В. В. Статистические методы в строительной механике. М., Госстройиздат, 1965.

29. Борзова Т. В. О распределении напряжений при растяжении волокнистых пластиков. «Вестник МГУ», 1966, № 2.

30. Ван Фо Фы Г. А. и Савин Г. Н. Об основных соотношениях теории тканых стеклопластиков. «Механика полимеров». 1965, № 1. К теории анизотропной ползучести стеклопластиков. «Механика полимеров», 1965, № 2. К теории усадочных напряжений в ориентированных стеклопластиках. «Механика полимеров», 1965, № 6.

31. Воронин М. Н. и Мотавкин А. В. Влияние масштабного фактора на прочность стеклопластика марки АГ-4в. Сб. трудов МВТУ, 1964, № 4.

32. Гершберг М. В. Исследование изменения модуля упругости стеклопластиков в произвольном направлении. «Технология судостроения», 1964, № 7.

33. Гильман Т. Н., Бухтияров Н. Т., Зацепин К. С. Исследование стеклопластиков фотоупругим и дифференциально-термическим методами. Сб. «Физико-химия и механика ориентированных стеклопластиков». М., «Наука», 1967.

34. Гмурман В. Е. Введение в теорию вероятностей и статистики. М., «Высшая школа», 1963.

35. Гольденблат Н. Н. и Копнов В. А. Прочность стеклопластиков при сложном напряженном состоянии «Механика полимеров», 1965, № 2.

36. Гольдман А. Я. и Рабинович А. Л. Зависимость упругих постоянных некоторых сетчатых полимерных связующих от температуры. Сб. «Физико-химия и механика ориентированных стеклопластиков». М., «Наука», 1967.

37. Гольдман А. Я. и Рабинович А. Л. О прочности и закономерностях деформаций при сдвиге некоторых сетчатых полимеров-связующих. «Механика полимеров», 1966, № 2.

38. Горбаткина Ю. А. Определение адгезии пленкообразующих смол к стеклянному волокну диаметром 100—200 мк. Сб. «Адгезия полимеров». М., «Наука», 1964.

39. Гуменюк В. С. В сб. «Синтез и физико-химия полимеров». Киев, «Наукова думка», 1964.

40. Дроздовский В. А. и Фридман Я. Б. Влияние трещин на механические свойства конструкционных материалов. М., Металлургиздат, 1960.

41. Дунин-Барковский И. В. и Смирнов Н. В. Теория вероятностей и математическая статистика в технике. (Общая часть). М., Гостехиздат, 1955.

42. Журков С. Н. и Абасов С. А. Зависимость прочности полимеров от молекулярного веса. ФТТ. Т. 4. Вып. 8, 1962.

43. Журков С. Н. и Нарзуллаев Б. Н. Временная зависимость прочности твердых тел. ЖТФ. Т. 23. Вып. 10, 1953.

44. Журков С. Н. Проблема прочности твердых тел. Вестник [illegible], 1957, № 11.

45. Журков С. Н. и Савицкий А. В. К вопросу о механизме разрушения твердых тел. Т. 129. Изд. ДАН СССР, 1959, № 1.

46. Журков С. Н. и Санфирова Т. П. Изучение временной и температурной зависимости металлических образцов. ФТТ. Т. 2 Вып. 6, 1960

47. Журков С. Н. и Санфирова Т. П. Температурно-временная зависимость прочности чистых металлов. Т. 101. Изд. ДАН СССР, 1955, № 2

48. Журков С. Н., Слуцкер А. И. и Марихин В. А. Образование формы субмикроскопических трещин в деформированных полимерах. ФТТ. Т.1. Вып. 11, 1959.

49. Журков С. Н. и Томашевский Э. Е. Исследование прочности твердых тел. Зависимость долговечности от напряжения. ЖТФ. Т. 25. Вып. 1. 1955.

50. Журков С. Н. и Томашевский Э. Е. Некоторые проблемы прочности твердого тела. ЖТФ, 1959.

51. Журков С. Н. Эффект повышенной прочности тонких нитей. ЖТФ. Т. 8, вып. 9, 1934.

52. Зак А. Ф. и Манько Ю. П. Научно-технический бюллетень ВНИИ стекловолокна. 1952, № 1.

53. Зак А. Ф. Физико-химические свойства стеклянного волокна. М., Гостехиздат, 1962.

54. Захаров К. В. К вопросу о прочности слоистых пластмасс. «Пластические массы», 1963, № 6.

55. Захаров К. В. Критерии прочности для слоистых пластмасс. «Пластические массы», 1963, № 6.

56. Зелинский Э. С., Куперман А. М. и Андреевская Г. Д. Прочность стеклянных волокон в момент вытягивания. Сб. «Физико-химия и механика ориентированных стеклопластиков». М., «Наука», 1967.

57. Зубов П. И. и Лепилкина Л. А. Прибор для изучения полимерных покрытий. «Вестник АН СССР», 1962, № 3.

58. Иванов Ю. М. О методах обработки результатов испытаний полимерных материалов на длительную прочность. «Заводская лаборатория», т. 27, 1961, № 4.

59. Картин В. А. и др. О прочности модельных образцов однонаправленных структур. Т. 157. Изд. ДАН СССР, 1967, № 6.

60. Киселев Б. А. и Степина И. А. Влияние механических свойств связующих на прочность стеклопластиков. «Пластические массы», 1966, № 12.

61. Кобеко П. П. Аморфные вещества. М., Изд. АН СССР, 1952.

62. Колосов Г. В. Применение функции комплексного переменного в теории упругости. М—Л., Главная редакция общетехнических дисциплин, 1935.

63. Константинов В. А. и Стреляев В. С. Влияние скорости деформирования на прочность эпоксифенольного стеклопластика. Сб. «Полимеры в машинах». Изд. НИИ МАШ, 1968.

64. Конторова Т. А. К теории прочности тонких нитей. ЖТФ. Т. 25, 1945, № 7.

65. Кортен Х. Т. Разрушение армированных пластиков. М., «Химия», 1967.

66. Кошелев П. Ф. и Степанычев Е. И. Влияние масштабного фактора на прочность стеклопластмасс. Сб. «Полимеры в машинах». НИИМАШ, 1968.

67. Кравцов Б. А. К расчету прочности стеклопластиков. Техническая информация научно-исследовательских работ. Изд. Ленинградской лесотехнической академии, 1967.

68. Крамер Н. Математическая статистика. М., Изд. иностр. лит., 1946.

69. Левицкая О. М. и др. О некоторых свойствах стекловолокнистого анизотропного материала (СВАМ). «Пластические массы», 1962, № 2.

70. Лехницкий С. Г. Анизотропные пластинки. М., Гостехиздат, 1957.

71. Ломакин В. А. и Колтунов М. А. Действие армирующих элементов при растяжении на деформацию и прочность стеклопластиков. «Механика полимеров», 1965, № 2.

72. Малинский Ю. М. и др. Изучение разрушения армированных пластиков. «Высокомолекулярные соединения», т. 17, 1964, № 5.

73. Митропольский А. К. Техника статистических вычислений. М., Физматгиз, 1961.

74. Молодцов Г. А. и Абибов А. Л. Исследование остаточных (внутренних) напряжений в армированном эпоксидном полимере. «Механика полимеров», 1965, № 4.

75. Мусхелишвили Н. И. Некоторые основные задачи математической теории упругости. М., «Наука», 1966.

76. Олдырев П. П. Определение усталостной долговечности пластмасс по температуре саморазогрева. «Механика полимеров», 1967, № 1.

77. Перри Г. Склеивание армированных пластиков. Л., Судпромгиз, 1964.

78. Поляков В. Л., Федоренко Л. Г. и Горбаткина Ю. А. Упругие характеристики связующего ПН-1 и их связь со структурой полимера. Сб. «Физико-химия и механика ориентированных стеклопластиков». М., «Наука», 1967.

79. Попов Г. Г. и Волосков Г. А. Усталостная прочность стеклопластиков холодного отверждения при симметричном цикле нагружения. Сб. трудов. Вып. 322. Изд. Всесоюзного научно-исследовательского института железнодорожного транспорта, 1966.

80. Пригоровский Н. И. Напряжения и деформации в деталях и узлах машин. М., Машгиз, 1961.

81. Рабинович А. Л. и Верховский И. А. Об упругих постоянных ориентированных стеклопластиков. «Инженерный журнал». Т. 4. Вып. 1, 1964.

82. Рабинович А. Л. Некоторые механические характеристики пленок бутварфенольного полимера. «Высокомолекулярные соединения». Т. 1. Вып. 7, 1959.

83. Рабинович А. Л. Об основных вопросах механики монолитных ориентированных стеклопластиков. Сб. «Физико-химия и механика ориентированных стеклопластиков». М., «Наука», 1967.

84. Рабинович А. Л. О прочностимодельных образцов однонаправленных структур. Т. 157. Изд. ДАН СССР, 1964, № 6.

85. Рабинович А. Л. О расчете ортотропных слоистых панелей на растяжение, сдвиг и изгиб. Труды ЦАГИ, 1948, № 675.

86. Рабинович А. Л. и Туразян А. В. Влияние скорости деформации на величину и прочность ориентированных стеклопластиков. Т. 148. Изд. ДАН СССР, 1963, № 6.

87. Работнов Ю. Н. Ползучесть элементов конструкции. М., «Наука», 1966.

88. Ратнер С. Б. Саморазогрев пластмасс при циклическом деформировании. «Механика полимеров», 1965, № 3.

89. Ребиндер Л. А. и Щукин Е. Д. Образование новых поверхностей при деформировании и разрушении твердого тела в поверхностно-активной среде. «Коллоидный журнал». Т. 20. Вып. 5, 1958.

90. Регель В. Р. и Лексовский А. М. Временная зависимость прочности при статическом и циклическом нагружении. ФТТ. Т. 4, Вып. 4, 1962.

91. Ржаницын А. Р. Применение статистических методов в расчетах сооружений на прочность и безопасность. «Строительная промышленность», 1952, № 6. Определение запаса прочности сооружений. «Строительная промышленность», 1947, № 8. Необходимость совершенствовать нормы расчета строительных конструкций. «Строительная промышленность», 1957, № 8.

92. Ржаницын А. Р. Расчет сооружений с учетом пластических свойств материала. М., Госстройиздат, 1954.

93. Розен В. Разрушение составных армированных материалов при растяжении. «Ракетная техника и космонавтика», т. 2, 1964, № 11.

94. Седракян Л. Г. К статистической теории прочности. Ереван, 1958.

95. Серенсен С. В. и Буглов Е. Г. О вероятностных представлениях переменной нагруженности деталей машин. «Вестник машиностроения», 1960, № 10.

96. Серенсен С. В. и Шнейдерович Г. П. Длительная прочность в аспекте накопления повреждений. «Вестник машиностроения», 1965, № 4.

97. Серенсен С. В. и Зайцев Г. П. Разрушение стеклопластиков при кратковременном нагружении. «Механика полимеров», 1965, № 1.

98. Серенсен С. В. и Стрелаев В. С. Об эффекте абсолютных размеров при испытании на разрыв конструкционных стеклопластиков. «Заводская лаборатория», 1962, № 4.

99. Смирнов Н. В. и Дунин-Барковский И. В. Курс теории вероятностей и математической статистики для технических приложений. М., «Наука», 1965.

100. Смирнова М. К. Прочность корпуса судна из стеклопластика. Л., «Судостроение», 1965.

101. Стрелаев В. С. Рассеяние характеристик кратковременной статической прочности стеклопластиков в связи с эффектом абсолютных размеров и неоднородного напряженного состояния. «Известия высших учебных заведений. Машиностроение», 1964, № 3.

102. Тарнопольский Ю. М. и Кинцис Т. Я. О механизме передачи усилий при деформировании ориентированных стеклопластиков. «Механика полимеров», 1965, № 1.

103. Тарнопольский Ю. М. и Скудра А. М. Прочность и деформативность конструкционных пластиков. Рига, «Зинатне», 1965.

104. Тростянская Е. Б., Пойманов А. М., Казанский Ю. П. Исследование влияния процессов, происходящих на границе стекловолокно-связующее, на прочность стеклопластиков. «Механика полимеров», 1965, № 1.

105. Физико-химия и механика ориентированных стеклопластиков. М., «Наука», 1967.

106. Швецов И. Т. В кн. В. А. Киселев. «Стеклопластики». М., Госхимиздат, 1961.

107. Akida Y., Ikeda K. Experimental Research on the Propagation of Brittle Fracture. Report of Transport. Technical Research Inst., 1959, N 40.

108. Akiba Y., Ikeda K. Welding J. 1941, V. 40.

109. Bevis R. E. and Thomas G. I. Glass fiber bundles, theoretica actual tensile strengths. 19-th Annual technical and management conference. SPI, Sec. 17—D, 1964.

110. Beyer W. Glasfaserverstärkte Kunststoffe. München, 1954.

111. Bock E. Glasfaserhaltige Schichtstoffe mit ungesattigten Polyesterharzen. Kunststoffe, Bd. 44, H. 12, 1954.

112. Boller K. H. Effect of pre-cyclic stresses on fatigue life of RP laminate. «Modern Plastics» v. 42, 1965, N 8.

113. Boller K. H. Fatigue characteristics of RP laminates subjected to axial loading. «Modern Plastics». v. 4, 1964, N 10.

114. Boller K. H. Fatigue Properties of fibrous glass — reinforcedplastics laminates, subjected to various conditions «Modern Plastics», v. 31, 1957, N 10.

115. Boyd A. R., Moore L. D. Properties and application of nonwoven unidirectional materials. 18-th Annual Technical and Management Conference, SPI, sec. 10—D. 1963.

116. Bouhal I. Výzkum strukturnich podmínek pevnosti konstrukčních termoplastu SVUM. Praha, 1967.

117. Broberg K. B. Archiv für Physik. v. 18, 1960.
118. Broutman L. J. Glass-resin joint strengths and their effect on failure mechanisms in reinforced plastics. Polymer Engineering and Science, July, 1966.
119. Broutman L. J., McGarry F. J. Glass-resin joint strength studies. 17-th Annual Technical and Management Conference SPI, Sec. 1—E, 1962.
120. Bueckner H. F. Bonndary Value Problems in Different. Equat. Univ. of Wiscons in Press 1960.
121. Charles R. Dynamic Fatigue of Glass «Journal of Applied Physics». Vol. 29, 1958, N 12.
122. Coleman B. A stochastic process model for mechanical breakdown. Trans of the Soc. of Rheogy. v. 1. 1957.
123. Coleman B. Statistics and Time Dependence Mechanikal Breakdoun in fibers. Journal of Applied Physics. v. 29, 1958, N 6.
124. Coleman B. Time Dependence of Mechanical Breakdown in Bundles of Fibers. Journal Physics. v. 29, 1957, N 7.
125. Cook J. and Gordon J. E. A mechanism for the control of crack propagation in all — brittle systems Proceeding of the Royal Society. London. Ser. A. v. 221, 1961, N 1391.
126. Cornish R. H., Nelson H. R. and Daily. J. W. Compressive fatigue and stress rupture performance of fibre-reinforced plastics. 19th Annual Technical and Management Conference, SPI, Sec. - 9E. 1964.
127. Cottrell A. H. Strong solids. Proceedings of the Royal Society London. Ser. A. v. 221. 1961, N 1389.
128. Cullen C. G., Johnston C. W. Epoxidezed polymers of butadiene in reinforced plastics. 17-th Annual Technical and Management conference, SPI, sec. — 3E. 1962.
129. Daniel I. M., Durrelli A. J. Photoelastic Investigation of Residual stresses in Glass-Plastic Composites. 16 th Annual Conference, Sec — 14A. 1961.
130. Daniels H. E. The statistical theory of the strength of bundles of threads. Proc. Royal. Soc. London. 183 A. 1945.
131. Dietz A. G. H. Design theory of reinforced plastics. Sonnebor R. H., Dietz A. G. H. «Fiberglass Reinforced Plastics» N—Y. 1954.
132. Felbeck D. K., Orowan E. Welding J. H. WRS 1955.
133. Felde W. Kerbwirkung bei glasfaserverstärkten Plasten. Plaste und Kautschuk. 1964, N 10.
134. Felde W. Kerbwirkung von Glasfaserkunstoffen bei Zugbeanspruchung. 11. Int. Tagung über GFK und Giessharze. Berlin. 1967.
135. Fisher J., Holloman J. American Inst. metallurgie Engineering. Technical Publication., 1947, N 2218.
136. Forscher F. Welding J., 11, WRS 1954.
137. Freund J. F. and Sivergleit M. Fatigue characteristics of glass filament reinforced plastic material, 21 th Annual Technical Conference, Sec. 17-B., 1966.
138. Fried N. and Kaminetsky J. The influence of material variables on the compressive properties of parallel filament rienforced plastics, 19-th Annual technical and management conference., SPI, Sec. 9A., 1964.
139. Fried N. The response of orthogonal filament wound materials to compressive stress. 20-th Anniversary Technical Conference Sec., 1-c, 1965.
140. Frost N. E., Dugdale D. S. J. Mech. and Phys. Solids, 6, 1958.
141. Gilman J. J. Cleavage, Ductility and Tenacity in Crystals (Fracture) New York, 1959.
142. Goldfein S. Lond-term Rupture and Impact stresses on Reinforced Plastics. ASTM Bulletin, 1957, N 224, Sept.
143. Griffith A. A. The Phenomena of Rupture and Flow in Solids. Philosophical transactions of the Royal Society. London. Ser. A v. 221, N 587, 1921.
144. Hasslet W. H., Cohen L. A. SPJ. J. 20, 1964, N 3.
145. Hatenkamp H., Ehrenstein G. W. Torsionsmessungen an glasfaserverstärklen Kunststoffen. Schiff und Hafen. 1964, N 9.
146. Hell J. Výzkum křehkého chování konstrukčních plastických hmot při korozi za napětí. Stubijni správa SVUM. Praha, 1967.
147. Inglis C. E. Transaction Institute Naval Architects, v. 60, 1913.
148. Irwin G. R. Report No 5 120 Naval Research Lab. 1958 TIAM Report No 213 Univ. of Illinois, 1962.
149. Irwin G. R. Structural Mechanic. N—Y., 1960.
150. Irwin G. R. Transactions ASME 6 (1957) 361 «Fracture» Handbuch der Physik. Vol. VI. Berlin. 1958.
151. Irwin G. R. Trans ASME J. Appl. Mech. (1962). sol. Welding. J. URS, 11, 1962.
152. Isida M. Proc. Fourth Congress of Appl. Mech. 1962.
153. Jaffe E. H. Boron fibers in composites. 21-th Annual Technical and Management Conference. SPI, Sec. 8C, 1966.
154. Jurajda D. Rozvoj a šíření únavové poruchy u konstrukčních termoplastu. SVUM, Praha, 1967.
155. Kabelka J. The Behaviour of Glass reinforced Polyester Under Long term Stress. V. International Reinforced Plastics Conference, London, 1966.

156. Kálna K. Mechanika křehkého lomu. Disertační práce, FJFI, 1966.
157. Katsuhiko ITO On mechanical properties especially anisotropy of reinforced plastics. Proceedings 5th Japan National Congress for Applied Mechanics.
158. Koshal R. Journal Textile Inst. 1930. N 21.
159. Krolikowski W. Das Last – Dehnungs - Diagramm glasfaserverstärkter Polyesterharze. Plaste und Kautschuk. 1962, N 8.
160. Kuhn W., Schmid R. Prüfmethoden für glasfaserverstärkte Epoxydharze. Kunststoffe. 1961, N 12.
161. Levenetz B. Compressive applications of large-diameter fiber reinforced plastics. 19-th Annual Technical and Mamagement Conference. SPJ, Sec. 11–D. 1964.
162. Levenetz B. Large-diameter fiber-reinforced plastic composite structures. 20 th Anniversary technical and management conference. Sec. 9 –F, 1965.
163. Linhart V. Výzkum šíření únavových trhlin u různě rozměrných částí (Zpráva SVUM Z — 63 — 1222) 1963. Šíření únavových trhlin (zpráva SVUM z — 65 — 1540) 1965.
164. Marin J. Theory of Strength for Combined stressos and Nonisotropic Mareriais. Journ. Aeronaut. Sci. 24, 1957.
165. Marine Design Manual For Reinforced Plastics, Mac Graw—Hill Book Comp. 1969.
166. Matting A., Wagener K. Über das Dauerfestigkeitsverhalten glasfaserstärkter Kunststoffe. Kunststoffe. 54, 1964, N 12.
167. Müller W. Über einige Probleme der Dauerschwinglestigkeit glasfaserverstärkter Kunststoffe. Technik. 17, 1962, N 11.
168. Murgotroyd J. B. The Delayed Elastic Effect in Glass Fibres and the Constitution of Glass in Fibre Form. Journal of the Society of Glass Technology, vol. XXXII. 1948.
169. Němec J. Tuhost a pevnost ocelových částí. NAČSAV, Praha, 1963.
170. Němec J. Strojírenství. 1967, N 7.
171. Neuber H. Kerbspannungslehre. Springer, Berlin, 1958.
172. Nichols R. W., Irwine W. H., Quirk A., Blewitt E. Limit approach to the prevention of Pressure Vessel Failure. «TRG» Rep, 1965.
173. Niederstadt G. Die mechanischen Eigenschaften der glasfaserstärkten kunststoife. Schiff und Hafen, 1963, N 8.
174. Orowan E. Phys. Soc. Rep. Progress Phys., 1949, 12. 142.
175. Otto W. H. and Preston F. W. Evidence Against Oriented Structure in Glass Fiberes. Journal of the Society of Glass Technology, Vol. XXXIV, 1950.
176. Outwater J. ASME Papers, 1956, 56-A.
177. Ogorkiewiez R. M. Mechanical properties of glass — fibre plastics. Automative Design Engineering, v. 3, Sept. 1964
178. Paffrath K. Dehn — und Festigkeitsverhalten von Kunststoifen in Zeitstand — Zugversuch. «Materialprüfung», 1962, 4, N 8.
179. Paris P. Stress Analysis of Cracks. «Fracture Toughness Testing and its Application. ASTM Special Technical Publication, N 381, Chicago, 1964.
180. Parratt N. J. Defects in Glass fibres and their Effect on the Strength of Plastic Mouldings. Rubber Plastics Age, March, 1960.
181. Patrick A. J., Hood J. H. Glass reinforcements for filament wound Composites. 20-th Anniversary Technical and Management Conference SPI. Sec — 9D, 1965.
182. Peirce F. T. Tensile Tests for cotton yarns. The weakest link Theoremens on the strength of long and of composite spesimens. The Journal of the textile Institute. Vol. 17 1926 N 7.
183. Petker J. The influence of resin strength and defects on the interlaminar shear strenght of filament — wound composites. SPE Transaction. v. 5, 1965, N 1.
184. Prosen S. P., Mueller C. E., Barned T. R. Interlaminar shear properties of filament wound composite materials for deep submergence. 19-th Annual Technical and Management Conference. Sec. 9—D, 1964.
185. Reinchardt K. G. Festigkeitsprobleme bei Glasfaserverstärkten Plastwerkstoffen. Plaste und Kautschuk, 1959, N 5, 6.
186. Reinkober O. Die Zerreißfestigkeit dünner Quarzfäclen. Physikalische Zeitschrift, 1931, N 6.
187. Rolfe S. T., Lyman T. M., Hall W. J. Studies of the Strain Distribution in Plates during Brittle Fracture Propagation, Zpráva IX 259—59.
188. Rosen W. Mechanics of composite strentheming fibre composite material, 1964.
189. Schmitz G. K. Characteristics of flaws on glass fibers. 20 th Annual Technical and management Conference. SPI, Sec. 3—A, 1965.
190. Schmitz G. Stress corrosion of E — Glass Fibers. Prod. Research and Development, 5, 1966, N 1.
191. Schulz J. Maximum stress and strains in the serin of a filament — wound structure. 18-th Annual Technical Conference, SPI, Sec. 7—D, 1963.
192. Serensen S. V. et al. Creep resistance and low — cycle Fatigue of Fibreglass Plastics. Proc. of the Jount. Internat Conf. on Creep, 1963.
193. Skudra A., Tarnopolskij J. Einige Grundfrage der Berechnung von GFK-Kunstruktionen, II. Int. Tagung über GFK und Giessharze. Berlin, 1967.

194. Smecal A. Die Festigkeitseigenschaften Spöder Körper. Ergebnisse exant. Naturwissenschaft. 1936, N 15.

195. Sneddon I. N. Proc. Phys. Soc. London. 187, 1946.

196. Strauss E. L. Effects of Stress Concentrations on the Strength of Reinforced Plastics Laminats. SPE 14 th An. Meet ing. of RP Division. 1953.

197. Strelasew W. S. Wytrzymelosc tworzyw sztusznych w ujeciu statystyeznym. Wybrane materialy III krajowej konferencje Wegtrzymalosciowej, 3—4 czeweo. Warzawa. 1963.

198. Sutton W. H., Rosen W. Whisker — Reinforced Plastics for Space Applications. SPE Journal. 1964, N 11.

199. Taichi Fajii, Shigehisa Otseeki, Kiyoshi Mizukawa and Ynichiro Masuda. Flexural fatigue strength of fibre reinforced plastics under constant deflection and load Proceedings of the Sereenth Japan Congress on testing Materials, 1963.

200. Taichi Fujii, Yoshiro Soyama. The Fatigye strength of Fibre Reinforced Plastics under Pulsating Testile Load, Memoir of the faculty oi engineering. Oseka city university., Vol. 4, 1962.

201. Thomas W. F. The strength and Properties of Glass Fibers Phys. chem. Glasses. v. 1, 1960, N 1.

202. Tobolsky A. Properties and structure of Polymers N. 4, 1960.

203. Tomeshot R., Fechek F. Reinforcement — air force approach to planned composite properties. 18-th Annual Technical and Management Conference. SPI 1963, Sec. 4-E.

204. Vejchar J. Některé vlastnosti polyesterových laminátu, Výzk. zpráva UVS c. 141/62.

205. Wallhäußer H., Huff H. Verhalten glasfaserverstärkter Preßstoffe bei längerer Beanspruchung. Kunststoffe. Bd. 51, H. 7, 1961.

206. Weibull W. A Statistical Theory of the Strength of Material. 1939. Stockholm. 6

207. Weiss B. S., Yukawa S. Critical appraisal of fracture mechanics. Fracture Taughness Testing and its Application. ASTM Special Technical Publication, No 381, Chicago, 1964.

208. Wende A. Herstellung von glasfaser verstärkten Polyester — Formteilen, Plaste und Kautschuk, Bd. 7, N 5, 1960.

209. Wende A. Erfahrengen beim Einsatz von glasfaser verstärkten Plasten im Boots — und Schiffbau. Bd. 10, N 4, 1963.

210. West D. Resin—fiber load transfer in fiber reinforced plastics. 19 th Annual Technical and Management Conference, SPI. Sec. 3A, 1964.

211. Westergaard H. M. J. Appl. Mech. 6 (1939) A. — 49, J. Amer. Concrete Inst. 2, 1933.

212. Wigglesworth L. A. «Matematika» 1957, N 4.

213. Yoffe E. H. The Phil. Mag. 42, 1951.

214. Zampachj J., Kabelka J. Pevnost polyesterového laminátu s PVC při kombinovaném namáhání v tahu a smyku, Výzk. zpráva UT CSAV. c. 111/62.

215. Zemánkova. Sireni krehkých trhlin z umelých hmotách, Výzkumná zpráva FTJF., 1967.

216. Zhurkov S. N. Kinetic concept of the Strength of solids. Internal. J. „Fracture Mech." 1965, N 4.

TABLE OF CONTENTS

STRENGTH OF REINFORCED PLASTICS

SYMBOL LIST

Russian	Meaning	Typed
ПРЕД	limit	lim
Д	not defined	d
ДИН	dynamic	dyn
ЭФ	effective	ef
УД	specific	sp
М	matrix	m
А	armoring (reinforcement)	a
В	breaking	b
СМ	static	st
СК	shear	sh
Р	tension	t
ДОГ	adhesive	adh
К	composite	c
С	compression	c
И	bending	b
ОКР	circumferential	cir
М	yield	y
ПРЕДВ	pre	pre
ПОВ	surface	sur
КР	critical	cr
Х·Э	characteristic energy	ce
ПЛ	plastic	pl
Т	yield	y
А	armoring (fiber)	a
ГЛ	principal	pr
РАСЧ	calculated	calc
ЭКСП	experimental	exp
Н	stressed	s

(Symbol list cont.)

Russian	Meaning	Typed
Д	effective	e
ДЛ	long-term	lt
СТАТ	static	stat
Р	tension	t
ЗАП	stored	sto
РАС	dissipated	dis
ЦИКЛ	cyclic	cyc
СР	average	av
Н·Д·С	stress rupture limit	srl
СЖ	compression	c
Р	failure	f
ДОП	permissible	per
ЦИЛ	cylinder	cyl
ПЛ	plate	pl
РАБ	working	wor
ЭКВ	equivalent	eq
Н	initial	i
К	final	f
ДИСК	disc	disc